HAL
open science

Apport des données LiDAR et hyperspectrales aéroportées pour la cartographie archéologique en milieux terrestres et immergés

Alexandre Guyot

▶ **To cite this version:**

Alexandre Guyot. Apport des données LiDAR et hyperspectrales aéroportées pour la cartographie archéologique en milieux terrestres et immergés. Géographie. Université Rennes 2, 2021. Français. NNT : 2021REN20054 . tel-03813861

HAL Id: tel-03813861

https://theses.hal.science/tel-03813861

Submitted on 13 Oct 2022

HAL is a multi-disciplinary open access archive for the deposit and dissemination of scientific research documents, whether they are published or not. The documents may come from teaching and research institutions in France or abroad, or from public or private research centers.

L'archive ouverte pluridisciplinaire **HAL**, est destinée au dépôt et à la diffusion de documents scientifiques de niveau recherche, publiés ou non, émanant des établissements d'enseignement et de recherche français ou étrangers, des laboratoires publics ou privés.

DOCTORAT SOCIETES BRETAGNE TEMPS LOIRE TERRITOIRES

UNIVERSITÉ RENNES 2

Thèse de doctorat de

L'UNIVERSITE RENNES 2

ECOLE DOCTORALE N° 604
Sociétés, Temps, Territoires
Spécialité : *Géomatique*

Par
Alexandre GUYOT

Contribution of airborne LiDAR and hyperspectral data to archaeological mapping in terrestrial and submerged environments

Thèse présentée et soutenue à Rennes, le 17 Décembre 2021

Unité de recherche : UMR 6554 LETG (Littoral, Environnement, Géomatique, Télédétection)

Rapporteurs avant soutenance :

Rosa LASAPONARA Professeure, Italian Research Council, Institute for Environmental Monitoring, CNR-IMAA
Clément MALLET Directeur de Recherche, LASTIG lab, Institut Géographique National (IGN)

Composition du Jury :

Membres: Grégor MARCHAND Directeur de Recherche, UMR 6566 CReAAH, CNRS, Président du Jury
Geert VERHOEVEN Senior Researcher, LBI ArchPro, Ludwig Boltzmann Institute

Dir. de thèse : Laurence HUBERT-MOY Professeure, UMR 6554 LETG, Université Rennes 2
Co-dir. de thèse : Marc LENNON Président, Hytech-Imaging

DOCTORAT SOCIETES BRETAGNE TEMPS LOIRE TERRITOIRES

UNIVERSITÉ RENNES 2

Thèse de doctorat de

L'UNIVERSITE RENNES 2

ECOLE DOCTORALE N° 604
Sociétés, Temps, Territoires
Spécialité : *Géomatique*

Par
Alexandre GUYOT

Contribution of airborne LiDAR and hyperspectral data to archaeological mapping in terrestrial and submerged environments

Thèse présentée et soutenue à Rennes, le 17 Décembre 2021

Unité de recherche : UMR 6554 LETG (Littoral, Environnement, Géomatique, Télédétection)

Rapporteurs avant soutenance :

Rosa LASAPONARA Professeure, Italian Research Council, Institute for Environmental Monitoring, CNR-IMAA
Clément MALLET Directeur de Recherche, LASTIG lab, Institut Géographique National (IGN)

Composition du Jury :

Membres: Grégor MARCHAND Directeur de Recherche, UMR 6566 CReAAH, CNRS, Président du Jury
Geert VERHOEVEN Senior Researcher, LBI ArchPro, Ludwig Boltzmann Institute

Dir. de thèse : Laurence HUBERT-MOY Professeure, UMR 6554 LETG, Université Rennes 2
Co-dir. de thèse : Marc LENNON Président, Hytech-Imaging

REMERCIEMENTS

Je remercie chaleureusement Laurence Hubert-Moy, ma directrice de thèse, pour son soutien, son énergie infaillible et ses nombreux conseils durant ce parcours débuté en 2016. J'adresse mes vifs remerciements à Marc Lennon, président d'Hytech-Imaging, sans qui cette thèse CIFRE n'aurait pas vu le jour et qui par sa disponibilité et son expérience a été un point d'appui scientifique et humain important durant ces trois dernières années.

Je tiens également à remercier les différents membres du jury pour avoir accepté d'examiner ce travail.

Ce travail de recherche n'aurait pas été possible sans le soutien de nombreuses personnes et organismes qui œuvrent à la connaissance, la protection et la gestion du patrimoine culturel. J'exprime toute ma reconnaissance au Service régional de l'archéologie de Bretagne et particulièrement à Yves Menez, conservateur régional de l'archéologie, pour la confiance qu'il m'a témoignée. Merci également à Thierry Lorho, conservateur du patrimoine et géomaticien, qui fut à l'initiative des réflexions concernant l'usage de la télédétection pour la carte archéologique, et qui m'a initié à ce vaste sujet, puis accompagné par ses conseils durant ce parcours. J'adresse également mes remerciements à l'ensemble des membres du SRA, et particulièrement à Christine Boujot et Olivier Kayser pour leur aide indispensable et leur partage de connaissances ainsi qu'à Laure Cadars et Jean-Manuel Conilleau pour leur disponibilité et enthousiasme. Je remercie également le DRASSM, et particulièrement Olivia Hulot, pour avoir rendu possible les opérations de vérification sur l'archipel de Molène, et pour m'avoir donné la chance d'entrevoir, depuis le pont de l'*André Malraux*, toute la complexité de la protection du patrimoine archéologique subaquatique. J'exprime ma reconnaissance à la Région Bretagne, pour son soutien au travers du projet « Mégalithes ». Je remercie également les équipes de l'OFB/PNMI, et en particulier Marie Hascoët et l'équipe de plongeurs du Parc naturel marin d'Iroise pour leur aide.

Que tous ceux qui, par leur partage de connaissances ou leurs conseils, m'ont permis d'enrichir ce travail de thèse soient également remerciés, je pense notamment à Marie-Yvane Daire, Pierre Stéphan, Philippe Gouezin, Guillaume Sicot, Florian Cousseau, Olivier Agogué, Serge Cassen, Henri Gandois, Thibaut Péres, Philippe Bodénès, Dimitri Lague, Thomas Corpetti, Eric Pottier et bien d'autres qui m'excuseront de ne pas les nommer.

L'accomplissement de cette thèse tient aussi au cadre de travail que j'ai eu la chance d'avoir durant ces trois années de doctorat. En cela je remercie toute l'équipe d'Hytech-Imaging, et en particulier Nicolas Thomas ainsi que Simon, Paul, Céline et Tristan, pour l'accueil, pour les échanges et discussions qui se poursuivront dans les prochaines années. J'adresse également mes sincères remerciements à toute l'équipe du laboratoire LETG-Rennes. Merci à Samuel Corgne qui par soutien aura été décisif dans l'aboutissement de mon projet de reprise d'études en 2016. Merci à Damien, Jean, Thomas & Thomas pour leurs conseils éclairés. Je remercie mes collègues

doctorants et post-doctorants du labo et particulièrement à Gwen et Emilien du millésime 2021-2022, pour avoir créé cet environnement de travail et d'échange si agréable.

Enfin, un très grand merci à ceux qui m'entourent. Ma famille, mes amis, que je remercie chaleureusement pour leur appui ou simplement pour m'avoir fait changer d'air. Bien sûr, rien n'aurait été possible sans le noyau essentiel. Merci Myriam pour ton soutien infaillible, je te dois beaucoup. Amandine, Louis, Valentin, merci d'être là, tout simplement ; cette thèse, vous n'êtes pas obligés de la lire, je la pose près des Kididocs, si à un moment ou un autre elle peut vous aider à suivre vos envies, ce sera -pour moi- une thèse réussie.

TABLE OF CONTENTS

REMERCIEMENTS ..... **III**

TABLE OF CONTENTS ..... **V**

LIST OF ACRONYMS ..... **IX**

GENERAL INTRODUCTION **13**

GENERAL INTRODUCTION 15

PART I. CONTEXT OF ARCHAEOLOGY AND OPTICAL REMOTE SENSING **19**

INTRODUCTION TO PART I. 21

CHAPTER 1. THE CONTEXT OF ARCHAEOLOGICAL MAPPING 23

1.1 Archaeological and cultural heritage *23*

1.1.1 Diversity of form, context and conservation state 23

1.1.2 Heritage at risk 24

1.2 Archaeological mapping *28*

1.2.1 The administrative and legal framework 28

1.2.2 Mapping for documenting the known and the unknown 31

1.2.3 Remote sensing archaeology 33

1.3 Challenges of archaeological mapping *43*

CHAPTER 2. LIDAR & HYPERSPECTRAL FOR ARCHAEOLOGICAL MAPPING 45

2.1 Airborne LiDAR *45*

2.1.1 Principles of airborne LiDAR systems 45

2.1.2 Airborne LiDAR data acquisition 47

2.1.3 Airborne LiDAR data characteristics 52

2.1.4 LiDAR data processing: from data to information 56

2.1.5 Topographic analysis for archaeological mapping 63

2.2 Airborne hyperspectral *75*

2.2.1 Principles of airborne hyperspectral imaging 75

2.2.2 Airborne hyperspectral data acquisition 77

2.2.3 Hyperspectral data characteristics 79

2.2.4 Hyperspectral data processing: from data to information 80

2.2.5 Hyperspectral analysis for archaeological mapping 83

2.3 The Current challenges and research questions *93*

CHAPTER 3. STUDY SITES AND DATA 97

3.1 Study sites *98*

3.1.1 The regional context 98

3.1.2 Study site 1: Carnac and the Gulf of Morbihan 101

3.1.3 Study site 2: the Molène archipelago 103

3.2 Data *106*

3.2.2 Archaeological reference data 118

3.2.3 *In situ* data & field campaign 124

SUMMARY OF PART I. 129

PART II. MULTISCALE TOPOGRAPHIC ANALYSIS AND DEEP CNN FOR IDENTIFICATION AND CHARACTERIZATION OF ARCHAEOLOGICAL STRUCTURES FROM LIDAR DATA..... 131

INTRODUCTION TO PART II..... 133
CHAPTER 4. COMBINED DETECTION AND SEGMENTATION OF ARCHEOLOGICAL STRUCTURES FROM LIDAR DATA USING A DEEP LEARNING APPROACH 135
4.1 Introduction 136
4.2 Materials and methods 138
4.2.1 Study area..... 138
4.2.2 Dataset 139
4.2.3 Methods 141
4.3 Results..... 144
4.3.1 Object detection and segmentation performances 144
4.3.2 Object characterization: initial results..... 150
4.3.3 Evaluation of the approach within an archaeological prospection scheme..... 152
4.4 Discussion 155
4.4.1 Sensitivity of the approach and generalization ability 155
4.4.2 Evaluation metrics for ambiguous reference data 157
4.4.3 One-class approach and post-detection characterization: potential for a new paradigm for (semi-)automatic mapping in archaeology 158
4.5 Conclusion 158
CHAPTER 5. OBJECTIVE COMPARISON OF RELIEF VISUALIZATION TECHNIQUES WITH DEEP CNN FOR ARCHAEOLOGY..... 161
5.1 Introduction 162
5.2 Materials and Methods 163
5.2.1 Study area..... 163
5.2.2 Dataset 164
5.2.3 Methods 165
5.3 Results..... 170
5.3.1 VT assessment through human-based interpretation..... 170
5.3.2 VT assessment through computer-based analysis 171
5.4 Discussion 173
5.4.1 Towards an objective creation of suitable VTs 173
5.4.2 Generalization of the benchmarking approach 173
5.4.3 Computer vision as a support for human interpretation..... 174
5.5 Conclusion 174
SUMMARY OF PART II 177

PART III. AIRBORNE HYPERSPECTRAL IMAGERY FOR MAPPING ARCHAEOLOGICAL STRUCTURES IN SUBMERGED ENVIRONMENTS 179

INTRODUCTION TO PART III 181
CHAPTER 6. AIRBORNE HYPERSPECTRAL IMAGING FOR SUBMERGED ARCHAEOLOGICAL MAPPING IN SHALLOW WATER ENVIRONMENTS 183
6.1 Introduction 184
6.2 Materials and Methods 185
6.2.1 Study Area..... 185
6.2.2 Airborne Hyperspectral Data 187

Guyot, Alexandre. Contribution of airborne LiDAR and hyperspectral data to archaeological mapping in terrestrial and submerged environments. 2021

6.2.3 Bathymetric Reference Data 187
6.2.4 Archaeological Reference Data 188
6.2.5 Dimensionality Reduction and Visualization 189
6.2.6 Unsupervised Anomaly Detection 189
6.2.7 Radiative Transfer Model over Shallow Water 190
6.3 Methodology 191
6.3.1 Workflow 191
6.3.2 Pre-processing 191
6.3.3 Simulation of True-color Image 192
6.3.4 Dimensionality Reduction Using MNF (Minimum Noise Fraction) transform 192
6.3.5 Automatic Anomaly Detection 193
6.3.6 Depth and Bottom Reflectance Estimation 193
6.4 Results 194
6.4.1 Analysis of the Simulated RGB Image 194
6.4.2 Automatic Detection of Archeological Structures 197
6.4.3 Characterization of Archeological Structures 198
6.5 Discussion and Perspectives 202
6.5.1 AHI: Potential for Application to Underwater Archaeology 202
6.5.2 Data Uncertainty and Statistical Results 202
6.5.3 From Anomaly to Archaeological Structure 203
6.5.4 Perspectives and Future Research Directions 203
6.6 Conclusion 204
CHAPTER 7. AIRBORNE HYPERSPECTRAL IMAGERY FOR ARCHAEOLOGICAL PROSPECTION OF SUBMERGED LANDSCAPES. A CASE STUDY OF THE STONE TIDAL FISHWEIRS OF THE MOLÈNE ARCHIPELAGO, FRANCE 205
7.1 Introduction 206
7.1.1 Coastal archaeology: underwater cultural heritage at risk 206
7.1.2 Archaeology of fishweirs 206
7.1.3 Mapping the seafloor 208
7.2 Study Area 210
7.3 Materials and methods 211
7.3.1 Airborne hyperspectral imagery 211
7.3.2 Reference data 211
7.3.3 Data processing 213
7.3.4 Evaluation of the approaches developed 216
7.4 Results 218
7.4.1 Analysis of results of the data-driven approach 218
7.4.2 Analysis of results of the physics-based approach 221
7.4.3 Prospection of shallow-water -bottom anomalies 225
7.5 Discussion 229
7.5.1 The data-driven approach 229
7.5.2 The physics-based approach 230
7.5.3 Complementarities of data-driven and physics-based approaches 231
7.5.4 Information provided by the spectral dimension 231
7.5.5 Hyperspectral imagery as a new tool for mapping submerged landscapes 232
7.6 Conclusion 233
SUMMARY OF PART III 235

GENERAL CONCLUSION & PERSPECTIVES 237

Guyot, Alexandre. Contribution of airborne LiDAR and hyperspectral data to archaeological mapping in terrestrial and submerged environments. 2021

GENERAL CONCLUSION & PERSPECTIVES 239

REFERENCES 247

LIST OF FIGURES 303

LIST OF TABLES 311

APPENDIX 313

Scientific publications 313

Peer-reviewed journal articles 313

Peer-reviewed conference papers 313

Conference presentations 314

Conference posters 314

Scientific reports 314

RESUME ETENDU (FRANÇAIS) 317

Guyot, Alexandre. Contribution of airborne LiDAR and hyperspectral data to archaeological mapping in terrestrial and submerged environments. 2021

LIST OF ACRONYMS

AD	*Anno domini*
AGL	*Above ground level*
AHI	*Airborne hyperspectral imagery*
ALB	*Airborne laser bathymetry /Airborne LiDAR bathymetry*
ALS	*Airborne laser system / Airborne LiDAR system*
ALTB	*Airborne laser topo-bathymetry /Airborne LiDAR topo-bathymetry*
ANN	*Artificial neural network*
AP	*Average precision*
ARVI	*Atmospherically Resistant Vegetation Index*
ASPRS	*American Society for Photogrammetry and Remote Sensing*
BBOX	*Bounding box*
BC	*Before Christ*
BCE	*Before common era*
BOA	*Bottom of atmosphere*
BP	*Before present*
CNN	*Convolutional neural network*
CONV	*Convolution (layer)*
DA	*Data augmentation*
DEM	*Digital elevation model*
DEV	*Deviation from mean elevation*
DFM	*Digital feature model*
DHM	*Digital height model*
DN	*Digital number*
DRAC	*Direction régionale des affaires culturelles*
DRASSM	*Département des recherches archéologiques subaquatiques et sous-marines*
DSM	*Digital surface model*
DTM	*Digital terrain model*
EA	*Entité archéologique*
ELF	*Empirical line fit*
EM	*Electro-magnetic*
EPSG	*European Petroleum Survey Group*
FC	*Fully convolutional (layer)*
FOV	*Field of view*
FPN	*Feature pyramid network*
FWF	*Full waveform*
FWHM	*Full width at half maximum*
GIS	*Geographic information system*

Guyot, Alexandre. Contribution of airborne LiDAR and hyperspectral data to archaeological mapping in terrestrial and submerged environments. 2021

GNSS	*Global Navigation Satellite System*
GPS	*Global positioning system*
HAT	*Highest astronomical tide*
HSI	*Hyperspectral imagery*
HS	*Hillshade*
ICOMOS	*International Council on Monuments and Sites*
IDW	*Inverse distance weighting*
IF	*Isolation forest*
IFOV	*Instantaneous field of view*
IGN	*Institut géographique national*
IMU	*Inertial measurement unit*
INS	*Inertial navigation system*
IoU	*Intersection over union*
IPCC	*Intergovernmental Panel on Climate Change*
LAT	*Lowest astronomical tide*
LD	*Local dominance*
LETG	*Littoral Environnement Télédétection Géomatique*
LiDAR	*Light detection and ranging*
LR	*Learning rate*
LUT	*Look-up table*
MBES	*Multibeam echo sounder*
MNF	*Minimum noise fraction*
MSTP	*Multiscale topographic position*
NAI	*Normalized archaeological index*
NDVI	*Normalized difference vegetation index*
NGF	*Nivellement général de la France*
NIR	*Near infra-red*
OFB	*Office français de la biodiversité*
OGC	*Open geospatial consortium*
OSUR / OSUNA	*Observatoire des sciences de l'univers de Rennes / de Nantes*
PCA	*Principal component analysis*
PDF	*Probability distribution function*
PNMI	*Parc naturel marin d'Iroise*
PRF	*Pulse rate frequency*
REIP	*Red-edge inflection point*
RF	*Random forest*
RGB	*Red-Green-Blue*
RGP	*Réseau GNSS permanent*
RMSD / RMSE	*Root mean square difference / error*
ROC	*Receiver operating curve*

Guyot, Alexandre. Contribution of airborne LiDAR and hyperspectral data to archaeological mapping in terrestrial and submerged environments. 2021

RPN	*Region proposal network*
RRIM	*Red relief image map*
RTE	*Radiative transfer equation*
RXD	*Reed-Xiaoli detector*
SAR	*Synthetic Aperture Radar*
SAVI	*Soil adjusted vegetation index*
SHOM	*Service hydrographique et océanographique de la Marine*
SLRM	*Simple local relief model*
SNR	*Signal-to-noise ratio*
SRA	*Service régional de l'archéologie*
SVF	*Sky-view factor*
SVM	*Support vector machine*
SWIM	*Shallow Water mappIng using optical reMote sensor(s)*
SWIR	*Short-wave infra-red*
TIN	*Triangulated irregular network*
TIR	*Thermal infra-red*
TOA	*Top of atmosphere*
TOF	*Time of flight*
T-SNE	*t-distributed stochastic neighbor embedding*
UAV	*Unmanned aerial vehicle*
UMAP	*Uniform Manifold Approximation and Projection*
VAT	*Visualization for Archaeological Topography*
VIS	*Visible*
VNIR	*Visible and near infra-red*
VT	*Visualization technique*

Pour les lecteurs francophones, un résumé étendu de ce manuscrit est disponible en fin de document (Résumé étendu)

Guyot, Alexandre. Contribution of airborne LiDAR and hyperspectral data to archaeological mapping in terrestrial and submerged environments. 2021

General introduction

General introduction

At the dawn of the 3rd millennium, archaeological heritage, whether at sea or on land, faces cumulative anthropogenic and natural threats. At a time of significant and rapid global environmental and social changes, the importance of preserving this finite and non-renewable heritage is increasingly pronounced (Egloff, 2008; Flatman, 2009; McManamon et al., 2008) for a better understanding of human history and its relationship with the natural environment, but also and especially to ensure its transmission to future generations (Holtorf, 2020).

In a report published in 2019, ICOMOS (International Council on Monuments and Sites), confirmed the severity of the threats affecting the cultural heritage, as well as the major role played by global climate change. It also highlighted the crucial contribution of cultural heritage in creating sustainable futures (Burke et al., 2019), and in particular its ability to provide a useful source of information and knowledge about the past to support climate change adaptation and mitigation strategies to be developed.

From diffuse archaeological artifacts to the cultural landscape, archaeological heritage is highly diverse in terms of the nature of materials, forms, and levels of preservation (Renfrew & Bahn, 2016). This physical complexity and the societal questions that arise from it have driven archaeological research for centuries (Bahn, 2014). While field and excavation investigations remain deeply linked to the archaeological approach, the 20th century, notably through the pioneering work of David L. Clarke (Clarke, 1968), saw the development of analytical approaches thanks to the emergence of other scientific disciplines such as computer science and geography. This multi-disciplinarity, integrated into archaeological practices of the 21st century, fosters the identification and documentation of archaeological sites or potential sites. This inventory and documentation work is the starting point for archaeological research and cultural heritage management concerns (Campana, 2007).

For more than a century with the acquisition of the firsts aerial photography, remote sensing has played an important role in documenting, from above, visible and invisible archaeological traces on the earth's surface (Agache, 1999; Bewley, 2003; Chevallier, 1964; Daire, 1992; Dassié, 1978; Gautier, Guigon, Leroux, et al., 2019; Reeves, 1936; Riley, 1985; Solecki, 1957; G. J. Verhoeven, 2017). In the last decades, with the rise of digital technologies, new vectors and sensors have been used for non-destructive archaeological mapping at fine spatial resolution, for large areas and beyond visible light (Parcak, 2017). A recent state-of-the-art review of remote sensing archaeology (Luo et al., 2019) illustrated the wide spectrum of data and methods available to scientists: from aerial to spaceborne platforms, from passive to active sensors operating in optical, thermal or microwave range of the electromagnetic spectrum.

The framework of this thesis is limited to airborne optical remote sensing data and more specifically to LiDAR (light detection and ranging) and hyperspectral imaging. Indeed, airborne

optical data play a key role in overcoming the limitations of the traditional archaeological mapping methods (Cavalli et al., 2007; Corns & Shaw, 2009; Devereux et al., 2005; M. Doneus et al., 2014; Fernandez-Diaz et al., 2014), as they allow access to information on archaeological landscape and sites at sub-meter spatial resolution and in environments largely opaque to the human aerial observation (Aqdus et al., 2008; M. Doneus et al., 2015; M. Doneus & Briese, 2011; Georges-Leroy et al., 2011). This type of data, mainly circumscribed to research until a few years ago, is increasingly used to perform large-scale surveys for land management concerns in operational contexts. This transition to a new use poses new methodological challenges for both data acquisition and analysis, especially for archaeological applications (D. Cowley et al., 2021; R. Opitz & Herrmann, 2018; Rączkowski, 2020; VanValkenburgh & Dufton, 2020; G. Verhoeven & Sevara, 2016).

First, airborne LiDAR data that provide topographic high-spatial resolution and high-accuracy information have transformed archaeological prospection, especially in forest environments. LiDAR data analysis, which is generally performed based on terrain visualization techniques, has led to major archaeological discoveries in recent years (Chase et al., 2011; D. H. Evans et al., 2013; Fisher et al., 2017; Inomata et al., 2020). At the same time, methods for processing airborne LiDAR data have significantly improved, particularly with the development of artificial intelligence-based approaches such as deep convolutional neural networks (Krizhevsky et al., 2012; LeCun et al., 2015). Though, while the respective contribution of LiDAR-derived terrain visualization techniques and deep learning image analysis have been highlighted, very few attempts have been made to evaluate their combined use, especially for archaeological applications. While an increasing amount of high spatial resolution LiDAR data is available in many areas, further investigation of these two types of methodological approaches and their synergy could help develop methods suitable for large-scale archaeological surveys, particularly through the detection and characterization of subtle anomalies in complex environments both in emergent and shallow-water environments.

Second, airborne hyperspectral data, which provide unique spectral information by allowing the simultaneous acquisition of information in hundreds of spectral wavelengths for each image pixel, has also largely contributed to the development of remote sensing applications (Jia et al., 2020) especially in geology, agroforestry, ecology as well as in archaeology (Cavalli et al., 2007; M. Doneus et al., 2014). However, hyperspectral imagery for coastal mapping in shallow waters is under-exploited due to the complex interactions between solar radiation and water (Kutser et al., 2020). When natural sunlight penetrates the water column, it undergoes significant attenuation, which varies according to the wavelength and characteristics of the observed environment (Mobley & Mobley, 1994). The remaining light emerging from the water and collected by a hyperspectral sensor provides an important source of information for the characterization of the marine environment (Bertels et al., 2008; Oppelt, 2012). Despite this observation and the increasing interest in hyperspectral imaging in coastal environments, no study, to our knowledge, has so far evaluated the use of airborne hyperspectral imagery applied to archaeological mapping in

Guyot, Alexandre. Contribution of airborne LiDAR and hyperspectral data to archaeological mapping in terrestrial and submerged environments. 2021

submerged environments. Indeed, while the land-sea interface zone is considered as one of the most complex areas to map and study due to its high dynamic and limited accessibility of the environment (Ouellette & Getinet, 2016), it is considered as an area of important archaeological potential (G. Bailey et al., 2020), once occupied by human populations progressively pushed inland during the rise of the sea level since the last glacial maximum (Lambeck et al., 2014).

Embedded in the "Digital Geoarchaeology" framework proposed by Siart et al. (2018) and defined at the interface between geosciences, computer sciences and archaeology (Figure I.1.1), **this thesis focuses on the evaluation of the contribution of airborne LiDAR and hyperspectral data for archaeological mapping in terrestrial and submerged environments.**

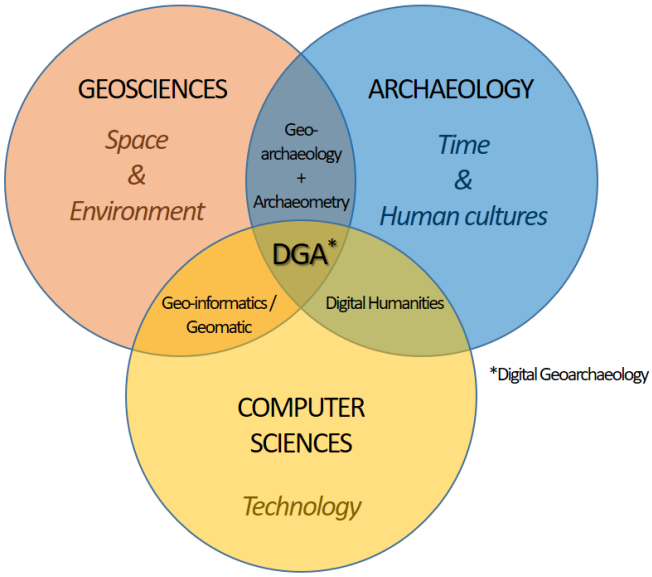

Figure I.1.1. Position of Digital Geoarchaeology, as an interface between geosciences, computer sciences and archaeology (adapted from Siart et al. (2018))

More specifically, the two main questions the thesis aims to answer are:

- Can the archaeological prospection methods based on LiDAR data be suited for large-scale archaeological surveys and more effective detection and characterization of subtle anomalies in complex environments?
- Can airborne hyperspectral imagery be identified as a source of information for archaeological mapping in shallow waters? What are the advantages and limitations of hyperspectral data in such context?

To address these questions, this thesis is structured in three parts:

- **The first part** presents the thematic and methodological framework of this thesis. **Chapter 1** examines the general context of archaeological mapping in terrestrial and submerged environments. This contextualization is followed, in **Chapter 2**, by a review of the state-of-the-art focusing on airborne optical remote sensing and its application to archaeological

Guyot, Alexandre. Contribution of airborne LiDAR and hyperspectral data to archaeological mapping in terrestrial and submerged environments. 2021

mapping. Then, **Chapter 3**, presents the study sites selected for this thesis and the related remote sensing data, as well as the reference and *in situ* data used in this research.

- **The second part** aims at proposing new methodological approaches to identify and characterize archaeological structures in woodland-dominated landscapes in Carnac and the Gulf of Morbihan using airborne LiDAR data. More specifically, in **Chapter 4**, we assess the use of multiscale topographical analysis combined with deep learning convolutional neural network to (i) (semi-)automatically detect and segment archaeological structures from LIDAR-derived terrain data and (ii) characterize the segmented structures morphologically and contextually. In **Chapter 5**, this approach is complemented by the use of the deep learning convolutional neural networks as a tool to objectively assess different LiDAR-derived terrain visualization techniques.

- **The third part** consists in suggesting new methodological approaches for archaeological mapping in submerged environments using airborne hyperspectral data. More specifically, in **Chapter 6**, we evaluated the potential of airborne hyperspectral VNIR imagery for mapping the submerged megalithic site of Er Lannic in the Gulf of Morbihan. **In Chapter 7**, we further develop the approach based on airborne hyperspectral VNIR imagery in the Molène archipelago. More precisely, we assess data-driven and physics-based hyperspectral analysis approaches to (i) document submerged ancient stone tidal fish weirs and (ii) identify water-bottom anomalies to orientate underwater archaeological surveys in shallow waters.

This research work was carried out within the framework of a Cifre thesis (*Convention industrielle de Formation par la recherche)*, with Hytech-Imaging, a R&D company in the field of earth-observation based in Plouzané (France), and the laboratory LETG-UMR6554 (*Littoral-Télédétection-Environment-Géomatique*) of the University of Rennes 2 (France).

The thesis was financially supported by the *Service de l'archéologie DRAC-Bretagne* and the *Region Bretagne* through the *Innovation* section of the *Mégalithes* program.

PART I. CONTEXT OF ARCHAEOLOGY AND OPTICAL REMOTE SENSING

Guyot, Alexandre. Contribution of airborne LiDAR and hyperspectral data to archaeological mapping in terrestrial and submerged environments. 2021

Introduction to Part I.

The first part of this manuscript exposes the thematic and methodological framework of this thesis through the presentation of the issues related to the archaeological heritage in terrestrial and submerged contexts and the approach to be implemented for its identification and characterization.

In the first chapter, we define the stakes of the preservation of the archaeological heritage, which constitutes the basic record of past human activities in space and time. This importance is put into perspective in a context where threats of human or natural origins are intensifying. We pose the administrative framework related to the management of the archaeological inventory, at international and national scales and in terrestrial and underwater contexts. We conclude by defining the general framework of remote sensing, and presenting the role of optical remote sensing for survey and mapping, as means of identification and characterization of the archaeological remains.

In the second chapter, we first focus on the principles and characteristics of airborne LiDAR and hyperspectral sensors, and their use in archaeological mapping. Then, after having presented a state-of-the-art on using airborne remote LiDAR and hyperspectral remote sensing data for archaeological mapping, we identify the current challenges and the issues addressed in this thesis.

In the third chapter, the study sites and data used for this thesis are described. First, we expose the geo-archaeological context at the regional and study site scales. Then, airborne LiDAR and hyperspectral remote sensing data, archaeological reference data and field surveys are presented in detail.

Guyot, Alexandre. Contribution of airborne LiDAR and hyperspectral data to archaeological mapping in terrestrial and submerged environments. 2021

Chapter 1. THE CONTEXT OF ARCHAEOLOGICAL MAPPING

The objective of this chapter is to demonstrate the complex nature of archaeological heritage and its fragility in a context of rapid environmental change. The background information to the study is provided through a brief definition of archaeology that outlines the importance of preserving this finite and non-renewable heritage. We also present the growing threats that this cultural wealth is facing. To this regard, archaeological mapping is considered as a way of preserving this heritage by inventorying it and supporting the development of knowledge on the societies that have preceded us.

1.1 Archaeological and cultural heritage

1.1.1 Diversity of form, context and conservation state

Every day in the world, a part of the material cultural heritage bequeathed by the generations that preceded us disappears. Whether the cause is natural (e.g. erosion, fire, rising waters) or human (e.g. armed conflict, land use planning), parts of our history and our relationship to the past are erased diffusely or brutally (Ravankhah et al., 2019). Archaeology, as a scientific discipline, is the study of the human past primarily through material remains (Olsen et al., 2012). In this respect, archaeology, by developing knowledge and understanding of the past, is one of the essential bases for the protection and transmission of cultural heritage for future generations.

In *Encyclopedia of Archaeology*, Pearsall (2008) defined archaeological sites with these terms :

"Archaeological sites are locations where former human activity is manifested. Possible evidence of events within sites includes structural features, artifacts, macro-, and microscopic flora and fauna, as well as molecular evidence such as lipids, DNA, and stable isotopes."

Demoule et al. (2020) further stressed that the definition of an archaeological site covers various temporal and spatial realities, as well as facts of different nature. The following examples illustrate only a small fraction of this diversity: the vestiges of a megalithic architecture, a deposit of ancient coins in a field, the fossilized traces of a plow on a piece of land that is now submerged by the sea, the localized accumulation of remains of consumption products of Mesolithic hunter-gatherers (shells for example) in a stratigraphic section, a ship-wreck lying at a depth of 2000m in the Atlantic Ocean.

Whatever its nature, whether submerged or terrestrial, an archaeological site is always the result of anthropogenic and/or natural formation processes. Before, during and after its occupation by man, these processes described by Stein (2001) influence the characteristics of the site (e.g. spatial extent, depth, internal state, surface state) as well as the site conservation status and its environment. Most often, these processes gradually transform the imprint of human occupation into traces or anomalies on the Earth's surface or subsurface, and depending on the conservation

Guyot, Alexandre. Contribution of airborne LiDAR and hyperspectral data to archaeological mapping in terrestrial and submerged environments. 2021

conditions, may even make it disappear. These dynamics of transformation are studied in particular through what is called archaeological taphonomy (from the Greek terms: τάφος taphos, "burial", and νόμος nomos, "law"). Although this term "taphonomy" was originally defined to describe the processes of transition of life forms from the biosphere to the lithosphere (Efremov, 1940), it was transposed to archaeology ("archaeological taphonomy") to describe the degradation of all remains (organic or otherwise) over time (Domínguez-Rodrigo et al., 2011). More generally, as the use of the term taphonomy remains debated (Lyman, 2010), we will use the terms of "site formation process" to describe the factors that create archaeological sites, as they appear to us today (Schiffer, 1987). These factors can be of natural or anthropogenic (human) origin.

Natural processes are multiple. Some of them, such as alteration, erosion or sedimentation, operate over a long period of time, while others, such as bioturbation by the growth of plants within an abandoned occupation site, can generate short-term transformations. Other processes have rapid or even brutal impacts (earthquake, fire, flood for example). These processes vary according to the geological, geographical and climatic context, and while some of them would tend to accelerate the disappearance of archaeological evidence (erosion for example), others would tend to preserve them (flooding, deposit of volcanic ashes for example) from subsequent transformations.

The natural transformation of the remains and their environment can be disrupted by degradations of human origin. On a time scale that varies from one site to another (sometimes from the moment the site was abandoned), human activities and consequent restructuration of the territory could affect the state of conservation of archaeological sites, whether voluntarily or not. Thus, the appearance of new cultural practices, modification, destruction or reconstruction of buildings, modification of land use, or simply the impact of human activities (e.g. plowing, dredging) disturb the state of the remains by modifying the transformation process in progress.

These complex transformations, associated with the original diversity of materials, necessarily lead to archaeological remains or earthworks, showing an important variety of forms: as a point or a surface, curved or linear, maculiform or geometrically organized, spatially continuous or discontinuous, elevated or hollow, having different textures, composition, density, or moisture (see (Edis et al., 1989). Without entering into considerations that would largely go beyond the scope of this thesis, these first elements of context allow us to highlight the diversity of archaeological sites, the variability of the environments in which they belong and the complexity of their life cycle (Wandsnider, 1996).

1.1.2 Heritage at risk

In the early 2000s, the ICOMOS International Committee for Archaeological Heritage Management (ICAHM) reported that much of the world's archaeological heritage was at risk[1]. Although no statistics have been published, this statement echoed a growing awareness of the

[1] https://www.icomos.org/risk/2001/icahm2001.htm

Guyot, Alexandre. Contribution of airborne LiDAR and hyperspectral data to archaeological mapping in terrestrial and submerged environments. 2021

threats to archaeological heritage in an increasingly uncertain environmental, social, economic and political world (Rick & Sandweiss, 2020).

The archaeological heritage, whether known or yet to be discovered, is a finite and non-renewable resource. The threats that weigh on this wealth are multiple and are sometimes the same ones that define the processes of formation and transformation mentioned above, and described as follows:

- **Anthropogenic threats**

  - **Development and land planning**

    Urbanization processes resulting from population growth, industrial and commercial activities, and infrastructure initiatives have direct (destruction) or indirect (degradation through pollution or soil acidification) effects on cultural heritage preservation (Agapiou et al., 2015). This threat is present across the globe and particularly important in territories under high demographic pressure and with few regulatory means for land use planning (Lane, 2011). The implementation of a preventive archaeology strategy can help to mitigate this risk while contributing to the understanding of our past (Demoule, 2007).

    While often being less visible, such threats are also affecting the underwater cultural heritage, especially in coastal areas where most human activities are taking place, such as trawling, fishing, energy and communication infrastructure development (A. M. Evans et al., 2009).

  - **Agriculture**

    Although damage to archaeology from plowing is not a new phenomenon, the intensification of farming especially since the 18th century accelerated its destructive effect (Noble et al., 2019). While it will not be possible to restrict cultivation on arable lands only to protect potential archaeological remains, initiatives[2] are being developed to guide the farming industry towards best practices and raise conscientiousness on the presence of the fragile and non-renewable traces of the past on arable land.

    Similar concerns also affect coastal environments subject to the exploitation of natural resources in the intertidal and subtidal zone. For example, the harvesting of algae by mechanized techniques such as the "Norwegian comb" can be a threat to submerged archaeological structures (Gandois et al., 2018).

[2] https://www.nps.gov/hocu/learn/historyculture/upload/Farming-the-Historic-Landscape-Caring-for-Archaeological-Sites-on-Arable-Land_2004.pdf

- **Vandalism and looting**

  Archaeological heritage is facing growing illegal and destructive excavations that aim to recover artifacts for sale on the international market (Blythe Bowman Proulx, 2013). Beyond the loss of the archaeological object itself, the irremediable destruction of the archaeological context it lied in is also lost (Elia, 1997), thus compromising its archaeological integrity. In the last decade, an increasing number of acts of archaeological vandalism and looting using metal detectors have been reported (Lecroere, 2016) despite the existence of legal enforcement (Deckers et al., 2016).

- **War and conflicts**

  We have in mind the images of the destruction of the Buddhas of Bâmiyân in Afghanistan in 2001, or those of the destruction of the temples of the ancient city of Palmyra in 2015. These destructions are the result of conflicts in areas of political or ideological instability. The effects of this risk factor are often rapid and irreparable and the means of protection are difficult, even impossible, to implement (Cunliffe, 2014).

- **Archaeological excavation**

  Archaeological resources are becoming increasingly well documented using rigorous and scientific excavation methods. Nevertheless, and paradoxically, archaeological excavation remains a factor of destruction of archaeological evidence by removing materials (and remains) from the ground, thus dismantling the relation between found deposits and their context, or irremediably losing information by considering that absence of evidence is evidence of absence (Wallach, 2019). While the "excavation is destruction" adage is widely repeated in the archaeological domain (Lucas, 2001), it remains rarely identified in the list of threats to cultural heritage, but rather identified as a destructive experiment because of its unrepeatable nature (Barker, 2002). This paradox can be mitigated by the fact that the acquisition of data and the search for scientific evidence justify the excavation ("*only excavation can uncover a sequence of structures or recover stratified and secure dating evidence*" (Barker, 2002)).

- **Lack of Administration and Legislation**

  If it does not present a direct threat to the archaeological heritage, the lack of administration can at least be considered as a factor of risk for its preservation. Examples include difficulty in defining protection zones, low integration of archaeology into development plans, unclear definition of the status of archaeological remains on private

Guyot, Alexandre. Contribution of airborne LiDAR and hyperspectral data to archaeological mapping in terrestrial and submerged environments. 2021

property (Palumbo, 2000). This factor of risk is often even more prevalent in the maritime domain for which conventional laws and regulations have little direct effect on activities relating to underwater cultural heritage (Frost, 2004).

❖ **Natural threats**

According to Kutut, Lepkova, and Zrobek (2021), based on the work of Nicu (2020) and Wang (2015), natural hazards threatening cultural heritage can be divided into five main groups: hydrological, geomorphological, seismic, climatic and biotic hazards. However, such typology omits the distinction between threats of endogenous or exogenous origin (Migoń, 2013), since several environmental factors described below can be emphasized by human factors through the effects of land management or global warming. The complex inter-relations of natural factors make it difficult to define a consensual typology within the scientific community. Ravankhah et al. (2019) have proposed a classification of natural threats in three main groups (geological, hydro-meteorological, biological) subdivided by two levels of temporal impact (slow-onset or sudden-onset) (Figure 1.1).

- **Geological threats** that refer to geological or geomorphological processes including for the sudden-onset: earthquakes, volcanic eruptions and mass movements (such as landslides, land subsidence or avalanches), and for the slow-onset: soil creep and coast/soil erosion.

- **Hydro-meteorological threats** such as heat/cold waves, surface runoff, prolonged wet periods, droughts, ocean acidification for slow-onset, and such as intense rainfall, coastal floods or wildfires for sudden-onset.

- **Biological threats** such as bioturbation by fungi or plants for slow-onset, and such as animal stampede for sudden-onset.

Guyot, Alexandre. Contribution of airborne LiDAR and hyperspectral data to archaeological mapping in terrestrial and submerged environments. 2021

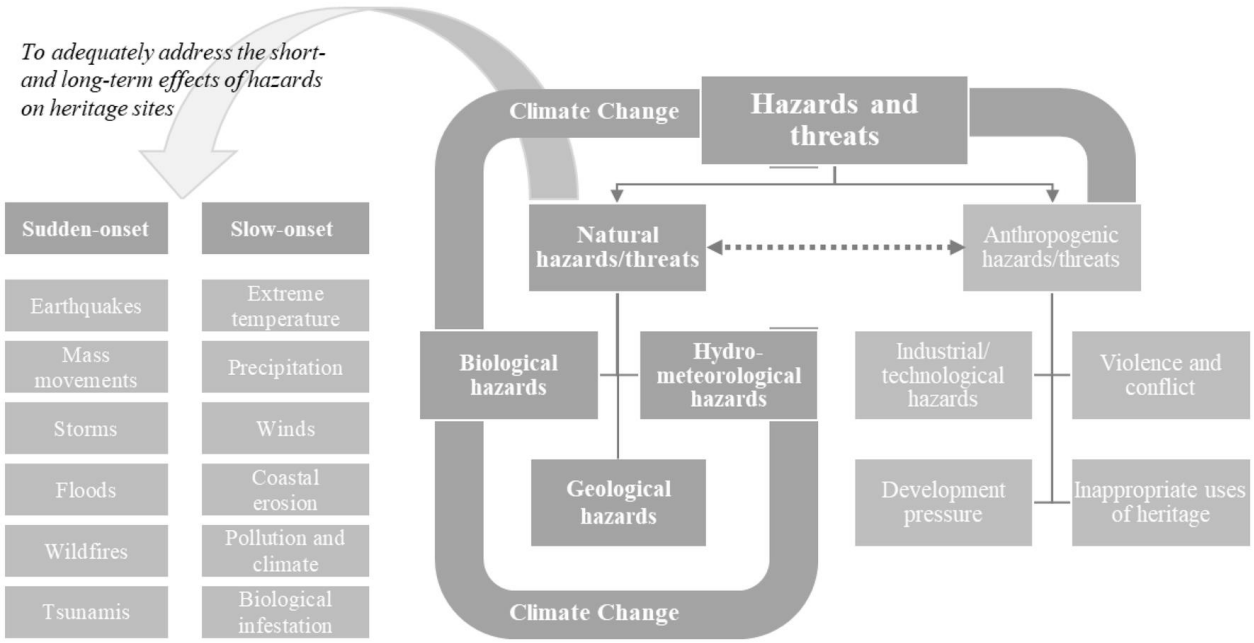

Figure 1.1. Classification of natural threats and relation to anthropogenic threats affecting cultural heritage (Ravankhah et al., 2019)

Due to the dynamics of the coastal environment, coastal sites are the most exposed to the risks of degradation or disappearance, especially in the context of global climate change (Sesana et al., 2021). The impact of natural processes (erosion, flooding) is also intensifying (Dawson et al., 2020) and puts cultural heritage at risk in these areas, which are in parallel often subject to increasing demographic pressure.

The recent report[3] of the Intergovernmental Panel on Climate Change (IPCC), which highlights the increase in intensity and number of extreme climatic phenomena (e.g. floods, droughts, storms, hurricanes) and which shares projections of sea-level rise reaching 50cm to more than one meter for 2100, is confirming the trend of this threat.

1.2 Archaeological mapping

1.2.1 The administrative and legal framework

The World Heritage Convention adopted by the general assembly of UNESCO in 1972 recognizes the obligation, for each signatory country, to ensure the identification, protection, conservation, presentation and transmission to future generations of the cultural and natural heritage situated

[3] https://www.ipcc.ch/report/sixth-assessment-report-working-group-i/

on its territory[4]. By signing the Convention, each country pledges to conserve the World Heritage sites situated on its territory, but also to protect its national heritage. In 2020, 194 countries[5] have signed this convention.

In Europe, the concept of cultural heritage was further revised in the European Convention on the Protection of Archaeological Heritage adopted in 1992 at the Valletta Convention[6].

In 2001, the UNESCO Convention on the Protection of the Underwater Cultural Heritage[7] was adopted to specifically enable states to better protect their submerged cultural heritage.

Despite such international agreements and increasing awareness raised by international organizations such as ICOMOS (International council on monuments and sites), the effective enforcement of national regulation to inventory and protect archaeological heritage is highly variable from one country to the other (Carman, 2014).

In France, the protection of the archaeological heritage defined in the *Code du Patrimoine* is under the control of the Ministry of Culture, represented by the following territorial services:

- On terrestrial land, the Ministry of Culture is represented at the regional level by the SRA (*Service regional de l'archéologie*) within the DRAC (*Direction Régionale des affaires culturelles*). The SRA, since 1991, carries out missions of inventory, study, protection and diffusion of the elements of knowledge of the archaeological heritage.
- On the maritime public domain under French jurisdiction, the DRASSM (*Département des recherches archéologiques subaquatiques et sous-marines*) leads the policy of inventory, study, protection, conservation and development of the underwater archaeological heritage. The DRASSM can also be called upon to exercise its expertise on archaeological operations carried out in inland waters in collaboration with the regional archaeological authorities (DRAC/SRA).

The inventory of archaeological heritage is a constant process, unified in France with the *carte archéologique nationale* (Chaillou & Thomas, 2007; Fromentin et al., 2006), which covers the terrestrial (641 184 km² including the metropolitan and over-sea departments and regions) and maritime territory (11 million of km² of the french exclusive economic zone).

The update and enrichment of this georeferenced archaeological heritage map are made quantitatively and qualitatively at the regional level under the responsibility of the DRAC/SRA. The qualitative enrichment includes updates of knowledge (chronological, geographical, contextual) regarding existing archaeological site records (named archaeological entities in the

[4] https://whc.unesco.org/en/conventiontext/
[5] https://whc.unesco.org/en/statesparties/
[6] https://www.coe.int/en/web/culture-and-heritage/valletta-convention
[7] http://www.unesco.org/new/en/culture/themes/underwater-cultural-heritage/2001-convention

databases). The quantitative enrichment includes the addition of new archaeological records (archaeological entities in the databases).

On land, archaeological sites and indices are georeferenced at the land-parcel level and the constantly updated archaeological map serves as a decision-making tool for the missions that are conducted under the DRAC/SRA authority, which (i) guide and supervise the archaeological research activities, (ii) ensure the protection and valorization of the archaeological heritage, (iii) support the elaboration of land use and management plans.

As an example, for the French region of Britany, where this thesis was carried out, the *carte archéologique* (Figure 1.2) consisted of nearly 22,000 recorded archaeological entities in July 2020 (latest published version[8]).

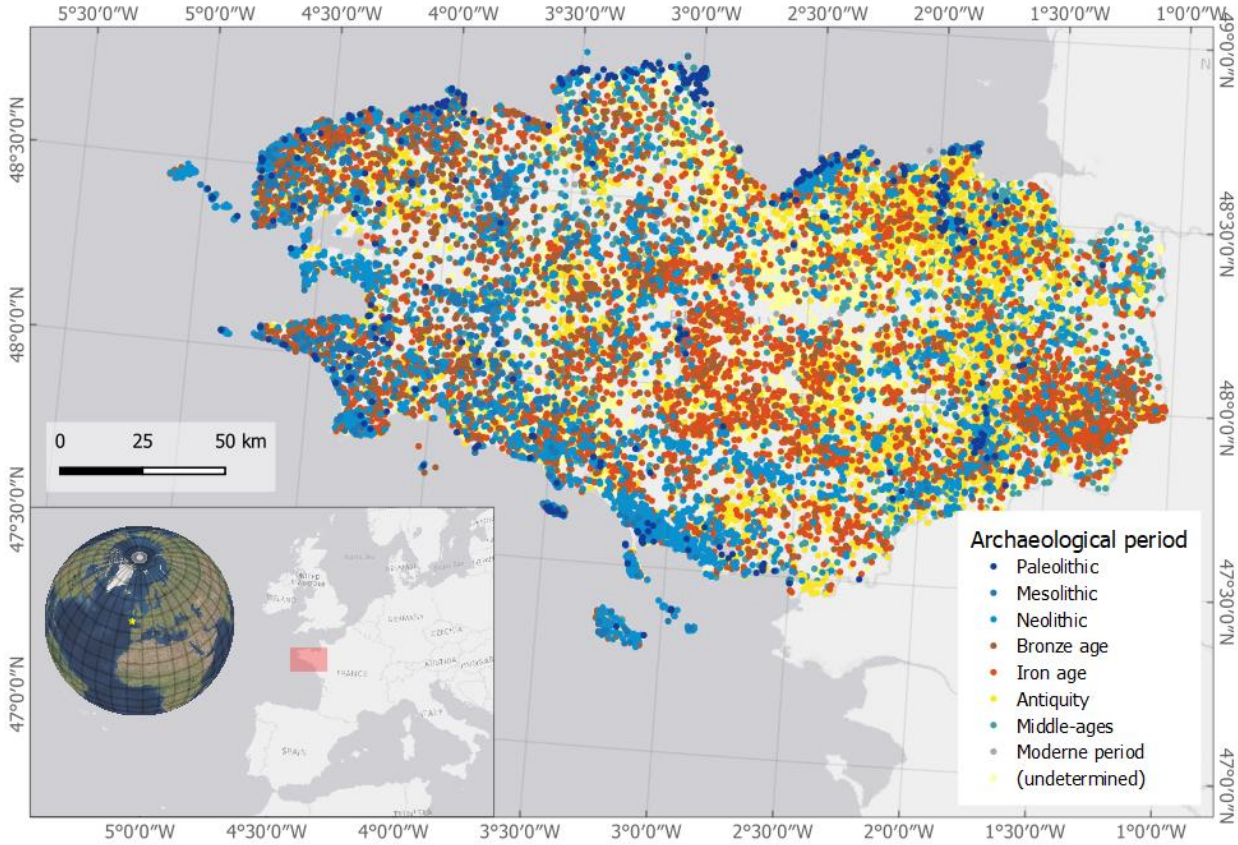

Figure 1.2. The archaeological entities (total of 21,814) recorded in the "carte archéologique" for the region of Brittany for different archaeological periods (source: Sra/DRAC, June 2020, available on Geobretagne)

In the public maritime domain, the DRASSM ensures the update of the *carte archéologique nationale*.

[8] Source : Géobretagne, Carte archéologique nationale - État de la connaissance archéologique en Bretagne (DRAC Bretagne)

Guyot, Alexandre. Contribution of airborne LiDAR and hyperspectral data to archaeological mapping in terrestrial and submerged environments. 2021

Diverse archaeological operations, controlled by the authorities under the *Code du Patrimoine*, and carried out by multiple actors (public or private sectors, academic or business sectors, professionals or volunteers), contribute to this knowledge enrichment, over land and maritime areas. The sources notably include archive records, archaeological excavations and surveys from the "rescued" (or "preventive") archeology or from the "planned" archaeology, archaeological prospection such as field-walking, diving, ground-based or surface-based geophysics, aerial or remote sensing archaeology as well as fortuitous discoveries.

1.2.2 Mapping for documenting the known and the unknown

Spatial information is a key component inseparable from temporal information in archaeology. Whether on a continental, regional, landscape scale or the scale of an archaeological site, space is an essential part of all archaeological questions (Seibert, 2006).

The object of archaeological research is above all material evidence of a very varied nature. Artifacts or structures have several spatial characteristics, including (i) an absolute position in the three dimensions of space, (ii) a morphology/shape that characterizes its three-dimensional footprint on the ground, in depth or elevation, (iii) a position relative to surrounding artifacts or structures (the topological context), (iv) a particular relationship it has in the surrounding landscape (the landscape context) and (v) an integration into a larger geographical context.

It is notably the research of these spatial characteristics (inherent and contextual) which allows, by interpretation and cross-checking, to propose a reconstruction of the human activity or occupation of a place. The mapping of archaeological elements is also the first condition for the conservation of cultural heritage (Campana, 2007).

The question of how to extract this spatial information at different scales is a major concern for increasing archaeological knowledge. This concern can be addressed differently, depending on:

- the spatial scale, which according to Gaydarska (2014), refers to two main levels of analysis: first, the intra-site level, for which the spatial relationships between artifacts or structures within a site (and often with the excavation extent) are considered; second, the inter-site level, related to the spatial relationship between sites or the relationship between a site and its landscape or surrounding environment.
- the archaeological research objectives, which can include the **identification of previously unknown sites**, and the **documentation of sites already inventoried** (for example before excavation), or the characterization of archaeological landscapes.

In this thesis, we defined the scale of analysis and archaeological research objectives within the framework of "archaeological prospection". According to Tabbagh (2018), archaeological prospection (or archaeological survey) differs from other archaeological operations such as excavation, by its non-destructive nature and by the extent of the land investigated. Analyzing ancient documents, carrying out field-walking, collecting and analyzing geophysical

Guyot, Alexandre. Contribution of airborne LiDAR and hyperspectral data to archaeological mapping in terrestrial and submerged environments. 2021

measurements, remote sensing data, underwater acoustic data are all prospection techniques likely to provide archaeological data that can be interpreted in terms of past human interactions with the environment (Dabas et al., 2006).

Large-scale archaeological prospection, in the above definition, is also related to the concept of landscape archaeology, for which archaeological remains are replaced in a wider framework of past human-environment interactions (Denham, 2017). Archaeological prospection is then not only related to the identification of cultural materials, but also to environmental aspects (climate, hydrology, landforms, vegetation and fauna, …) that interacted through time with anthropogenic processes to shape the present landscape. Landscape archaeology is therefore intrinsically an interdisciplinary approach including quantitative methods that aim at mapping and documenting landscapes, whereas anthropological approaches aim at understanding landscapes from the point of view of past human societies (Kluiving & Guttmann-Bond, 2012).

Field-walking, based on the use of human senses, remains the most accessible mean to search and inventory potential archaeological elements. However, despite being an essential in-situ approach, it expresses some important limitations. For example, field-walking is often not relevant (due to the observer's point of view) for perceiving indices or evidence occurring at large scale or of diffuse nature, which is often the case for cropmarks or soilmarks. Also, field-walking is essentially suitable in open-land context and hardly practical in forest or densely vegetated territories, where ground variations are hardly readable due to the lack of visual openness (Carrer & Gheller, 2015). Finally, large-scale coverage is highly consuming in time and human resources.

For a few decades now, the traditional archaeological prospection method of field walking has been complemented by sensor-based archaeological prospection methods to overcome the limitations of field walking. These methods include satellite and aerial remote sensing or ground-based geophysics surveys in terrestrial contexts and hydrographic surveys in submerged contexts. These digital approaches have become important tools for a quantitative approach of archaeological mapping and landscape archaeology, notably for predicting, detecting and visualizing archaeological sites and landscapes (Verhagen, 2012). The development and accessibility of massive digital data from ground-based or remote-based sensors, GIS tools, global positioning systems, and computer science tools, as support of extensive fieldwork, have revolutionized the discipline (Daly & Evans, 2005).

Amongst those methods, remote sensing has the unique characteristic of not being in physical contact with the object or area being investigated[9] (Lillesand et al., 2015) and this implies a change of paradigm in the archaeological prospection, with a large spatial perception of the subject of interest (area or object) in its environment (Crawford, 1923; X. Wang et al., 2020).

[9] Based on this definition, all surface-based measurements such as ground-based geophysics and water-based acoustic measurements are excluded from the concept of remote sensing because of their physical contact with the earth surface (this not always the case in scientific literature, where surface-based or ground-based geophysics are defined as part of the wider remote sensing framework).

Guyot, Alexandre. Contribution of airborne LiDAR and hyperspectral data to archaeological mapping in terrestrial and submerged environments. 2021

1.2.3 Remote sensing archaeology

1.2.3.1) Remote sensing framework

According to the definition proposed by Lillesand et al. (2015), *"Remote sensing is the science and art of obtaining information about an object, area, or phenomenon through the analysis of data acquired by a device that is not in contact with the object, area, or phenomenon under investigation."*

Most sensors –including biological sensors such as the eyes- are encompassed in the above broad definition. Lillesand thus narrowed down the concept of remote sensors to:

"Electromagnetic energy sensors that are operated from airborne and spaceborne platforms to assist in inventorying, mapping, and monitoring earth resources. These sensors acquire data on the way various earth surface features emit and reflect electromagnetic energy, and these data are analyzed to provide information about the resources under investigation."

This definition leads to the definition of the sub-concepts that cover a remote sensing system (Figure 1.3), including: (i) the source of energy (ii) the target, as the Earth surface from which the upwelling radiation is reflected or emitted (iii) the instrument (or sensor) used to measure this upwelling radiation, (iv) the transformation by analysis and interpretation of the measurements (data) into information to document the surface being studied and support decision making.

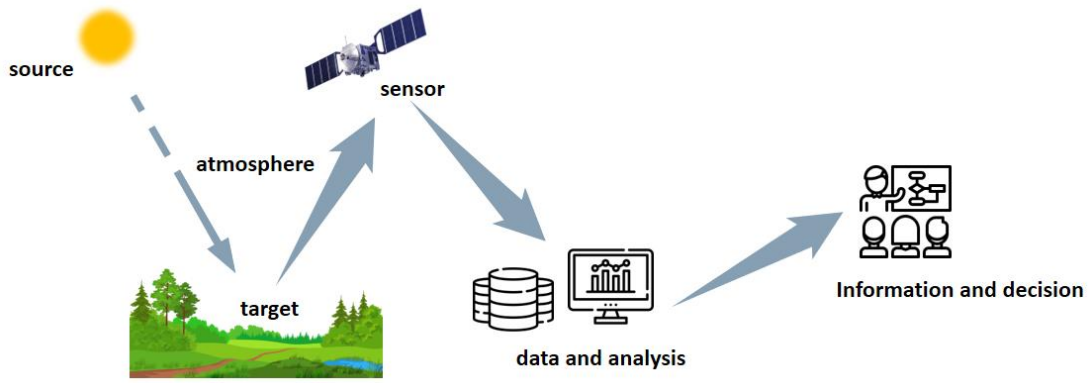

Figure 1.3. Components of a remote sensing system (adapted from Lillesand et al. (2015))

The source of energy

A remote sensing system measures electromagnetic energy reflected or emitted by a surface. The source of energy can be artificial (such as an opto-electronic source of light) or natural (the sun).

Remote sensing sensors are commonly distinguished as active and passive remote sensing (Figure 1.4). Active remote sensors, such as radar and LiDAR, are using their own source of energy to generate the electromagnetic (EM) radiation that illuminates (or irradiates) the surface. Passive remote sensors, such as multispectral or hyperspectral imaging systems, rely on an external source of energy, which is for Earth observation, the Sun.

Figure 1.4. Passive remote sensing vs active remote sensing

The electro-magnetic radiation

Radio waves, microwaves, infrared, (visible) light, ultraviolet, X-rays, and gamma rays are all examples of electromagnetic energy (radiation) composing the EM spectrum (Figure 1.5).

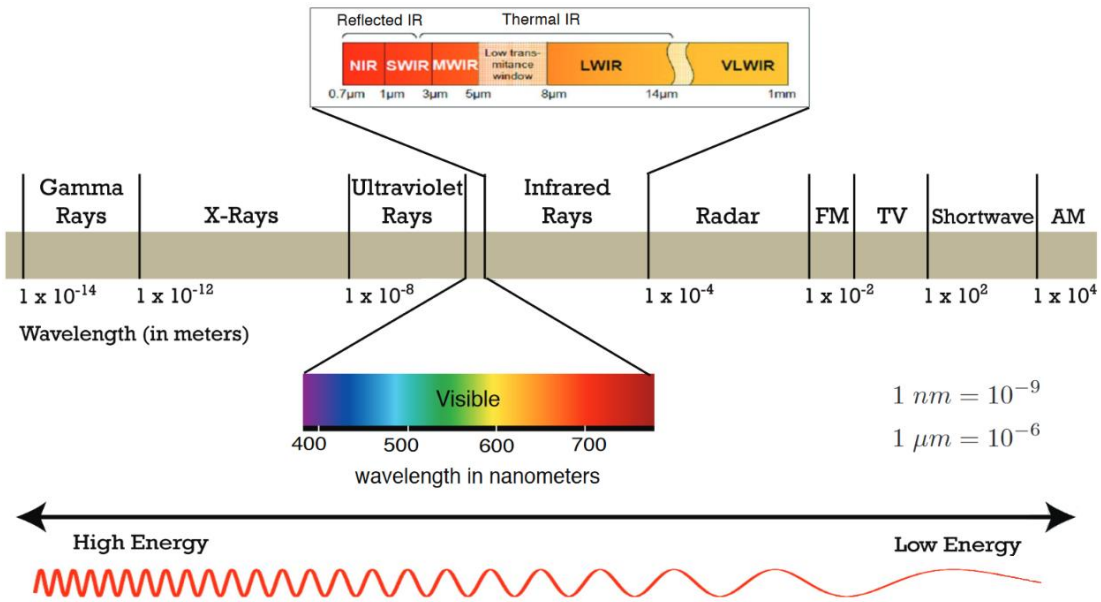

Figure 1.5. The electromagnetic spectrum with the spectral subdivisions of the visible and infrared wavebands

EM spectrum is a continuous domain defined by the wavelength (λ in m) or its frequency (f in Hz, with the relation $f = c/\lambda$, with c the speed of the wave in m.s^{-1}) of a wave, the spectrum is typically segmented in different domains. The visible (VIS) part (with wavelengths between 400nm to 700nm) being one of them -the narrowest-.

Surface materials, are in the VIS (from 400nm), NIR and SWIR domains (up to 2500nm) characterize by their spectral reflectance (the ratio of reflected radiation to incident radiation as a function of wavelength). This reflective remote sensing (Dorigo et al., 2007) is part of the optical remote sensing domain.

Vectors and sensors

Guyot, Alexandre. Contribution of airborne LiDAR and hyperspectral data to archaeological mapping in terrestrial and submerged environments. 2021

The instrument of remote sensing measure can be defined as the combination of a vector (satellite, aircraft, UAV) and a sensor measuring the EM radiation previously described.

The vector is the platform carrying the sensor as well as the trajectory measurement systems such as global navigation satellite system (GNSS) and inertial measurement unit (IMU) required to respectively compute the absolute position and orientation of the sensor during data acquisition.

A correlation exists between the distance from vector to earth surface, the spatial coverage, and the spatial sampling density (spatial resolution) that can be obtained from the sensor (Figure 1.6).

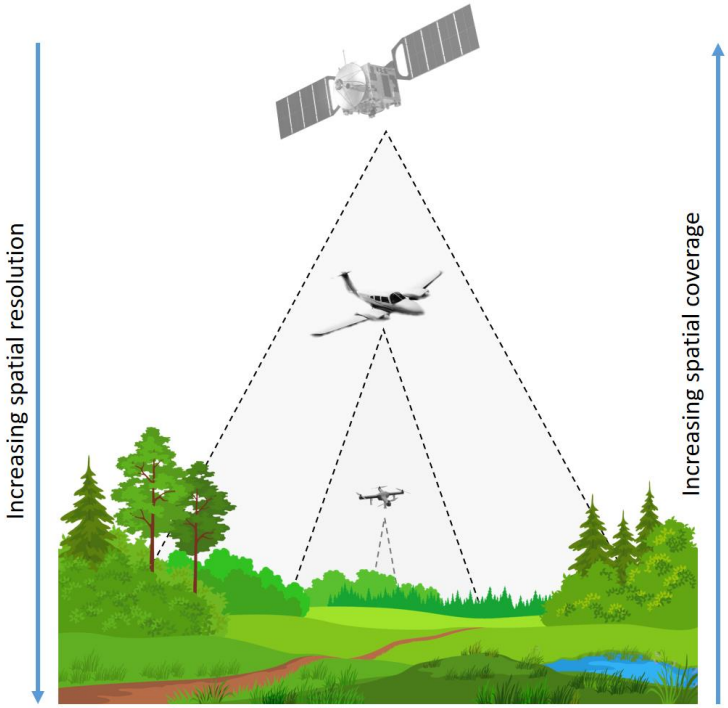

Figure 1.6. From spaceborne to airborne remote sensing vectors (adapted from Liao et al. (2018))

Remote sensing analysis and interpretation

The last component of the remote sensing framework is the data analysis and its transformation to information (within a geographical information system), then into insights (Star et al., 1997). Considering the characteristics of remote sensing data (which are multi-source, multi-scale, high-dimensional, dynamic-state, isomer and non-linear according to P. Liu (2015)), this final stage component is closely related to the fundamentals of data science in general and big data in particular, with applications requiring such as data visualization, feature extraction or pattern recognition.

1.2.3.2) 100 years of remote sensing archaeology

First views from above

Very early on in the history of archaeology, the need to look down from above became apparent. One of the first usages of aerial imagery in archaeology appeared while aviation was still in its infancy. The overflight of the Stonehenge site in the United Kingdom was carried out from a balloon by Lieutenant P.H. Sharpe in 1906 (Figure 1.7).

Figure 1.7. Aerial photography of the archaeological site of Stonehenge (United Kingdom) by Lieutenant P.H. Sharpe in 1906 (source: Historic England)

As it can be perceived on this centenary photograph, beyond the description of the megalithic structures (morphology, orientation, relative position), the general context (recent construction of ways) and the presence of traces on the ground (peripheral ditch, circular and quadrangular traces) also appear to the eye, with different colors and textures. It is the combination of these elements that offers a vision - at the time unprecedented for this site - and allowed to refine the existing knowledge of Stonehenge and led to new hypotheses that animated the archaeological research during the 20th century (D. R. Wilson, 1982).

Beyond this example of Stonehenge, the 20th century saw the joint development of military aviation and aerial photography that brought an important contribution to archaeological mapping work (Crawford, 1923; Poidebard, 1928). This interest in aerial photography rapidly led to the emergence of a full-fledged discipline: aerial archaeology (Reeves, 1936).

Guyot, Alexandre. Contribution of airborne LiDAR and hyperspectral data to archaeological mapping in terrestrial and submerged environments. 2021

Surface anomalies as potential archaeological signs

Aerial archaeology has developed after the 2nd world war, with the use of aerial survey photography (vertical imagery) in the Sahara desert to map remains of Roman structures in large territories (Baradez, 1949). In metropolitan France, aerial archaeology took off in the 1960s with the work of pioneering archaeologists such as Raymond Chevallier and Roger Agache (Chevallier, 1964). Considering the climatic conditions, territorial development and fragmentation of the landscapes that were surveyed, these archaeologists regained interest in aerial prospection at low altitude and using oblique photography.

From the outset of this new field, theoretical questions related to the relation between visual perception and archaeological evidence were raised and debated (Agache, 1999). Methods were developed and assessed (Dassié, 1978; Riley, 1944; Solecki, 1957; D. R. Wilson, 1982), and gradually converged to best practices in the process of flight-planning, aerial identification and acquisition techniques. At an early stage of the discipline visual anomalies or indices, marking the presence of a potential archaeological site on the surface or sub-surface, have been divided into variants determined by their cause of appearance:

- **Crop marks** are the result of uneven growth of vegetation (cultivated or uncultivated) over buried structures or ditches and banks (Figure 1.8). The variation of tone or plant development is directed related to the supply of water and nutrients in the soil. The presence of leveled foundations (shallow soil) generally affects vegetation growth, while the presence of a ditch (deep soil) improves vegetation growth. The contrast between the two conditions is usually exacerbated in periods of drought.

- **Soil marks** are revealed by a variation in nature of the bare soil, most often in plowed land. The difference of color or texture visible on surface can be related to archaeological remains being brought up by deep plowing, or by the natural organic deposit filling ancient ditches. Closely related are **damp marks** which are the result of the difference in soil drainage capability and can be related to the presence of subsurface structures.

- **Topographic marks** or **shadow marks** are caused by subtle topographical variations highlighted by low sun illumination. These marks can be proxies of man-made off-ground structures (standing stones, remains of walls or parcels delimitations) but also earthworks integrated into the topography (tumulus or mounds, buried-wall, ditches or embankments).

Guyot, Alexandre. Contribution of airborne LiDAR and hyperspectral data to archaeological mapping in terrestrial and submerged environments. 2021

Figure 1.8. Cropmarks showing multiple structures of a Gallic necropolis in Grésac of France (credit: J. Dassié)

In Brittany, for more than 40 years, the approach of aerial archaeology has been widely used to complete the archaeological knowledge of the territory. Despite a landscape context firstly considered unfavorable (nature of the soils, landscape fragmentation), a handful of "flying archaeologists" have been able to identify thousands of archaeological sites in arable land since the 1980s (Gautier, Guigon, & Leroux, 2019). Aerial photography has also been regularly carried out for the identification of ancient fish-trap structures (Figure 1.9) in the intertidal zone (Billard & Daire, 2019; Daire & Langouet, 2008).

Guyot, Alexandre. Contribution of airborne LiDAR and hyperspectral data to archaeological mapping in terrestrial and submerged environments. 2021

Figure 1.9. Aerial view of the remains of an ancient fish-weir visible at low tide in Servel-Lannion (credit: M. Mahéo & L. Langouët)

The limits of traditional aerial archaeology

Traditional aerial archaeology, based on on-demand low-level flights and oblique photography has produced a considerable amount of archaeological data. However, it has some limitations.

First, traditional aerial archaeology is largely limited to open-land context and remains practically ineffective over forested and highly limited in drowned coastal landscapes. Second, traditional aerial archaeology does not provide purely synoptic information but rather operates as a punctual source of information thus excluding any analysis of the landscape continuum beyond the framing of the photography. Third, traditional aerial archaeology only relies on one pair of eyes at a single point in time and space and thus is not a fully reproducible experiment. The interpretation bias concomitant to all visual perceptions cannot be challenged (although this bias is also present in desk-based visual interpretation, it can there be confronted to other interpretations). Finally, traditional aerial archaeology is highly dependent on the local landscape context as well as seasonal and weather conditions to allow for the perception of relief, soil or vegetation related contrasts (G. Verhoeven & De Vliegher, 2004).

From an archaeological point of view, the above limitations of traditional approaches of archaeological prospection have gradually created imbalances in archaeological knowledge. First, a territorial imbalance was created as a result of the gradient in the density of identified sites according to location and landscape context: open landscapes close to the main airfields have

Guyot, Alexandre. Contribution of airborne LiDAR and hyperspectral data to archaeological mapping in terrestrial and submerged environments. 2021

spontaneously been the subject to more observations than complex landscapes far from the take-off points. Second, a chronological imbalance was also created due to the bias generated by the more easily perceived traces of occupation relative to certain typo-chronologies (Bronze Age and Iron Age enclosures in particular for aerial archaeology).

The advent of a digital era

In parallel to the use of low-level oblique aerial photography prospection method, the end of the millennium has seen the emergence of the digital era in Earth observation domain. Operated from spaceborne or airborne platforms, active and passive sensors operating in optical, thermal or radiowave parts of the EM spectrum were progressively used for identifying, documenting and monitoring archaeological heritage from above (see L. Luo et al. (2019) for a review). This development of remote sensing resulted in new capabilities of observation at large, regional and global scale and new abilities to perceive surface patterns and features that were not visible to the human eye (Elachi, 2007).

The use of passive multispectral optical sensors was initiated in archaeology in the ’60s (Schaber & Gumerman, 1969) and complemented the perception capabilities of the low-level oblique aerial photography by (i) increasing the spatial dimensions of the survey (ii) increasing the spectral dimensions of the acquired data. The first aspect aimed at solving the question of spatial exhaustivity and large-scale coverage, the second aimed at enhancing the perception, beyond visible light, of subtle traces on the Earth surface, related to the potential presence of subsurface archaeological remains. As for the low-level oblique aerial photography, the objective is to identify surface anomalies resulting from spectral differences between a potentially buried archaeological structure and its surrounding environment: rather than being scrutinized by human eyes from the window of a plane, the anomalies are spotted on the acquired images by their difference in spectral reflectance (for VNIR and SWIR domains) or spectral emissivity (in the TIR domain) compared to the surrounding environment.

Multispectral imagery, which can include up to a dozen of broad spectral bands in the optical domain has been used for archaeological research, acquired from aerial platforms (Donoghue & Shennan, 1988; Hampton, 1974), but more largely from satellite platforms (Lasaponara & Masini, 2012; Parcak, 2009; Tapete & Cigna, 2019) with spatial resolution ranging from 30m (Landsat imagery) to 0.3m (Worldview-3 imagery) in the VNIR, SWIR or TIR spectral domains. Recently, the miniaturization of panchromatic thermal sensors or VNIR multispectral sensors has allowed the emergence of UAV-based archaeological surveys at very fine spatial resolution (centimetric) (Agudo et al., 2018; Poirier et al., 2014). However, these surveys remain limited to relatively small areas (few hectares at centimetric resolution) and are therefore hardly operational for large-scale archaeological prospection. The use of hyperspectral imagery, with the acquisition of continuous and narrow bands, extended the capabilities of multispectral imagery on the optical-VNIR spectral domain for archaeological prospection (Aqdus et al., 2008; Cavalli et al., 2007; M. Doneus et al., 2014; Traviglia, 2006a). Mostly operated from airborne platforms, a few attempts were

Guyot, Alexandre. Contribution of airborne LiDAR and hyperspectral data to archaeological mapping in terrestrial and submerged environments. 2021

although also made from spaceborne sensors, such as Hyperion, at the expense of low spatial resolution, thus reducing the capabilities to coarse-scale documentation (Alexakis et al., 2009; Savage et al., 2012).

Active remote sensing, such as Radar or LiDAR, by relying on the emission of their own radiations (respectively in the radio and optical part of the EM spectrum) have also been largely exploited for archaeological research. Radar, and particularly SAR (Synthetic Aperture Radar), essentially operated from satellites, have for example been used for their penetration capabilities for the archaeological prospection of buried structures (Lasaponara et al., 2017) or the identification of traces of looting (Tapete et al., 2016). Indisputably, the emergence of LiDAR technology based on the emission/reception of a laser signal fired at high-density and with high-accuracy has provided a whole new perception of the Earth topography, even under dense forest canopy (Glenn et al., 2006; Hofton et al., 2002). This unique capability transformed the integration of remote sensing approaches in the archaeological domain and led to the definition of new archaeological prospection approaches (Bewley et al., 2005; Kokalj et al., 2013; Štular et al., 2012) as well as new insights into the human-past (Chase et al., 2011; D. H. Evans et al., 2013; Inomata et al., 2020). Although LiDAR instruments have been developed for satellite platforms, their current capabilities make them unsuitable for high-resolution topographic mapping intended for archaeological applications (Kokalj & Mast, 2021). While most LiDAR acquisition projects are based on aircrafts, mirroring the miniaturization of passive sensors, UAV-based LiDARs have also been developed and are an interesting alternative to aircraft platform for surveying areas of few hectares (S. Khan et al., 2017; Poirier et al., 2020).

Remaining conceptual challenges

All of the survey tools and methods used in archaeological prospection, including remote sensing, are based on the assumption that there is some perceptible contrast between the archaeological feature and its surrounding environment (Linford, 2006). These perceptions are manifestations of surface or sub-surface anomalies. Understanding the origin of these contrasts, although they may be associated with archaeological evidence, remains limited in the absence of archaeological excavation. We are thus facing the paradox of archaeological prospection, which by non-destructive and non-intrusive means, contributes to the protection of the archaeological heritage, but which, to confirm and complete the perception it offers, would require a necessarily destructive archaeological excavation.

Nevertheless, archaeological interpretation can be provided, either as first-level interpretation based on remote sensing data (including morphological and contextual information), but this interpretation should always be built upon external archaeological information, knowledge or expertise (Figure 1.10).

Guyot, Alexandre. Contribution of airborne LiDAR and hyperspectral data to archaeological mapping in terrestrial and submerged environments. 2021

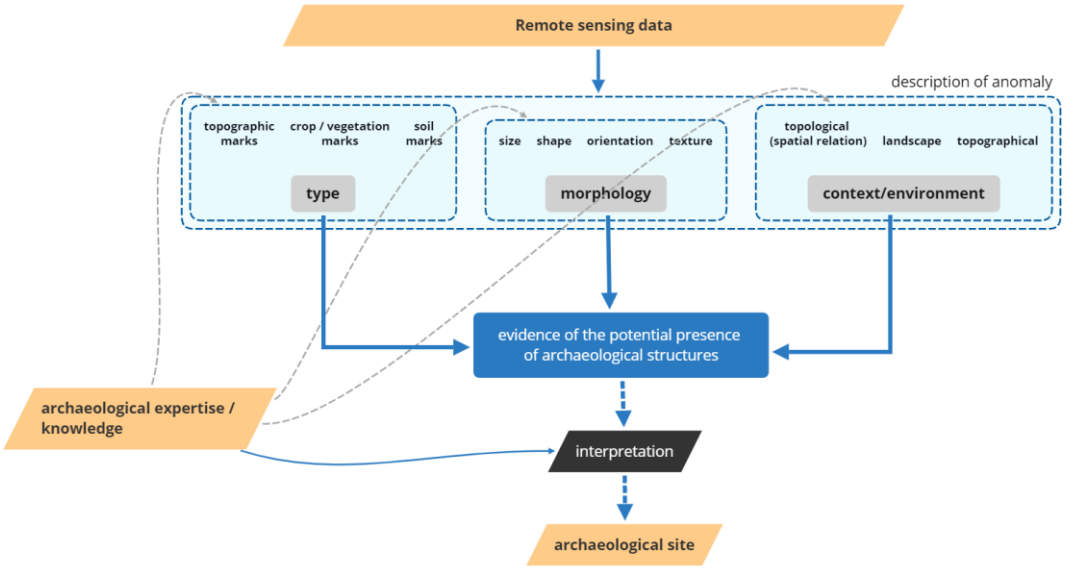

Figure 1.10. Conceptual diagram presenting the relation between remote sensing data, surface anomaly and the interpreted archaeological site

The complex relationship between remote sensing data and archaeology leads to the mention that "Remote sensing data can never be a mandatory or sole source to investigating the landscape. Landscape archaeology must be holistic or 'total' by building up a complementary body of data from multiple distinct survey approaches which, when properly integrated, constitute a digital landscape to explore." (G. J. Verhoeven, 2017)

This vision is key to the integration of remote sensing approaches in the field of archaeology. Remote sensing must be seen as a support for a subsequent human-based archaeological interpretation, as it only brings partial - yet useful - information in a wider archaeological questioning.

This "partial" view from above also brings useful information to the landscape dimensionality which goes beyond the identification of structures and sites. The concept of Landscape Archaeology as defined by Denham (2017) is the understanding of archaeological remains in terms of the wider spatial realms (both physical and meaningful) of past human experience. It therefore refers to the human-environment interaction within a spatially or culturally bounded area. This interaction can partially be seen by the traces or "sociocultural fingerprints" left by specific human societies across landscapes at multiple scales (Tarolli et al., 2019). This interaction can also be perceived, not by the presence/absence of anthropogenic geomorphic features, but by considering the landscape as a natural and cultural frame (Figure 1.11) holding elements of understanding of past human behaviors in space and time.

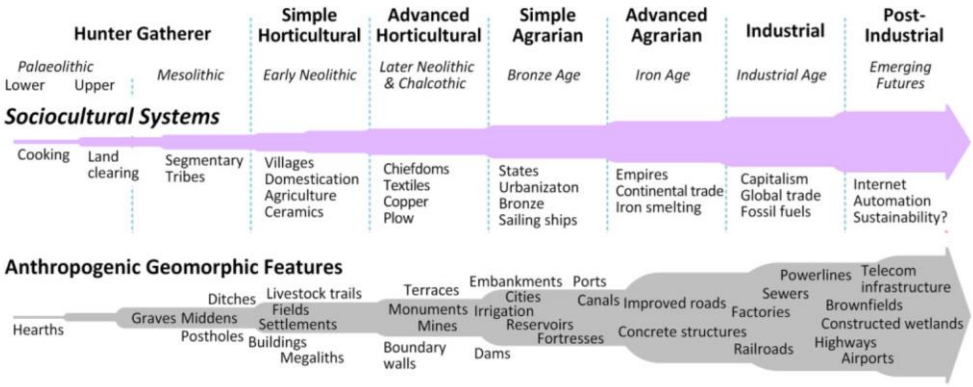

Figure 1.11. Conceptual diagram of long-term changes in sociocultural systems, cultural inheritances, societal scale, energy use and anthropogenic geomorphic features across landscapes (adapted from Tarolli et al. (2019)

The above points (uncertainty on the nature of the anomaly, complex relationship between cultural and physical traces) directly affect the concept of "ground-truth" or more adapted "reference data" so important in quantitative analysis. In archaeology, the reference data is not as easily defined nor accessible as in other fields of Earth-observation where targets are usually semantically known (or at least validated) and spatially defined. Here archaeological imprints can be spatially diffuse and are –unless already excavated and documented- rarely confirmed in terms of nature or chronology.

1.3 Challenges of archaeological mapping

While entering the 3rd millennium, the archaeological heritage is under increasing anthropogenic and natural threats. Considering the effects of global climate changes and the densification of human occupation, the coastal areas are amongst the most vulnerable environments regarding this concern.

The inventory of this finite and non-renewable resource is one of the main challenges to be met to better protect it. Archaeological prospection and mapping methods, which have been developed for nearly a hundred years, have provided an immeasurable amount of knowledge about our past and have served as an important support to protection strategies implemented by governmental or non-governmental institutions. However, within the scope of quantitative and qualitative enrichment of archaeological inventory, multiple challenges remain regarding archaeological mapping, from conceptual, methodological and operational points of view.

Some of the conceptual challenges were raised in this chapter, including the lack of formalized models that can support the ontological description of archaeological records (features, sites, landscapes) in their heterogeneous forms (D. Davis, 2021). Other important concerns, stressed in (R. Opitz & Herrmann, 2018) are the social and technical obstacles that have to be overcome to integrate remote sensing data and methods in the broad domain of archaeological research. Although the use of non-destructive remote sensing approaches contributes greatly to cultural heritage management, the increasing quantity and variety of data sources and algorithms can be seen as advances made at the margins and at the expense of theoretical and methodological expertise in the archaeological interpretation process.

These issues are indeed highly important for better integration of non-destructive survey approaches (such as remote sensing) in archaeological mapping. Nevertheless, they should not prevent the technical and methodological challenges of the discipline of remote sensing from being met, nor hinder the development of new approaches to map archaeological landscapes that are still difficult to access at a larger scale, with greater accuracy, and higher efficiency.

These issues led to the definition of the scope of this thesis, with a focus on two remote sensing data, airborne LiDAR and airborne hyperspectral, that still have to be evaluated to identify and characterize archaeological structures respectively in complex inland landscapes (including under canopy) and underwater environments.

Guyot, Alexandre. Contribution of airborne LiDAR and hyperspectral data to archaeological mapping in terrestrial and submerged environments. 2021

Chapter 2. LiDAR & HYPERSPECTRAL FOR ARCHAEOLOGICAL MAPPING

The objectives of this second chapter are to review the current state-of-the-art of airborne LiDAR & hyperspectral remote sensing for archaeological mapping and highlight the current challenges in this field of research. Then, the main research questions of this thesis are defined.

2.1 Airborne LiDAR

2.1.1 Principles of airborne LiDAR systems

LiDAR (light detection and ranging) is a remote sensing technology that uses time-of-flight and line-of-sight to calculate the accurate locations of physical objects in a known space (the known space is in relation to the scanner) (Lato et al., 2010). . Unlike the radar (radio waves) and the sonar (acoustic waves), LiDAR functions in the optical range of the electromagnetic spectrum, usually in the visible or near-infrared region.

To determine the distance between the sensor and a target, a collimated laser beam pulse is sent by the sensor (emitter part) and travels at the speed of light towards the target that reflects a part of this light energy towards the sensor (receiver part). The time difference (Δt) between emission and reception (also called Time of Flight, TOF) is measured and the distance (d) is calculated using the light speed ($c = 299\,792\,458\ \mathrm{m}.s^{-1}$) :

$$d = \frac{\Delta t.c}{2} \tag{1}$$

LiDAR instruments are used in a wide range of configurations (e.g. terrestrial in static or mobile mode, airborne, spaceborne), and for various applications (e.g. autonomous cars, atmospheric measurements, topography) (Mehendale & Neoge, 2020).

In the context of earth observation and mapping, the most common configuration is the airborne LiDAR (also referred to as Airborne Laser System (ALS)). It consists of a LiDAR scanning instrument coupled with GNSS/INS instruments for position and orientation information (Figure 2.1). The LiDAR is scanning the Earth's surface with a swath by firing laser pulses at high-frequency (several hundred thousand per second). By knowing the exact position and orientation of the sensor, the 3 -dimensional coordinates of the “echo” (or return) of light can be determined.

Guyot, Alexandre. Contribution of airborne LiDAR and hyperspectral data to archaeological mapping in terrestrial and submerged environments. 2021

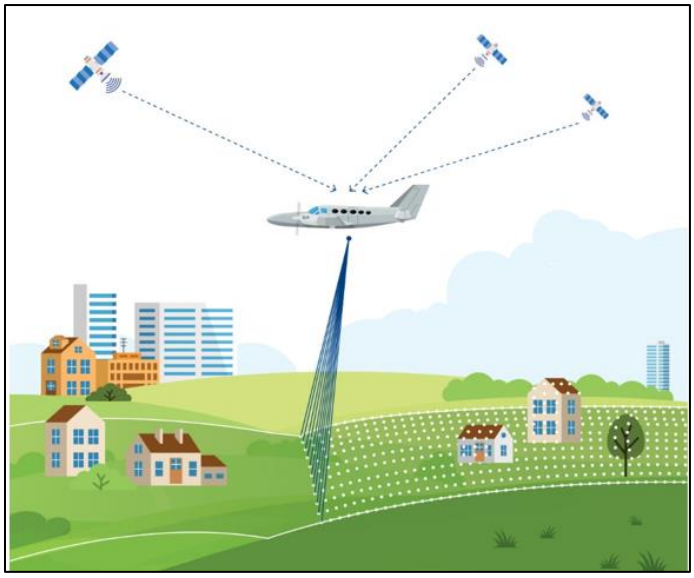

Figure 2.1. Airborne LiDAR systems (modified from IGN sources)

While the LiDAR system uses the properties of light, it cannot see through opaque material and directly identify sub-surface features. Nevertheless, because it uses a narrow collimated beam of light, a portion of the emitted signal can penetrate "open" volumes such as forest canopies (where the light can find its path through leaves and branches) and interact with sub-canopy elements (leaves, branches, trunks and eventually ground). This is a key characteristic of LiDAR, that allows the detection of multiple returns for from a single emitted pulse (Figure 2.2).

This multi-return (or multi-echo) capability, combined with a high-density (number of measurement points per m²) and centimetric accuracy of measurements, rapidly placed Airborne LiDAR as an outstanding remote sensing solution for high-resolution topographical mapping and forestry application (Brock et al., 2002; Dubayah & Drake, 2000; Webster et al., 2006).

The first usage of ALS in archaeological applications emerged almost twenty years ago (Bewley, 2003; Bewley et al., 2005; Devereux et al., 2005). In contrast to 2D remote sensing data, the 3D data provided by LiDAR data was rapidly confirmed as valuable information for the representation of subtle topographical variations of natural (Webster et al., 2006) or anthropogenic origin (M. Doneus et al., 2008). Since, LiDAR sensors have continually been developed for topographic mapping, but also for bathymetric application with the use of adapted laser wavelengths: a green laser provides a much better water penetration capability than an infra-red laser almost entirely absorbed by water surface (M. Doneus et al., 2015; Mandlburger et al., 2011).

Guyot, Alexandre. Contribution of airborne LiDAR and hyperspectral data to archaeological mapping in terrestrial and submerged environments. 2021

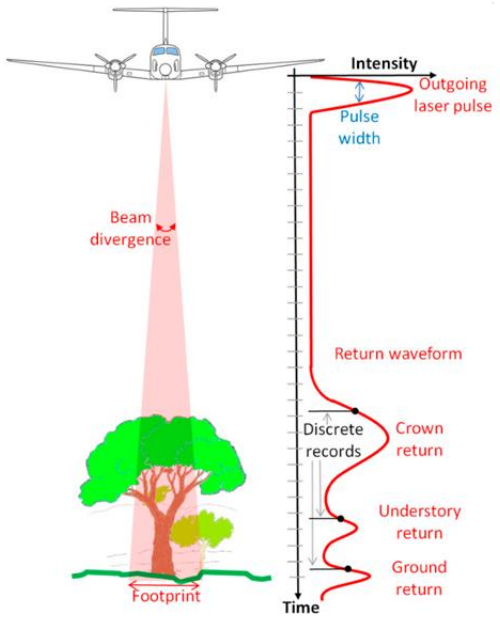

Figure 2.2. Representation of an Airborne LiDAR pulse (source: Fernandez-Diaz et al., (2014))

2.1.2 Airborne LiDAR data acquisition

Airborne LiDAR data acquisition project is driven by the data requirements such as point density or coverage, which themselves determine the flight plan. The flight time being the major cost factor of a LiDAR project, the challenge is to define the best compromise between data suitability and acquisition cost (Ussyshkin et al., 2008). Technical characteristics of airborne LiDAR sensors being various and numerous (Fernandez-Diaz et al., 2014) (Figure 2.3), they also have to be considered for LiDAR data acquisition. For topographical applications (including archaeological mapping), the flights have to be carried out in the leaf-off season, in such a way that the signal can penetrate densely vegetated areas.

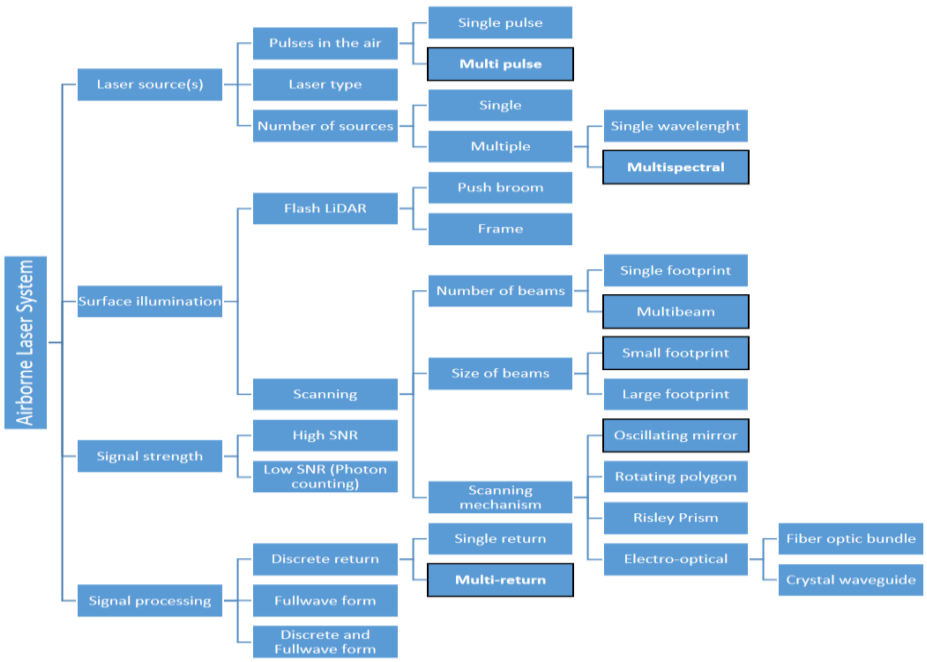

Figure 2.3. Technical classification of Airborne Laser Scanning Systems (adapted from Fernandez-Diaz et al. (2014). The technical characteristics of the ALS system (Optech Titan) used within the scope of this thesis are shown with a black outline.

Typical flight parameters (referred to as the vector parameters) that can be adjusted to design the acquisition project include flight speed, operating above ground level (AGL), and flight-line overlap:

- A faster flight speed reduces the point density (faster speed means fewer points collected on a per unit area) while increasing the coverage (km² par hour);
- A lower operating AGL increases the point density and the incident energy reaching per unit area of the target surface by reducing (i) the beam footprint on the surface (the laser beam divergence being a static characteristic of the optical element) and (ii) the optical path length in the atmosphere (less absorption and diffuse scattering). The maximum operating AGL mainly depends on the emitted power, while the minimum operating AGL usually depends on national/local regulations and eye-safety regulations;
- A higher flight line overlap (commonly between 20% to 50%) increases the available point density on the overlapping area. On the other hand, it creates a less uniform distribution of points and reduces the effective surface that can be covered during a flight.

Typical sensor parameters that can be controlled include pulse rate frequency (PRF), the scan Field of View (FOV) and the scan frequency:

- Typical pulse rate frequency (PRF, in Hz.) is now exceeding one million pulses per second (Seitsonen & Ikäheimo, 2021). The greater the PRF the denser the point cloud (usually at the detriment of energy available for each pulse). Considering the operational altitude of airborne laser systems and the speed of light, a high PRF implies that a pulse is fired from the emitter before returns of the precedent pulse have reached the receptor. To resolve the resulting range ambiguity in high repetition rate airborne LIDAR, manufacturers have developed multi-pulse technologies (Roth & Thompson, 2008) allowing multiple pulses at the same time.

- The scan Field of View (FOV, commonly around +/-20°) corresponds to the angle covered by the sensor. A large FOV increases the observation angle and thus can also affect the accuracy of the range measurement (Ahokas et al., 2003), by spreading the beam footprint on the surface and inaccuracy due to beam deflection (Ussyshkin et al., 2008). However, a large FOV increases the acquisition swath and can help to avoid occluded areas in complex landscapes (R. Opitz, 2016).

Other important characteristics of ALS inherent to the sensor are the laser beam properties, the scan pattern and the recording capabilities of the LiDAR system:

- The laser beam properties define the characteristics of the emitted pulse of light. These characteristics include:
    - The spectral properties: typically, ALS are operating with a Nd-YAG (neodymium-doped yttrium aluminum garnet) laser whose wavelength is 1064 nm (near-infrared). Although, bathymetric or topo-bathymetric LiDAR are also using laser whose wavelength is 532 nm (green). The spectral characteristic is important as surface reflectance varies depending on the surface material properties and the wavelength (Figure 2.4). As a result, the pulse return intensity, not only varies according to the geometry of the target but also according to its reflectance at the laser wavelength. One other consideration regarding spectral properties is that the signal emitter is designed with a narrow and sharp spectral edge (usually < 2nm FWHM) and that the signal receiver has a narrow bandpass filter centered on the emitter wavelength to reduce the environmental noise (Baltsavias, 1999).

Guyot, Alexandre. Contribution of airborne LiDAR and hyperspectral data to archaeological mapping in terrestrial and submerged environments. 2021

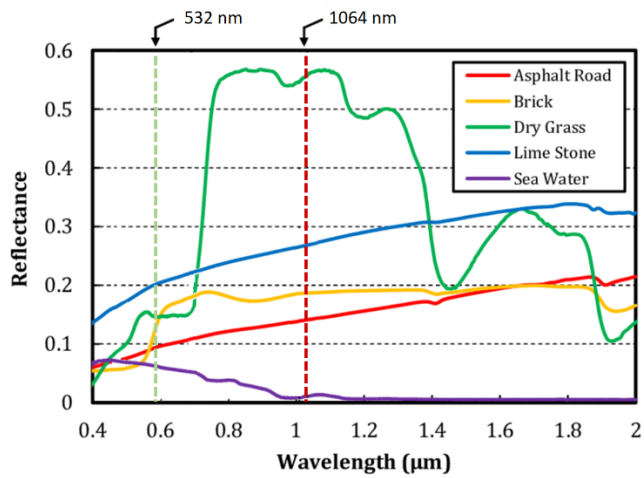

Figure 2.4. Reflectance at typical laser wavelength (532nm, green and 1064nm, near-infrared) for various surface materials (adapted from Yan et al.(2015))

- The beam divergence: it characterizes the quality of the beam collimation and is expressed in mrad. The smaller the divergence the more focused is the beam, thus the smaller the beam footprint when hitting a target surface. Typical values of beam divergence (γ) are in the range of 0.1 to 1 mrad (usually given at 1/e of the peak signal, thus representing 36.8% of its maximum). At an operating AGL (h) of 1000m, and for nadir pulse hitting a flat surface, this represents a beam footprint diameter ($D_{beam} = 2h.\tan(\frac{\gamma}{2})$) of 10cm to 1m. The footprint diameter has to be considered with the point density, as overlapping beam footprint leads to redundant information, while spatially distant footprint leads to under-sampling of the target surface (Baltsavias, 1999). While an ideal configuration to reach would be a point spacing equivalent to the footprint diameter, this is not possible for scanning patterns such as "seesaw" which provides a variable point spacing, with increasing point density at the swath edge (Balsa-Barreiro, 2012).

- The beam duration or pulse width: it characterizes the time of emission of a pulse (in ns). For accurate distance measurement, it is preferable to have a narrow pulse width (Fernandez-Diaz et al., 2016). For topographic ALS, the pulse width is of few ns, and commonly increasing for shallow-bathymetric and deep-bathymetric LiDAR systems that require high energy per pulse to penetrate the water column.

- The scanning pattern: it is related to the mechanism used to deviate the laser beam over the target surface (Vosselman & Maas, 2014). Depending on the mechanism (e.g. oscillating mirror, rotating polygon, rotating mirror, rotating wedge prism) the spatial distribution of beam footprints on the ground is different (Figure 2.5). The scanning

Guyot, Alexandre. Contribution of airborne LiDAR and hyperspectral data to archaeological mapping in terrestrial and submerged environments. 2021

pattern has an impact on the spatial distribution of measurement points (i.e. non-uniform density of points with an oscillating mirror).

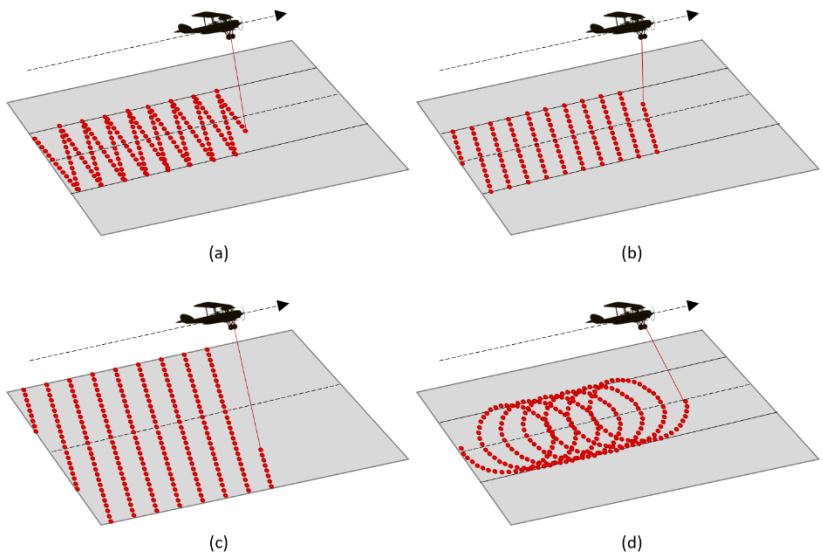

Figure 2.5. LiDAR scanning patterns obtained with various laser beam deviation mechanisms, (a) oscillating mirror ("seesaw pattern"), (b) polygon mirror, (c) rotating mirror, (d) rotating wedge prism. (source: Pentek, (2020))

- The recording capacities of airborne LiDAR can be represented by two major approaches depending on the way the system is handling the EM signal received at the sensor (Figure 2.6) :
    - Discrete returns recording: it consists of the recording of one or multiple discrete returns during the flight. The backscattered EM signal received at the sensor is processed instantaneously using peak detection method to generate time-stamped returns and associated backscattered intensity (Jutzi & Stilla, 2005).
    - Fullwave form digitization: it corresponds, for each emitted pulse, to the recording of the fullwave form (FWF) received at the sensor (see Mallet & Bretar (2009) for a review). The analysis of the FWF is performed in post-processing (after flight), and accessing the shape of the returned signal can be useful to infer the nature of a target, improve range determination or detect weak returns that could not be recorded by the in-flight discrete return detection system (Wagner et al., 2004). Most FWF LiDARs also provide discrete in flight-detection capabilities, since full waveform recording generates an important volume of data and can be complex to process.

Guyot, Alexandre. Contribution of airborne LiDAR and hyperspectral data to archaeological mapping in terrestrial and submerged environments. 2021

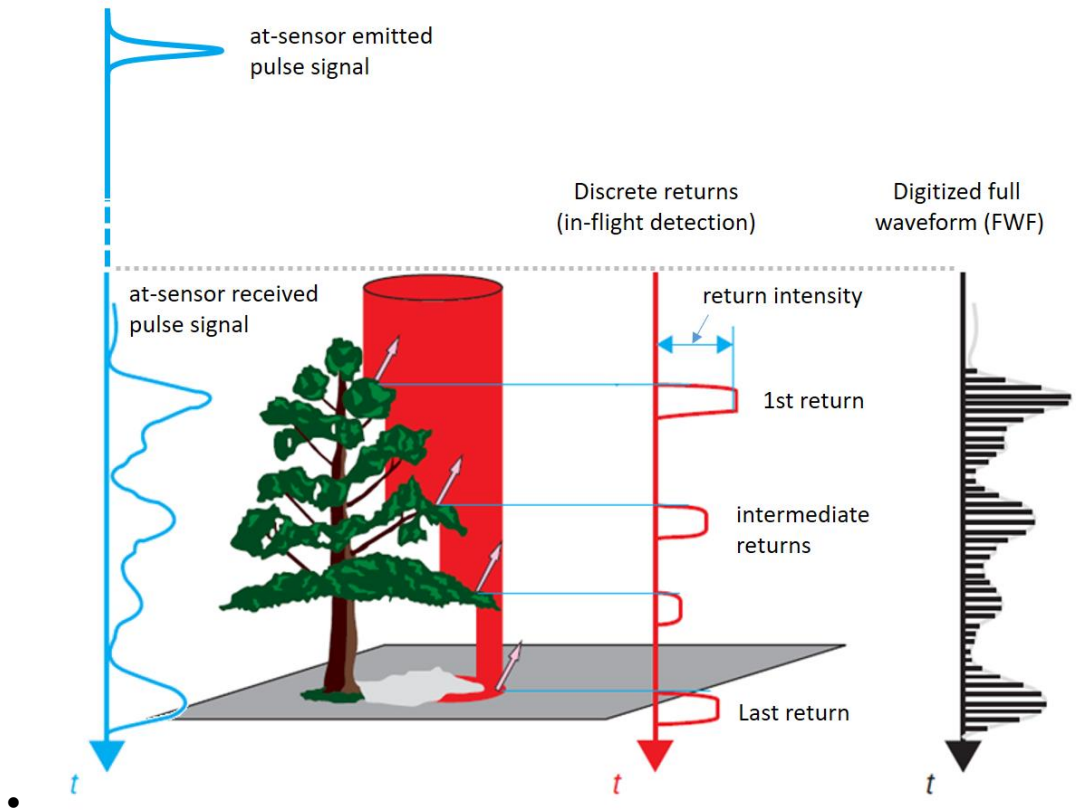

Figure 2.6. Difference between discrete returns and full waveform digitization (adapted from Vosselman & Maas (2014))

Positions and orientation of the sensor have to be observed during acquisition to be properly positioned in time and space, and attached to a unique spatial reference system such as the WGS -84 system. This is performed using additional equipment based on GNSS and IMU technologies, now often integrated into INS (Inertial Navigation System). Attached to the sensor, The INS measures and integrates the orientation, position, velocity and acceleration of the sensor during the flight.

The trajectory data computed from the INS can be corrected in post-processing using differential GNSS correction. Subsequently, post-processing adjustments between flight lines (strip alignment) are also performed. Strip alignment methods commonly use extraction of linear features and planar information to minimize systematic errors in LIDAR strips (Lindenthal et al., 2012).

2.1.3 Airborne LiDAR data characteristics

2.1.3.1) Technical characteristics

Airborne LiDAR data is commonly delivered in the form of a georeferenced point cloud (Figure 2.7) including, for each point (return), the following attributes:

- The coordinates of the return (X,Y,Z)
- An intensity value (usually not calibrated)
- The return number
- The total number of returns (associated with the emitted pulse)
- The scan angle
- The GPS Time (usually the GPS time of the emitted pulse)
- A classification code, eventually set by post-processing analysis and defining the nature of the point (ground, building, vegetation, noise, …)

The above attributes are stored in standardized formats such as the LAS format[10] defined by the OGC (Open Geospatial Consortium) to store point cloud data records.

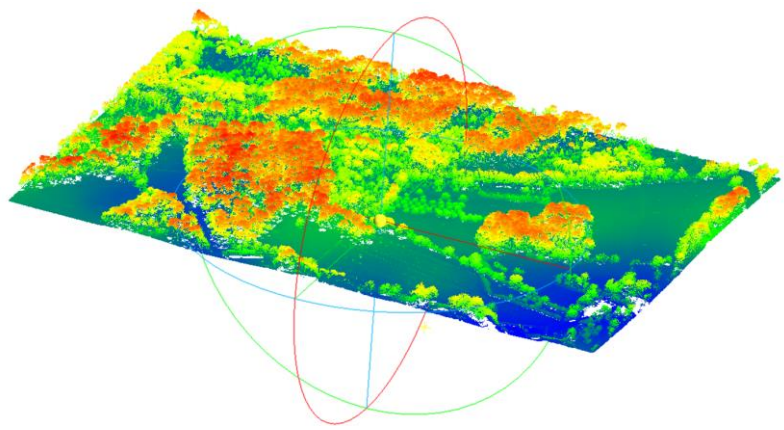

Figure 2.7. Airborne LiDAR raw point cloud colorized by elevation (Z attribute)

2.1.3.2) Source of errors or uncertainties

2.1.3.2.a) 3D coordinates measurements

ALS data are affected by random and systematic errors and several studies provide insight on the modelling of the errors (Baltsavias, 1999; Glennie, 2007; Schaer et al., 2007).

The 3D coordinates of a laser return can be expressed as a function of the exterior orientation of the laser sensor and the laser range vector (Toth et al., 2002). The observation equation (eq. 2.1) is:

$$r_{M,k} = r_{M,INS} + R_{INS}^{M} \cdot \left(R_{L}^{INS} \cdot r_{L} + b_{L}^{INS}\right) \qquad \text{(eq. 2.1)}$$

with,

- $r_{M,k}$, the 3D coordinates of a laser return (k) in the mapping frame (M). These values are the coordinate of a point in the georeferenced point cloud.
- $r_{M,INS}$, the 3D coordinates of the navigation system in the mapping frame (m). These values are measured by the INS/GNSS system.

[10] https://www.ogc.org/standards/LAS

- R_{INS}^{M}, the rotation matrix between the INS frame (INS) to the mapping frame (M), defined by three rotation angles: roll (ω), pitch (φ) and yaw (κ). These values are measured by the INS/IMU subsystem.
- R_{L}^{INS}, the boresight matrix between the laser scanner frame (L) and the INS frame (INS), defined by three rotation angles ($d\omega, d\varphi, d\kappa$) These values are determined by a system boresight calibration.
- r_L, the 3D coordinates of the target point in the laser scanner frame (L). These coordinates are measured by the laser scanner and function of the scan angle (α) and range (d).
- b_{L}^{INS}, the lever-arm offset between the laser scanner frame (L) and the INS frame (INS)

The final accuracy of a measured coordinate data is therefore related to the system calibration (erroneous calibration of the GPS, IMU and scanner assembly) and measurements errors (ranging measurements errors and trajectory errors). Environmental errors are also contributing to the measurement uncertainty. This can be explained by the complexity of the target (sloping surfaces lead to more uncertainty in X, Y and Z coordinates) or the light path (in the case of multipath reflections, the laser beam is reflected by different objects before reaching the detector). One other source of errors that can be mentioned is the post-processing errors, including strip-adjustments mentioned earlier as well as coordinate transformation and geoid correction.

While many factors affect the accuracy of LiDAR data (Ussyshkin et al., 2008), in practice, absolute vertical and horizontal accuracies (at 1σ) of a typical ALS point cloud are usually reaching 10cm to 20cm (Ren et al., 2016).

2.1.3.2.b) Radiometric measurements and detection limits

The absolute accuracy of the coordinate measurements is not the only criteria defining the quality of an ALS point-cloud to reliably represent a 3-dimensional scene. The radiometric detection capabilities of a laser system are also considered as a key-factor determining the quality and comprehensiveness of an ALS acquisition.

Under the assumption of a Lambertian surface that intercepts the entire laser beam, the power of the received laser pulse can be determined from the range equation (eq. 2.2), which describes the influence of sensor, target and atmosphere (Kashani et al., 2015):

$$P_r = \frac{P_t D_r^2 \eta_{sys} \eta_{atm} \rho}{4R^2} \cdot \cos(\alpha_i) \qquad \text{(eq. 2.2)}$$

with,

- P_r, the received signal power (watt),
- P_t, the transmitted signal power (watt),
- D_r, the diameter of receiver aperture (meter),

- R, the range between sensor and target (meter),
- η_{sys}, the system transmission factor (dimensionless),
- η_{atm}, the atmospheric transmission factor (dimensionless),
- ρ, the target reflectance at the LiDAR wavelength (dimensionless),
- α_i, angle of incidence (degree)

Hence, multiple factors are affecting the amount of energy back-scattered to the receiver. While sensor (receiver/emitter) characteristics are static for an acquisition, the target characteristics (including reflectance, bidirectional reflectance diffusion function) are varying within a scene and as such primarily define the level of detection by a laser system. Moreover, the above formula is considering a Lambertian, perfectly diffusing target, but most surfaces are not Lambertian, as well as the angle of incidence, and depend on the surface properties.

As stated by Baltsavias (1999), the minimum size detectable object within the laser footprint primarily depends on its reflectivity (or reflectance ρ at the LiDAR wavelength). As an example, considering the same sensor-to-target distance, for a laser beam footprint of 50cm in diameter, a flat surface of 50cm in diameter made of a 5% reflectance material (i.e. wet dark concrete), would backscatter the same amount of energy that a flat surface of 12.5 cm in diameter made of 80% reflectance material (e.g. dry white sand).

Below are some examples of weak or no-return situations:

- Water surfaces (with low reflectance in the near-infra red) are often not measured by topographic LiDARs. This can also be the case –no returns-, for wet slate roofing surfaces having a low reflectance and whose slope and smooth surface can generate specular reflections away from the sensor.
- Under-canopy features are hit by a pulse progressively lowered in energy as the signal goes down towards the ground and interacts with above features. Beyond, optical opacity due to dense foliage (all signal reflected), these conditions can also cause a lack of understorey or ground returns.

Another detection limit, not related to radiometry, can be related to the vertical context of the target within the scene. Baltsavias (1999) used the term of vertical resolution, or minimum separation between objects along the pulse path, to describe this characteristic. This characteristic is related to the minimum time difference between two received echoes, itself usually defined as half the pulse duration (Fernandez-Diaz et al., 2016). As an example, for a typical pulse-width (t_{pulse}) of 4ns, and considering the speed of light ($c = 299\,792\,458\ m.s^{-1}$), the minimum vertical separation (ΔH_{min}) between 2 returns of the same emitted pulse would be ($\Delta H_{min} = \frac{t_{pulse}}{2} \cdot c$) about 0.6 m. This demonstrates, for example, the impossibility of capturing ground returns if the last return of the same emitted pulse occurred 50cm above ground (i.e. high-grass or low-bush).

2.1.4 LiDAR data processing: from data to information

An airborne LiDAR point cloud often provides a unique highly detailed 3D representation of an observed scene. However, the visualization of a large amount of 3D coordinates data is usually not sufficient to explore and gain information on study areas.

To this aim, LiDAR data must be processed and analyzed to generate derived-products, thus converting data to information. These derived-products principally include classified-point clouds and digital elevation models, the first being a prerequisite to the second.

2.1.4.1) From Point cloud to digital elevation model

One of the most common derived-product of airborne LiDAR is digital elevation model (DEM). DEM (Figure 2.8) refers to the generic term for elevation data represented in a gridded surface or raster. DEM is further defined as digital terrain model (DTM) when representing (i) bare-ground elevation, (ii) digital surface model (DSM) when representing unfiltered scene surface including above-ground elements such as vegetation and building, (iii) digital height model (DHM) or nDSM for normalized DSM, when representing the height of above ground object (DHM = DSM – DTM), (iv) digital feature model (DFM), which corresponds to DTM with additional above ground-elements of interest, for example for archaeological prospection (Pingel et al., 2015; Štular et al., 2021b).

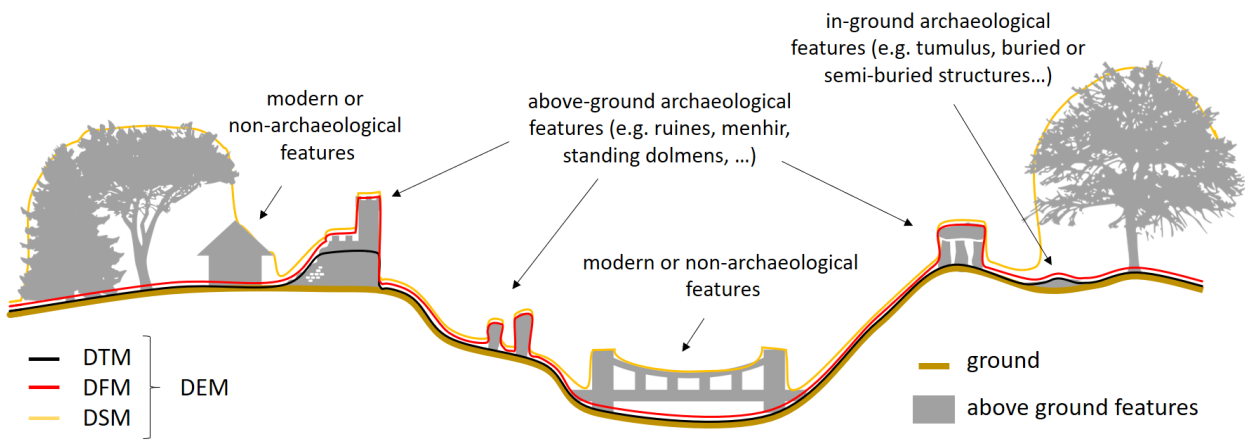

Figure 2.8. Differences between DEMs : DTMs, DSMs and DFMs (adapted from Štular et al.(2021)). The outline illustrates the conceptual definition of DFM and the degree of subjectivity and archaeological interpretability which are important drawbacks for its use for large-scale prospection

The concept of DFM is particularly interesting, however, it is yet to be developed for large-scale mapping (Štular et al., 2021b). For now, it requires a common definition of what an above-ground archaeological element of interest is, which varies depending on the geo-archaeological context. Moreover, the current DFM and DTM algorithms share the same empirical parameters (Pingel et al., 2015) to be tuned for creating the most adapted representation of the terrain surface. DFM, therefore, requires extensive manual point cloud editing. It also implies a degree of subjectivity

and archaeological interpretability to define what should and should not be identified as archaeological features and automatically or manually filtered as such. These points are important conceptual and technical drawbacks for the use of DFM for operational large-scale archaeological prospection.

In this thesis, we will consider the use of DTM, since we aim at capturing subtle topographic variations within large-scale landscapes while considering the uncertainty related to their automatic extraction.

The creation of DTM from ALS point cloud is a key element in topographic analysis. All developed approaches are based on the identification of ground and non-ground points from a raw ALS point cloud (Figure 2.9). The identification is named "point filtering" (or ground filtering) and is usually integrated into a global workflow (Z. Chen et al., 2017) including noise or outliers removal, ground filtering and interpolation.

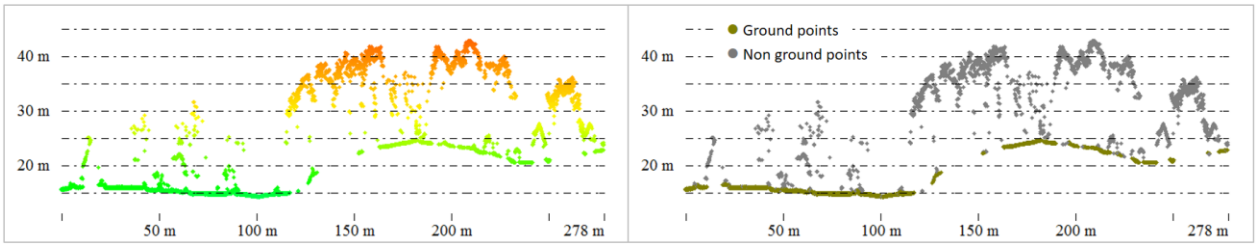

Figure 2.9. Profile view of a ground filtering result (right) of a raw point-cloud (left)

Outlier removal

ALS point-cloud is often affected by noise or outlier points occurring above (sensitivity to atmospheric effects, birds, dust) or below (multipath scattering inflating the measured range (J. S. Evans & Hudak, 2007)) the surface. The outlier removal issue can usually be addressed in a two-step process. First, global outliers (extreme values) can be excluded by defining a minimum and maximum altitude range for the entire scene. This "valid" range can either be defined manually or based on statistical approach assumptions. Second, local outliers (isolated or clustered measurements errors within range of valid elevation values), are usually detected and removed using local neighborhood analysis and applying parametric surface fitting, spatial frequency filters, statistical filters or morphological filters (Carrilho et al., 2018). Spatial frequency filters, such as the one implemented in LasTools (Isenburg, 2020), and Statistical Outlier Removal filters implemented in PCL (Rusu & Cousins, 2011) are amongst the most commonly used filters in operational applications.

Ground filtering

The ground filtering process is the central element of the creation of DTM, and multiple algorithms have been developed to progressively improve the filtering of ground versus non-grounds points (Z. Chen et al., 2017). Most algorithms are based on the assumption that terrain

surface is continuous and sudden vertical changes across a short horizontal distance are not related to terrain features, but to above-ground features. This simplified description does not reflect the complexity of this task that aims at automatically conserving subtle topographical variations while excluding above-ground vegetation and buildings in variation terrain configurations. Multiple reviews and comparison studies have been focusing on ground filtering (Meng et al., 2010; Podobnikar & Vrečko, 2012; Montealegre et al., 2015; Z. Chen et al., 2017), including for archaeological applications (Štular & Lozić, 2020). The principal approaches used are commonly divided into the following categories (Briese, 2014):

- Morphological filtering is based on the concept of mathematical morphology for which erosion and dilation operations are performed on an image using a structural element (kernel). Adapted to point-cloud ground filtering, this approach requires the data to be transformed in a gridded data structure, before a morphological opening (erosion then dilation) is performed and the result tested against a threshold for height difference between the original and eroded point. Multiple variants of morphological filters, including progressive morphological filters, or slope-based morphological filters have been developed (Vosselman, 2000; Q. Chen et al., 2007; Pingel et al., 2013).

- Surface-based filtering is based on the creation of terrain surface based on the selection of the lowest points within a moving window and interpolation techniques. Using an iterative process, the terrain is progressively refined based on the elevation residue between remaining points and the interpolated surface (Kraus & Pfeifer, 1998). Various surface-fitting algorithms have been developed based on diverse approaches, such as active shape models (Elmqvist et al., 2001) or cloth simulation algorithm (W. Zhang et al., 2016).

- Progressive densification filtering is based on the selection of an initial subset of the lowest ground points (seeds) to create a coarse version of the terrain (Figure 2.10). The subset is then iteratively densified by adding new ground points if their relative position to the estimated terrain fulfills some slope/distance criteria. The reference algorithm, which is the progressive TIN densification proposed by Axelsson (2000), has the advantage of evaluating all points of the cloud rather than relying on a predefined grid resolution.

Guyot, Alexandre. Contribution of airborne LiDAR and hyperspectral data to archaeological mapping in terrestrial and submerged environments. 2021

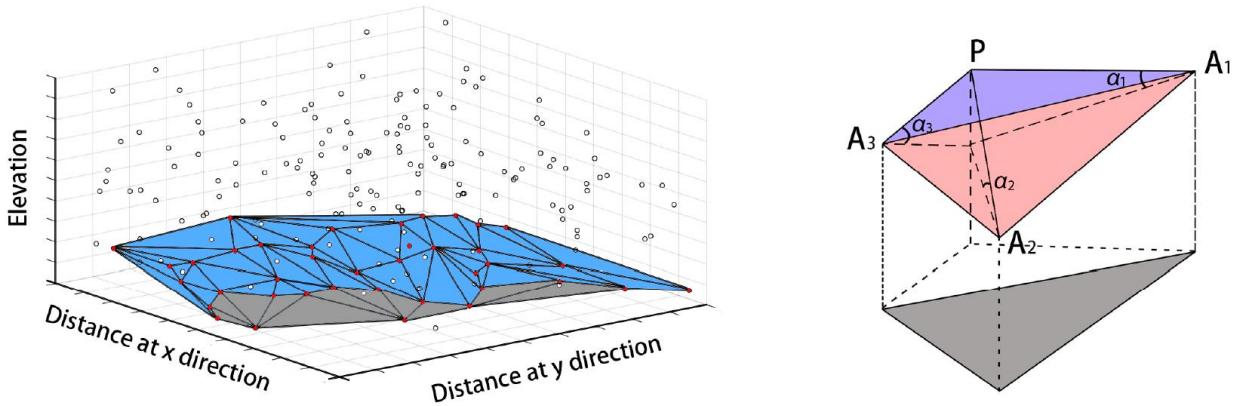

Figure 2.10 Diagram of the progressive TIN densification proposed by Axelsson (2000), (source: Z. Chen et al., (2017))

- Segmentation-based filtering is based on applying the filtering strategy on segments of points rather than individual points (Sithole & Vosselman, 2005). The segmentation ground is performed by surface-growing approach and the classification is performed removing entire segments according to their vertical relation to connected segments.

The development and evaluation of filtering algorithms is still an active theme of research, especially in archaeological applications (M. Doneus et al., 2020; Štular & Lozić, 2020). To enable reproducibility of processing results, these authors are stressing the importance of describing the raw data, the filtering process and related parameters involved with the creation of DTM. The evaluation of theresulting DTM also required quantitative and qualitative assessment methods and tools. Two common metrics of accuracy were defined to quantitatively assess ground filtering (Sithole & Vosselman, 2004). First, type I error provides the number of ground points that were incorrectly identified as non-ground points (omission errors), whereas the type II error provides the number of non-ground points that were incorrectly classified as ground points (commission errors). These metrics were for example used to assess 8 filtering algorithms on twelve experimental datasets (Sithole & Vosselman, 2004). The main conclusions were that all filters performed well in smooth rural landscapes, but had much more difficulties in urban areas or steep terrain with complex vegetation. Similar conclusions were reached by subsequent studies (Z. Chen et al., 2017; Meng et al., 2010), leading to the fact that there is not one best-performing algorithm but that the selection of the most adapted algorithm should be made considering the landscape context, the data characteristics and the project objectives (Štular et al., 2021b).

Despite all the efforts in developing and evaluating novel approaches, it is interesting to note that the oldest algorithms, such as the progressive TIN densification (Axelsson, 2000) and slope-based

filters (Vosselman, 2000) are still amongst the more robust and best-performing filtering approaches in qualitative assessment (Štular & Lozić, 2020).

Classification

The classification step consists in labeling the above-ground points of a point cloud into different classes related to their nature. Water, building, bridge, low, medium or high-vegetation, are some of the standard classes (along with noise and ground) defined by the ASPRS LiDAR classification scheme. In archaeology, above ground classification is not commonly used, since the interest lies in the topography. However, in landscape analysis, or particular ground-filtering workflow, the classification of point cloud can be of interest. Such an approach can be exemplified by the use of above-ground classification to improve an iterative ground-filtering approach considering lowest classified points as potential ground candidates (Guyot et al., 2018).

Interpolation

The interpolation stage aims at transforming the unstructured ground point cloud into a gridded surface (raster). It is an important processing step that has a direct impact on the quality of the resulting DTM. Multiple interpolation algorithms exist, including linear interpolator (such as TIN interpolation), inverse distance weighting (IDW), kriging and local polynomial.

There exists no specific peer-review study evaluating the interpolation techniques for ALS-based archaeological prospection (although a preprint addressing this aspect has been recently made available: Štular et al. (2021a) as a non-reviewed manuscript). Nevertheless, the choice of interpolation techniques has to consider the following points:

- The point density of an ALS is natively not regular across the scene (especially for seesaw acquisition pattern, see 2.1.2), and becomes even less regular after ground filtering (lower density of ground points below vegetation). Nevertheless, a fixed pixel size has to be defined to transfer unstructured elevation data to gridded elevation data. The optimal pixel size can be defined by the nominal point spacing value calculated as PointSpacing=√(1/PointDensity). The nominal point density is determined by the average density along the center of a flight line on a homogeneous open area.
- Considering the large volume of data associated with large-scale ALS projects, the robustness and computational resources required for the interpolation are key factors.
- The interpolation process in low point-density areas (under canopy), which necessarily generates estimated elevation values, influences the DTM accuracy. For example, spline-based interpolation smoothes the interpolated surface, while linear TIN interpolation generates sharp terrain artifacts due to the triangle facets. Despite a usually more appealing representation of the interpolated surface, non-linear interpolation increases the risk of over-interpreting interpolation artifacts as natural terrain variations, because the perception of the original measurements is lost.

Guyot, Alexandre. Contribution of airborne LiDAR and hyperspectral data to archaeological mapping in terrestrial and submerged environments. 2021

2.1.4.2) Full 3D point cloud processing

In some particular cases, LiDAR point clouds can be analyzed using full 3D approaches (without the need for DEM representation) for classification or visual representation purposes.

Such 3D analyses methods are based on non-regular or regular representations:

- Non-regular 3D representations (unstructured 3D point clouds) include the determination of local neighborhood point distribution using principal component analysis (Chehata et al., 2009; Brodu & Lague, 2012; Blomley et al., 2014). For each point of the point cloud, geometrical descriptors (e.g. linearity, planarity, sphericity, etc.) are derived based on the volumetric distribution of the points in a local neighborhood. These descriptors can either be used for training a classifier, or for visualization (Figure 2.11). In archaeological context, very few studies (R. Opitz & Nuninger, 2013) addressed the direct analysis of unstructured 3D point clouds for identifying structures.

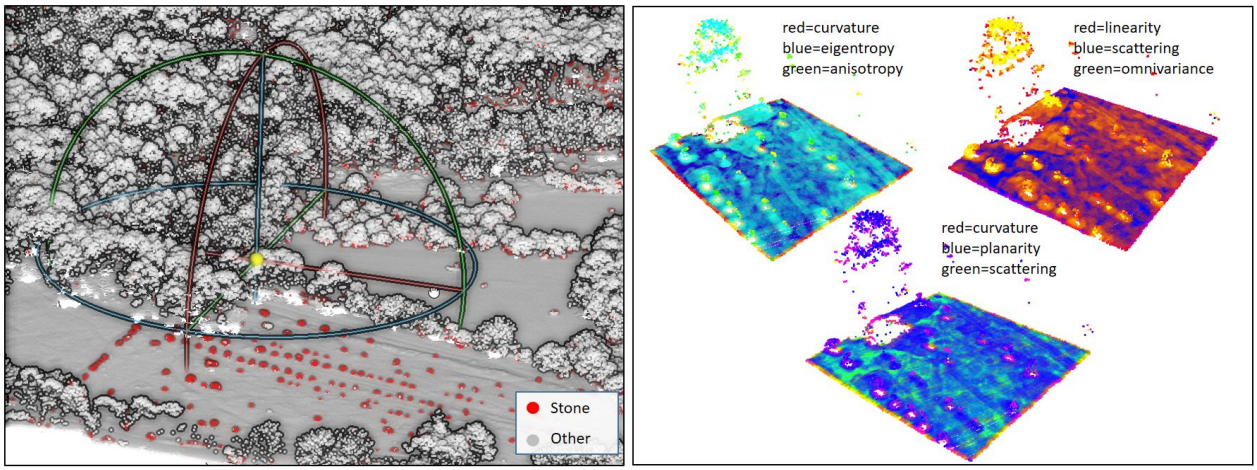

Figure 2.11. Analysis of a 3D point cloud using local neighborhood analysis in the Kerlescan stone alignments of Carnac France (left: classification of points, right: 3D point-cloud visualization colored according to 3 local descriptor combinations)

- Regular 3D representation (voxel) (Figure 2.12) is often a pre-processing step required for 3D point cloud labeling using convolutional neural networks (CNN) (Bello et al., 2020).

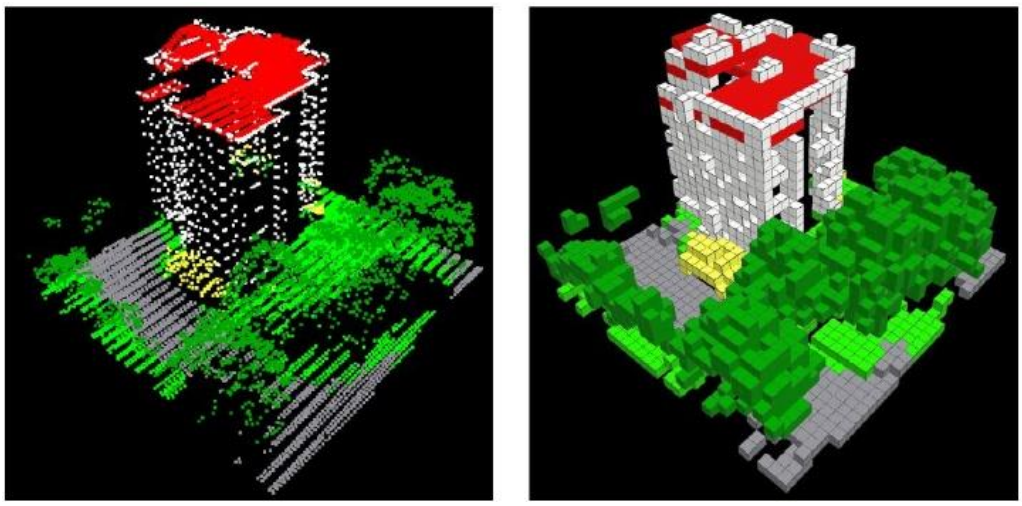

Figure 2.12: 3D structured voxel grid (right) generated from a 3D unstructured point cloud (left) (sources : Schmohl & Sörgel, (2019))

2.1.4.3) Full waveform processing

As seen earlier in 2.1.2, a full-waveform LiDAR system can digitize the full signal being received at the sensor. The advantages of FWF are (Mallet & Bretar, 2009) :

- to improve the detection of return pulses (increase pulse detection reliability, accuracy and resolution) (Chauve et al., 2009);
- to provide additional information (reflectance and geometry) about the target surface through the analysis of backscattering properties (Anderson et al., 2016).

In archaeological prospection based on airborne topographic LiDAR, FWF processing has not been largely developed (M. Doneus et al., 2008). Despite valuable improvements for separating ground and non-ground points, FWF analysis is still underused in operational context (Anderson et al., 2016), notably because of the large-volume of data involved with FWF digitization and also because the difficulties in inferring, through analysis of the physical interactions occurring between the laser beam and targets along the laser path, the nature and morphology of complex structures. In the meantime, research advances originated from the FWF analysis (such as weak echo detection) have progressively been integrated in system performing in-flight discrete return recording, thus partially explaining the nonappearance of FWF analysis for operational projects aiming at the creation of high-quality elevation models. Though the use of FWF is still largely used in LiDAR bathymetric processing workflow (Collin et al., 2008; M. Kim et al., 2016; Lague & Feldmann, 2020; Launeau et al., 2019; C. Wang et al., 2015),

2.1.4.4) LiDAR bathymetry

Airborne LiDAR bathymetry (ALB) is a laser system dedicated to the measurement of water depth. This technology was actually at the origin of the optical remote sensing approach over shallow waters (Hickman & Hogg, 1969).

ALB as its topographic counterpart is also based on the laser emission/reception principles. However, the ALB system, which was designed for hydrography, differs on some keys characteristics such as the use of a green laser (532nm) and a high power per pulse for water penetration. The high power requirement, especially for ALB operating in deep waters (beyond visible water bottom), usually implies lower pulse frequency and larger laser footprint diameter (for eye safety compliance) (Feygels et al., 2019). A green laser of ALB aiming at reaching the seafloor is commonly associated with a NIR laser that aims at detecting the sea surface with greater precision (Lague & Feldmann, 2020) and also separating sea/land surfaces (Allouis et al., 2010). Dual-wavelength systems are commonly developed for hybrid sensors, named Airborne LiDAR topo-bathymetry (ALTB), operating at the land and sea transition zone.

LiDAR bathymetric data have been assessed on few occasions for archaeological mapping. ALTB was for example used, with the extraction of bathymetric DEM, for documenting drowned roman sites of the Mediterranean coast (M. Doneus et al., 2013, 2015, 2020; N. Doneus et al., 2020). It was also used to identify ship wrecks in shallow waters (Shih et al., 2014). An assessment was also performed on deep waters (D. S. Davis et al., 2020). However, data used are most often derived from DBM combining ALB and shipborne acoustic measurements (MBES), thus making it difficult to discuss the potential of ALB on its own.

2.1.5 Topographic analysis for archaeological mapping

2.1.5.1) Visualization techniques

Originally developed for general cartographic needs (Yoëli, 1967), the transformation of DEMs into meaningful visualizations is certainly the most common approach used in archaeology to perceive complex landscapes and identify subtle relief variations that can be related to the presence of archaeological features (Bennett et al., 2012a; Bewley et al., 2005; Devereux et al., 2005, 2008; Fernandez-Diaz et al., 2014; Georges-Leroy, 2010; Hesse, 2010; Kokalj et al., 2011; Pingel et al., 2015; Štular et al., 2012; Zakšek et al., 2011).

Commonly referred to as visualization techniques (VTs), these approaches are applied on one-band regular gridded data (elevation raster). The advent of ALS technology which provides large-scale high-resolution elevation data has played an important role in the assessment and the development of VTs. However, it is to be noted that such derived data are not ALS specific but can be applied to any elevation data based on various techniques, including surface from motion (SfM), bathymetry (acoustic or optic based), or SAR (Synthetic aperture radar).

Despite countless diversity, especially with the use of blending techniques (Kokalj & Somrak, 2019), the most common VTs used in archaeological prospection are based on standard VTs.

Analytical hillshading (HS) (Figure 2.13) is the most commonly used VT, for its computational simplicity but also for its interpretability. It provides an intuitive representation of the relief as a grey scale image based on the use of a fictive light source illuminating the relief. The light source

is hypothetically positioned at an infinite distance, with a constant azimuth and angle of elevation. For a particular pixel position on the image, the intensity of illumination is calculated proportionally to the incidence angle on the local plane or facet defined by the pixel neighborhood (Yoëli, 1967). With an angle of incidence of 0° (facets perpendicular to the light source) the pixel is completely illuminated (white), with an angle incidence of 90° (parallel to the light source) or more (back to the light source) the pixel appears dark. Adjusting the light source azimuth and the angle elevation can help in visualizing different small-scale features (depending on their orientation and subtle elevation), but this also stresses the main drawback of HS whose anisotropy (directional dependence) can be problematic (Tzvetkov, 2018), particularly in archaeology (Devereux et al., 2008).

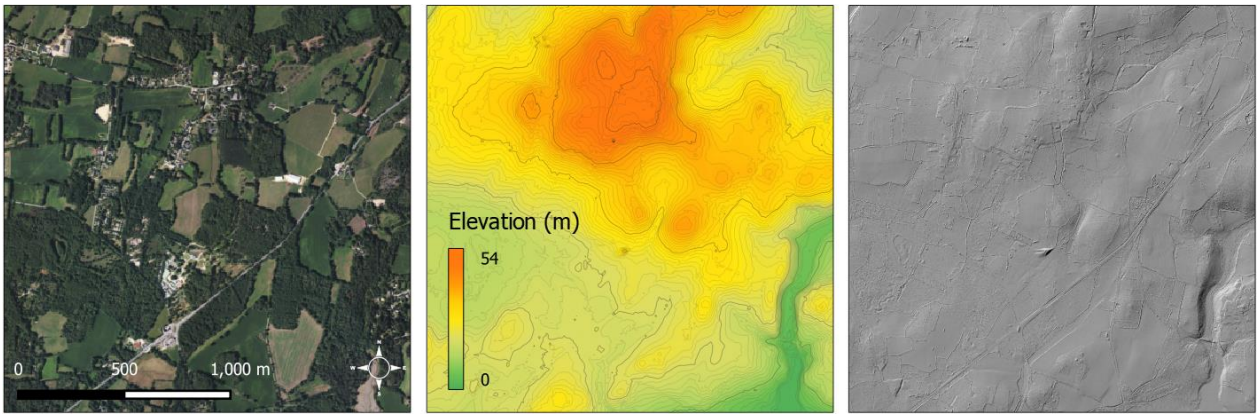

Figure 2.13. Analytical hillshaded relief visualization (right) compared with orthoimage (left) and hypsometrically colored terrain (center). Analytical hillshading parameters: sun elevation = 35°, sun azimuth = 315°

To overcome the limitation of HS, various approaches have been developed, such as locally adapting the position of the light source (Brassel, 1974), or combining images of hillshading results from multiple light sources (Brassel, 1974). Such multi-directional HS (Figure 2.14) has been extended with the multi-directional HS PCA, and successfully applied in archaeology. Specifically, it consists in computing HS from 16 different directions and compressing the information using a principal component analysis (PCA). The first 3 components of the PCA are then displayed as RGB color-composite image (Devereux et al., 2008).

Guyot, Alexandre. Contribution of airborne LiDAR and hyperspectral data to archaeological mapping in terrestrial and submerged environments. 2021

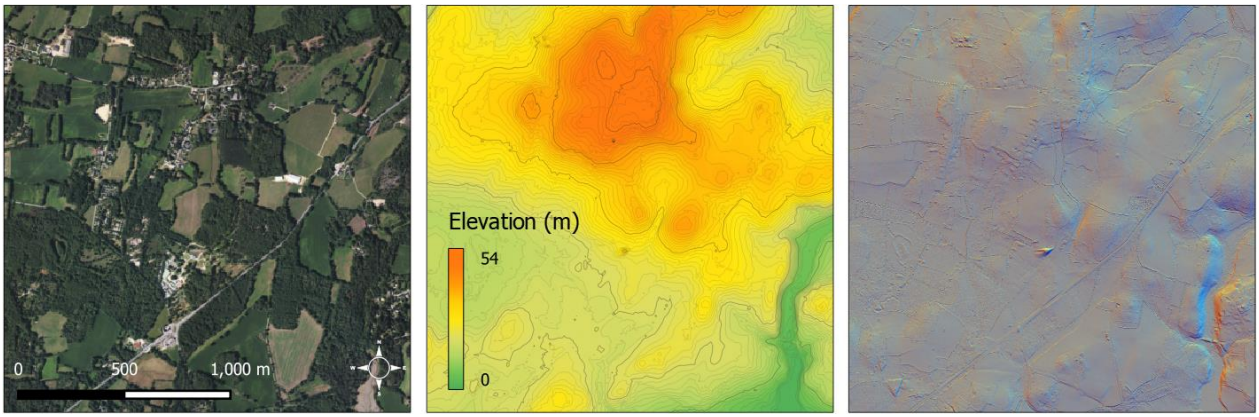

Figure 2.14. Multidirectional (PCA) analytical hillshaded relief visualization (right) compared with orthoimage (left) and hypsometrically colored terrain (center). Multidirectional (PCA) analytical hillshaded parameters: sun elevation = 35°, number of directions = 16

Slope is also a common VT approach. Slope is the gradient of elevation, thus computed using the first derivative of the elevation raster (Figure 2.15). Unlike HS, slope value represents a physical topographic quantity (the maximum rate of change, in degree or percentage, between a pixel and its neighborhood). In archaeology, despite some limitations such as common representation for convex and concave features of equal gradient, slope has been frequently used as a main or complementary VT (Challis et al., 2011; M. Doneus & Briese, 2006, 2011).

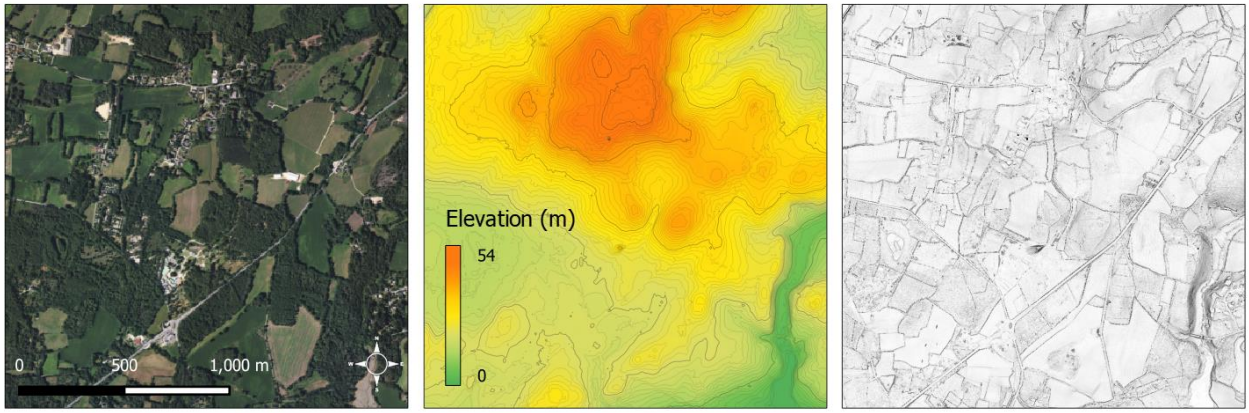

Figure 2.15. Slope relief visualization (right) compared with orthoimage (left) and hypsometrically colored terrain (center)

The concave/convex concern can be addressed by the use of sky-view factor (SVF) which represents for each pixel of the scene the portion of visible sky (Kokalj et al., 2011; Zakšek et al., 2011). SVF is based on the concept of diffuse illumination and thus also aims at overcoming the limitations of hillshading uni-directional illumination source. The SVF algorithms (Figure 2.16) are developed based on the following principle: for each observation point (pixel) the elevation angle of the local horizon (limited by a maximum radius of analysis) is computed for *n* azimuthal directions on the hemisphere. The *n* results are then averaged to obtain the SVF value that ranges

from 1 to 0. High SVF values correspond to open or convex morphological features (a large portion of the sky is visible from the observation point), low SVF values correspond to depression or concave morphological features (a small portion of the sky is visible from the observation point).

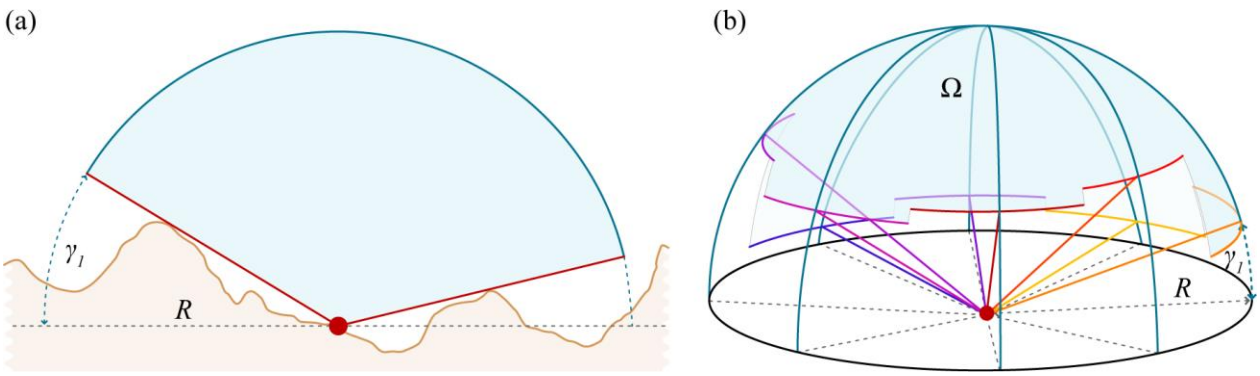

Figure 2.16. Principles of Sky-view factor (SVF). SVF calculation principle is shown in 2D (a) and 3D (b) for a single observation point (source: Zakšek et al. (2011))

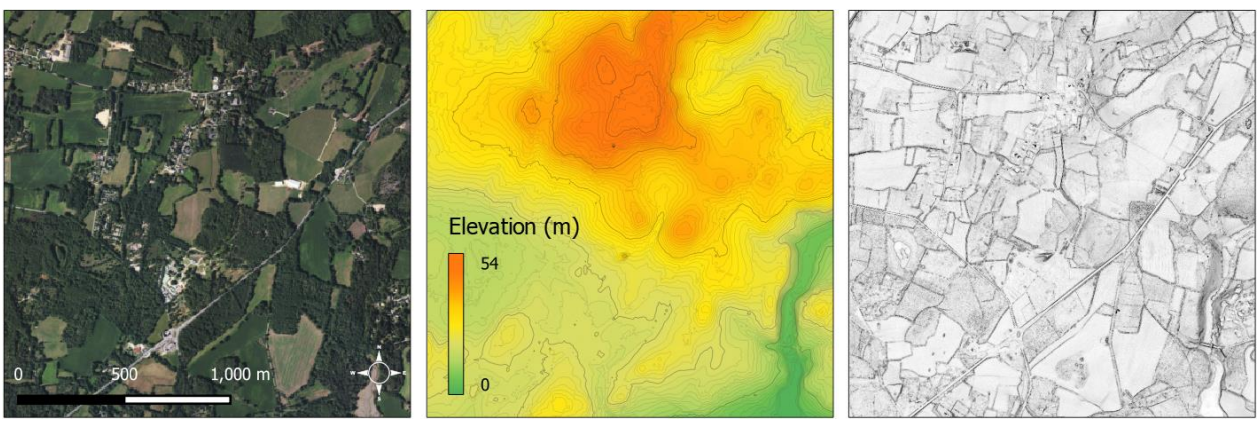

Figure 2.17. Sky-view-factor relief visualization (right) compared with orthoimage (left) and hypsometrically colored terrain (center). Sky-view-factor parameters: number of directions = 16; maximum radius = 10 pixels

Relatively similar to SVF (Figure 2.17), VTs based on topographical openness (Yokoyama et al., 2002) have been proposed for archaeological prospection (M. Doneus, 2013). In contrast to SVF, which is computed using the horizontal plane at the elevation of the observer point (same SVF value for a peak or a perfectly flat area), openness also includes angles beyond the horizontal plane. In the case of slope or dominating position, SVF and openness differ. In practice, for a small topographic elevation such as tumulus, the openness value of the structure would be similar in tilted or horizontal terrain, which is not the case for SVF (Figure 2.18). In addition, openness is computed for both negative (ground factor) and positive (sky factor) angles (Figure 2.19).

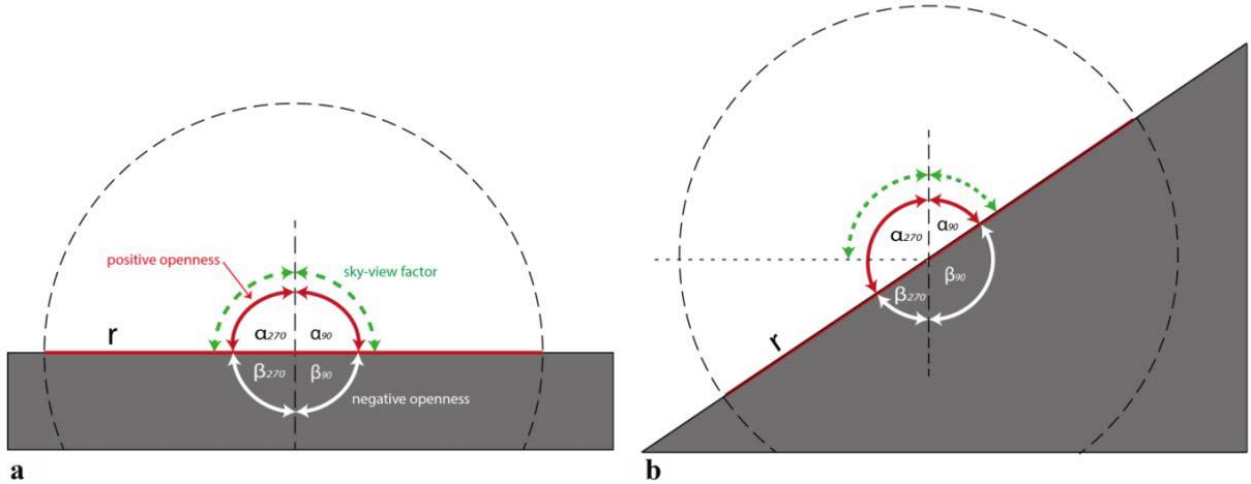

Figure 2.18. Positive and negative openness compared to sky-view-factor on a flat terrain (a) and a slope terrain (b) (source: M. Doneus (2013))

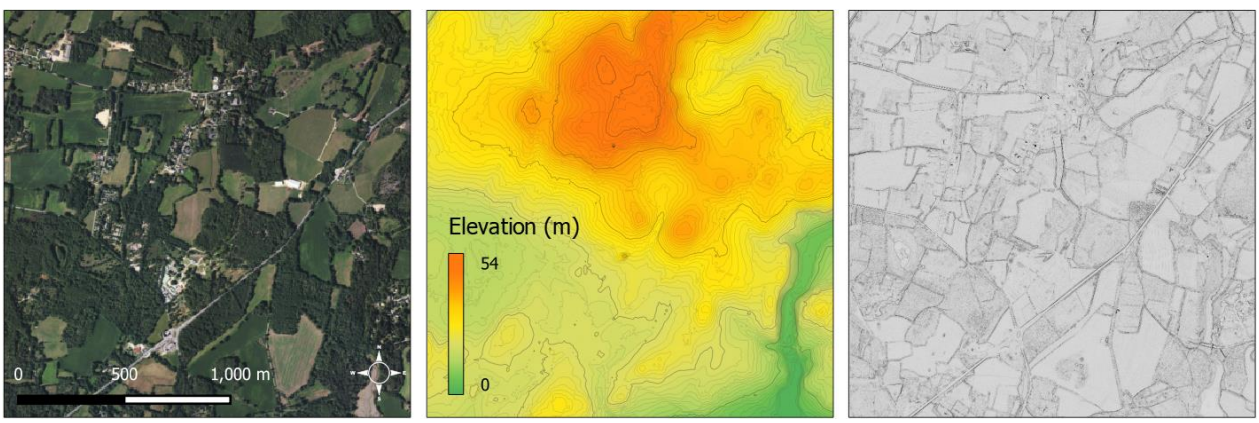

Figure 2.19. Positive openness relief visualization (right) compared with orthoimage (left) and hypsometrically colored terrain (center). Openness parameters: number of directions = 16; maximum radius = 10 pixels

Gaining independence from the global terrain trend is also the approach used for trend removal algorithms such as simple local relief model (SLRM) (Figure 2.20). The concept of SLRM is to enhance the representation of local elevation differences after removing larger trend from the data (Hesse, 2010). The algorithm starts by computing a smoothed version of the DEM (usually using a low-pass filter whose size is defined according to the maximum feature size to be enhanced). Then the difference between the smooth and original DEM is computed to extract a 0m contour line, which is used to extract the original DEM values. This value corresponds to the large-scale elevations which are interpolated to create the global DEM (without local positive and negative variations). Finally, this global DEM is subtracted from the original DEM. One advantage of the SLRM is that positive and negative topographic features are maintained with their relative elevation values, and can be further visualized as color-ramp elevation or combined with hill shading applied to SLRM results. SLRM provides interesting results in gentle topographical

context, but it is highly dependent of the filter size which reduces its applicability to the enhancement of pre-defined scale of feature.

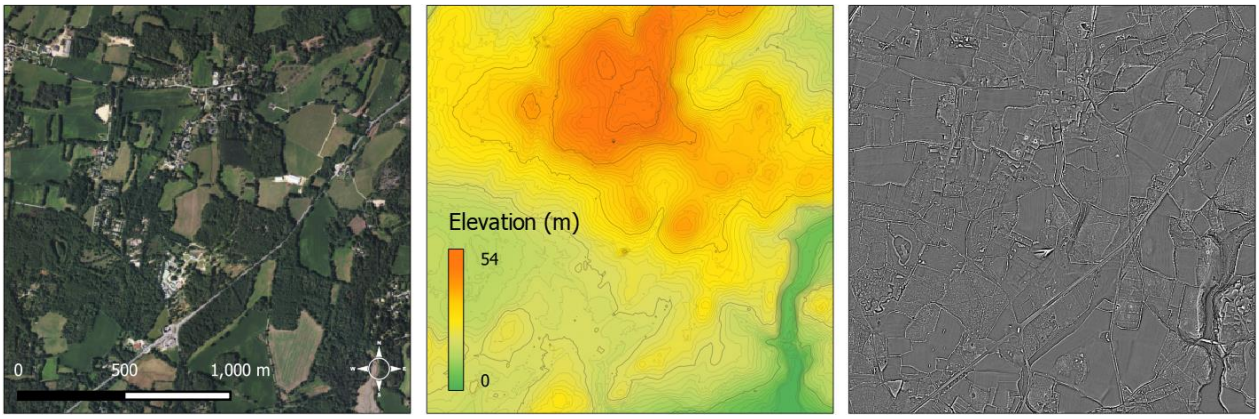

Figure 2.20. Simple local relief visualization (right) compared with orthoimage (left) and hypsometrically colored terrain (center). Simple local relief parameters: radius = 10 pixels

The main limitation of the commonly used approaches is that they are very dependent on the scale of analysis. For example, the calculation of openness or local dominance is carried out with a fixed and predefined radius, thus constrained to enhancing the perception of anomalies of specific size or morphology (Guyot et al., 2018), and reducing the global perception of the intrinsically multiscale terrain variations. To overcome such limitations, multi-scale approaches have been assessed for ALS-based archaeological prospection (Guyot et al., 2018; Orengo & Petrie, 2018). The Multiscale relief model (MSRM) was proposed as an extended version of LRM and consists of the application of several low pass filters of the original DEM with different kernel sizes (Orengo & Petrie, 2018). The Multiscale topographic position image (MSTP) was developed by Lindsay et al. (2015) based on a topographic index: deviation from mean elevation (DEV) (J. P. Wilson & Gallant, 2000), computed at different scales with an integral image transformation (Crow, 1984) of the original DEM to efficiently address multiple large kernel sizes. The results of multiple DEVs are reduced to a domain of scales (micro, meso, macro) and used as a composite RGB image (Figure 2.21).

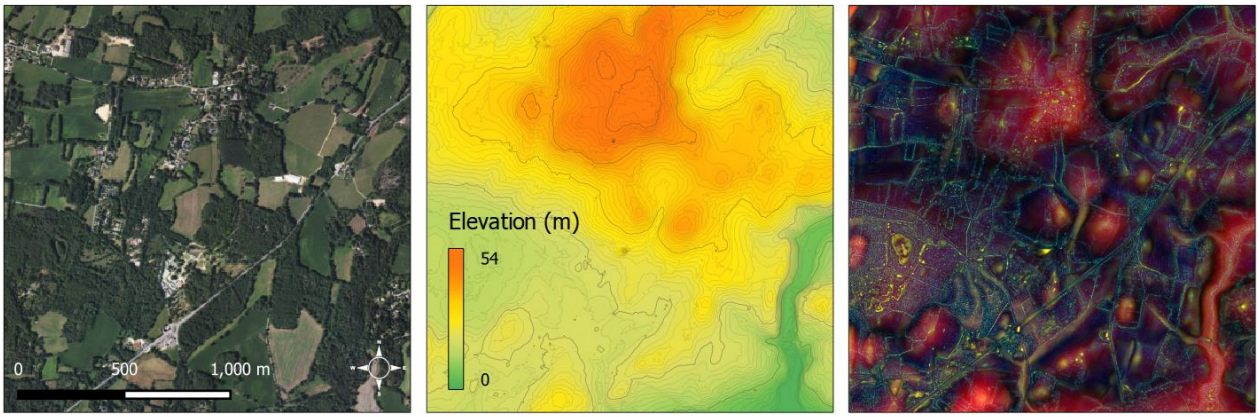

Figure 2.21. Multiscale topographic position image (rigth) compared with orthoimage (left) and hypsometrically colored terrain (center). Multiscale topographic position parameters: micro = [1 to 10 pixels], meso=]10, 100 pixels], macro=]100, 1000 pixels]

More recently, with the use of blending techniques (Kokalj & Somrak, 2019), combining different VTs into a new hybrid one, offers an unlimited number of possibilities. Behind this great potential, the concern of identifying one or several VTs adapted to an archaeological prospection project remains a challenge. Each project being dependent on the landscape and topographical context, the archaeological context but also on the data resolution, several authors have stressed the difficulty in designing an "all-in-one" VT (Kokalj & Somrak, 2019; R. S. Opitz & Cowley, 2013; Štular et al., 2012). This is especially true for large-scale mapping covering multiple geo-archaeological contexts and objectives and often different data sources.

2.1.5.2) (Semi-)automatic detection of archaeological sites

In the last decade, the growing amount of remote sensing data made available, notably in open-data, have increased the integration of data science approaches for the automatic processing and extraction of information in archaeology (L. Luo et al., 2019; Sevara et al., 2016; Toumazet et al., 2017).

Started with aerial and satellite-based archaeology, various unsupervised and supervised (semi-)automatic strategies have been developed and assessed for remote sensing archaeological prospection. These strategies can be separated into two main approaches: pixel-based or object-based strategy (D. S. Davis, 2019; Sevara et al., 2016).

2.1.5.2.a) Pixel-based approach

The pixel-based approach, first, considers pixels individually and relies on their individual characteristics (spectral or topographic) to detect potential archaeological sites or orient the image interpretation using probability map (Guyot et al., 2018).

The pixel-based approach can further be defined as rule-based or machine-learning approach. The rule-based approach relies on predefined rules usually used in a decision tree to discriminate

potential targets from the background. It requires the definition of suitable feature descriptors (such as elevation, VT value, topographic position index) and adapted threshold for the decision tree. The machine-learning approach relies on examples or samples of reference which are used to build a classification model by fitting a mathematical function to map input (attributes or explanatory variables) to output (class or label) (Mohri et al., 2012). Such an approach has been used in different conditions and using different topographic descriptors and different classification algorithms (Guyot et al., 2018). Typical machine-learning algorithms for this purpose include Random-Forest (Breiman, 2001) or support vector machine (SVM) (Hearst et al., 1998). The pixel-based approach (Figure 2.22) often lacks spatial homogeneity (noise, structure complexity) and often requires post-processing filtering before the results can be considered for further interpretation or characterization.

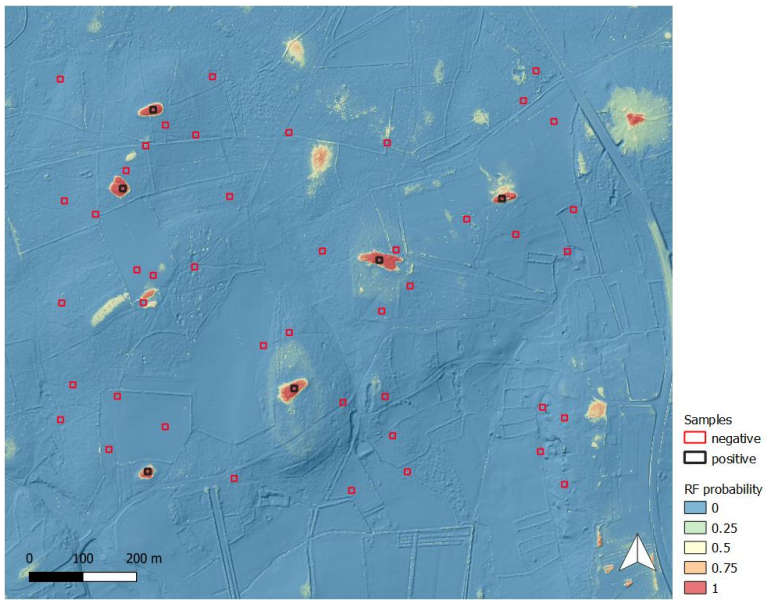

Figure 2.22. Pixel-based results of the presence of burial mounds (probability from 0 to 1) using a supervised machine-learning model (random forest) trained on multiscale topographic descriptors computed from LiDAR-derived terrain model

2.1.5.2.b) Object-based approach

The object-based approach in contrast to pixel-based methods, identify features not by considering individual pixel, but by considering aggregated region of pixels thus including are-based information such as shape, textural information, neighborhood analysis and geographic context (Blaschke, 2010).

Object-based can be carried out using segmentation methods which require an initial stage of analysis consisting of creating the object thought image segmentation approaches. Common methods of segmentation are using region-based analysis (such as super-pixel) where the entire image is segmented and every pixel is associated to one segment, usually corresponding to neighboring pixels forming a contiguous and homogeneous patch. Super-pixel methods such as

graph-based segmentation (Felzenszwalb & Huttenlocher, 2004), region-growing or and commonly used to perform the segmentation. One major shortcoming of such method is the fact that the segmentation parameters can be difficult to set to reach robust and stable results especially with archaeological or landscape features of different morphologies and sizes and showing complex integration with the local topography (D. S. Davis et al., 2019). The segmentation results therefore strongly affect subsequent analysis (e.g. an archaeological feature can improperly be separated into multiple segments or integrated into a much wider segment, thus affecting the relationship between the image-object attributes and the archaeological entity being searched for). Another segmentation approach is using edge-based analysis (such as active contours or level-set method) where the image is not entirely segmented but starting from a seed (or initial position or shape) a contour is progressively warped for delineating one or several objects of interest in the image. This kind of approach is particularly useful in object detection and has been assessed in remote sensing archaeology to detect linear archaeological features from aerial imagery (D'Orazio et al., 2012; Figorito & Tarantino, 2014). Nonetheless, important drawbacks have yet prevented its use in large-scale ALS-based mapping. These drawbacks include the need for prior knowledge of the object position (seed or initial shape) and the fact that active contours are usually not robust to complex background or varying gradient within the object outline (Baswaraj et al., 2012).

Object-based segmentation can also be carried out using template matching, consisting in computing correlation coefficient between each part of the image and a predefined template representing the feature of interest (D. S. Davis et al., 2019; Schneider et al., 2015; Trier & Pilø, 2012). Most adapted to simple morphological structures, template-matching approach remains difficult to generalize because the prototypical template(s) usually cannot include the high morphological diversity and heterogeneous backgrounds of archaeological structures (D. S. Davis, 2019; R. Opitz & Herrmann, 2018).

To tackle this limitation, pixel-based and object-based can also be implemented in parallel. As an example, Toumazet et al. (2017) combined the use of pixel-based and template-matching approach for the detection of complex grazing structures from an ALS-derived local relief model, while Niculiță (2020) used a pixel-based peak detection algorithm and a subsequent region-based segmentation and descriptive statistics of geomorphometric variables used in a Random Forest classifier for the delineation of burial-mounds.

2.1.5.2.c) Deep CNN

More recently, the computer vision field has been profoundly transformed by the advent of deep convolutional neural networks (deep CNN).

First developed at the turn of the millennium by pioneers such as Yann LeCun, Yoshua Bengio and Geoffrey Hinton, deep learning computational models are expanding the use of artificial neural networks (ANN) with a large number of stacked layers (thus the term "deep") to reveal intricate data structures in massive data sets (LeCun et al., 2015). Deep learning uses the

backpropagation algorithm to progressively adjust a very large number of internal parameters (up to billions) to define the best mathematical function (the model) relating the input (raw data) to an output (such as a label). This model is then used to predict the output value related to a new input.

Applied to image pattern analysis, deep convolutional neural networks (deep CNN) are partly inspired by biological vision processes (Hubel & Wiesel, 1962) and use convolutional filters to learn hierarchical representations from the data, through multi-level feature descriptors (A. Khan et al., 2020). One of the first real work tasks based on deep CNN was the automatic recognition of handwritten zip codes (LeCun et al., 1989), but the important computational resources required to train deep CNN refrained from the diffusion of such method. It took several years before deep CNN led to a breakthrough in the computer-vision community. This markedly occurred in 2012, with the use of deep CNN that led to outstanding results (almost halve the error rate) for object recognition tasks (Krizhevsky et al., 2012) in a computer vision contest. Whereas traditional machine-learning pattern recognition methods rely on hand-crafted feature descriptors subsequently used by a classifier (O'Mahony et al., 2020), deep CNN architectures can design (learn) their own descriptors to build highly complex models for creating high-level of abstractions and complex representations of data (Figure 2.23).

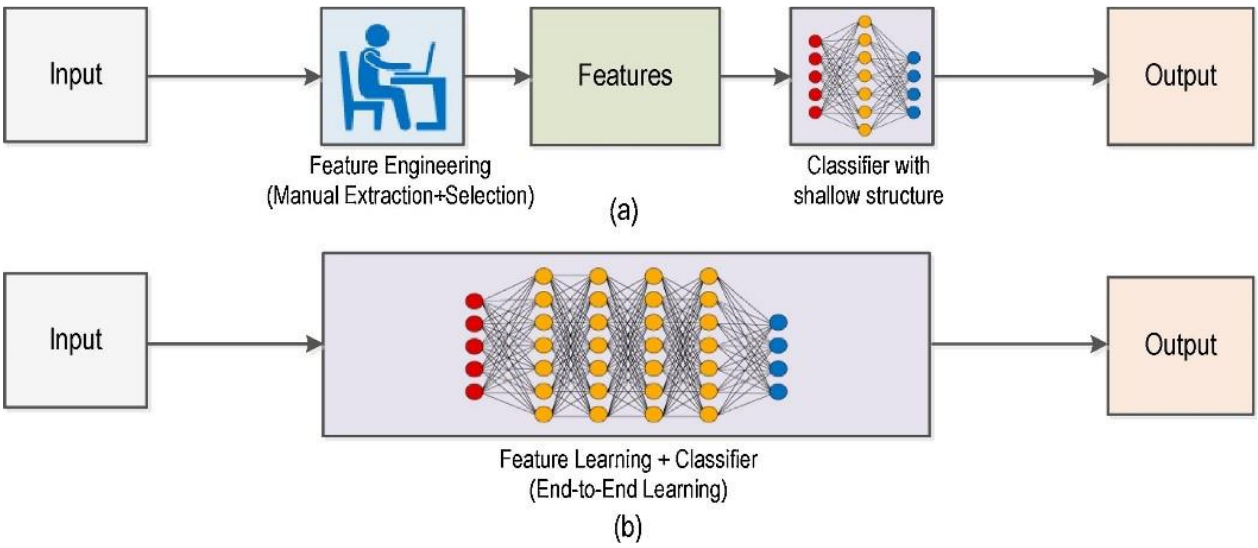

Figure 2.23. (a) Traditional Computer Vision workflow vs. (b) Deep Learning workflow (source: J. Wang et al. (2018)

Deep CNN rapidly evolved as one of the essential imagery analysis methods for various image analysis tasks, such as image classification, image segmentation, object detection and instance segmentation (Figure 2.24).

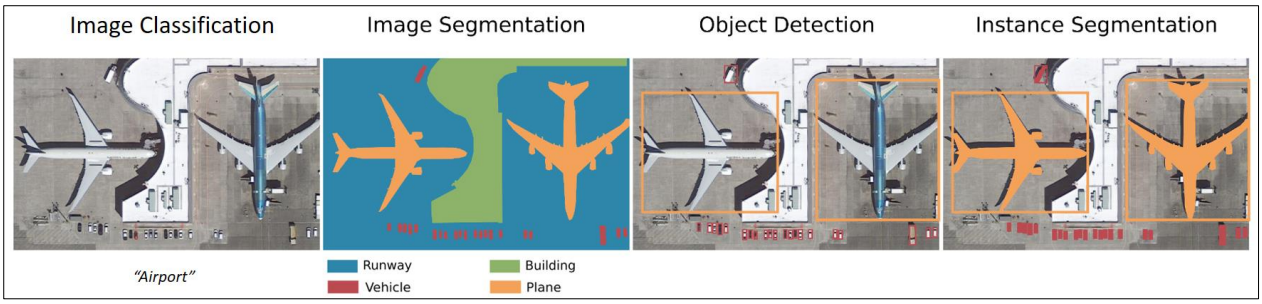

Figure 2.24. Examples of tasks using deep CNN: image classification, assigns a single label to a whole image; image segmentation, densely classifies each pixel; object detection: locates and classifies specific objects in an image by providing a bounding box; and instance segmentation, provides a segmentation mask for detected objects within a bounding box (adapted from Hoeser & Kuenzer, 2020)

Often developed for generalist image analysis applications, a large number of deep CNN architectures have been proposed and evaluated in the remote sensing field (see. Zhu et al. (2017) and Ma et al. (2019) for a review). Most architectures however are composed of elementary layers: convolutional (CONV), pooling and fully connected (FC) layers (Figure 2.25).

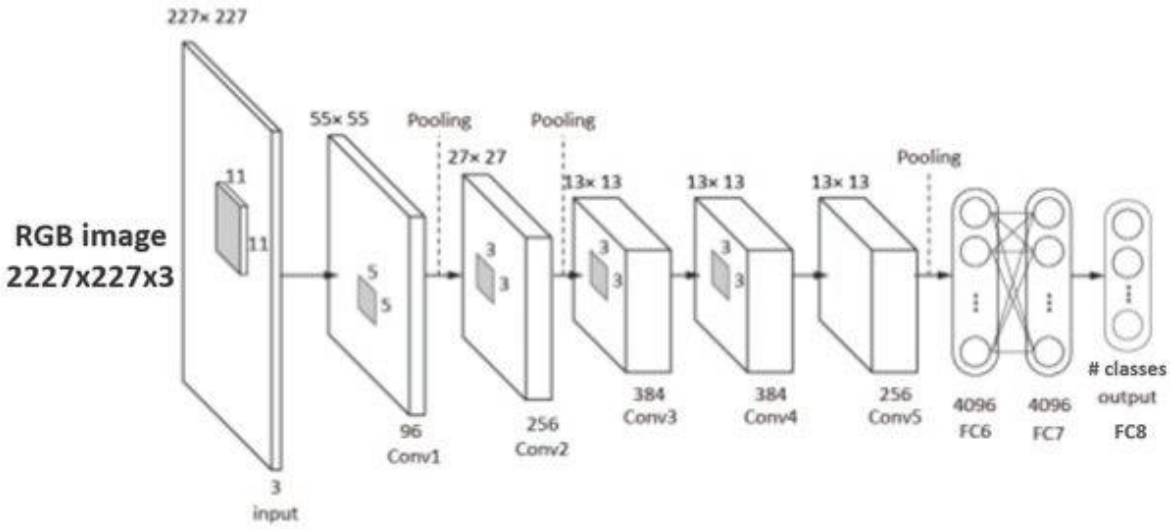

Figure 2.25. A typical deep convolutional neural network composed of convolutional (CONV), pooling and fully connected (FC) layers

Convolutional layers (CONV) use simple convolution filters (or kernels) that perform convolution operations on the input image or preceding layers of the network to generate feature maps. A convolution layer is commonly associated with an activation layer that aims at introducing non-linearity to the network (a common activation function is ReLU, for rectified linear unit). While the size of each convolutional filter is fixed by design, its values (values of the kernel) are adjusted using the back-propagation algorithm during training (see below).

Pooling layers (POOL) are commonly interspersed between convolution layers to reduce (downsample) the spatial size of the feature map before it is provided as input to a subsequent convolutional layer. Downsampling is usually performed with simple operations such as maximum or average pooling (respectively keeping the maximum or average value within the pooling window).

The type of layer is commonly a fully connected (FC) layer as found in standard artificial networks, where the results of previous layers are flattened to a 1D vector before being used by a classifier to infer the result that would be compared to the expected output during training.

In a deep CNN, the training phase adjusts the weights (weights of the FCN and weight of the CONV layers) using a backpropagation algorithm. The adjustment is dependent on the loss, which defines, through a loss function, the difference between the current prediction and the expected output. Since the objective of the training is to reduce this difference (the error), a gradient descent algorithm is used to progressively move towards a local minimum by adjusting the weights of the network. The calculation proceeds backward through the network to propagate the change that minimizes the error from the last to the first layer of the network.

Because of their complexity, deep CNN can be prone to overfitting (the model can be perfectly adapted to predict accurate results from the training example it was given, but fails to predict expected results on new observations). To reduce overfitting, regularization technics have to be used to penalize the complexity of a network. This commonly includes L1 or L2 regularization (which reduces weight values), dropout layer (which randomly deactivates some neurons of a layer), or early stopping (which stops the training process if the -validation- loss reaches a plateau or starts to increase).

This high complexity also implies a major shortcoming for the use of deep CNN (or deep learning in general): the large volume of data or samples required for training a model. Indeed, because a newly designed network has to be initiated with random weights, a very large amount of data (and associated labels) are required to create a reliable model from scratch. As an example, ImageNet, which is a public dataset used to train and evaluate different deep CNN architectures for various image analysis tasks, is built upon more than 14 million images with annotations.

Because many application domains do not offer the possibility to access such volume of data (archaeology is a good example, for which reference data is sparse in reality –limited number of archaeological sites- and in accessibility –no global archaeological remote sensing databases-). To overcome such limitations, several approaches have been proposed. A first strategy consists in using data-augmentation. Data-augmentation involves the creation of multiple altered versions of the same sample to virtually increase the number and variability of examples to be used during model training. In deep CNN, data-augmentation typically includes spatial and radiometric image transformations, such as vertical or horizontal flip, rotation or histogram adjustment. A second strategy consists in using the concept of transfer-learning. Because deep CNNs are designed to learn different levels of concepts related to images, a highly trained model (for

Guyot, Alexandre. Contribution of airborne LiDAR and hyperspectral data to archaeological mapping in terrestrial and submerged environments. 2021

example trained using ImageNet) already has gained a high-level of proficiency in image analysis, especially for low-levels of abstraction such as shapes, color variations or patterns. Those levels of abstraction are common concepts amongst different image-based domains, such as medical imagery, autonomous driving, or archaeology). Based on that, a pre-trained model (initially trained for a source application, such as autonomous driving) can be partially reused to a target domain (such as archaeology). Conceptually, the model which is already proficient in standard imagery analysis would only require few training steps -so fewer examples are required- to gain new knowledge on the target domain specificities. Technically, this is done by initializing the model with pre-trained weights, instead of random initialization. Specific training is then commonly limited to layers handling the highest-level of abstraction, while low-level layers are "frozen" to avoid affecting the initial capability of the model.

In the context of LiDAR-based archaeological prospection, the first use of deep CNN was proposed by Trier et al. (2016) based on Krizhevsky's deep CNN architecture (Krizhevsky et al., 2012) to identify Charcoal kilns position from a LiDAR-derived DTM. A similar approach was assessed in Scotland with extended archaeological structure types and the use of a visualization techniques (SLRM) rather than normalized DTM values (Trier et al., 2018). The interest for the remote sensing archaeology community led to subsequent studies of the use of Deep CNN for LiDAR-based archaeological prospection, most often designed for the task of image classification (Caspari & Crespo, 2019; Kazimi et al., 2020; Somrak et al., 2020) or object detection (Gallwey et al., 2019; Verschoof-van der Vaart & Lambers, 2019).

2.2 Airborne hyperspectral

2.2.1 Principles of airborne hyperspectral imaging

Hyperspectral imaging is a passive remote sensing technique that uses the spectral properties of light to infer characteristics of a target surface. Also named imaging spectrometer, it combines the capabilities of an imaging system (for spatially continuous measurements) to those of spectro-radiometer (for spectrally continuous radiometric measurements). All passive optical imaging systems rely on the properties of light and its interaction with a target surface (this is the principle of photography). A hyperspectral imaging system, however, decomposes the energy received at the sensor, into hundreds of narrow bands (or wavelengths), instead of one large band for panchromatic sensor, or a few large bands (typically between 3 to 15) for multispectral sensor (Figure 2.26). This fine-grained spectral measurement is used to extract the physical properties that govern how the scene materials reflect or absorb radiation. These spectral measurements can be done for different ranges of wavelength, typically in the VNIR (the range evaluated for this thesis) and SWIR spectral domains.

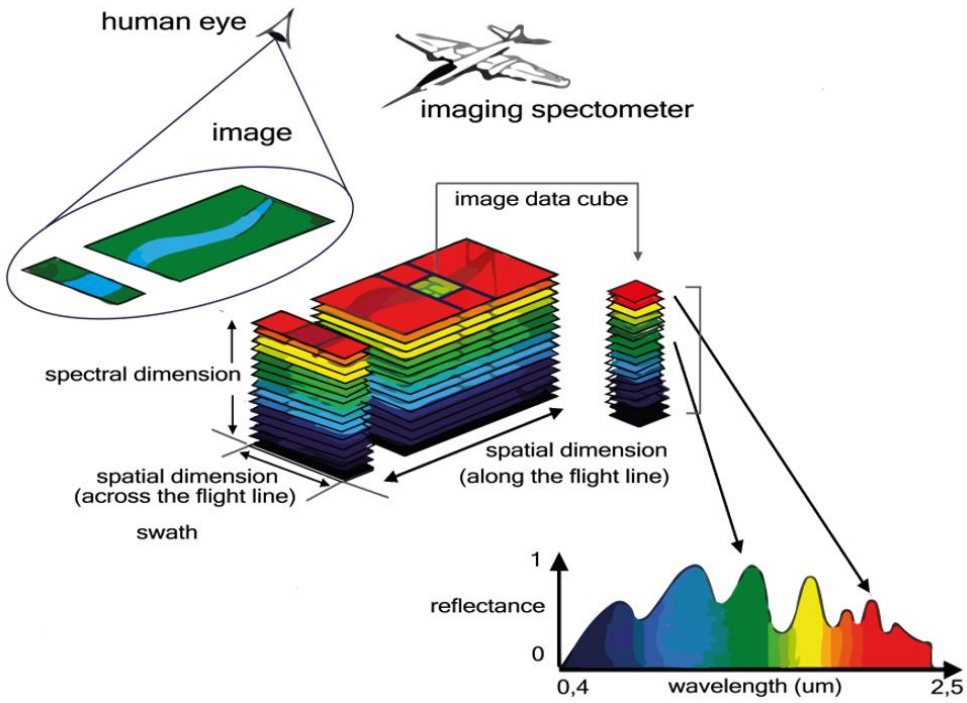

Figure 2.26. Hyperspectral imaging principles (credit: VITO - Flemish Institute for Technological Research)

Several studies (Agapiou, Hadjimitsis, & Alexakis, 2012; K. S. Lee et al., 2004; Marshall et al., 2016) have stressed that broadband spectral information is often not sufficient or adapted for fine discrimination of targets, and that the narrow and continuous bands representation, as a spectral signature offered by hyperspectral data, allows much more possibilities for the discrimination of target bio-physical characteristics, especially when those characteristics are signified by subtle relatively narrow spectral variations.

AHI sensors collect the spectral radiance of a scene. This spectral radiance L, expressed in $(W.m^{-2}.sr^{-1}.nm^{-1})$, is defined as the radiant flux received by the sensor, per unit solid angle, unit surface and wavelength. Spectral radiance is related to the properties of the observed surface, but also the illumination conditions and the absorption and scattering effects occurring in the atmosphere between the sensor and the target. While it is possible to directly analyze the spectral radiance, the data is commonly normalized by the sun irradiance to obtain the apparent spectral reflectance ρ, expressed as (D. G. Manolakis et al., 2016):

$$\rho(\lambda) = \frac{\pi.L(\lambda)}{E_s(\lambda).\cos(\theta_s)} \tag{2.3}$$

with $L(\lambda)$ and $E_s(\lambda)$ respectively the radiance and sun irradiance for a given wavelength λ, and θ_s the solar zenith angle.

The surface reflectance can be retrieved from the apparent spectral reflectance after atmospheric correction (cf. 2.2.4.3). The surface reflectance has the advantage of being an intrinsic property of the target surface and a normalized quantity, making the comparison of signatures comparable between sensors, and conditions of observations.

The capabilities of AHI for determining surface properties has proved its interest in multiple earth-observation applications such as geological mapping, environmental monitoring, agriculture and forestry management, atmospheric characterization, biological and chemical detection, or disaster assessment (see Jia et al. (2020) for a recent review of applications). In archaeology, three decades after the first assessments of multispectral images to push back the limits of cropmark identification using near-infra red bands (Hampton, 1974; Hampton et al., 1977), the use of hyperspectral effectively emerged in the 2000s with the evaluation on *MIVIS* sensor operating in the VNIR, SWIR and TIR domains (Emmolo et al., 2004; Traviglia, 2006b).

Since, AHI has been continually developed in multiple domains of application including coastal and shallow waters mapping (Dekker et al., 2011; Z. Lee & Carder, 2001; Petit et al., 2017). The capability of measuring spectral information beyond the water surface is gaining interest for coastal management and bathymetry estimation, but for the archaeological domain, this remains largely unexplored.

2.2.2 Airborne hyperspectral data acquisition

As for airborne LiDAR, an airborne hyperspectral data acquisition project is driven by the data requirements (spatial coverage, spatial resolution) and the sensor characteristics.

Several optical systems have been developed in the last decades but the most common types are push broom and whisk broom sensors (Figure 2.27). Also known as an along-track scanner, a push broom sensor collects one line of pixels (using a CCD array) at a time. Per measurement, two dimensions are acquired (one dimension is the spectral information, the other dimension is the spatial dimension –line of pixel-, perpendicular to the flight direction). The scene is scanned with subsequent line acquisitions as the aircraft is moving forward in the flight direction. Push-broom sensors are to be distinguished from whiskbroom sensors, which only collect one spectrum at a time and sweep perpendicularly to the flight direction line using a scanning mirror. At similar flight speed, a push-broom sensor provides a better signal-to-noise ratio, as each spectral measurement is done for a longer integration time (Rogass et al., 2014). Push-broom sensors also tend to have superior spatial resolution capabilities. One drawback however is that the array must be perfectly calibrated to avoid differences of spectral measurement across line (Tan, 2016).

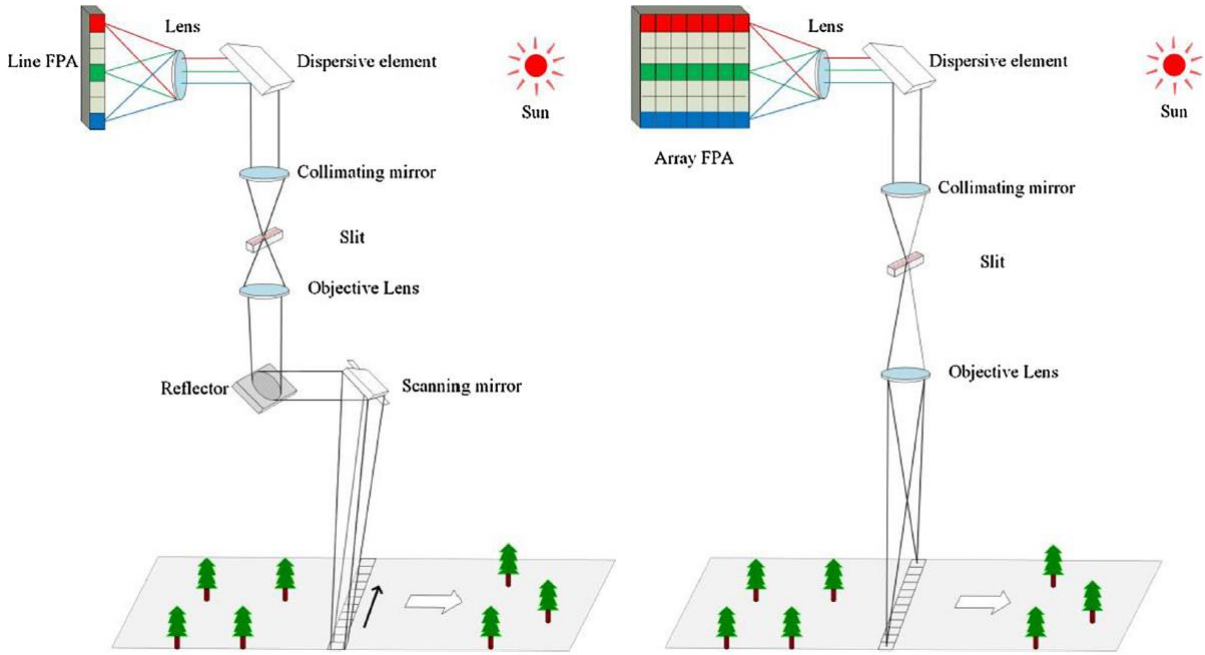

Figure 2.27. Whiskbroom (left) and pushbroom (left) hyperspectral sensors (Jia et al., 2020)

Positional and trajectory systems are equivalent to those detailed in ALS. An inertial navigation system is used to collect the XYZ position of the platform as well as the roll, pitch and yaw angles of the platform. Unlike standard aerial surveys, which are most often performed in frame mode (bi-dimensional scene), hyperspectral acquisitions are highly sensitive to the determination of the position and orientation of the sensor. This is a critical point in the geometric accuracy of the final image product.

In terms of spectral information, the acquisition parameters must be defined to maximize the signal-to-noise ratio (SNR). First at the sensor level, beyond the sensitivity and efficiency of the sensor which cannot be controlled, the integration time has to be defined. The integration time is defined to get the best SNR compromise (sufficiently high to record as many photons as possible, sufficiently low to avoid the detector saturation). For pushbroom sensors, the integration time, related to the frame-period (integration time plus read out time), must also be defined according to the speed of the aircraft. Second, at the scene level, external factors such as the solar irradiance available at the time of acquisition, and the atmospheric conditions between the sensor and the target have to be considered (water vapor or optically active elements involves scattering and absorption phenomena affecting the at-sensor measured signal). Over coastal areas, additional conditions of observations have to be taken into account. Because of the low reflectance of water (less than 2% on average in the VNIR domain), only a small portion of the solar energy is reflected back to the sensor. To penetrate the water column, the solar energy reaching the surface must be maximum, thus with a high sun elevation angle (usually above 30°) and clear sky conditions. Moreover, in areas subject to tides, a low water height (low tide / high tidal coefficient) would increase the capability of acquiring spectral information of the water bottom.

In terms of spatial information, in a typical acquisition project, the spatial resolution or more precisely the ground sampling distance (GSD) usually reaches sub-metric figures.

2.2.3 Hyperspectral data characteristics

2.2.3.1) Technical characteristics

Hyperspectral imaging data are provided in form of per flight-line datacubes, including 2 dimensions for the spatial (scene) representation and one dimension for the spectral information.

In its spatial dimension, the characteristics include the coverage of the image (spatial coverage), its ability to discern individual objects (spatial resolution) and its accuracy (spatial or geometric accuracy). The spatial coverage is variable from one project to another, but hundreds of km² can be covered in few hours. It depends on the flight altitude (above ground level), the field-of-view (FOV), the flight speed (knots) and the overlap between flight lines. The second main spatial characteristic is the spatial resolution, related to the ground sampling distance (GSD), itself related to the IFOV (instantaneous Field of View) and the altitude of acquisition. The GSD corresponds to the projected size of a pixel (in meters) of an AHI datacube. The higher the spatial resolution, the higher the capability of identifying small-size targets on the observed surface. In AHI, the spatial resolution typically reaches sub-metric figures.

In its spectral dimension, the spectral domain, the number of bands, the spectral resolution and the radiometric resolution are important characteristics. The spectral domain defines the wavelength range acquired by the sensor. In this thesis, we focus on the VNIR spectral-domain raging from 400nm to 1000nm. The number of bands and spectral resolution represent respectively the number of individual bands used to decompose the spectrum, and their spectral width (usually express in FWHM). A fine spectral resolution corresponds to narrow bands and allows for discrimination of target signatures based on small spectral variations. Finally, the radiometric resolution (the term quantization is also used) describes the sensitivity of a sensor to small difference of energy. The radiometric resolution is defined in bits per pixel.

2.2.3.2) Source of errors or uncertainties

2.2.3.2.a) Sensor-based errors or uncertainties

At the sensor level, the radiometric, spectral, and geometric performances of the imaging system influence data quality (Lenhard et al., 2015). The relationship between the raw digital numbers at the sensor and the corresponding physical quantity (spectral radiance) is affected by multiple sensor-related errors such as instrumental noises (e.g. shot noise, dark noise), shape and position of the spectral response, or optical distortions (e.g. smile and keystone effects) (Figure 2.28).

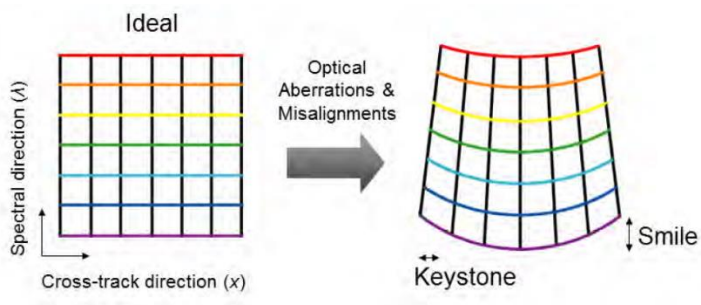

Figure 2.28. Smile and keystone effects in hyperspectral camera (source: Yokoya et al. (2010))

The radiometric, spectral and geometric characteristics of each pixel of the array are measured in laboratory. This characterization allows to define calibration coefficients (per pixel and wavelength) to be applied during post-flight processing to convert the raw data into measurable physical quantities.

Accurate sensor calibration is essential to improve the usability of acquired hyperspectral data (Kabir et al., 2020). Performances of a hyperspectral sensor are mainly synthetized in the signal-to-noise ratio (SNR) (Y. Chen et al., 2012) and the radiometric relative and absolute calibration accuracy (Kabir et al., 2020).

2.2.3.2.b) System-based errors or uncertainties

Like LiDAR acquisitions, AHI acquisitions are also affected by position and orientation measurements, not on the quality of the spectral information itself, but on its relation to a geographically defined target. System calibration (calibration of the GPS, IMU and scanner assembly, boresight calibration) and angular and positioning errors measurements are particularly important, especially for pushbroom scanner, to reach a suitable spatial precision and accuracy (see 2.2.4.2) for geometric correction). A spatial accuracy in the order of magnitude of 1 pixel is usually recommended.

2.2.3.2.c) Observation errors or uncertainties

Illumination and atmospheric conditions, topographic and surface configurations are also affecting the measured signal. Some of the exogenous factors can be accounted for during pre-processing steps (for example by correcting the signal for atmospheric effects), but none of them have perfect correction methods (empirical or physics-based models have their own uncertainties) and some of them are often not considered in operational acquisition projects (e.g. adjacency effects, topographic effects, BRDF effects).

2.2.4 Hyperspectral data processing: from data to information

Once acquired, hyperspectral imagery is provided in form of per flight-line datacubes that have to be post-processed before being further analyzed. The post-processing chain usually consists of

three steps: the radiometric calibration, the geometric correction/georeferencing and the atmospheric correction.

2.2.4.1) Radiometric correction

Radiometric corrections are required to convert the raw measurements (expressed in non-calibrated digital numbers DN) to the physical quantity it represents: the radiance, expressed in $W.m^{-2}.sr^{-1}.nm^{-1}$ (Pandey et al., 2020). This correction is commonly performed using laboratory derived calibration coefficients (offset and gain) provided by the manufacturers. These coefficients, given per pixel and per wavelength, account for the radiometric characteristics of each element of the array.

2.2.4.2) Geometric correction

AHI data are subject to geometric distortions of different origins: the vector instability (uncontrolled movement of the aircraft), the sensor (optical deformation) and the topography of the observed scene. To obtain a georeferenced hyperspectral image, these geometric distortions have to be corrected (Pandey et al., 2020).

Geometric corrections, therefore, consist to associate each image coordinates (row, column) to terrestrial coordinates (lat., long or easting, northing) on a defined reference system. The correction is performed using the sensor internal orientation (i.e. the geometric sensor model) as well as the navigation parameters defined by the position of the optical center during the flight (X, Y, Z coordinates), and its orientation (yaw, pitch, roll angles). These data, acquired by GNSS/INS instruments, are post-processed and synchronized with the image acquired frames to ensure the 6 parameters are known for each line of the image. The correction of distortions due to topographical effects can further be corrected using an external digital elevation model as reference.

The geometric corrections imply some deformation of the raw datacube on its spatial dimension. This deformation requires an interpolation of the measurements into projection grid. To conserve the spectral fidelity of the measurements, a nearest neighbor interpolator is usually recommended (Schlapfer et al., 2007).

2.2.4.3) Atmospheric correction

Because atmospheric gases and aerosols absorb and scatter the light differently depending on its wavelength, correction of the atmospheric effects have to be performed to convert the at-sensor spectral radiance measurement, to a corresponding surface spectral reflectance measurement. Two main approaches can be used to perform the atmospheric correction.

The first one is based on *in situ* reference measurement, such as the empirical line fit (ELF) method (Conel et al., 1987; Roberts, 1985) which uses transformation coefficients (gain and offset for each wavelength) to convert at-sensor radiance spectra to surface reflectance spectra. The coefficients

are determined by a linear regression between target at-sensor radiance selected on the imagery and their known surface reflectance (either using calibrated targets, or target directly measured *in situ* by a field spectrometer). On the assumption of uniform atmospheric conditions (temporally and spatially) during the imagery acquisition, and a per-wavelength linear relation between at-sensor and surface measurements, the coefficients determined on the reference pixels are used for the entire hyperspectral imagery acquired. The main advantage of this method is its simplicity and its low computational cost. However, the assumption of atmospheric uniformity is rarely confirmed in reality and the acquisition of *in situ* spectra requires the choice of temporally invariant targets or an additional constraint of synchronicity between the airborne and the ground measurements.

The second one is based on radiative transfer models which explicitly describe the absorption and scattering of gases and aerosols in the atmosphere (J. Gao, 2009). Atmospheric correction models require inputs regarding the solar and acquisition geometry, and atmospheric conditions including aerosol types and concentration, and gaseous atmospheric components. Models such as MODTRAN or 6S are commonly used to generates lookup tables (LUT) between path radiance spectra and their related physical atmospheric conditions. Atmospheric correction methods are commonly relying on such LUT to infer, based on physical conditions given as inputs –either manual or automatically extracted from the data-, the estimation of the atmospheric contribution to be corrected for.

The two approaches can also be combined in a hybrid method, that commonly includes two steps : (i) atmospheric correction based on radiative transfer model to transform the at-sensor spectral radiance measurement to a first estimation of the surface reflectance, (ii) empirical line fitting that adjusts the estimated surface reflectance by applying ELF coefficients obtained by linear regression between the estimated and corrected reflectance spectra on invariant targets. Such a hybrid method can help in reducing the residual atmospheric absorption and scattering effects that remain after the model-based correction (B.-C. Gao et al., 2009).

2.2.4.4) Noise reduction

AHI data are affected by instrumental and environmental noises which consequently affect the analysis of spectral information (Rasti et al., 2018). Noise can either be considered as part of the data and processed without any particular pre-processing stage, but one can also decide to reduce noise before any information extraction analyses.

Some dimensionality reduction techniques are adapted to the reduction of noise in spectral signatures. This is for example the case for MNF, where the image and its individual spectra are first reduced and projected in their new subspace (forward transformation); then an inverse transformation, using only the most informative components, is performed to reproject the data back to their original space (G. Luo et al., 2016). Because MNF orders components by decreasing SNR, image spectra are reconstructed in a noise-reduced version.

Guyot, Alexandre. Contribution of airborne LiDAR and hyperspectral data to archaeological mapping in terrestrial and submerged environments. 2021

Another common noise reduction technique used in AHI is spectral filtering. Smoothing methods such as Savitzky-Golay filter (Savitzky & Golay, 1964) or Whittaker filter (Whittaker, 1922) are particularly used in spectral denoising. The first is based on a local linear least-squares fit using a polynomial of a given degree (Vaiphasa, 2006); the second, considered faster, is based on a penalized least-square to minimize the deviation from the original data and the roughness of the reconstructed data (Eilers, 2003). Whittaker filter was for example implemented in the ARCTIS toolbox specifically developed for hyperspectral analysis in archaeological context (Atzberger et al., 2014).

Noise reduction techniques can be applied to improve noise-affected spectral signatures, but depending on the objective the choice of the algorithm and its parametrization can be complex. While ideally, the denoising algorithm reduces the measurement errors to their minimum (often present as high-frequency noise), it remains difficult to preserve all useful spectra information, which in their subtle form is often entangled with noise. Depending on the application and objectives, the noise reduction methods should therefore not systematically be applied.

2.2.5 Hyperspectral analysis for archaeological mapping

2.2.5.1) Band selection and spectral indices

In the 2000s, in their first attempts to leverage the high level of spectral information contained in AHI, researchers typically evaluated single spectral bands on their capacity to capture spectral variations related to cropmarks (Bassani et al., 2009). The selection of the optimal spectral band was therefore a challenge on its own (Cavalli et al., 2009).

AHI for archaeology was most uniquely dedicated to the identification and documentation of cropmarks in agricultural areas (Aqdus et al., 2008, 2012; Bennett et al., 2013; Emmolo et al., 2004; Pascucci et al., 2010; Traviglia, 2006a, 2006b), so not surprisingly the red (~650nm) and near-infra red (~750nm) portions of the spectrum were particularly interesting to identify variations of vegetation conditions. Naturally, the computation of vegetation indices from surface reflectance became a common approach for archaeological prospection, like the normalized difference vegetation (NDVI) introduced by Rouse et al. (1973) and defined as a function of the reflectance (ρ) in the red and near-infrared wavelength, by :

$$NDVI = \frac{\rho_{nir} - \rho_{red}}{\rho_{nir} + \rho_{red}} \tag{2.4}$$

Although the calculation of the NDVI is simple and its interpretation useful in several conditions, it turns out to be sensitive to several perturbing factors such as atmospheric conditions, or soil effects (Xue & Su, 2017). A very large number of vegetation indices have since been developed with some of them designed to tackle NDVI limitations, such as the atmospherically resistant vegetation index (ARVI) proposed by Kaufman & Tanre (1992), or the soil-adjusted vegetation index (SAVI) proposed by Huete (1988).

Because spectral indices can highlight useful spectral features, for example on vegetation health and growth, more effectively than the study of either individual bands or true/false-color composition images, over 150 vegetation indices have been published in remote sensing literature (Bennett et al., 2012b). In archaeological applications, attempts have been made to evaluate the most frequent indices. Recently, Cerra et al. (2018) proposed a comparison on more than 30 indices with an objective assessment based on mutual information (Cover et al., 1991) to rank indices according to their correspondence with the reference archaeological data in archaeological areas. Nevertheless, temporal and spatial variations of the indices related to the presence of various archaeological subsurface structures remain a challenge. Using field spectroscopy, interesting attempts (Agapiou et al., 2013) were for example made to better characterize the temporal variability of cropmarks compared to non-archaeological vegetated surfaces (Figure 2.29), or identify the most important spectral characteristics of archaeological and non-archaeological soils (Thabeng et al., 2019).

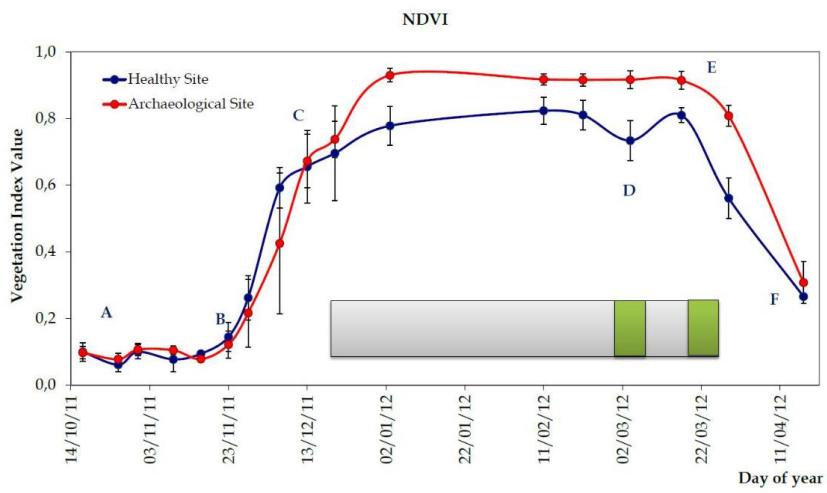

Figure 2.29. Temporal variation (from October to April) of NDVI for a standard healthy site (non-archaeological) and an archaeological site / crop-mark. The green markers identify the period of most discriminative NDVI values (source: Agapiou et al. (2013))

Among those approaches, two specific indices are worst mentioning because they were designed specifically designed for remote sensing archaeology.

The first one is the Normalized Archaeological Index (NAI) that was introduced by Agapiou et al. (2012) and is defined as :

$$NAI = \frac{\rho_{800} - \rho_{700}}{\rho_{800} + \rho_{700}} \tag{2.5}$$

With ρ_n the reflectance at wavelength n.

The author defines NAI as an optimal index for distinguishing crop marks, compared to standard normalized vegetation index (Agapiou et al., 2013).

The second one is named REIP (Red Edge Inflexion Point) introduced by Doneus et al. (2014). It aims at characterizing vegetation stress by focusing on the red-edge portion of the spectrum (between 680nm and 730nm). REIP is computed using the first derivative of the reflectance spectrum to extract, within the red-edge region, the wavelength of the maximum gradient, the gradient value at this wavelength, and the reflectance amplitude at this wavelength. The three components of REIP are then respectively displayed as red, green, blue color-composite.

The same authors (M. Doneus et al., 2014), also proposed a new index based on distribution fitting also introduced in the ARCTIS toolbox (Atzberger et al., 2014). For each pixel of the scene, a frequency distribution histogram of reflectance values is computed, and a predefined probability distribution function (PDF) is then fitted to it in a least-squared sense. The parameters of the PDF (mean and standard deviation for a normal distribution, or form and intensity for a gamma distribution) are then directly used to generate the multiband composite image (the number of bands equals the number of parameters).

2.2.5.2) Dimensionality reduction

AHI is high-dimensional data. A typical AHI VNIR datacube contains hundreds of spectral bands which implies some important considerations regarding their analysis: contiguous spectral bands are highly correlated, the volume of data is important, and specific to AHI the high-dimensional spectra are affected by noise.

In general, the accuracy of any classification and clustering algorithm is influenced by the number of dimensions in a dataset. This is known as the curse of dimensionality or the Hughes phenomenon introduced by Bellman & Kalaba (1961) and Hughes (1968). Increasing dimensionality also has side effects such as increasing computational effort or complexity of data representation. Considering the high-dimensionality of AHI data, it is therefore not surprising that dimensionality reductions technics are most often used in the AHI analysis workflow. Dimensionality reduction technics provide a way to project the high-dimensionality data onto a low-dimensionality subspace without losing significant information (D. G. Manolakis et al., 2016). The projected data can be further used for visualization, noise reduction, data compression or statistical analysis including anomaly detection and classification.

Many dimensionality reduction methods have been developed since the 1960s. Below we will focus on the most commonly used ones for AHI data and describe their usage in archaeological remote sensing contexts. Methods can be defined as linear (data are transformed to a low dimension space as a linear combination of the original variables), or non-linear (data are transformed to a low dimension space as a nonlinear combination of the original variables applied when the original high dimensional data contains nonlinear relationships.

2.2.5.2.a) Linear dimensionality reduction

The most commonly used technique of linear dimensionality reduction is principal component analysis (PCA). PCA, introduced by Pearson (1901) consists of an orthogonal linear projection that decorrelates data by diagonalization of the covariance matrix. The new variables (the principal components) are constructed as linear combinations of the initial variables, they are uncorrelated and ordered by increasing variance so that most information carried by the initial variables is stored into the first components. In remote sensing archaeology, PCA has often been used as an enhancement process for the visualization of spectral variation of surfaces (Aqdus et al., 2012; Cavalli et al., 2007; Emmolo et al., 2004; Traviglia, 2006a) for which principal components can be examined as a single band (greyscale) or as a combination of three different components. PCA is fast to compute and provides a first idea of the spectral variation of a scene. However, PCA can be strongly affected by noise, because it is based on variance maximization. As an example, because the variance often seen in the first or the last bands is mostly due to sensor and environmental noise, blindly computing PCA on all bands of a hypercube might results in the noise being highly dominant in the first resulting components, since the maximum variance is due to noise (Cerra et al., 2018). To mitigate this issue, one strategy can be to use selective PCA that consists in selecting a spectral or spatial subset of data to perform the analysis (thus excluding noisy or uninformative bands, or focusing on a particular geographical area) (Traviglia, 2006a).

Another strategy is to use the Minimum Noise Fraction (MNF) introduced by Green et al., (1988). MNF, also named noise adjusted PCA (NaPCA) is derived from the PCA. While PCA is ordering the components according to their variance, MNF is ordering components according to the image quality, measured by the signal to noise ratio (SNR). MNF is computed with two PCAs. The first PCA consists of the decorrelation and rescaling of the noise in the original data. This step, known as noise whitening (the noise gets unit variance and no band-to-band correlations), requires the determination of the noise covariance matrix. The second PCA is then applied to the noise-whitened image, with the resulting principal components ordered by their SNR according to the estimated noise. The determination of the noise statistics is a key aspect of MNF and should include both system and environmental noise to reach an effectively noise-reduced result. Several strategies have been proposed to estimate the noise covariance matrix. A common one is based on spatial auto-correlation which considers that neighboring pixels tend to be similar, and thus determines the local noise as the difference between adjacent pixels. It is also recommended to compute the noise on a homogeneous and dark subset of the data (such as homogeneous water surface), but in complex datasets, the noise statistics directly extracted from the whole image is a common strategy. MNF transform has been used to visually enhance spectral variations of surfaces in archaeological prospection context (Masini et al., 2012; Traviglia, 2006a) with results outperforming PCA. However, important drawbacks remain on the complex interpretation of the components, their physical meaning and the selection of the optimal components to enhance subtle spectral variations of archaeological origin.

Guyot, Alexandre. Contribution of airborne LiDAR and hyperspectral data to archaeological mapping in terrestrial and submerged environments. 2021

Other interesting linear dimensionality reduction methods are available, such as projection pursuit (Friedman & Tukey, 1974), but to our knowledge, these have not yet been evaluated for VNIR AHI in archaeological context.

2.2.5.2.b) Non-linear dimensionality reduction

AHI imagery is often defined as having non-linear characteristics in the spectral domain (Han & Goodenough, 2008). The use of linear dimensionality reduction can therefore fail to represent some of the complexity inherent to the data (complex spectral pattern not visible under linear transformations alone). This shortcoming can be addressed by using non-linear dimensionality reduction methods such as kernel-PCA (Schölkopf et al., 1998), kernel-MNF (L. Gao et al., 2017), autoencoder (Kramer, 1991), t-SNE (Pouyet et al., 2018) or Umap (McInnes et al., 2018).

Despite their potential, very few studies have assessed non-linear dimensionality reduction in the context of remote sensing archaeology (Cavalli et al., 2013). This can probably be explained by the relative complexity of these algorithms and their parametrization compared to linear-dimensionality reduction methods, as well as their usually low computational efficiency, often not adapted to large real imagery datasets in operational conditions.

Moreover, dimensionality reduction techniques are by essence unsupervised approaches (data annotation is not required), although data reduction can be driven by the selection of only a subset of the data. This is effectively the case in AHI projects for which the original data consists of millions or billions of samples (pixels) of hundred dimensions. In this case, the projection model defined by the dimensionality reduction method is commonly based on a subset of the image (random or selected based on the image characteristics) and then applied to the rest of the data. The drawback of such a strategy is that the projection is not locally optimal, but it has the advantage of providing a seamless representation of the whole dataset within the same subspace.

2.2.5.3) Derivative spectroscopy and continuum removal

The derivative spectroscopy is a suite of methods based on the computation of first, second and higher-order derivatives of the reflectance spectra. Initially developed for qualitative analysis and quantification of absorption features from spectra collected in a controlled environment (Talsky et al., 1978), it is also applied on AHI collected spectra (Tsai & Philpot, 1998). The computation of derivatives provides an effective way to analyze a reflectance spectrum (Figure 2.30). For example, the first derivative can be used to filter unwanted contents and identifying signal peaks corresponding to absorption or reflection features (their position corresponding to the zero-crossing position in the first derivative signal). The characteristics of these features can further be characterized by the 2nd or higher-order derivative (Louchard et al., 2002). Despite being highly useful tools for spectral characterization, derivative spectroscopy is also highly sensitive to noise (Tsai & Philpot, 1998) and can be particularly difficult to use with airborne spectroscopy. Spectral smoothing (cf. 2.2.4.4) is therefore often a prerequisite to the use of derivative spectroscopy on AHI.

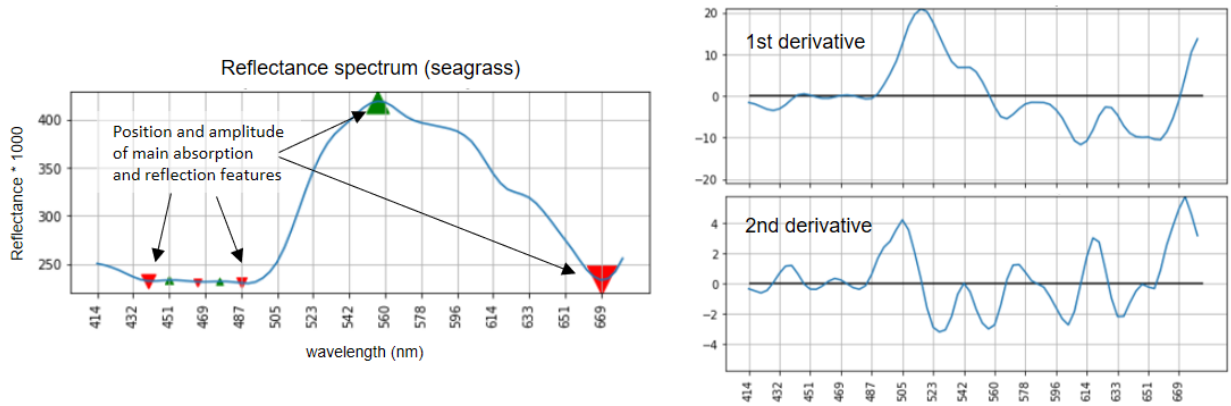

Figure 2.30. Example of a reflectance spectrum (seagrass) in the visible domain, analyzed by 1st and 2nd derivative spectroscopy

Absorption and reflection features can also be identified and characterized in a spectrum by using a continuum removal approach. Continuum removal is based on the assumption that a spectrum is composed of a continuum (or broad shape) and individual absorption features (Mohan & Porwal, 2015). The continuum can be approximated as a convex hull fitting the top of a spectrum. The original spectrum can then be normalized by its approximated continuum, thus providing an enhanced representation of the absorption features (Figure 2.31). Absorption characteristics such as position, width and depth can then be extracted automatically from the normalized spectrum.

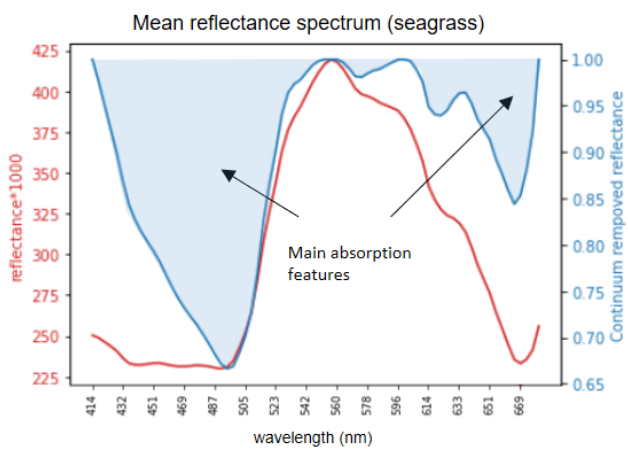

Figure 2.31. Example of a reflectance spectrum (seagrass) in the visible domain, analyzed by continuum removal

Whether there are extracted from derivative spectroscopy, continuum removal or other methods, these feature characteristics can be used on a per-pixel basis for further special/spectral visualization or feeding supervised or unsupervised machine-learning algorithms.

2.2.5.4) Spectral unmixing

As we have seen in the section related to the source of uncertainties in AHI, the characteristics of any pixel can rarely be considered truly homogenous and often includes different spectral mixtures. For this reason, spectral unmixing has been used as a technique for extracting the individual spectral signature (endmember) and their respective contribution (abundance) in the pixel signature (Bioucas-Dias et al., 2012; Keshava, 2003). This unmixing question has been a scientific subject on its own within the remote sensing community for more than 30 years, and many approaches have been developed to tackle this concern (see Dobigeon et al. (2016) for a review). Commonly, unmixing methods are defined as either linear or nonlinear. Linear unmixing is based on the assumption that a measured spectrum is a linear combination of endmembers with their respective abundance. Nonlinear unmixing is based on the fact that complex nonlinear spectral interactions occur at the pixel level.

Spectral unmixing methods are used in all AHI domains of application (agriculture, forestry, geology, etc.). In archaeological mapping, linear spectral unmixing has commonly been used in satellite-based approaches (Agapiou, Hadjimitsis, Sarris, et al., 2012; Cavalli et al., 2009; Kwong et al., 2009), but much less frequently with AHI (Pascucci et al., 2010; Savage et al., 2012)

Beyond the complexity of nonlinear methods and relative difficulty to find the most suitable approach, it is important to note that the spectral unmixing concern appeared with the rise of satellite remote sensing and especially with hyperspectral imagery because of their limited spatial resolution compared to multispectral or panchromatic sensors (Dobigeon et al., 2016). Nowadays, with the increase of spatial resolution, the complex physical interaction of spectral mixture is still present, but one could argue that its modeling is progressively related to the complex interactions also occurring with field spectroscopy which is commonly used as reference (pure spectra) for unmixing methods. In field spectroscopy, the observed spectrum is itself a mixture of constituent spectra, but at a different (sub-centimetric) scale level. In a typical field spectrometry measurement, the field-of-view for a handheld spectrometer is 4°, and the measurement is performed 1m above ground surface, thus representing a spectral measurement with a footprint of 7cm in diameter. The assumption of spectral purity for *in situ* measurements could thus progressively being challenged as a reference to model mixtures on AHI, with pixel size reaching the same order of magnitude.

2.2.5.5) Target detection and anomaly detection

In the large scope of AHI analysis methods, target detection and anomaly detection arise from the detection theory (Kay, 1998) and aims at detecting pixels whose spectra are either significantly similar to a known spectrum (target detection) or significantly different from the background spectra (anomaly detection) (Chein-I Chang & Shao-Shan Chiang, 2002). They can respectively be seen as supervised and unsupervised detection techniques (Racetin & Krtalić, 2021) although the scope of anomaly detection can also include methods requiring prior knowledge of background spectra, thus also relating it to supervised detection.

Many algorithms have been proposed to tackle the detection of targets or anomalies in AHI (see Racetin & Krtalić (2021) for a recent review).

One of the most common methods, often used as a reference in remote sensing, is the RX detector (RXD) introduced by Reed & Yu (1990) and derived from the generalized likelihood ratio test. Under the assumption that the background follows a multivariate normal distribution (with mean $\mu_b$and covariance matrix Σ_b), the anomaly score of a pixel (an observation x) is calculated as the squared Mahalanobis distance between the observation (x) and the normal distribution :

$$RXD(x) = (x - \mu_b)^T \Sigma_b^{-1} (x - \mu_b) \tag{2.6}$$

Several derived RXD have been developed by considering different ways of determining the background (Głomb & Romaszewski, 2020) or by using different subspaces, for example, derived from PCA (Borghys et al., 2012). As an example, the common Local RXD uses a moving window approach with an inner and outer size to estimate the background covariance matrix locally and which can be adapted to the size of the anomaly being searched for. In archaeological context using AHI, local RXD was for example evaluated and compared to other RX detector (Rejas et al., 2013) for unsupervised detection of potential remains.

Amongst the wide range of anomaly detection methods, Liu et al. (2008) introduced a new approach, named Isolation Forest (IF), which is based on tree-ensemble (such as the widely used Random Forest (RF) classification algorithms introduced by Breiman (2001). IF works by partitioning the data using decision trees. For AHI, partitions are created by recursively splitting observations according to randomly selected features (wavelengths) and randomly selected values (reflectances) for these features. On the assumption that anomalies are spectrally distant from normal observations, anomalies tend to be rapidly isolated while normal data are requiring a deeper partitioning to be isolated. Using multiple decision trees, the anomaly score of a pixel (an observation x) is calculated as a function of the average depth ($E(h(x))$) required to isolate this observation :

$$IF(x, n) = 2^{-E(h(x))/c(n)} \tag{2.7}$$

where $h(x)$ is the path length for observation x and $c(n)$ is the average path length for unsuccessful search. Unlike most anomaly detection methods, IF therefore explicitly identifies anomalies instead of profiling normal observations. Like other tree ensemble methods, IF is based on multiple decision trees, which improves its generalizability and robustness over a single estimator. IF was assessed for anomaly detection on AHI and outperformed other anomaly detectors including Local RX (K. Zhang et al., 2019).

Another different and innovative approach of anomaly detection in archaeological context was proposed by Traviglia & Torsello (2017) with the use of wavelets. The authors used a bank of Gabor filters of various scales and orientations to detect directional periodic spatial patterns on airborne hyperspectral imagery. The filters were successfully applied to different RGB composites or greyscale images (spectral indices) to identify potential axes of the Roman Centuriation system.

Guyot, Alexandre. Contribution of airborne LiDAR and hyperspectral data to archaeological mapping in terrestrial and submerged environments. 2021

2.2.5.6) AHI classification

Image classification is an important task in remote sensing. For hyperspectral imagery, it encompasses a broad range of related analyses (including spectral unmixing, dimensionality reduction, feature extraction –for example using derivative spectroscopy–), as well as unsupervised or supervised classification algorithms (see Ghamisi et al. (2017) for a review).

One might find surprising not to find a section on AHI classification state-of-the-art on this thesis. The reason for this is that image classification is by essence classifying subtle continuous information derived from the spectrum into a simplified discrete decision (classified map), based on distance metrics. Visualizing the continuous information (features) or the distance metric itself is much more adapted to the archaeological mapping objectives, which by essence always includes a part of human-based interpretation and indecision (see Chapter 1).

2.2.5.7) Spectral analysis and shallow water mapping

We have seen earlier in this chapter that in light radiation penetrates water, especially in the visible domain, and is attenuated differently depending on the wavelength (Figure 2.32). Remote sensing data and especially hyperspectral imagery have been particularly used to study this light and water interaction and to extract useful information on shallow water areas (Kutser et al., 2020).

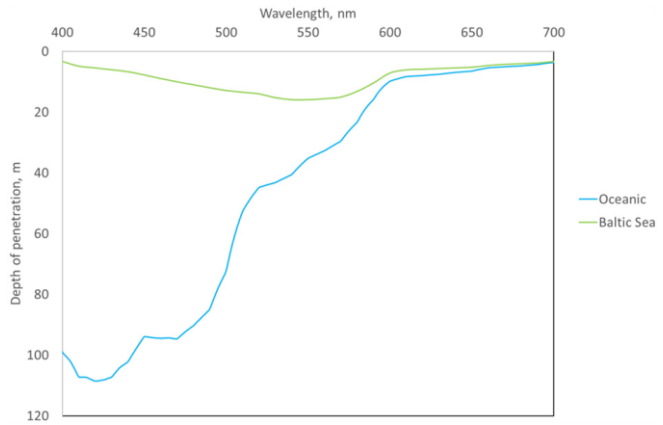

Figure 2.32. Depth of penetration of light in the visible spectral domain, calculated from the diffuse attenuation coefficient (Kd) measured in the Great Barrier Reef (Oceanic) and central parts of the Baltic Sea (source: Kutser et al. (2020))

The shallow water areas can be defined as submerged areas where the effect of the bottom substrate is detectable in the water-leaving radiance or reflectance (Kutser et al., 2020). The water-leaving radiance is dependent on various factors such as the depth, the turbidity, the reflectivity of the bottom substrate but also the downwelling solar irradiance. Therefore, shallow waters cannot be defined as a static extent of water according to a global depth limit, but is preferably a dynamically defined area, varying in space and time according to geographical and

environmental conditions. The variability of shallow water depths can be between a few centimeters in turbid waters, to several tens of meters in clear waters and light sand bottom.

In the last decades, with passive optical remote sensing systems able to capture spectral information on the visible spectral domain, different approaches have been developed to estimate water column depth, constituents of the water column, and benthic cover types from AHI in shallow water context. These approaches can be categorized into two main families: empirical and physics-based approaches (Dekker et al., 2011).

The empirical approaches (Lyzenga, 1981; Philpot, 1989; Stumpf et al., 2003) are based on direct observations of water-depth to calibrate a log-linear relation between the water depth and the water surface reflectance. As an example, the formula proposed by Stumpf et al. (2003) for water depth estimation (z) is defined :

$$z = m_1 \frac{\ln(nR_w(\lambda_i))}{\ln(nR_w(\lambda_j))} - m_0 \tag{2.8}$$

where m_1 is a tunable constant to scale the ratio to depth, n is a fixed constant for all areas, m_0 is the offset for a depth of 0m and $R_w(\lambda)$ are water surface reflectance for two bands of wavelength λ_i and λ_j, proposed as the blue and green bands by the author.

The physics-based approaches are based on complex radiative transfer (RT) models describing the relationship between a water surface reflectance spectrum and bio-physical parameters (Mobley & Mobley, 1994), including water depth, water constituents and bottom reflectance.

The forward models estimating a water-surface reflectance spectrum based on bio-physical parameters can be inverted to estimate bio-physical parameters from a known water-surface reflectance spectrum. Two main approaches can be used for this inversion (lookup tables or optimization algorithms) (Kutser et al., 2020).

With lookup tables (LUT) approach, numerical RT models such as Hydrolight (Mobley, 1999), are used to generate a LUT consisting of large numbers of modeled water reflectance spectra computed according to different bio-physical parameters (independently of the remote sensing data). The inversion is then performed on a per-pixel basis by comparing measured spectrum and all modeled spectra of the LUT to infer the related bio-physical parameters of the scene corresponding to the best match. The main drawbacks of this solution is the complexity of creating the LUT that could encompass sufficient combination of possibilities encountered in shallow water observation (infinity of water depth, water constituents and water bottom reflectance combinations).

With inversion using optimization algorithms, semi-analytical RT models such as Lee's model (Z. Lee et al., 1998, 1999) are used and the optimal bio-physical parameters are iteratively searched for to obtain a modeled water reflectance spectrum as close as possible to the observed water reflectance spectrum (Figure 2.33). Water depth, water constituents and water bottom reflectance

Guyot, Alexandre. Contribution of airborne LiDAR and hyperspectral data to archaeological mapping in terrestrial and submerged environments. 2021

can therefore be estimated without any prior *in situ* calibration information. This approach has been further developed and used for different shallow water mapping research projects (Bertels et al., 2008; Lennon et al., 2013), and many aspects of the inversions workflow, such as the pre-processing, the parametrization of the model and its optimization) have been studied (Brando et al., 2009; Hedley et al., 2012; Jay et al., 2017; Petit et al., 2017; Sicot et al., 2015), however its use in operational conditions for large scale mapping has rarely been assessed.

Lee's model is expressed here:

$$R_{rs}^{-} = R_{rs}^{\infty}\left(1 - A_1 e^{-(K_d + k_{uW})Z}\right) + A_2 R_{rs}^{B} e^{-(K_d + k_{uB})Z} \tag{2.9}$$

where R_{rs}^{-} is the remote sensing reflectance just below the water surface, R_{rs}^{∞} is the remote sensing reflectance for optically deep water; K_d, k_{uW}, k_{uB} are diffuse coefficients related to downwelling irradiance, upwelling radiance of the water column, and upwelling radiance from bottom reflection, respectively; A_1 and A_2 are constants; R_{rs}^{B} is the bottom reflectance and Z is the bottom depth.

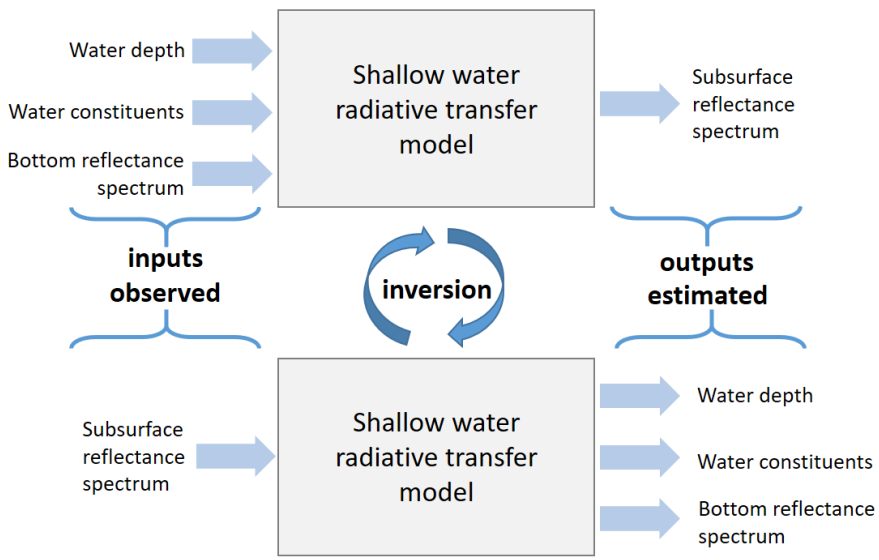

Figure 2.33. Principles of the shallow water radiative transfer model inversion.

More generally, while AHI has largely been used in coastal contexts for environmental concerns (Asner et al., 2020; Bajjouk et al., 2019; Jay et al., 2017; Z. Lee & Carder, 2001), its application for submerged archaeological prospection was, according to our knowledge, never evaluated.

2.3 The Current challenges and research questions

As we have seen previously, current challenges in archaeological mapping relate to representation and visualization issues, statistical pattern classification and target recognition, and integration of archaeology and remote sensing.

To face these current challenges related to archaeological mapping, we identified research questions concerning the evaluation of airborne LiDAR and hyperspectral data, and more generally remote sensing archaeology.

For about two decades, airborne LiDAR, as an active remote sensing system, has largely been evaluated for archaeological mapping and for its ability to document forested landscapes and identify subtle topographic changes potentially related to archaeological structures. The use of visualization techniques has been at the forefront of LiDAR-based archaeological mapping research projects. More recently, (semi)automatic detection methods, such as deep CNN, were also assessed, but these are relatively new research approaches. Thus, the following questions can be addressed:

- Can we use multiscale information in archaeological prospection for an enhanced perception of landscapes and sites by encompassing topographical context?
- Can Deep CNN be used in archaeology without large reference datasets? Can we move beyond the simple localization/detection of structures, but also include the delineation of complex structures to include computer-aided characterization?
- Can all of these computer-based approaches be integrated into an expert-based approach, not only for supporting the archaeological prospection workflow, but also to objectively identify new design strategies, for example in terms of LiDAR-based visualization techniques?

Concerning airborne hyperspectral imaging, this passive remote sensing system has shown great value in archaeological mapping to identify subtle spectral characteristics related to cropmarks or soilmarks in open areas. In the VNIR spectral domain, AHI has also been used for mapping shallow-water areas, especially for environmental concerns such as natural habitat mapping or water-quality assessment. The use of AHI in the context of shallow waters could therefore be a real opportunity for archaeological mapping of submerged coastal areas that are often of high archaeological potential. The following questions are consequently raised:

- Can airborne hyperspectral imagery be used as a prospection method in shallow waters? What are the potential and limits of AHI data in this context?

More globally, regarding the evaluation of airborne LiDAR and hyperspectral data, the position of remote sensing in the field of archaeology is posed. Unlike the above questions, which are specific to this thesis, the question of the position of remote sensing is regularly raised in archaeology, particularly concerning the relationship between desk-based and field-based approaches:

Guyot, Alexandre. Contribution of airborne LiDAR and hyperspectral data to archaeological mapping in terrestrial and submerged environments. 2021

- Which convergence strategies can be developed between desk-based and field-based archaeological approaches? How can both approaches benefit from each other to improve the perception and understanding of archaeological landscapes and sites?
- Considering the potential and limits of the remote sensing approaches, and the challenges and constraints associated with the archaeological domain, which directions could be followed to improve the integrated use of remote sensing data for a better understanding of the human past and better protection of the cultural heritage?

Guyot, Alexandre. Contribution of airborne LiDAR and hyperspectral data to archaeological mapping in terrestrial and submerged environments. 2021

Chapter 3. STUDY SITES AND DATA

The objective of this part is to present the geographical and archaeological context as well as the data used for the thesis.

In a first section, a brief description of the geographical and archaeological context of Brittany is proposed, followed by a particular focus on the two study sites (Carnac and the Gulf of Morbihan, and the Molène archipelago), to highlight the local framework in which the approaches developed for this thesis were placed in.

Second, the data used are presented. Remote sensing data (LiDAR and hyperspectral) are described and analyzed from their acquisition phases to their post-processing. Archaeological reference data are also presented and analyzed. Finally, the *in situ* data collected in terrestrial and underwater contexts are described.

To evaluate airborne LiDAR and AHI remote sensing data for archaeological mapping in terrestrial and submerged contexts, datasets from three airborne remote sensing surveys were collected on the two study sites (Figure 3.1 and Table 3.1).

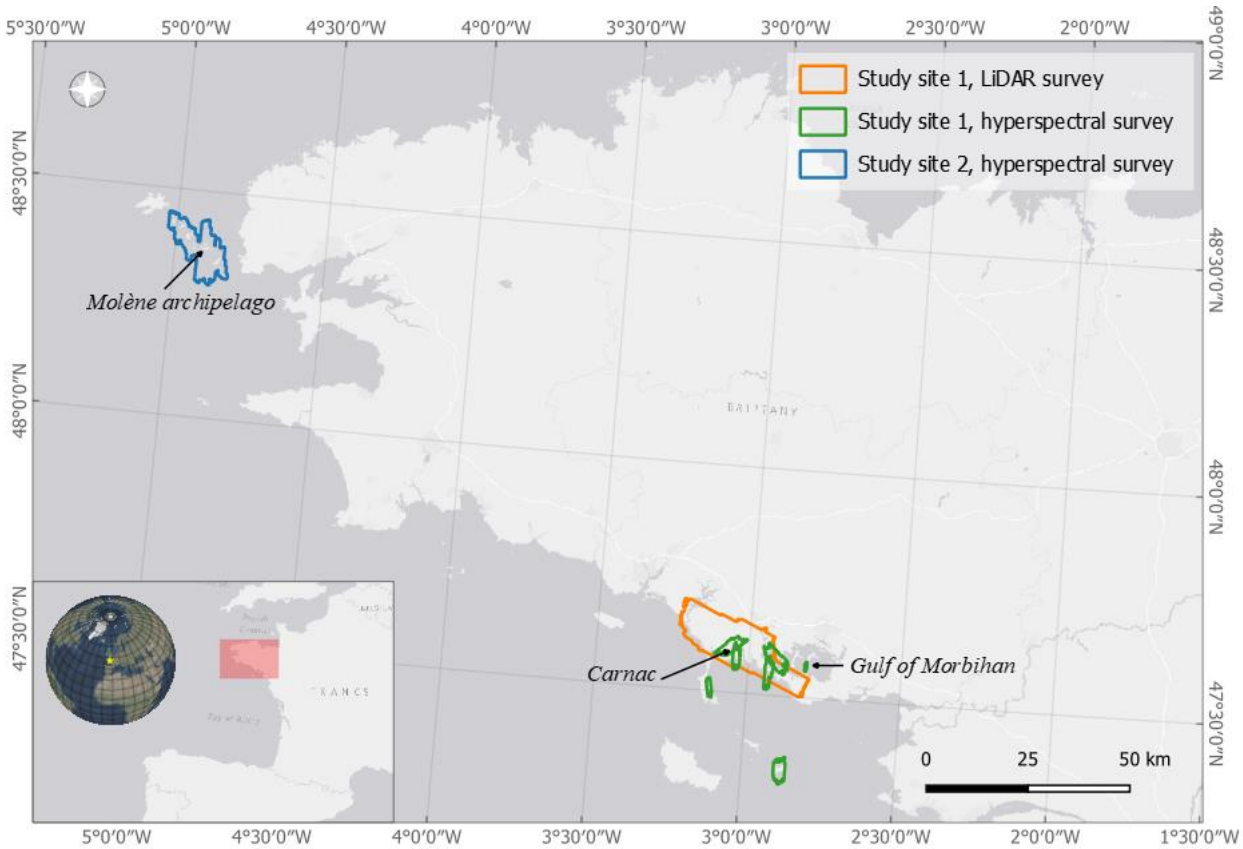

Figure 3.1. Study sites and remote sensing surveys used for the thesis

Table 3.1. Remote sensing dataset used in the thesis

Site	Airborne Sensor	Acquisition period
Study site 1, Carnac and Gulf of Morbihan	LiDAR (14 pnts/m² density)	March, 2016
Study site 1, Carnac and Gulf of Morbihan	Hyperspectral VNIR (50cm resolution)	September, 2018
Study site 2, Molène archipelago	Hyperspectral VNIR (1m resolution)	May, 2020

3.1 Study sites

3.1.1 The regional context

Brittany (*Bretagne* in French) is the westernmost region of France, covering an area of 27,209 square km for a population of 3,3 million inhabitants. Administratively divided into 4 departments (Côtes d'Armor, Ille-et-Vilaine, Finistère, Morbihan), the peninsula faces the Atlantic Ocean and is bounded by the Bay of Biscay on the south-west, and the English Channel in the north (Figure 3.2). With a coastline of about 2470 km long, Brittany is the first maritime region of France and represents one-third of the French metropolitan maritime façade[11].

[11] Because the length of a coastline is dependent of the scale of analysis, often referred to as the "coastal paradox" (Mandelbrot, 1982), different values can be found for the coastline of Brittany. The given figure of 2470 km refers to the reference provided by CEREMA and based on the SHOM/IGN Histolitt dataset.

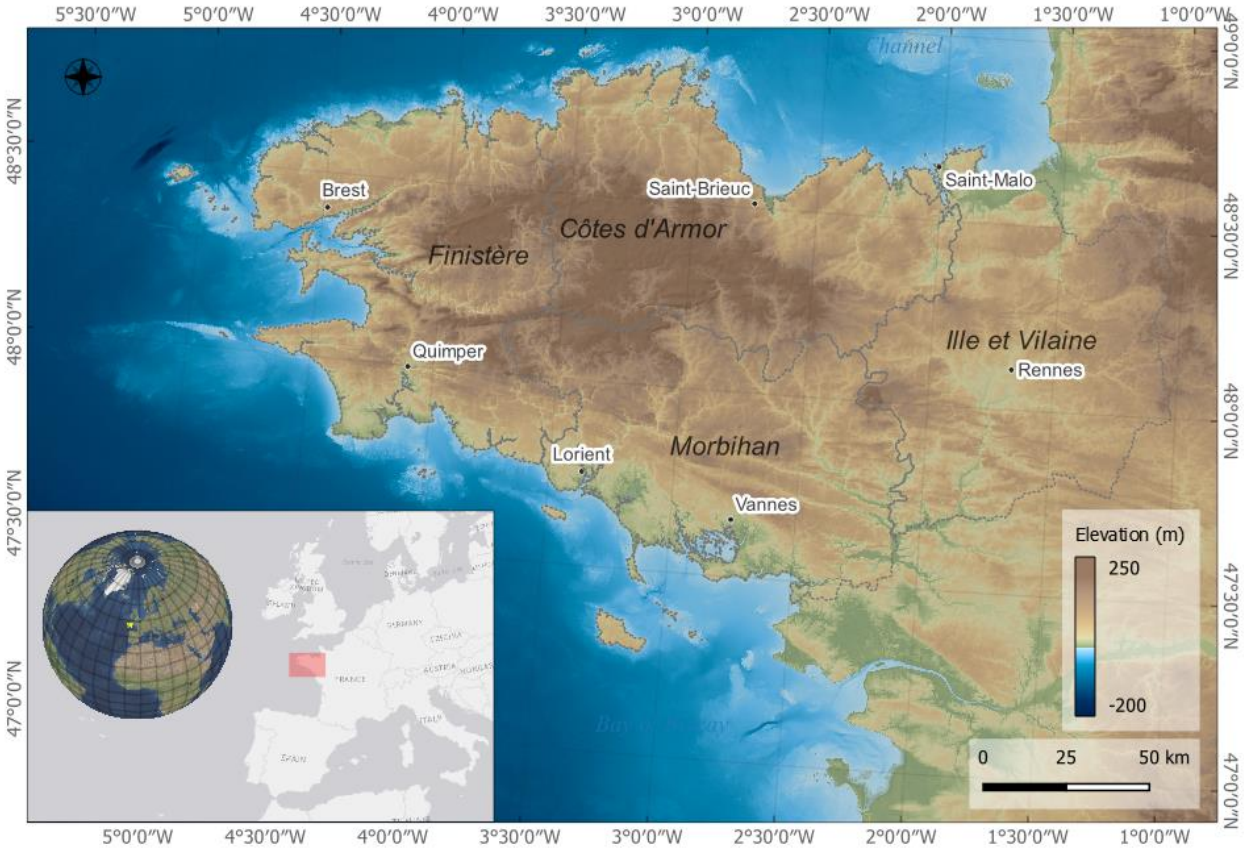

Figure 3.2. Region of Brittany

For the most part, the relief of the region is made up of plateaus, hills and ridges of low-altitudes (never exceeding 400m) characterizing the gentle topography and landscape of the ancient Armorican massif strongly flattened by erosion during a complex and multiphase geological formation (Ballevre et al., 2013). This complexity implies a great diversity of sedimentary, metamorphic and magmatic rocks principally resulting from the Cadomian and Hercynian orogenies and their subsequent peneplanations. During the quaternary period, erosion and sedimentation were dominantly controlled by glacial-interglacial cycles and the sea-level fluctuations they induced. From the last glacial maximum, the coastal landscape was progressively submerged by sea-level rise (Figure 3.3) before reaching its current physiognomy (Stéphan, 2019).

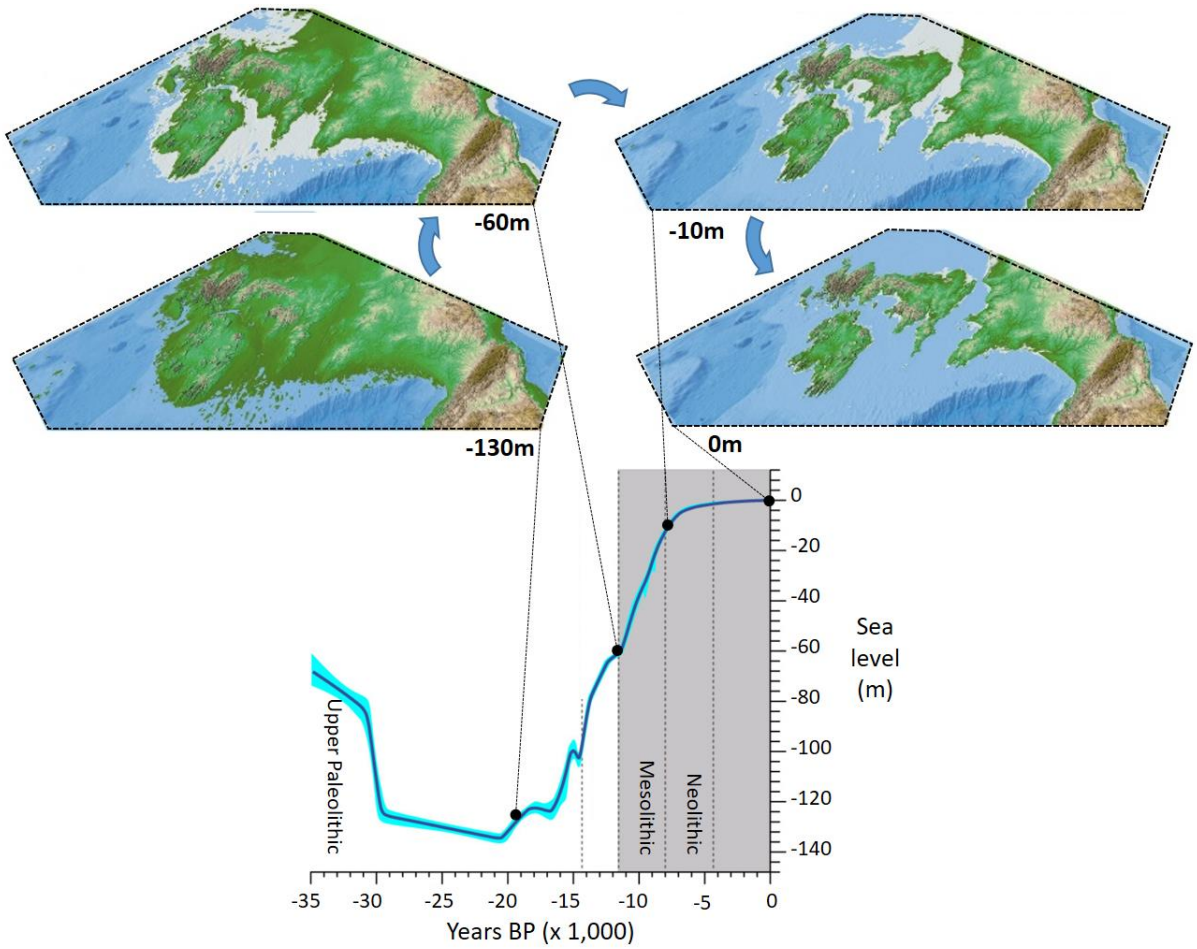

Figure 3.3. Sea-level variations from the Upper Paleolithic to current days (bottom), and related western Europe costal representations for sea-level at -130m, -60m, -10m and 0m (top) (adapted from Stéphan (2019))

The archaeological context of the Armorican peninsula is particularly rich and complex and cannot be detailed in a contextual section. The following paragraph highlights some regional particularities from Paleolithic to the Roman conquest of the Celtic Gaul in 52 BC.

Despite a soil acidity (the region has an average pH of 6.3, mainly due to the granitic basement) that accelerates the degradation of bone remains, evidence of human presence since Paleolithic are attested and are amongst the most emblematic of western Europe. The marine cave of Menez-Dregan (Plouhinec) situated at the southern tip of the region, for example, is a major site where the presence of fireplaces dating back to 465 000 BP have been uncovered (Ravon, 2017). The rock shelter of the Rocher de l'Impératrice (Plougastel), which dominates the Elorn valley in the west part of the region, is also a site of major importance which has revealed artifacts attributed to the end of the Paleolithic period (14 500 BP), with engraved plates of figurative horses or aurochs (Naudinot et al., 2017). The last populations of Hunter-Gatherers have also left several pieces of evidence throughout the region, notably attested in major Mesolithic sites such as Teviec, Hoedic

or Ber Er Vil (Marchand, 2020). The Neolithic, characterized by sedentarization and the emergence of agriculture, probably remains the most characteristic period associated with Brittany. The term "Neolithic" itself, first defined by Lubbock (1865), referred to the finely polished stone axes such as those found a few years earlier in the Tumulus Saint-Michel in Carnac (Galles, 1862). Megalithic architectures of this period punctuate the landscape of Brittany and form a complex matrix of sites, whose chrono-typology is still being discussed[12], in particular with the opposition of a linear evolution or a polymorphism of the funeral monuments (Cousseau, 2016). In any case, judging by the exceptional character of megalithic sites in Brittany, such as the Cairns of Barnenez, and Gavrinis, the region was certainly an important pole of influence at continental scale during the Neolithic. According to Schulz Paulsson (2019) the megalithic culture was even diffused from the west of France at the beginning of the 5th millennium, notably based on maritime and navigation knowledge. A few millennia after this emergence, megalithism was fading but Brittany remained still an important pole of richness locally controlled by organized societies. This increasing sense of territoriality, can for example be illustrated by the Armorican Tumulus culture of the Bronze Age (4200 to 2800 BP) and the exploitation of the Armorican tin deposits for an emerging metal industry (Briard, 1984). Attributed to this period, an engraved slab found in a princely tumulus of central Brittany was recently interpreted as a cartographic representation of a territory, and thus could be the oldest cartographic representation in Europe (Nicolas et al., 2021). During the first millennia BC, the transition to the iron metallurgy corresponds to a period of economic change and an important development of the agriculture, notably seen through the territorial coverage of Gallic farms, whose enclosures are identified by aerial prospection (in Brittany, 1/3 of the sites identified by aerial photography are attributed to this period (Gautier, Guigon, Leroux, et al., 2019). The first century BC marked the beginning of the Romanization of the Gallic peoples of Armorica, notably with the battle opposing the Roman army and the Veneti (a Gallic tribe of southern Brittany), which took place on the coast of Morbihan in 56 BC.

3.1.2 Study site 1: Carnac and the Gulf of Morbihan

The area of Carnac and the Gulf du Morbihan (Figure 3.4) is the first study site of this thesis. Located in the south of Brittany, it comprises the territory of 26 municipalities between the Rhuys peninsula in the east and the ria of Etel in the west. The terrestrial surface of 376 km² is largely increased by including the adjacent maritime domain of the Gulf of Morbihan and the bay of Quiberon.

[12] The terminologies employed in the thesis are "tumulus", as a general term for the external envelope encompassing internal structures, which are here designed as "dolmen" (Cousseau, 2016).

Guyot, Alexandre. Contribution of airborne LiDAR and hyperspectral data to archaeological mapping in terrestrial and submerged environments. 2021

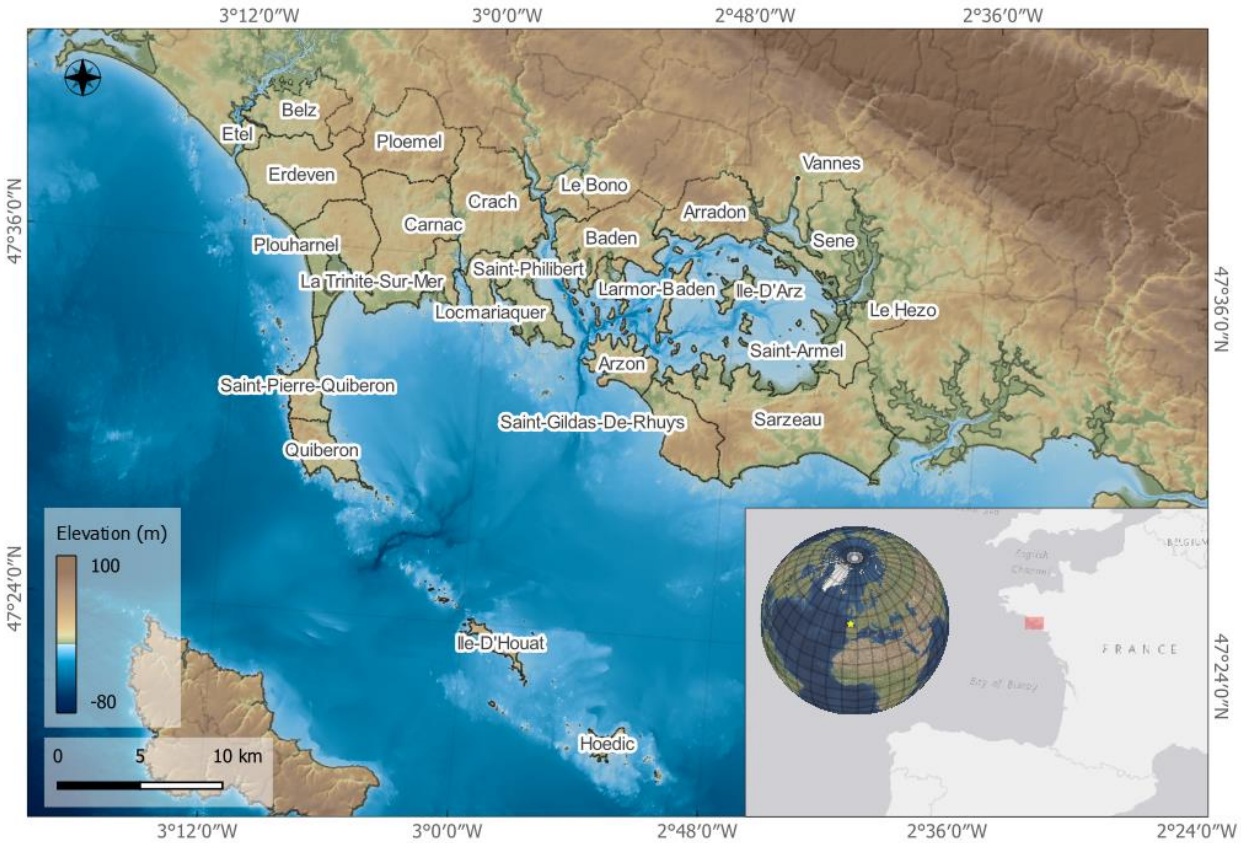

Figure 3.4. Carnac and the Gulf of Morbihan

The south Morbihan follows the geological history of this part of Armorican Massif and particularly of the south Armorican domain of NW/SE orientation. The substratum is made of various rocks (sedimentary, metamorphic and magmatic) characteristic of the Hercynian chain dominated by gneiss, migmatites, granites and micaschists. This eroded formation forms a peneplain with undulating reliefs (rarely exceeding 40m of altitude on the northern part) marked from east to west by the rias of Auray, Crac'h and Etel.

The landscape matrix, on the coastal part or the inland part, is very fragmented. The morphology of the coast is varied with an alternance of sandy bays, rocky coasts, marshes and urbanized surfaces. The Gulf of Morbihan, separated from the Bay of Quiberon by a narrow gully delimited by the tips of Kerpenhir and Port-Navalo, forms a shallow inland sea (23m maximum) with powerful and complex currents circulating around more than 40 islands and islets. The hinterland also forms a landscape mosaic dominated by the bocage and a high density of deciduous and coniferous forests (maritime pines in particular).

The archaeological wealth of this environment, in particular its megalithic architecture, is internationally recognized and is currently the subject of a project for inclusion on the UNESCO

heritage list[13]. The emblematic sites of the area, such as the alignments of Carnac, the Grand Menhir Brisé and the dolmen of the Table des Marchand (Locmariaquer), the carnacean tumulus of St Michel (Carnac), the double hemicycle of standing stones, partially submerged in Er Lannic (Arzon), the imposing cairn of Gavrinis and its engraved slabs, participate in the exceptional richness and diversity of the megalithic heritage. The relationship with the coastal environment is particularly striking insofar as an important part of this heritage is gradually being reached by the shoreline, with some sites already submerged by the transgressive marine phenomenon at work for thousands of years (Cassen, Grimault, et al., 2019).

While this thesis is based on a diachronic archaeological prospection approach, the archaeological research in this area is largely dominated by megalithism, which has concentrated most of the studies for the last two centuries.

The landscape of southern Morbihan forms a particularly complex matrix where wooded and hedged areas make traditional aerial prospections, based on photography, difficult to carry out. This archaeological and landscape context contributed to the choice of this study area for the evaluation of remote sensing approaches using LiDAR (for the terrestrial part, and notably under forest cover) and hyperspectral (mainly for the submerged part).

3.1.3 Study site 2: the Molène archipelago

The Molène archipelago forms a string of islands (Molène island being the largest) and islets emerged off the Iroise sea at the extreme west of the Armorican peninsula (Figure 3.5). Composed of 9 main islands and hundreds of islets and outcrops stretching on more than 15 kilometers on a south-east/north-west axis between the Pointe de Saint-Mathieu and the Ushant island (Ouessant), the archipelago is separated from the continent by the shallow Four channel (about 10m deep), and from Ushant Island by the deep Fromveur channel (about 50m deep).

[13] https://www.culture.gouv.fr/Regions/Drac-Bretagne/Politique-et-actions-culturelles/Valorisation-du-patrimoine-archeologique/Proposition-d-inscription-au-patrimoine-mondial-des-megalithes-de-Carnac-et-des-rives-du-Morbihan

Guyot, Alexandre. Contribution of airborne LiDAR and hyperspectral data to archaeological mapping in terrestrial and submerged environments. 2021

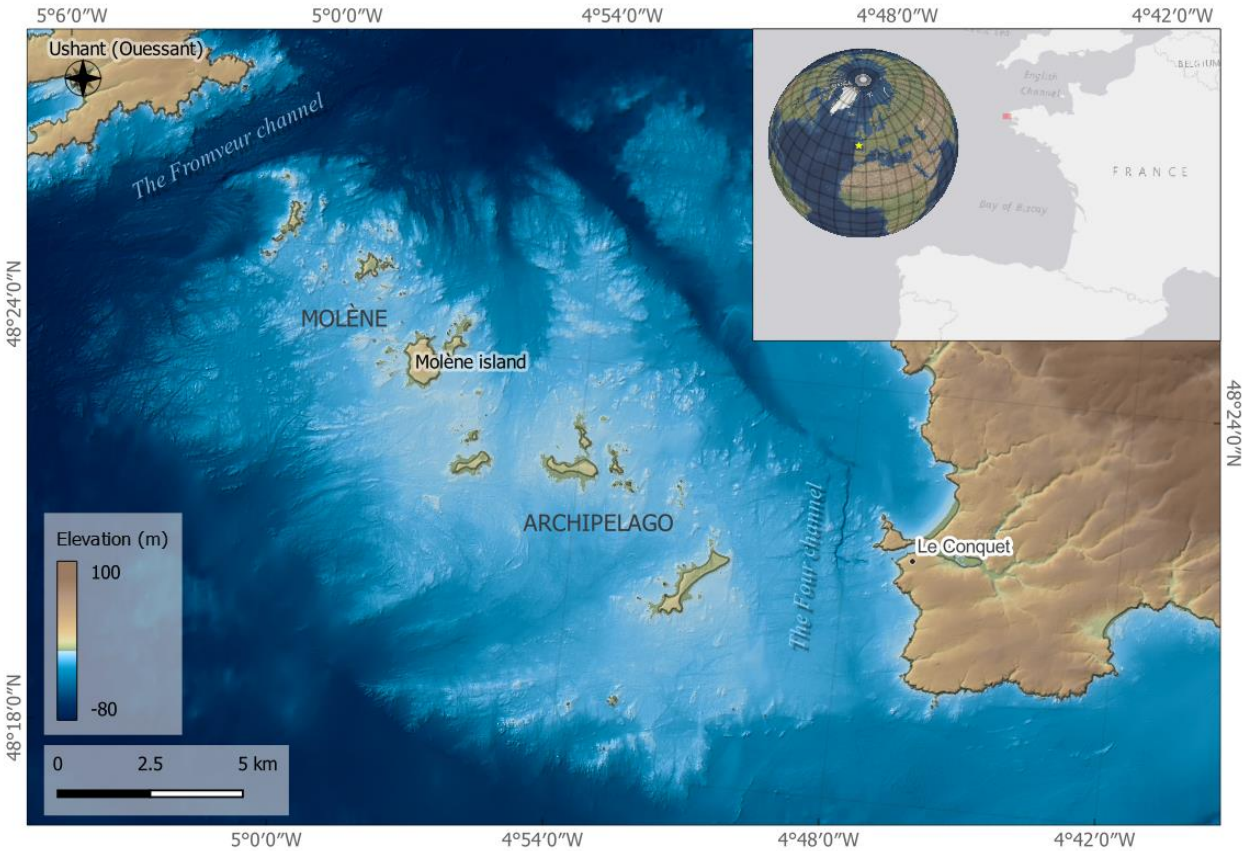

Figure 3.5. The Molène archipelago

Part of the Armorican Massif, the geology of the archipelago is the western continuity of the Hercynian metamorphic and magmatic formations of the Léon basement which extend towards Ushant island (Ehrhold et al., 2017).

With a relatively low relief (the highest point, on Molène Island, culminates at 26 m NGF), the numerous islands and islets of the archipelago form the emerging part of a vast submerged plateau of more than 150 km² (Guilcher, 1959) and whose depth rarely exceed 10m. While the terrestrial part (above the highest astronomical tide) represents about 2.5 km² of land, at the lowest astronomical tide level, with the important tidal range (more than 7m), the land territory increases to over 16 km² including the foreshore area.

The particular position of the Molène archipelago, characterized by its shallow plateau and strong currents, is a refuge for biodiversity. As part of the Iroise sea, it has been designed as a UNESCO Biosphere Reserve in 1988[14], and is also part of the Armoric Regional Natural Park and Iroise Marine Natural Park.

[14] http://www.unesco.org/new/fr/natural-sciences/environment/ecological-sciences/biosphere-reserves/europe-north-america/france/iles-et-mer-diroise/

The cultural and archaeological heritage is also one of the archipelago's richness. While, very few elements attest a human presence during the Paleolithic (Molines, 1992) and Mesolithic periods, archaeological sites attributed to the Neolithic are numerous. From early in the 20th century, the archaeologist P. Du Chatellier (Du Châtellier, 1902) identified multiple megalithic funeral structures throughout the archipelago. Since the beginning of the 2000s, the archipelago is the subject of an important archaeological program including the excavation of an important Bronze Age habitat of Beg ar Loued on Molène Island (Pailler & Nicolas, 2019). Archaeological field and aerial surveys were carried out on land (Pailler & Sparfel, 2001) but also on the intertidal zone, especially for the prospection of stone tidal fish-weirs (Daire & Langouët, 2010; Gandois et al., 2013, 2018; Gandois & Stéphan, 2015; Stéphan, Gandois, et al., 2019).

According to paleogeographic reconstructions (Stéphan et al., 2013), the archipelago was gradually submerged during the post-glacial transgression, but its insularity, due to the shallowness of the Four channel, was probably not effective before the Mesolithic period, with a sea-level around 15 m below the present level (Figure 3.6).

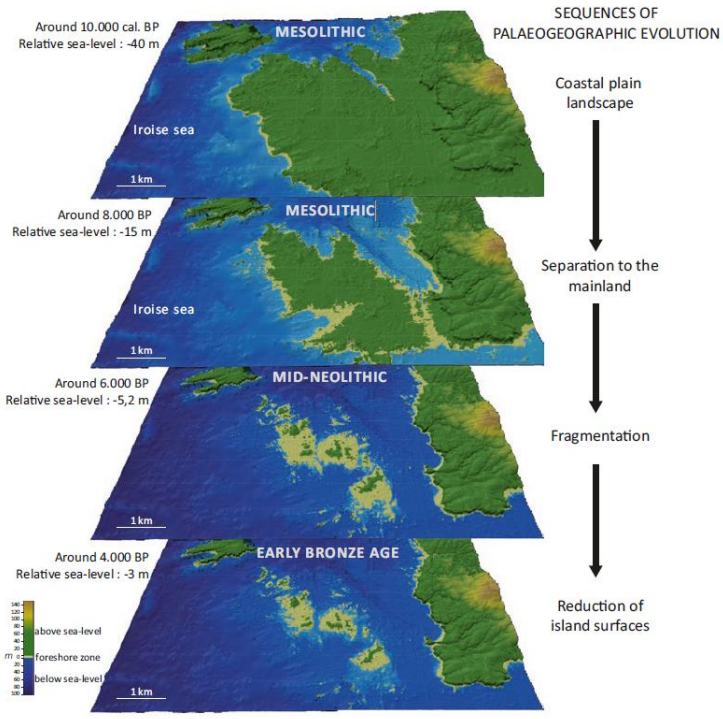

Figure 3.6. Paleogeographic evolution of the Molène archipelago between 10,000 BP to 4000 BP, by P. Stéphan (source : Billard et al., 2020)

Since the Neolithic, this access to vast foreshore areas favored the exploitation of natural marine resources by the insular communities, who built monumental fish weirs structures on suitable intertidal to create impermanent pools filling and emptying at the rhythms of tides. Despite the complexity associated with radiocarbon dating of such structures (most of them being mineral and hardly accessible underwater), Daire & Langouët, (2011) proposed a method to infer their

functioning period based on their proposed morphology (height) and their current depth in comparison to past sea-level estimations. Applying this method with the most recent and reliable sea-level curve (Stéphan, Fichaut, et al., 2019) indicated that the deepest structure could have been used from the Early Neolithic (Stéphan, Gandois, et al., 2019).

The geoarchaeological context (drowned landscape, active research program, cultural heritage management concerns) led to define the Molène archipelago as the ideal study area for the evaluation of airborne hyperspectral imagery for large-scale archaeological prospection of submerged landscapes.

3.2 Data

3.2.1.1) LiDAR data

3.2.1.1.a) Data Acquisition

The airborne LiDAR data used on the area of Carnac and the Gulf of Morbihan (Site 1) were collected in march 2016. The acquisition was carried out by GeoFIT-Expert company (Nantes, France) under the supervision of OSUR/OSUNA on an area of 246.7 km² (Figure 3.7). The sensor was an Optech Titan (Figure 3.8) operating a bi-channel laser of 532nm (Green) and 1064nm (near infra-red).

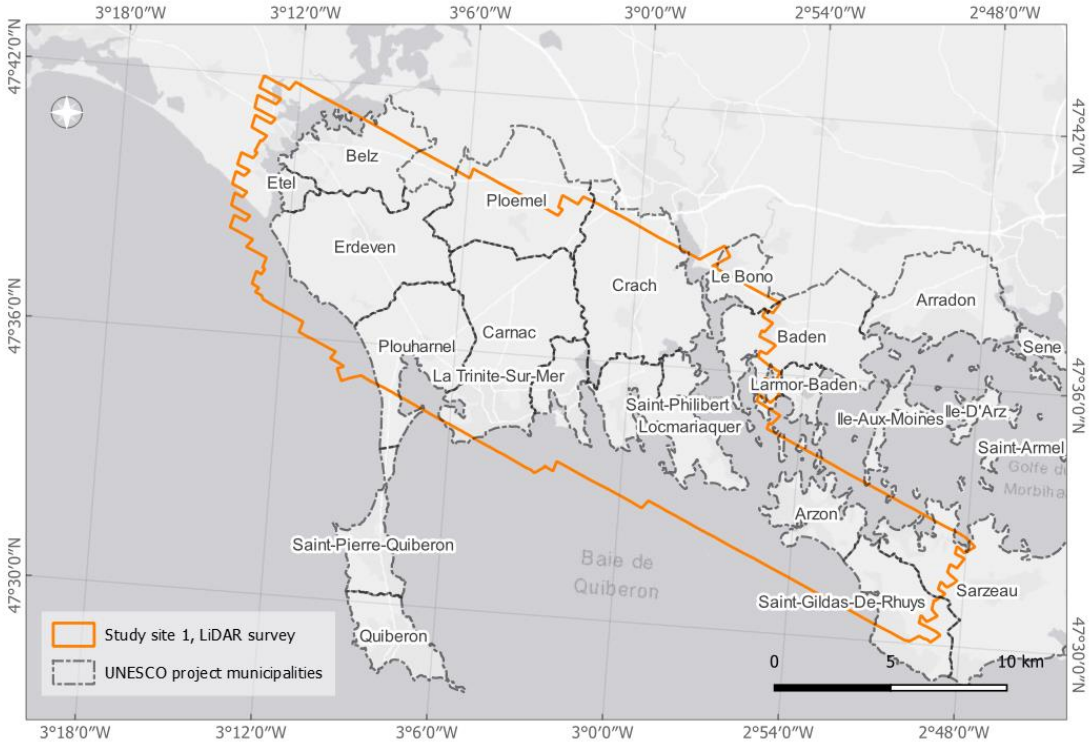

Figure 3.7. LiDAR survey (2016) over Carnac and the Gulf of Morbihan

The main acquisition and sensor parameters are provided (Table 3.2):

Table 3.2. Main characteristics of the airborne LiDAR survey on the area of Carnac and the Gulf of Morbihan

Parameters	Value
Flight date	March 16th, 2016
Area covered	246.7 km² (~200 km² of land)
Flight altitude	1300 m
Side overlap	20-25%
Acq. Mode	Topographic, discrete multi-echo (up to 5 returns)
Nominal point density	14 points / m²
Laser wavelength	1064 nm (near infrared), 532 nm (green)
Beam divergence	0.35 mrad (near infrared), 0.7 mrad (green)
Scan frequency	61 Hz
Pulse repetition frequency	300 kHz
Field of view	26° (ground swath of ~600m at flight altitude)
Absolute vertical accuracy	8 cm (RMSE)
Absolute horizontal accuracy	12 cm (RMSE)

Figure 3.8. Airborne LiDAR Optech Titan sensor (credit: Teledyne Optech)

The collected LiDAR point cloud represented a total of 5.2 billion points (60% from the NIR channel, 40% from the green channel).

3.2.1.1.b) Post-flight processing

Post-flight processing, including trajectory calculation and flight-line adjustments, was performed by GeoFIT-Expert company, Nantes (France). Trajectory data were computed from post-processed differential GNSS measurements and the nearest ground stations of the IGN permanent GNSS network (RGP), and enriched by IMU measurements using Inertial Explorer software. Upon trajectory computation, the LiDAR point cloud was further improved for flight lines relative adjustments. Optech LiDAR Mapping Suite (LMS) was used to perform this operation. The

georeferenced raw point cloud was finally provided in Lambert-93/RGF93 (EPSG:2154) coordinate system with elevation provided as a reference to the IGN-69 datum. The planimetric and vertical accuracy of the data were respectively better than 0.12 m and 0.08 m (RMSE), based on comparison with reference surfaces. The data was delivered as an unclassified point cloud in a compressed LAZ format, organized per flight line and laser channel (infra-red and green).

3.2.1.1.c) From data to information

a. Point cloud to DTM

The georeferenced raw point cloud was pre-processed to filter ground points and generate a high-resolution DTM following an automatic workflow developed with LASTools software (Isenburg, 2020) and described below :

- LAZ files, organized per channel and flight-line were merged and reorganized in a tiling system (tiles of 500m x 500m) by considering a 50m overlap between tiles to avoid any boundary effects during the analysis. Tiles were then spatially indexed to speed up the workflow.
- Outliers measurements were identified and tagged as *noise* in a two-step procedure: 1) points outside the elevation range of [-5m; 60m] were excluded. 2) Spatially isolated points were identified using *lasnoise* tool with a 1m step (step_xy, step_z), which represents a neighborhood analysis within a cube of 27m3 in volume) and a minimum threshold of 10 neighbors. Outliers were excluded from further processing.
- The ground filtering process was performed in a two-step procedure specifically developed for this dataset, considering the lack of measurements in some building roof slopes (discussed in 3.2.1.1.d).
    - The first step of ground filtering was performed using *lasground* tool (based on a progressive TIN densification approach) configured a with a large step of 25m. This parameter value was chosen to ensure a coarse ground filtering (very few micro-reliefs included) with a suitable exclusion of above ground features such as vegetation and buildings. Non-ground points more than 1.5m above ground were further classified in vegetation or building according to the following local planarity or ruggedness criteria: local planarity factor of at least 0.15 were classified as building, local ruggedness factor of at least 0.4 were classified as vegetation. All points below the 1.5m threshold, were kept as unclassified.
    - The second step of ground filtering was performed using *lasground* tool configured with a with a small step of 3m. This parameter value was chosen to ensure a much finer ground filtering than in first step. This iteration was run on all points, excluding already classified above ground points (building and vegetation). This strategy improved the ground filtering (densification and

inclusion of micro-reliefs) while ensuring the exclusion of above ground features.

- Final ground points were used to generate the DTM using a linear TIN interpolation and gridded at 50cm resolution.

b. DTM to multiscale visualization technique

The LiDAR-derived DTM generated from the above workflow served as input data to subsequent multiscale analysis which especially included the resulting visualization technique MSTP image. The workflow of creation of MSTP (Figure 3.9), used in Chapter 4 and Chapter 5, consisted of two main steps.

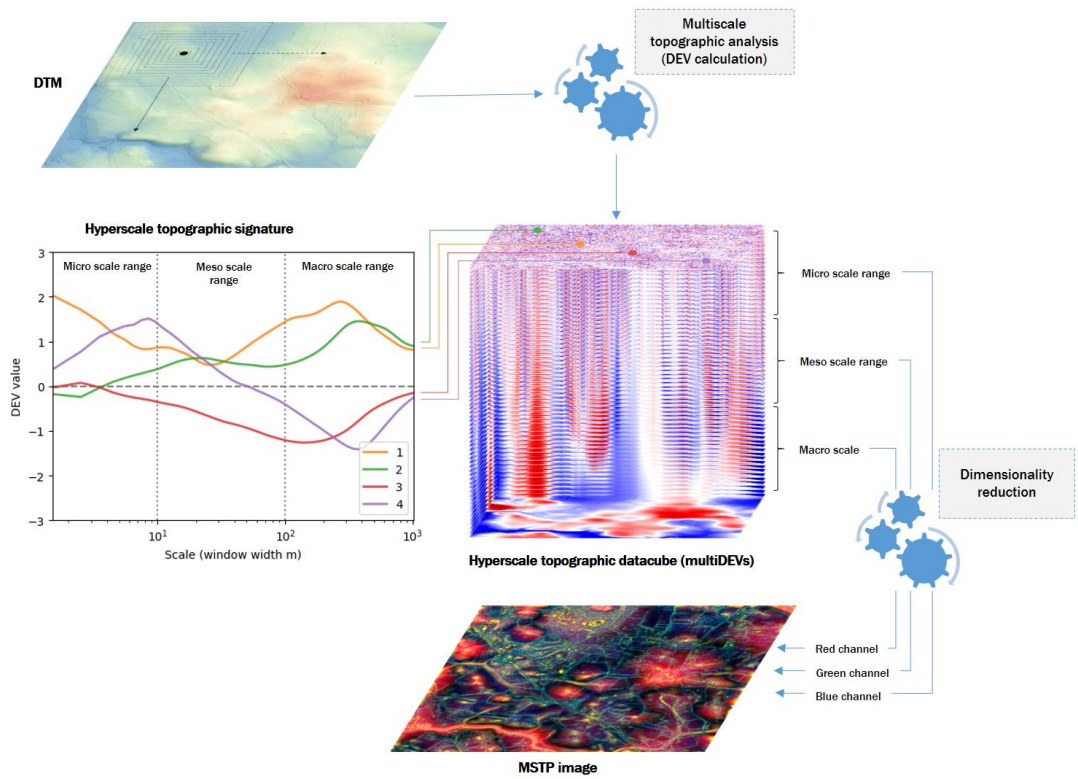

Figure 3.9. Diagram describing the workflow to compute a Multiscale Topographic Position image (MSTP) from a Digital Terrain Model (DTM)

First, the LiDAR-derived DTM was processed to generate a 30-band hyperscale datacube of the topographic metric DEV (Deviation from mean elevation) (J. P. Wilson & Gallant, 2000), defined by equation 3.1 and computed using a sliding window approach:

$$DEV_{i,j,w} = \frac{Z_{i,j} - \mu_{i,j,w}}{\sigma_{i,j,w}} \tag{3.1}$$

where Z is the elevation at window central pixel, and μ and σ are respectively the mean and standard deviation of elevations within a window of size w, centered on position i, j.

The computation of DEV at 30 different window sizes (Table 3.3) was performed efficiently in WhiteboxTools (J. Lindsay, 2020) which includes a prior integral image transformation (Crow, 1984). The resulting datacube containing hyperscale topographic signatures was kept aside for the characterization of segmented structures (see 0).

Second, the datacube was being reduced to 3 bands to create the MSTP image. The dimensionality reduction was performed by selecting the maximum absolute value of DEV (eq. 3.2) within 3 scale ranges as defined in equation 3.2.

$$DEV_{i,j,S} = max\left(\left|DEV_{i,j,w}\right|\right) \tag{3.2}$$

with $w \in [w_{min}^{s}; w_{max}^{s}]$ and where S corresponds to the scale range (micro, meso or macro) and w_{min}^{s} and w_{max}^{s} are respectively the Window minimum and maximum width for the corresponding scale S.

The dimensionality reduction of micro, meso and macro scale range analyses were respectively associated to the Blue, Green and Red bands and normalized from 0 to 255, with an absolute DEV range value limited to 3 standard deviations.

Table 3.3. Parameters of the scale ranges used for the multiscale topographic position analysis (MSTP)

Scale range (S)	**Number of windows**	**Window min. width (w_{min}) (px | m)**	**Window max. width(w_{max}) (px | m)**	**Incremental step**
Micro	10	3px | 1.5m	21px | 10.5m	2px | 1m
Meso	10	23px | 11.5m	203px | 101.5m	20px | 100m
Macro	10	223px | 111.5m	2023 px | 1011.5m	200px | 200m

The multiscale analysis was performed on the entire LiDAR coverage, specifically retiled to ensure a consistent multiscale signature especially at larger scale (macro). The tiling system was based on a 4096x4096 tile size with an additional overlap of 2048px defined above the maximum window size. Resulting tiles were then cropped back to the original 4096x4096, and assembled in a seamless virtual mosaic.

3.2.1.1.d) Some considerations about the data

3.2.1.1.d.i) Canopy penetration

The data were acquired in mid-March 2016. This period usually corresponds to the end of the leaf-off season suitable for LiDAR aerial survey for topographic application. However, during winter

2015-2016, the average temperature over France was 2.6°C above normal temperature[15] and induced an early development of the vegetation. These particular conditions, while included in the acceptable range, resulted in a canopy above the expected development state and thus not optimal at the date of airborne LiDAR acquisition

Post-flight, the canopy penetration was further analyzed by comparing the number of returns (total and filtered) for 3 different environments (open area, canopy dominated by deciduous trees, canopy dominated by coniferous trees, principally maritime pines). The analysis showed two important aspects of canopy penetration in bi-spectral LiDAR (Figure 3.10). First, an important difference of canopy penetration rate (ground points vs all returns) between deciduous (~98% penetration rate), and coniferous (~25% penetration rate), and second, an important difference – between environments- of the number of LiDAR returns reaching back to the sensor, especially for the Green channel (532nm). This was explained by the fact that pulse energy of the 532nm laser beam was strongly absorbed by deciduous trees and almost entirely absorbed by coniferous trees, leading to a reduction of available returns at two stages of the acquisition. First a reduction (*loss 'A'*) mainly due to the absorption of green laser pulse by the canopy, followed by a second reduction (*loss 'B'*) due to the masking of the persistent canopy (65% of the remaining returns blocked by foliage).

Weak signal returns on the green channel and over trees were explained by (i) lower reflectance values at 532nm than 1024nm, as well as (ii) the larger beam footprint of the green channel, reducing the amount of energy available per unit area.

[15] http://www.meteofrance.fr/climat-passe-et-futur/bilans-climatiques/bilan-2016/hiver

Guyot, Alexandre. Contribution of airborne LiDAR and hyperspectral data to archaeological mapping in terrestrial and submerged environments. 2021

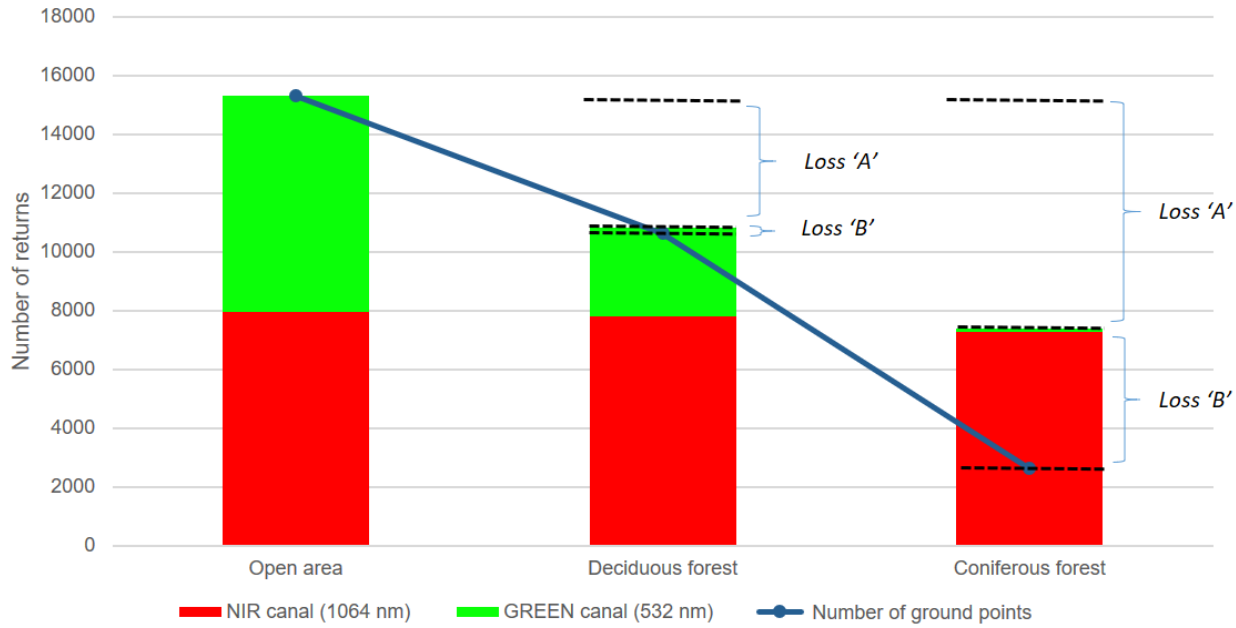

Figure 3.10. Number of LiDAR returns (total and ground filtered) differentiated by laser wavelength (NIR and Green) for three different environments (open-area, deciduous forest, coniferous forest) covering 900m². Loss 'A' was mainly due to strong absorption of green laser pulse by the canopy elements, followed by a second reduction, loss 'B' due to the masking of the persistent canopy elements.

For this LiDAR survey with a nominal point density of 14 points/m² (here the sampled open-area showed a 17 points/m² in average due to overlapping flight-lines), the effectively available point density decreased (due to loss 'A' and loss 'B') to density as low as 10 points/m² and 2 points/m² respectively for deciduous and coniferous forest environments.

These are average densities (computed here on a 900m² sample area), the effective ground point density being locally highly variable, especially under coniferous coverage. This has to be taken into consideration when exploiting the derived terrain model since the representation in the form of a regular grid (unique cell size) necessarily encompasses some large void areas (no signal returns) that can cover reach several meters in width under canopy and are only composed of interpolated elevation values.

3.2.1.1.d.ii) Low-reflectivity roof surface

As shown above with coniferous trees, it is not uncommon to experience a lack of returns using airborne LiDAR data due to low reflectance values of the target surface (e.g. few near-infrared backscattering on water surfaces, few green backscattering on coniferous canopy). It is thus expected to have void areas in the resulting point cloud. For this survey, void areas were also noticed on built-up structures, mainly on slate roofs. This could be caused by specular reflections orienting the return signal away from the sensor, or low-reflectivity properties of the surface, emphasized by a relatively high flight height (1300m). Whatever the case may be, this situation

affecting building structures affected the ground filtering process based on a slope-threshold progressive TIN densification (Figure 3.11).

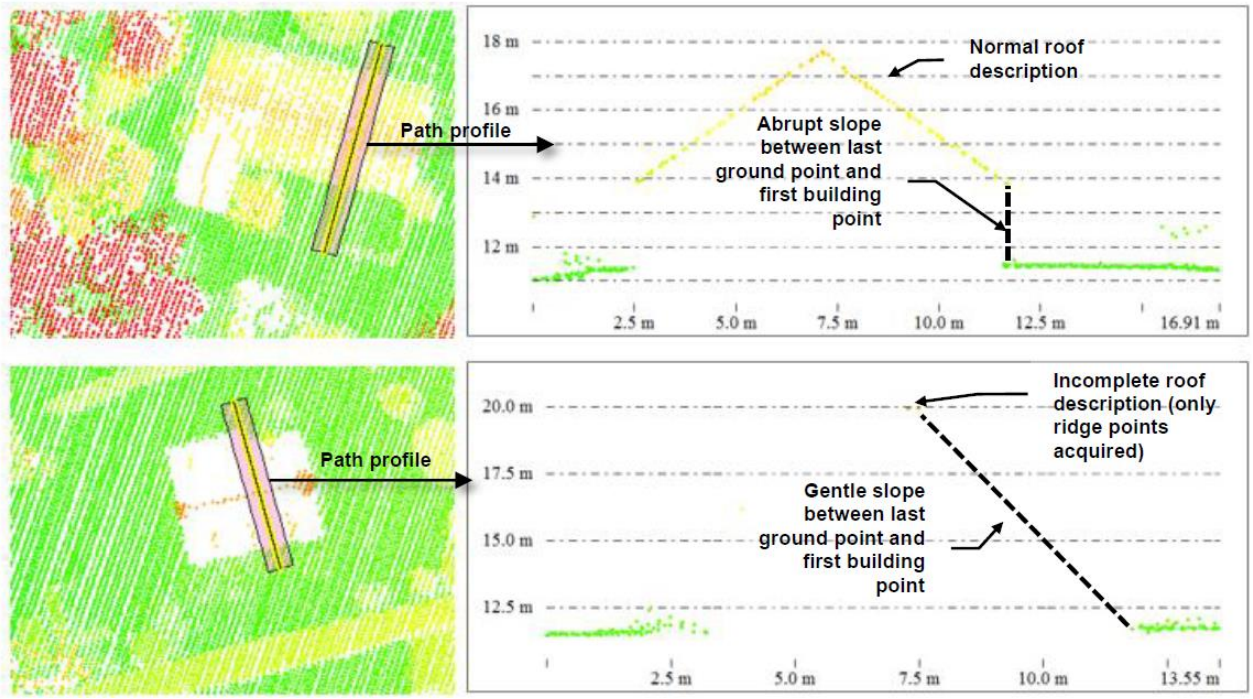

Figure 3.11. (Top) Building roofs without void area. (Bottom) Building roofs with void areas (no returns except for roof ridges). The bottom situation is posing problem for the ground filtering algorithm due to the gentle slope formed between the building points and their nearest ground points. This example justifies the development of the two-step ground filtering operation.

The solution proposed to solve this data acquisition issue was to implement the two-step ground filtering operation described in section 3.2.1.1.c). The first iteration excluded isolated roof ridges from the coarse DTM generation based on coarse ground filtering. Isolated roof ridges were tagged as above-ground objects (as above the 1.5m threshold), and excluded for the second iteration of ground filtering to generate the fine DTM.

3.2.1.2) Hyperspectral data

3.2.1.2.a) Data acquisition

3.2.1.2.a.i) Data acquisition on the study site 1

The airborne hyperspectral data used on the area of Carnac and the Gulf of Morbihan was collected in September 2018. The acquisition was carried out by Hytech-Imaging for the *Service régional de l'archéologie* on 7 different areas (Zone1 to Zone7) for a total of 77.6 km² (Figure 3.12) at a ground sampling distance of 50cm. The sensor was a NEO HySpex VNIR-1600 push broom sensor (Figure 3.13) operating in the spectral range of 400nm to 1000nm.

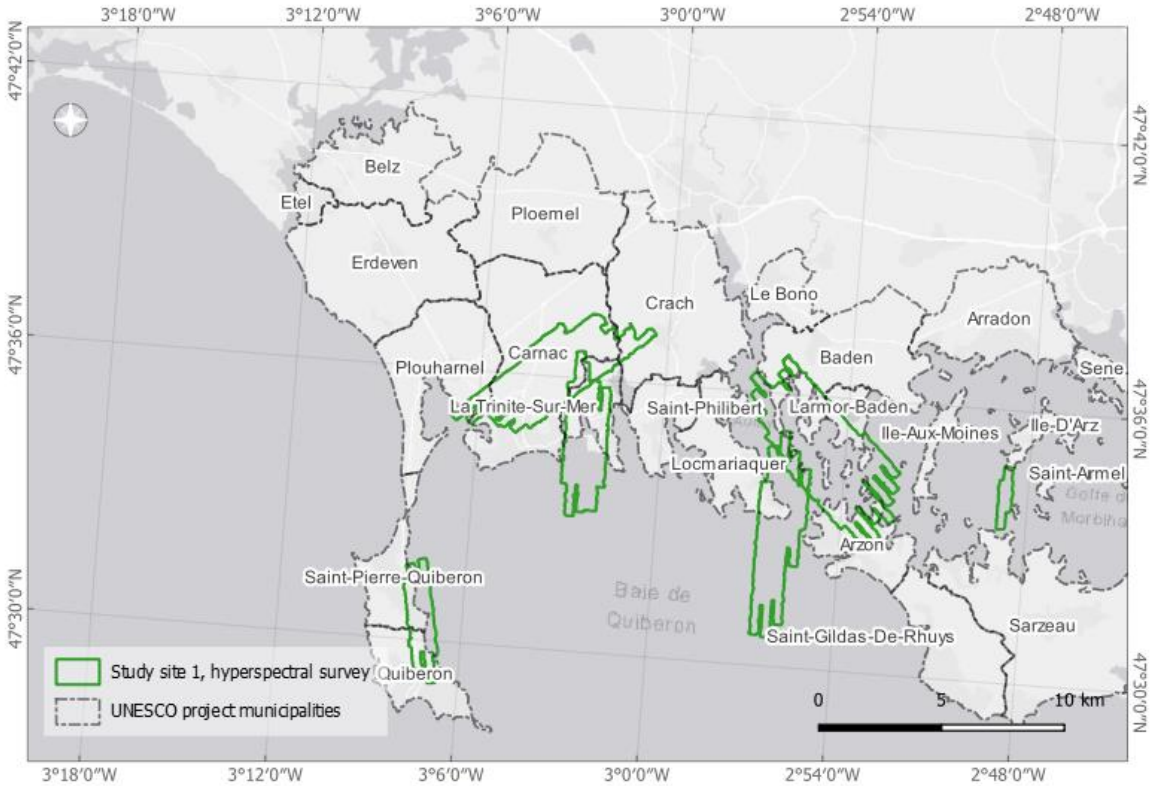

Figure 3.12. Hyperspectral survey (2018) over Carnac and the Gulf of Morbihan

The main acquisition and sensor parameters are provided (Table 3.4):

Table 3.4. Main characteristics of the airborne hyperspectral survey on the area of Gulf of Morbihan

Parameters	Value
Flight date	September 14th, 2018
Area covered	77.6 km²
Flight altitude	1200 m
Ground sampling distance	50cm
Side overlap	30%
Spectral range	VNIR [400nm, 1000nm]
Nbr. of bands	160
Spectral resolution	4.5nm
Frame period	10.1 ms
FOV	17° (ground swath of ~358m at flight altitude)

The sensor was coupled with an IMAR iTrace-RT-F200 navigation system and an OmniSTAR L1/L2 GNSS antenna for kinematic measurements such as acceleration, angular rate, attitude, true heading, velocity and position of the system at update rate of 200 Hz. Differential corrections were

Guyot, Alexandre. Contribution of airborne LiDAR and hyperspectral data to archaeological mapping in terrestrial and submerged environments. 2021

received and processed in real-time using correction information provided via geostationary satellite, through the Fugro OmniSTAR service.

Figure 3.13. VNIR-1600 HySpex sensor and IMAR iTrace-RT-F200 navigation system (left), P68-Partenavia aircraft (right) used for the hyperspectral survey *(credit: Hytech-imaging)*

The survey was carried out in clear sky and relatively calm sea conditions centered around low tide (tide coefficient of 85).

3.2.1.2.a.ii) Data acquisition on Study site 2

The airborne hyperspectral data used on the area of Molène archipelago were collected in May 2020. The acquisition was carried out by Hytech-Imaging for the *Office Français de la Biodiversité / Parc Naturel Marin D'Iroise* on a total area of 125.7 km² (Figure 3.14) at a ground sampling distance of 1 m. The sensor was a NEO HySpex VNIR-1600 pushbroom sensor operating in the spectral range of 400nm to 1000nm.

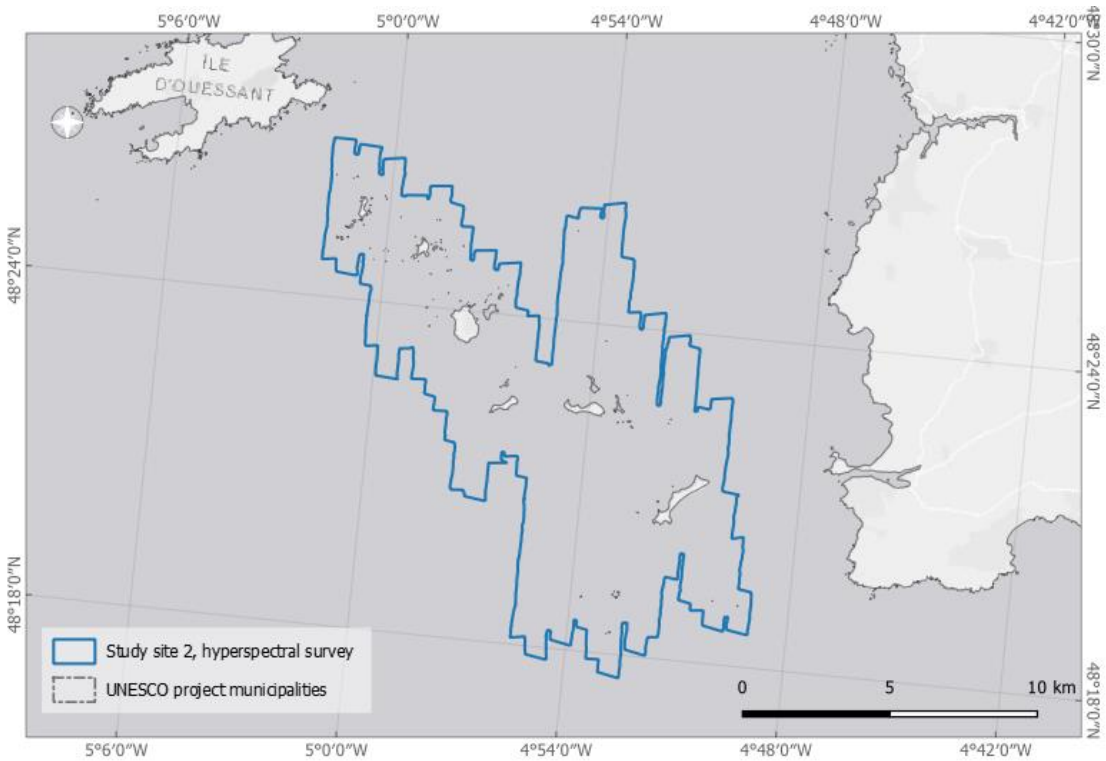

Figure 3.14. Hyperspectral survey (2020) over Molène archipelago

The main acquisition and sensor parameters are provided (Table 3.5):

Table 3.5. Main characteristics of the airborne hyperspectral survey on the area of Molène archipelago

Parameters	Value
Flight date	May 8th, 2020
Area covered	125.7 km²
Flight altitude	1200 m
Ground sampling distance	1 m
Side overlap	30%
Spectral range	VNIR [400nm, 1000nm]
Nbr. of bands	160
Spectral resolution	4.5nm
Frame period	16 ms
FOV	34° with a FOVexpander (ground swath of 707m at flight altitude)

The sensor was coupled with an IMAR iTrace-RT-F200 system and an OmniSTAR L1/L2 GNSS antenna for kinematic measurements such as acceleration, angular rate, attitude, true heading, velocity and position of the system at update rate of 200 Hz. Differential corrections were received

and processed in real-time using correction information provided via geostationary satellite, through the Fugro OmniSTAR service.

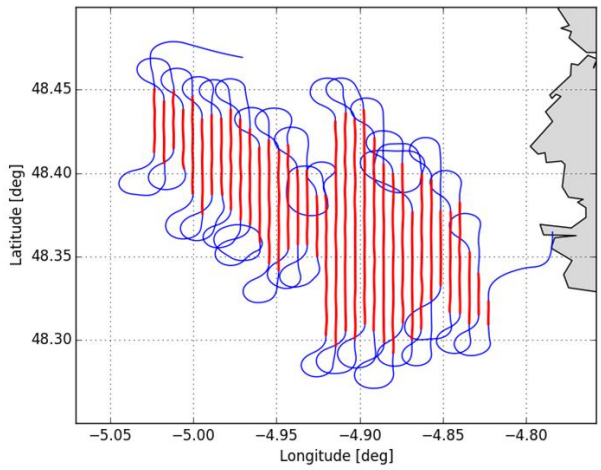

Figure 3.15. Example of trajectory for the hyperspectral survey on Molène archipelago (credit: Hytech-imaging)

Weather and sea conditions were good on the area of interest with a light wind of about 5 knots throughout the acquisition. Locally, a moderate sea surface roughness (ripples) caused some specular reflection of the sun on the water surface (sunglint).

3.2.1.2.b) Post-flight processing

The hyperspectral images acquired on the study site 1 and 2 were post-processed using the integrated and post-processing chain HYPIP® developed by Hytech-Imaging and including the following post-processing solutions: HyspexRad® (from NEO) for radiometric calibration, PARGE® for geometric corrections and ATCOR® for atmospheric corrections (from ReSe Applications LLC).

The radiometric calibration, to transform the DN spectra into at-sensor radiance spectra ($W.m^{-2}.sr^{-1}.nm^{-1}$) included the application of calibration coefficients provided by the manufacturer (NEO) for each cell of the sensor array, as well as a spatial binning x2 (average of 2 pixels across the 1600-pixel array of the sensor to improve the SNR). The IFOV across-track and along-track being respectively 0.18mrad and 0.36mrad (or x2 with FOV expander), the spatial binning produced a square pixel.

Geometric corrections were performed using the trajectory data acquired and corrected in real-time during the flight. An additional correction was made for the boresight angles (offset angles, roll/pitch/yaw, between the sensor and the INS system). The boresight calibration was carried out using GCPs coordinates on identified ground markers (airport runaway markers) visible on the imagery, and applied to the trajectory data. The orthorectification was performed using an

external DEM publicly available (respectively from Geobretagne[16] and Litto3D®[17] for sites 1 and 2) with water surface set to 0m. The final geometric accuracy was within 1-2 pixels on flat areas.

Atmospheric corrections were performed in a two-step approach. First, a correction based on radiative transfer model was applied (using ATCOR-4) with a "maritime" aerosol model and an estimated visibility of 60km. The spectral absorption band of oxygen at 760nm was interpolated during the process. Second, an empirical line fit (ELF) correction was used for the final adjustment of the reflectance with coefficients computed by linear regression between image reflectance spectra and *in situ* reflectance spectra acquired on multiple calibration tarps (black, white, grey, red, green and blue) positioned on the area of interest (Figure 3.16) during each survey.

Figure 3.16. Calibration tarps positioned on the area of interest during the survey of site 2 and used for improving the atmospheric correction through empirical line fit

The data was delivered as a surface reflectance hyperspectral datacube in a ENVI format, organized per flight line, and projected in Lambert-93/RGF93 (EPSG:2154) coordinate system.

Data were delivered as a surface reflectance hyperspectral datacube in a ENVI format, organized per flight line, and projected in Lambert-93/RGF93 (EPSG:2154) coordinate system. All further processing and analysis were performed on per-project basis, described in Chapter 5 and Chapter 6.

3.2.2 Archaeological reference data

3.2.2.1) The archeological map

For this thesis, the main archaeological reference dataset used on the area of Carnac and the Gulf of Morbihan is the *Carte archéologique* maintained by the regional archaeological authority, the *Service regional de l'archéologie de Bretagne.*

[16] https://geobretagne.fr/geonetwork/srv/fre/catalog.search#/metadata/fr-geobretagne.alti.wcs
[17] https://diffusion.shom.fr/pro/risques/litto3dr-finistere-2014.html

This dataset is publicly available and regularly updated by the SRA. It is published as a WMS/WFS layer through the regional open-data webportal Geobretagne with the layer name "*État de la connaissance archéologique en Bretagne*"[18]. The data itself is extracted from the national GIS-based software application "Patriarche", dedicated to the management of the archaeological mapping data in France (Chaillou & Thomas, 2007; Fromentin et al., 2006).

The "*État de la connaissance archéologique en Bretagne*" is an extract of the EA (*entités archaeologiques* or archaeological entities) set included in the administrative region of Brittany. As mentioned in Chaillou & Thomas (2007), the EA set can be defined as the unit of analysis of archaeological sites, and this unit can be either a place characterized by a coherent set of remains testifying to past human activities or a place containing or potentially containing archaeological remains determined or undetermined in nature. This definition echoes some considerations highlighted in the first chapter and stresses the unsuitable use of the term "ground-truth" in an archaeological context. Nevertheless, the EA set is the actual authoritative reference for all archaeological sites in France and is therefore used as reference data in this thesis.

For Brittany, the EA set is extracted from *Patriarche* and published on *Geobretagne* as a GIS dataset including for each record a spatial component associated with attribute information:

- The spatial component consists of a point coordinates (X, Y) in the national reference coordinate system (Lambert 93 / RGF93). Its position accuracy varies from site to site. Most often, the coordinates correspond to the centroid of the cadastral parcel that includes the EA, which can represent positional errors in the range of several hundred meters (for example in large forests or agricultural parcels). Although some EA positions may have been manually modified by the authority to improve their accuracy, they have not been differentiated from those that have not been modified.

- The attribute information consists of different numerical and textual elements, such as a unique identifier (NUMERO), a name (NOM), information about EA nature (NATURE), structural information (STRUCTURE), chronological information (DEBUT/FIN), year of discovery (ANNEE_DECO), municipality and Insee code (COMMUNE, INSEE). The nature, structural and chronological information are not mandatory, but if filled in, these fields follow the data-model (thesaurus) of *Patriarche.*

[18] https://geobretagne.fr/geonetwork/apps/georchestra/?uuid=cd3bc8a0-a3b0-4c0e-bcc4-df7fbb8c213b

Guyot, Alexandre. Contribution of airborne LiDAR and hyperspectral data to archaeological mapping in terrestrial and submerged environments. 2021

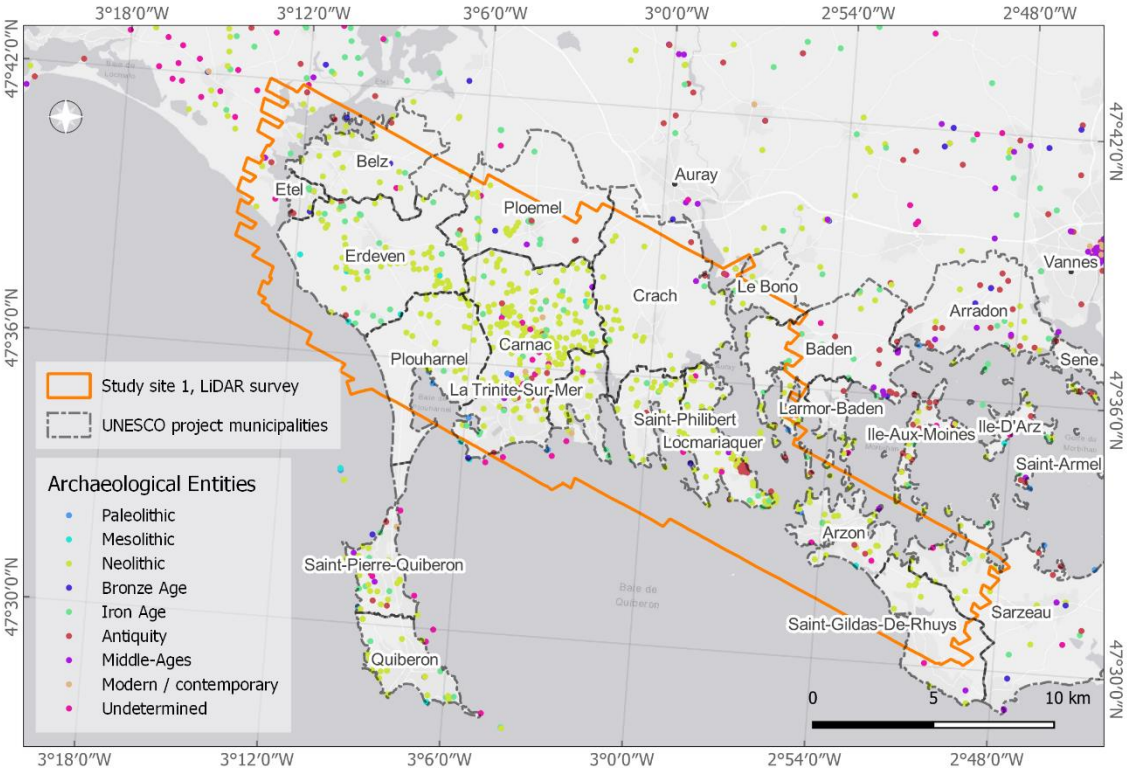

Figure 3.17. Archaeological entities (EA) on the area of Carnac and the Gulf of Morbihan. The dominance of Neolithic archaeological records is observable in the UNESCO project area

In addition to the EA dataset providing point coordinates (Figure 3.17), some archaeological sites were spatially improved by the SRA-Bretagne with polygonal representation (approximated 2D coverage). These sites were related to the project of inscription of the megaliths of Carnac and the banks of Morbihan on the UNESCO World Heritage List covering an area of 26 municipalities. The global dataset comprised a total of 657 features.

In the area of study covered by the LiDAR dataset, a total of 195 polygons were available for the data processing exposed in Chapter 4 and Chapter 5. The selected sites had to be perceivable on the LiDAR data to create the input datasets since the objective was to evaluate computer vision / deep learning approaches for LiDAR-based prospection. For example, all sites that related to off-ground structures such as menhirs or blocs, isolated or in spatial arrangements were excluded from the DTM (see Chapter 2) and were also excluded from the selected sites. Highly modified structures in open areas (such as the cairn de Petit-Mont in Arzon) due to restoration works were also ignored to avoid unrealistic representation of archaeological sites to be identified/detected. Beyond, archaeological sites related to the UNESCO project, some sites perceived on the LiDAR-data but recorded as EA (point representation) were converted to polygon representation and added to this specific dataset. In final, the 195 polygons of the reference dataset (Figure 3.18) included 176 funeral structures attributed to the Neolithic period, 10 funeral structures attributed to protohistoric periods, 1 motte, 3 promontory forts and 5 ruined windmills.

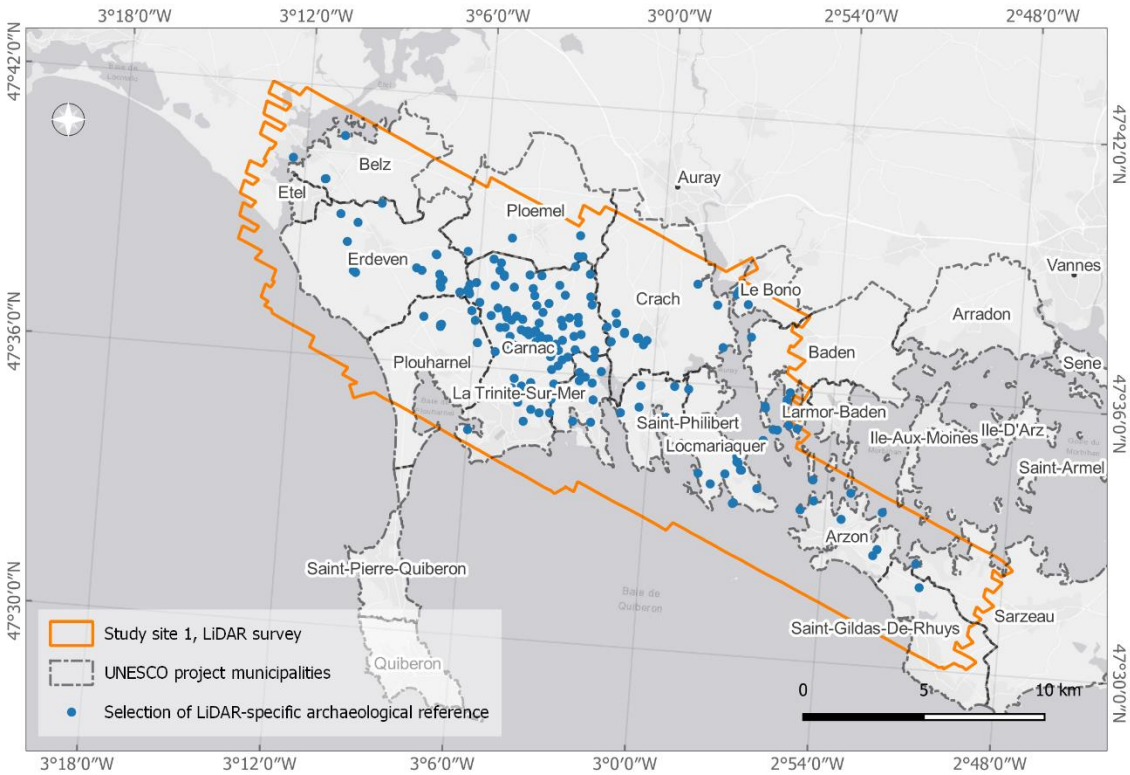

Figure 3.18. LiDAR-specific archaeological reference (195 entities) used on the area of Carnac and the Gulf of Morbihan, for the data processing in Chapter 4 and Chapter 5

3.2.2.2) Fish-weirs inventory

The reference fish weirs database, which was used for study site 2, was extracted from the inventory published in Stéphan et al. (2019). This inventory (Figure 3.19, Table 3.6) was elaborated using various sources including *in situ* observation, aerial prospection, bathymetric sonar and LiDAR prospection. It comprises 36 fish weirs structures or related sea-bottom anomalies, with only a few of them confirmed by archaeological *in situ* observations or dives. Each structure is described by its geographic position (latitude, longitude, depth) as well as morphological characteristics (length, width, height).

Table 3.6. Fish weirs inventory in the Molène archipelago, published by Stéphan et al. (2019) and used as reference database

	Prospection sources*				Characteristics				Coordinates (Lambert 93/RGF93)		
#	A	P	D	B	depth (m)**	length (m)	width (m)	height (m)	X	Y	ref.
1				x	-3.9	45	5	0.6	110994	6842410	Stéphan et al. 2019
2	x			x	-0.53	85	4	0.4	110963	6839820	Daire et Langouët, 2010

3	x			x	-1.3	120	8	0.3	111048	6839940	Daire et Langouët, 2010
4				x	-3.32	118	4	0.3	111259	6841000	Stéphan et al. 2019
5				x	-0.74	105	7	0.7	112501	6839970	Stéphan et al. 2019
6				x	-3.84	190	2	0.5	113434	6839900	Stéphan et al. 2019
7				x	-4.04	157	2.5	1	113481	6839770	Stéphan et al. 2019
8				x	-3.7	75	2	0.25	113400	6839960	Stéphan et al. 2019
9				x	-2.94	100	4	0.3	113297	6839790	Stéphan et al. 2019
10	x				0.12	65	7	0.2	112427	6840950	Gandois et al., 2013
11	x	x			-0.52	90	5	0	112511	6841200	Gandois et al., 2013
12				x	-3.2	106	6	0.3	112965	6840570	Stéphan et al. 2019
13				x	-3.2	102	6	0.25	113005	6840500	Stéphan et al. 2019
14				x	-2.9	49	6	0.45	112962	6840410	Stéphan et al. 2019
15				x	-2.38	108	8	0.7	112942	6840990	Stéphan et al. 2019
16				x	-5.16	55	5	0.45	112474	6841600	Stéphan et al. 2019
17				x	-2.5	110	5.5	0.6	113688	6838880	Stéphan et al. 2019
18				x	-2.13	190	4	0.25	113562	6838710	Stéphan et al. 2019
19			x	x	-3.69	548	3	0.6	114164	6838420	Gandois et al., 2013
20				x	-3.5	140	6	0.8	114695	6838600	Stéphan et al. 2019
21		x			-0.1	100	2	1	115219	6838090	Pailler et al., 2009
22		x			-0.02	50	1	0.4	115678	6838450	Gandois et al., 2011
23		x			-0.18	75	1	0.4	115576	6838400	Gandois et al., 2011
24	x	x			-0.3	60	1	0.5	116242	6838560	Pailler et al., 2009
25	x		x	x	-2.24	125	1.5	1	116482	6838880	Gandois et al., 2011
26	x		x	x	-2.99	260	1.5	1	116508	6838990	Gandois et al., 2011
27	x			x	-1.77	325	5	0	117308	6837640	Daire et Langouët, 2010
28		x			-0.54	70	1.5	0.7	116877	6838020	Gandois et al., 2013
29				x	-2.07	230	7	0.9	117578	6837190	Stéphan et al. 2019
30				x	-4.07	130	4	0.15	117830	6837500	Stéphan et al. 2019
31				x	-4.61	160	8	0.3	117960	6837580	Stéphan et al. 2019
32				x	-0.9	60	2.7	0.5	117236	6836730	Stéphan et al. 2019
33			x	x	-4.02	140	2.5	0.9	118996	6836590	Gandois et al., 2013

Guyot, Alexandre. Contribution of airborne LiDAR and hyperspectral data to archaeological mapping in terrestrial and submerged environments. 2021

34				x	-4.54	230	4	0.8	118246	6837230	Gandois et al., 2013
35		x		x	3.2	30	4	0.1	118787	6834710	Gandois et al., 2015
36				x	-1.1	75	6	0.45	119403	6835380	Stéphan et al. 2019

* A: Aerial photography, P: Pedestrian survey, D: Dive, B: Bathymetry (Sonar & bathymetric LiDAR)
** Chart datum (French hydrographic datum reference), here a negative value indicates below LAT

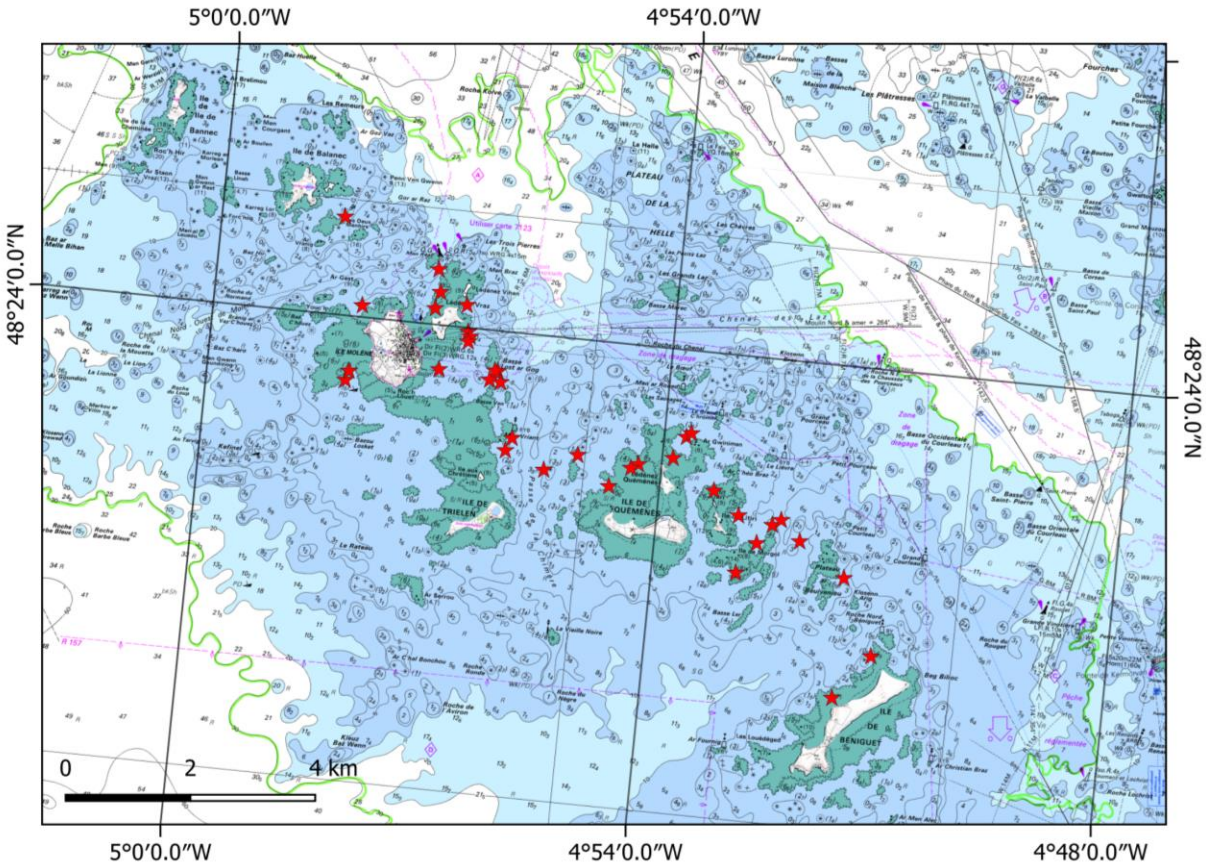

Figure 3.19. Map of the fish weirs inventory (Stéphan et al., 2019) in the Molène archipelago and used as reference database (background: SCAN Littoral® from Shom/IGN)

As for all archaeological reference databases, such inventory is subject to continuous update or modification from the research community and the authorities in charge of the cultural heritage in the French public maritime domain (DRASSM). The exhaustiveness of this reference material may therefore be discussed, nevertheless, it was recently made publicly available -through a peer-reviewed scientific publication- and as such was considered as the most comprehensive reference for fish weirs mapping and was therefore used as a baseline for our research.

3.2.3 *In situ* data & field campaign

3.2.3.1) Field surveys for study site 1

During three years, several field surveys have been carried in terrestrial context in the area of Carnac and the Gulf of Morbihan. These verifications were organized with the support of the *SRA* that provided the administrative authorizations as well as the archaeological interpretation expertise.

The objectives were to:

1. better understand (potential and limits) the multiscale analysis results compared to *in situ* topographic positions and structures
2. verify the presence and the nature of anomalies identified using LiDAR-derived data
3. guide the remote sensing analysis based on feedback collected from *in situ* observations

In the meantime, these field campaigns based on remote sensing data were used to progressively improve qualitatively and quantitatively the archaeological mapping reference:

- Qualitative improvement by specifying the geographical location of existing archaeological entities recorded in the national archaeological reference map;
- Quantitative improvement through the discovery of previously unidentified archaeological entities, which will then be recorded on the national archaeological reference map.

Targeted anomalies were selected from LiDAR-derived data either by manual interpretation or (semi)automatic detection and considering the following criteria:

- Visual perception on LiDAR-derived VT images, especially on MSTP image and its derivatives;
- Geo-archaeological context (considering nearby recorded archaeological entities as well as environment type, with a priority on forested areas).

This subjective target selection, varied along the timeline with the experience gained from previous field verification results. The protocol of verification was also adapted to the complexity of under-canopy perception and archaeological interpretation. The field materials were composed of:

- A handheld GPS or a differential GPS depending on the target morphology (sub-metric precision was not required for the location of decametric structures);
- A prospection reference data:
  - Initially, this data was physically printed "prospection assistance sheet" (Figure 3.20) that included, for each targeted anomaly, all information extracted from the remote sensing data (such as coordinates, visual representation, topographic profiles), as well as external GIS-based

information (such as cadastral information, nearby recorded archaeological entities).

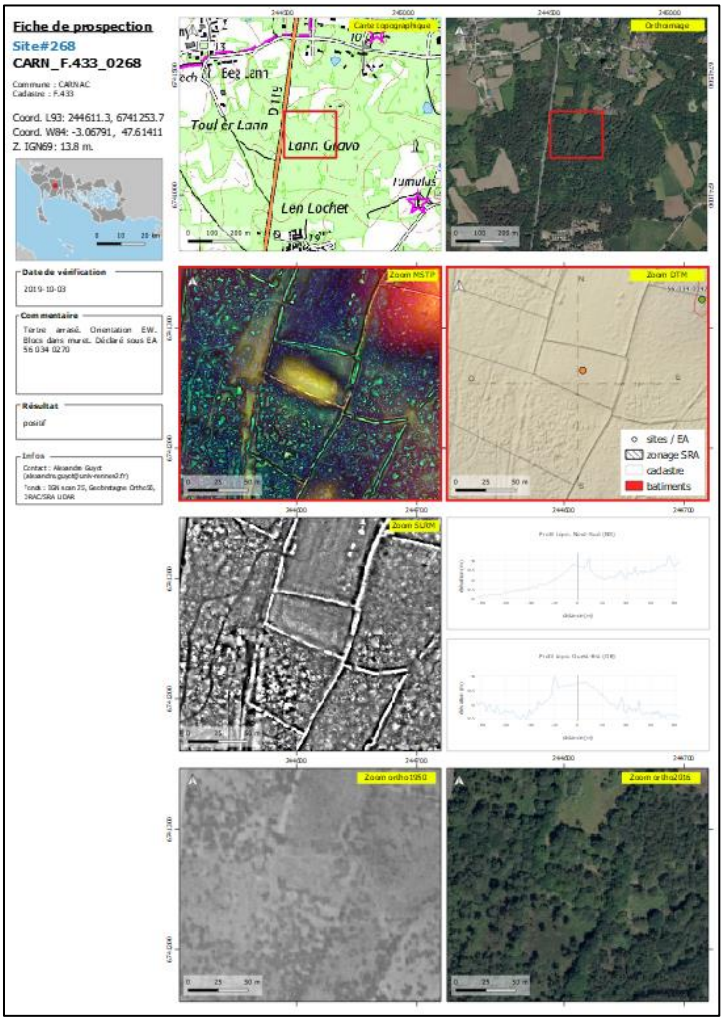

Figure 3.20. An example of a "survey assistance sheet" for a targeted anomaly identified by LiDAR-based analysis and used during field campaign

- Lately, this data was directly integrated into a GIS-based tool (QField, (QField, 2021)) on a GNSS-enabled tablet (Figure 3.21). All information on the survey assistance sheet was therefore accessible in the field, and moreover, the GNSS information was used in real-time to facilitate the perception of the relation between remote sensing data and *in situ* observation. This approach also facilitated the recording and integration of *in situ* observations (photos, notes)

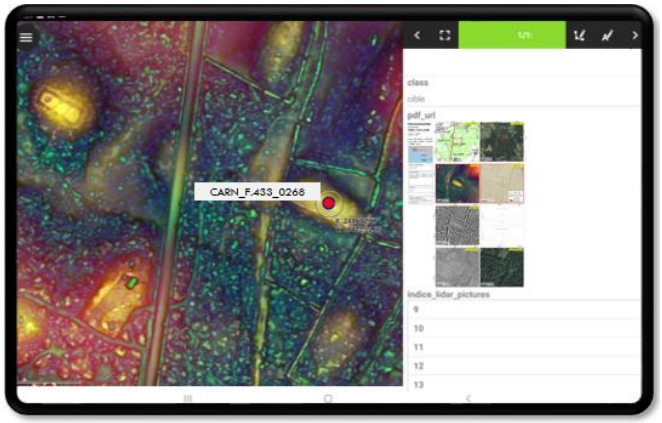

Figure 3.21. An example of a targeted anomaly identified by LiDAR-based analysis and visualized with QField tool on a GNSS-enabled tablet used during field campaign. The digital version of the "prospection assistance sheet" is linked to the GIS entity related to the target anomaly.

Photos and notes were collected in the field for each anomaly that was identified with a unique code automatically generated based on geographical information including the municipality, land parcel and a globally incremented number. When possible, the nature of the anomaly was inferred by archaeologists of the SRA (natural or anthropogenic origin, possible period), and if applicable associated with the declaration of archaeological discovery.

As an example of *in situ* data, the photography and notes reported in Figure 3.22 correspond to the anomaly *CARN_F_433_0268* shown in Figure 3.20 and Figure 3.21 :

Anomaly id. *: CARN_F_433_0268*

Verification date *: 19/03/2020*

Notes *: Possible tertre de 50m par 15m, orienté NO/SE. Présence de blocs dans parcellaire. Autres sites à proximité (<200m) : 56 034 0143 / 56 034 0043 / 56 034 0042*

Figure 3.22. Photography and notes collected during field campaign for a targeted anomaly identified by LiDAR-based analysis

To date, 73 anomalies have been subject to field verification:

- 9 anomalies were verified between November 2018 and February 2019 (Report 2018)
- 46 anomalies were verified between March 2019 and February 2020 (Report 2019)

- 18 anomalies verified between March 2020 to February 2021 (Report 2020)

These 3 phases correspond to the three years of remote sensing-based diachronic prospection carried out with the support of SRA-Bretagne. Annual reports on this work are available online in the SRA-Bretagne digital library:

- **Guyot, Alexandre**, Marc Lennon, Laurence Hubert-Moy. "Rapport 2018 de Prospection Archéologique Diachronique Par Télédétection, Zone Unesco : Carnac, Baie de Quiberon et Golfe Du Morbihan.", Report number RAP03683. Rennes, France : Service régional de l'archéologie de Bretagne, 2019. http://bibliotheque.numerique.sra-bretagne.fr/items/show/3789.
- **Guyot, Alexandre**, Marc Lennon, Laurence Hubert-Moy. "Rapport 2019 de Prospection Archéologique Diachronique Par Télédétection, Zone Unesco : Carnac et Rives Du Morbihan.", Report number RAP03986. Rennes, France: Service régional de l'archéologie de Bretagne, 2020. http://bibliotheque.numerique.sra-bretagne.fr/items/show/4108.
- **Guyot, Alexandre**, Marc Lennon, Laurence Hubert-Moy. "Rapport 2020 de Prospection Archéologique Diachronique Par Télédétection, Zone Unesco : Carnac et Rives Du Morbihan.", Report number RAP04008. Rennes, France: Service régional de l'archéologie de Bretagne, 2021. http://bibliotheque.numerique.sra-bretagne.fr/items/show/4133.

3.2.3.2) Underwater verifications for study site 2

To evaluate the AHI-based method developed for the prospection of fish weirs in submerged areas of the Molène archipelago (see chap. 7) and fuel the discussions regarding the integration of remote sensing approach in submerged archaeological context, an *in situ* underwater verification campaign was organized in July 2021.

The dives, co-organized with OFB/PNMI were authorized by the DRASSM (Ministry of Culture) under the authorization n°OA4831. OFB/PNMI provided the human and material resources for the underwater verifications that were performed by three professional divers.

Considering the resources required for such campaign, the verification dives were limited to 3 anomalies identified by AHI and described in Chapter 7.

At sea, the field protocol was facilitated with a GIS-enabled tablet. QField tool (QField, 2021) was installed on a GNSS-enabled Samsung Galaxy Tab A. Before the field campaign, all data of the project (including reference data, identified anomaly, hyper-spectral derived results) were loaded in QField as served to (1) geolocate the target anomaly at the sea-surface level with a precision of few meters and (2) to visually provide spatial/spectral representations of the sea-bottom anomaly to be searched-for and documented. These visual representations were shared with the divers just before diving (Figure 3.23a,b). Photos and videos were gathered underwater to fuel archaeological interpretations and discussions (Figure 3.23c).

Figure 3.23. Underwater verification campaign in Molène archipelago. (a, b) Briefing of divers before the dive. Spatial/spectral visualizations of the hyperspectral-derived anomaly to be verified were shared with a GIS & GNSS enabled tablet. (c) Underwater image of one of the anomalies being verified (credit: L. Schweyer / OFB).

Guyot, Alexandre. Contribution of airborne LiDAR and hyperspectral data to archaeological mapping in terrestrial and submerged environments. 2021

Summary of Part I.

In this first part, we highlighted the importance of mapping the archaeological heritage for its preservation but also a better understanding of the human past. The current global environmental changes and social transitions affecting the world at a high rate are a challenge for the current generation that has the responsibility to transmit this finite and non-renewable heritage of humanity to future generations.

Archaeological mapping is a continuous challenge with qualitative and quantitative enrichments of the inventories constantly required. The improvement of archaeological inventories is based on multiple means such as documentary research, field surveys, preventive archaeology operations or aerial archaeology. Initiated in the 20 century, oblique photography acquisitions from low-altitude airplanes have led to important discoveries on large territories. By interpreting surface anomalies, such as cropmarks or soilmarks revealed by color or texture contrasts at suitable periods of the year, aerial archaeologists have changed the perception of archaeological landscapes in the scale of space and time. This approach is still commonly applied and is a great source of information. Nevertheless, the traditional aerial archaeology, which has important constraints and limitations (limited to open-land territory, dependent on specific time-space conditions, usually non-repeatable), is facing some difficulties in the renewal of practices and practitioners. During the last decades, the digital era in remote sensing has progressively changed the archaeological mapping perspectives. Rather than replacing aerial photography, the development of new sensors and methods has led to the acquisition of complementary data to enrich the archaeological inventory. The key changes were notably led by large spatial coverage capabilities, frequent revisit time and above all by the development of sensors operating beyond visible light, for example in the infra-red part of the spectrum. This ability to collect non-visible information, progressively at finer spatial and spectral resolution, provided a unique vision of the Earth's surface and original information to identify and characterize archaeological landscapes and sites. Amongst others, LiDAR (light detection and ranging), as an active sensor, is particularly useful for acquiring highly detailed topographic data in archaeological context, even under vegetation coverage. Hyperspectral imagery has also proven its great ability to measure subtle spectral variations that can be used to enhance the perception of surface anomalies of archaeological origin.

Nevertheless, concepts, data and methods related to these relatively new data remain to be evaluated and developed. Challenges have been raised in all the steps along the processing chain, from data acquisition to data analysis and interpretation. From a methodological point of view, the following questions can be raised:

- In a terrestrial context, especially under forest canopy inaccessible by other means of archaeological prospection than airborne LiDAR data, can we question the standard

approaches used to process these data and which are based on the visual interpretation of digital terrain models?

We hypothesis that (i) multiscale terrain visualization techniques can provide more information than standard visualization techniques, and that (ii) multiscale terrain visualization techniques open a way to large-scale mapping with the support of (semi)automatic detection and characterization methods.

- In a submerged context, especially in shallow waters that are of high archaeological potential and certainly one of the most difficult environments to survey (Fontaine et al., 2017), can airborne hyperspectral data be used to provide original information on the sea-bottom in archaeological context?

Beyond these two research questions, necessarily focused and constrained by the framework of the thesis, there is also the question of the integration of remote sensing approaches in archaeological research. What are the potential and limits, strengths and weaknesses of airborne LiDAR and hyperspectral remote sensing in archaeological applications? How can we use them to better identify, understand and preserve the archaeological heritage for its transmission to the future generations?

In order to address these questions, two study sites were selected based on their geo-archaeological characteristics in Brittany: Carnac and the Gulf of Morbihan, and the Molène archipelago. Airborne LiDAR and hyperspectral remote sensing data were acquired and used with archaeological reference data and field surveys to design the research methods described in Part II and Part III of this thesis.

Guyot, Alexandre. Contribution of airborne LiDAR and hyperspectral data to archaeological mapping in terrestrial and submerged environments. 2021

PART II. MULTISCALE TOPOGRAPHIC ANALYSIS AND DEEP CNN FOR IDENTIFICATION AND CHARACTERIZATION OF ARCHAEOLOGICAL STRUCTURES FROM LIDAR DATA

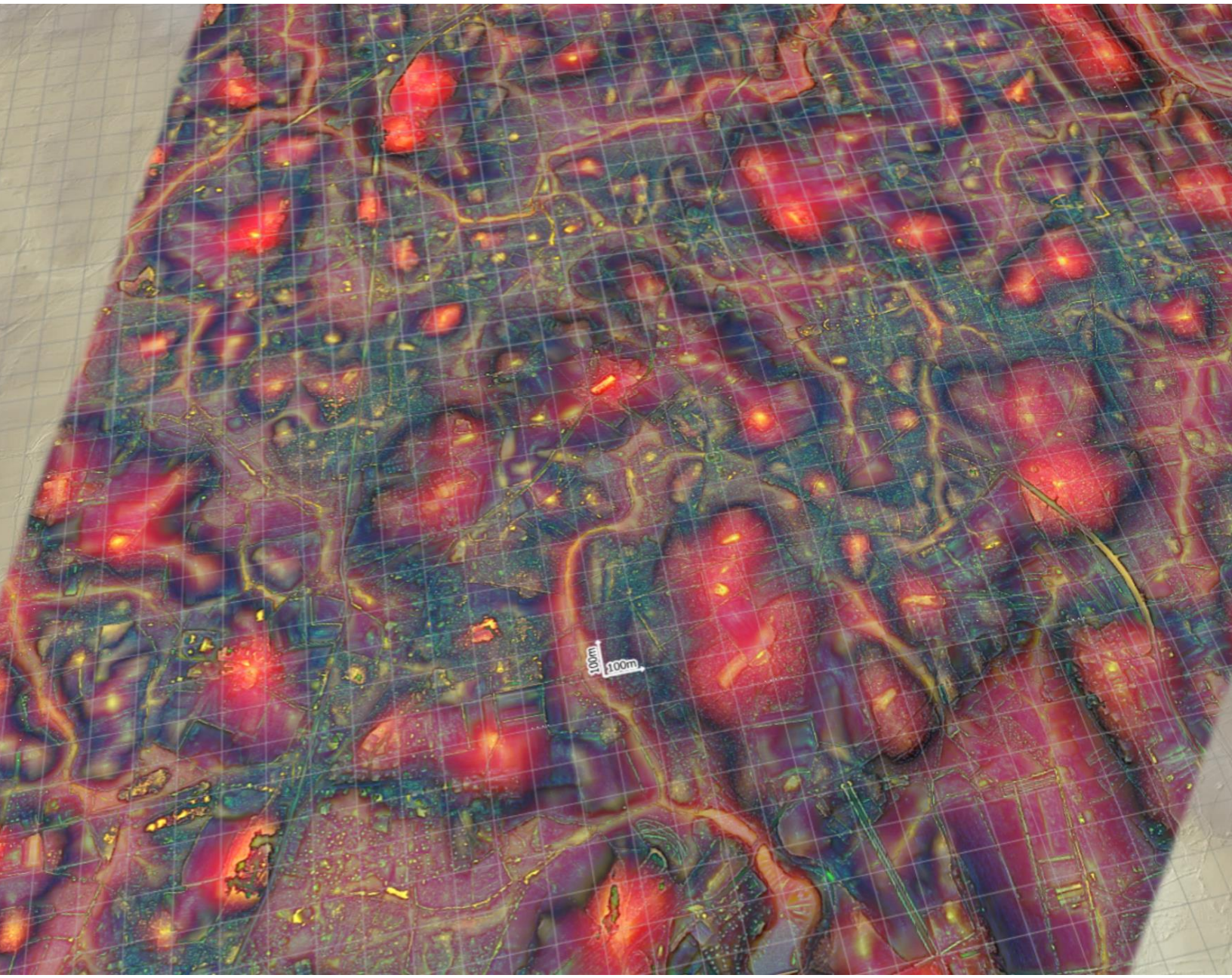

Introduction to Part II.

The second part of this manuscript presents an evaluation of airborne LiDAR data for the (semi)-automatic identification and characterization of archaeological structure in terrestrial context in the area of Carnac and Gulf of Morbihan. The evaluation was carried out using multiscale topographic analysis and deep convolutional networks applied to LiDAR-derived terrain data. This part is developed in two chapters.

In Chapter 4, the objective is to assess the contribution of deep learning methods for detecting and characterizing archeological structures from multiscale visualization of LiDAR-derived terrain data. The main questions addressed in the chapter are: (i) Can the (semi-)automatic segmentation of archaeological structure be implemented with a limited training set? How sensitive is the model to the size of the training set, which is commonly very sparse in archaeological application? (ii) Beyond object detection, what is the value of instance segmentation for the characterization of archaeological structures?

Chapter 5, is a complementary study that aims at assessing the deep CNN instance segmentation approach for performing an objective assessment of different LiDAR-derived terrain visualization techniques. The main questions addressed in the chapter are: (i) Can a deep CNN approach be used as tool to objectively assess the effectiveness of LiDAR-derived VTs in the context of archaeological prospection? (ii) Indirectly, what can such approach, integrating computer-based vision and human-based vision, provide to address some of the archaeological mapping challenges?

Chapter 4. Combined detection and segmentation of archeological structures from LiDAR data using a deep learning approach

This chapter is entirely reproduced from the peer-reviewed article published during the thesis in *Journal of Computer Applications in Archaeology:*

> Guyot, A., Lennon, M., Lorho, T., & Hubert-Moy, L. (2021). Combined detection and segmentation of archeological structures from LiDAR data using a deep learning approach. *Journal of Computer Applications in Archaeology*, 4(1), 1–19. https://doi.org/10.5334/jcaa.64

journal of computer applications in archaeology

ubiquity press

Article

Combined detection and segmentation of archeological structures from LiDAR data using a deep learning approach

Alexandre Guyot [1,2,*], Marc Lennon [2], Thierry Lorho [3], and Laurence Hubert-Moy [1]

1. Laboratoire LETG - UMR 6554, Université Rennes 2, Place du recteur Henri Le Moal, 35043, Rennes, France
2. Hytech-Imaging, 115 Rue Claude Chappe, 29280, Plouzané, France
3. DRAC Centre-Val de Loire, Service régional de l'archéologie/UMR 6566 CReAAH, Orléans, France

* Correspondence: alexandre.guyot@univ-rennes2.fr

Received: 14 September 2020; Accepted: 15 January 2021; Published: 03 February 2021

Abstract: Until recently, archeological prospection using LiDAR data was based mainly on expert-based and time-consuming visual analyses. Currently, deep learning convolutional neural networks (deep CNN) are showing potential for automatic detection of objects in many fields of application, including cultural heritage. However, these computer-vision based algorithms remain strongly restricted by the large number of samples required to train models and the need to define target classes before using the models. Moreover, the methods used to date for archaeological prospection are limited to detecting objects and cannot (semi-)automatically characterize the structures of interest. In this study, we assess the contribution of deep learning methods for detecting and characterizing archeological structures by performing object segmentation using a deep CNN approach with transfer learning. The approach was applied to a terrain visualization image derived from airborne LiDAR data within a 200 km² area in Brittany, France. Our study reveals that the approach can accurately (semi-)automatically detect, delineate, and characterize topographic anomalies, and thus provides an effective tool to inventory many archaeological structures. These results provide new perspectives for large-scale archaeological mapping.

4.1 Introduction

The past decade has seen an increasing interest in remote sensing technologies and methods for monitoring cultural heritage. One of the most relevant changes is the development of airborne light detection and ranging (LiDAR) systems (ALS). With the ability to measure topography accurately and penetrate the canopy, ALS has been a key tool for important archaeological discoveries and a better understanding of past human activities by analyzing the landscape (Bewley et al., 2005; Chase et al., 2011; D. H. Evans et al., 2013; Inomata et al., 2020) in challenging environments.

Most archaeological mapping programs based on ALS do not use LiDAR 3D point clouds directly, but use instead derived elevation models that represent bare soil in the topographic landscape. Perception of the terrain is usually enhanced by specific visualization techniques (VT) (Bennett et al., 2012a; Devereux et al., 2008; M. Doneus, 2013; Hesse, 2010; Štular et al., 2012) that are used to visually interpret landforms and archaeological structures (Kokalj & Hesse, 2017). These visualizations have resulted in better understanding of the human past in different periods and different regions of the world. For example, LiDAR-derived terrain combined with VT has been used to provide new insights into a prehistoric hillfort under a woodland canopy in England (Devereux et al., 2005), discover a pre-colonial capital in South Africa (Sadr, 2019), supplement large-scale analysis of a human-modified landscape in a Mayan archaeological site in Belize (Chase et al., 2011) and explore long-term human-environment interactions within the former Khmer Empire in Cambodia (D. Evans, 2016). However, these expert-based and time-consuming approaches are difficult to replicate in large-scale archaeological prospection projects.

A variety of (semi-)automatic feature-extraction methods have been developed to assist or supplement these visual interpretation approaches. Object-based image analysis (Freeland et al., 2016) and template-matching (Trier & Pilø, 2012) methods, which rely on prior definition of purpose-built spatial descriptors or prototypical patterns, respectively, are difficult to generalize because they cannot include the high morphological diversity and heterogeneous backgrounds of archaeological structures (R. Opitz & Herrmann, 2018). Supervised machine-learning methods have been assessed to address these limitations (Lambers et al., 2019). Data-driven classifiers (e.g. random-forest, support vector machine) applied to multi-scale topographic or morphometric variables have provided interesting results for detecting archeological structures (Guyot et al., 2018; Niculiță, 2020). However, detection was either performed at the pixel level without considering the target as an entire object (archaeological structure) with spatial aggregation and internal complexities, or was based on previous image segmentation, which prevents them from being applied to complex structures. In recent years, deep learning Convolutional Neural Networks (deep CNNs) have resulted in a new paradigm in image analysis and provided ground-breaking results in image classification (Krizhevsky et al., 2012) or object detection (Girshick, 2015). Deep CNNs are composed of multiple processing layers that can learn representations of data with multiple levels of abstraction (LeCun et al., 2015). In the context of LiDAR-based

archaeological prospection, they were first applied in 2016 (Trier et al., 2016) to detect charcoal kilns and were further evaluated in different archaeological contexts and configurations (Caspari & Crespo, 2019; Gallwey et al., 2019; Kazimi et al., 2018; Trier et al., 2018; Verschoof-van der Vaart et al., 2020; Verschoof-van der Vaart & Lambers, 2019). These studies focused on image classification (predicting a label/class associated with an image) (Figure 4.1a) or object detection (predicting the location (i.e. bounding box (BBOX)) of one or several objects of interest within the image) (Figure 4.1b). While these deep CNN methods have detected archaeological structures adequately, they could not provide information that (semi-)automatically characterized them because structures must be delineated to move from detection to characterization. Recent deep CNN methods, such as Mask R-CNN (He et al., 2017), have object-segmentation abilities (Figure 4.1c) that delineate objects. These deep CNN methods remain strongly restricted by the large number of samples required to train models and the need to define target classes before using the models. While the lack of ground-truth samples (reference data) is a known constraint in remote sensing archaeological prospection, two strategies can address this limitation: transfer learning and data augmentation. The first strategy applies a pre-trained source domain model to initialize a targeted domain model (Weiss et al., 2016), while the second strategy uses transformers that modify input data for training. These strategies are known to improve model performance for small datasets and to increase model generalization (Shorten & Khoshgoftaar, 2019). Defining target classes before using a model is based on one-class approaches that define only a generic "archeological structure" class without dividing it into several sub-classes, assuming that the object characterization can identify types of archaeological structures.

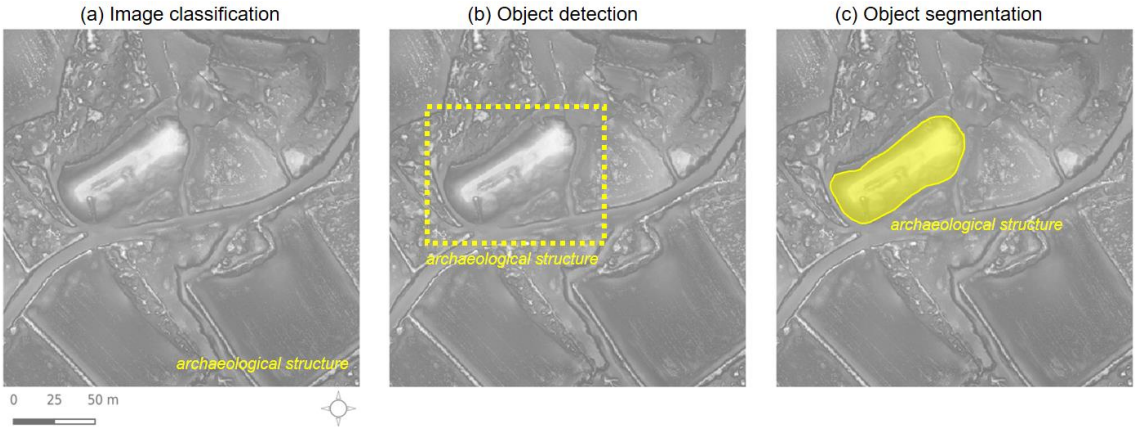

Figure 4.1. Image analysis using deep learning Convolutional Neural Networks for an archaeological site (Tumulus du Moustoir, Carnac, France). (a) Image classification: a class or label associated with the image, (b) Object detection: a labeled bounding box that locates the object of interest within the image, and (c) Object segmentation: a labeled footprint that locates and delineates the object of interest within the image.

Using deep CNN for archaeological prospection of LiDAR derived-terrain (Caspari & Crespo, 2019; Gallwey et al., 2019; Trier et al., 2018; Verschoof-van der Vaart et al., 2020; Verschoof-van

der Vaart & Lambers, 2019) is in its infancy, and to our knowledge, these studies have not evaluated the object-segmentation abilities of the CNN, except the evaluation of Mask R-CNN for simple circular-based landforms (Kazimi et al., 2019, 2020). In the present study, we assess the contribution of deep CNN to the combined detection and segmentation of archeological structures for further (semi-)automatic characterization.

More specifically, we aim to provide new insights into object segmentation using deep CNN for archaeological prospection to address two key issues: i) the extent to which the approach is sensitive to the amount of sample data, since data are a sparse resource in archaeology, and ii) after object detection, the utility of object segmentation for characterizing archaeological structures.

4.2 Materials and methods

4.2.1 Study area

The study area (Figure 4.2) is located in southern Morbihan (Brittany, France) and covers an area between the Ria of Etel and the Rhuys Peninsula on the Atlantic coast. The region is a complex and fragmented mosaic of landscapes. The hinterland is composed of woodlands, moorlands and farmland that form a rural environment oriented to agriculture. The coastal area is also diverse, with estuaries and small islands near the intricate Gulf of Morbihan and large open, sandy areas in the Bay of Quiberon that concentrates most of the economic activities of tourism and fisheries.

The area is home to a unique megalithic heritage. Erected between the 5th to 3rd millennia BC, the Neolithic architecture (standing stones and megalithic tombs) represents an exceptional corpus of archaeological sites that are candidates for the UNESCO World Heritage List. Beyond this emblematic heritage, the coast of Morbihan includes a wide variety of archaeological sites that marked the gentle topography of the area and encompass different prehistorical and historical periods.

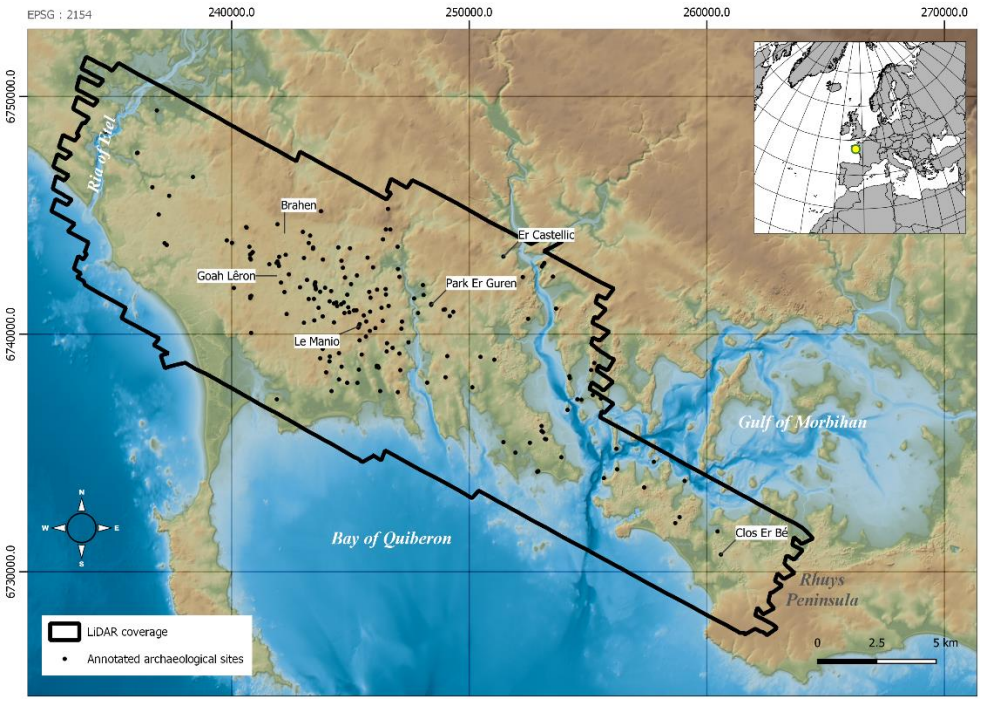

Figure 4.2. The study area with the location of the 195 annotated archaeological sites used in the study. Areas mentioned in the text are labeled.

4.2.2 Dataset

4.2.2.1) LiDAR-derived visualization image

The workflow for processing LiDAR data consisted of several steps (Figure 4.3). The image dataset was derived from a LiDAR point-cloud collected over the area in 2016 (200 km², excluding water area). The raw point-cloud was collected from a bispectral (1064 and 532 nm) Optech Titan LiDAR sensor operated from a fixed-wing vector 1300 m above ground level at a pulse repetition frequency of 300 kHz per channel and a 26° field of view to obtain a nominal point density of 14 points/m². The 3D point-cloud recorded was processed with LasTools (rapidlasso GmbH, Gilchin, Germany) to perform ground-filtering and gridding operations to create a Digital Terrain Model (DTM) at a spatial resolution of 50 cm (Guyot et al., 2018). The terrain model was then used to perform two VTs.

First, a multiscale topographic position (MSTP) image (J. B. Lindsay et al., 2015) was created based on a previous archaeological prospection study (Guyot et al., 2018). The MSTP image was generated from a hyperscale datacube (30 bands corresponding to 30 window sizes) of the topographic metric DEV (deviation from mean elevation) (J. P. Wilson & Gallant, 2000) and reduced to three dimensions by extracting the absolute maximum value from micro, meso, and macro scale ranges, which had window sizes of 3-21, 23-203 and 223-2023 px, respectively. Second, a morphological VT was created by combining a red-toned elevation gradient (slope) and a greyscale positive/negative topographic openness based on Chiba et al. (2008). Finally, MSTP and

morphological VT were blended into a single composite image using a soft-light blending mode with 100% and 70% opacity, respectively.

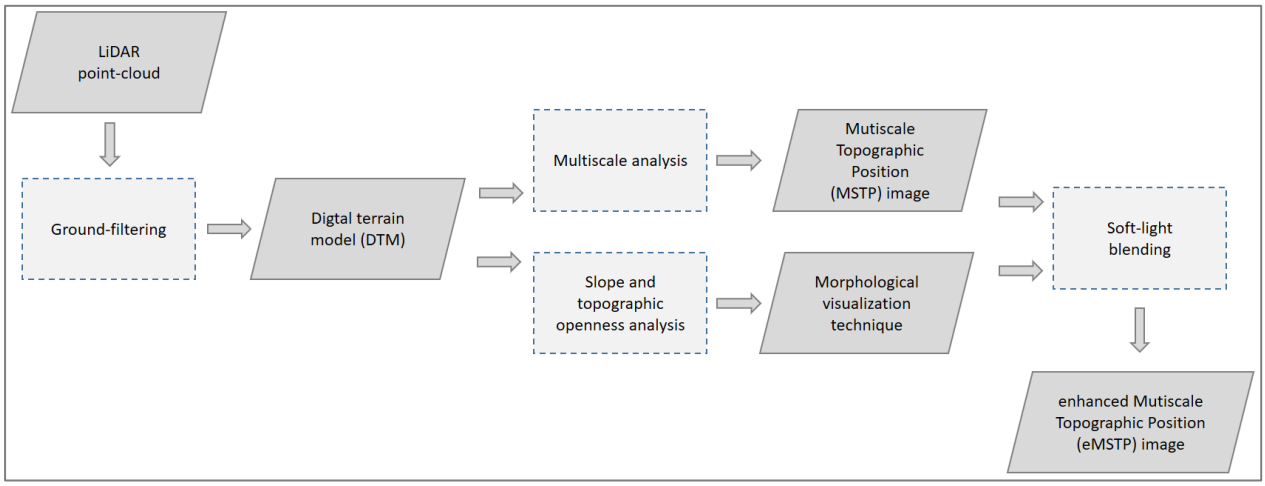

Figure 4.3. Image dataset's workflow from DTM to enhanced Multiscale Topographic Position (eMSTP) image.

The resulting enhanced multiscale topographic position (eMSTP) image (Figure 4.4) was proposed as an optimal VT for this study. It provided effective and informative multiscale visualization of archaeological structures and enhanced perception of local morphological characteristics of the terrain (a known limitation of MSTP (Guyot et al., 2018)). A 3-channel image was used as input of the network to facilitate transfer-learning from models trained on natural RGB images.

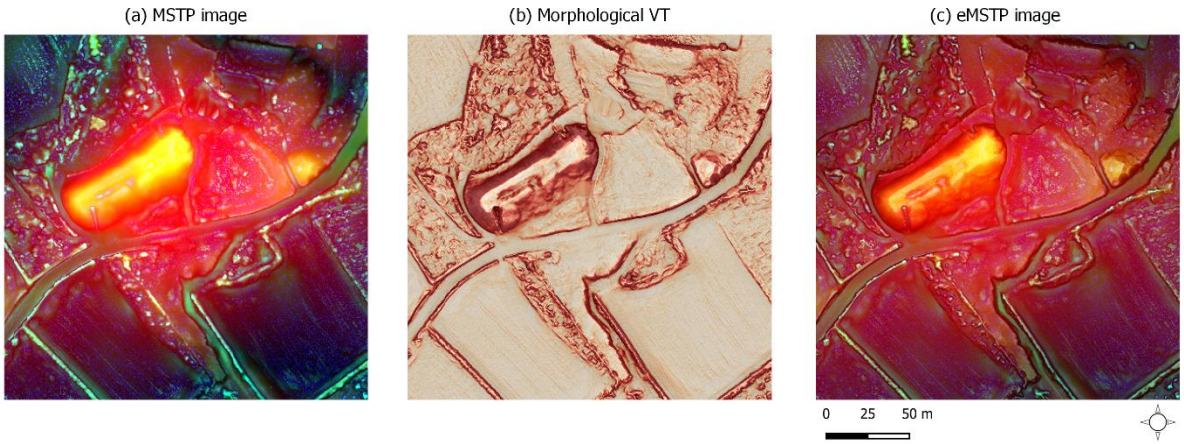

Figure 4.4. (a) Multiscale Topographic Position (MSTP) image, (b) Morphological visualization technique (VT) and (c) resulting enhanced multiscale topographic position (eMSTP) image of a Neolithic monument (Tumulus du Moustoir, Carnac, France).

eMSTP images were cropped from the overall mosaic as 150 images, 512 px × 512 px in size, to be input into the deep CNN architecture and cover the annotated archaeological sites.

4.2.2.2) Archaeological annotated reference data

The reference dataset consisted of 195 georeferenced polygons that represented footprints of known archaeological sites in the study area. The sites were selected from the regional archaeological reference dataset provided by the *Service Régional de l'Archéologie* (SRA Bretagne). Only archaeological structures of which topographic characteristics could be perceived on the LiDAR-derived DTM were kept (thus excluding sites related to small-object deposits, such as potsherds, and sites considered as above-ground structures with no influence on the bare-earth topography, such as standing stones).

The selected archaeological sites had diverse chronologies, morphologies, and landscape contexts. Their state of conservation also varied greatly, from long-known restored monuments to unexcavated little-documented structures. The reference dataset included 195 archaeological structures, including 176 funeral structures attributed to the Neolithic, 10 funeral structures attributed to protohistoric periods, 1 motte, 3 promontory forts and 5 ruined windmills.

Given the highly imbalanced dataset (over-representation of Neolithic structures) and the tasks to evaluate (object detection and segmentation), the annotations were intentionally grouped into a single "archaeological structure" class with no further distinction. The reference dataset was converted from a geospatial format to an annotation one (JSON COCO) in which each annotation was associated with its corresponding eMSTP tile to be input into the deep CNN architecture. Due to spatial proximity between some archaeological sites, 150 eMSTP images covered the 195 annotations (a mean of 1.3 annotations per image).

4.2.3 Methods

4.2.3.1) Overall workflow

From the eMSTP images input, the overall workflow (Figure 4.5) of the approach consisted of two main parts:

- Object detection and segmentation
- Object characterization

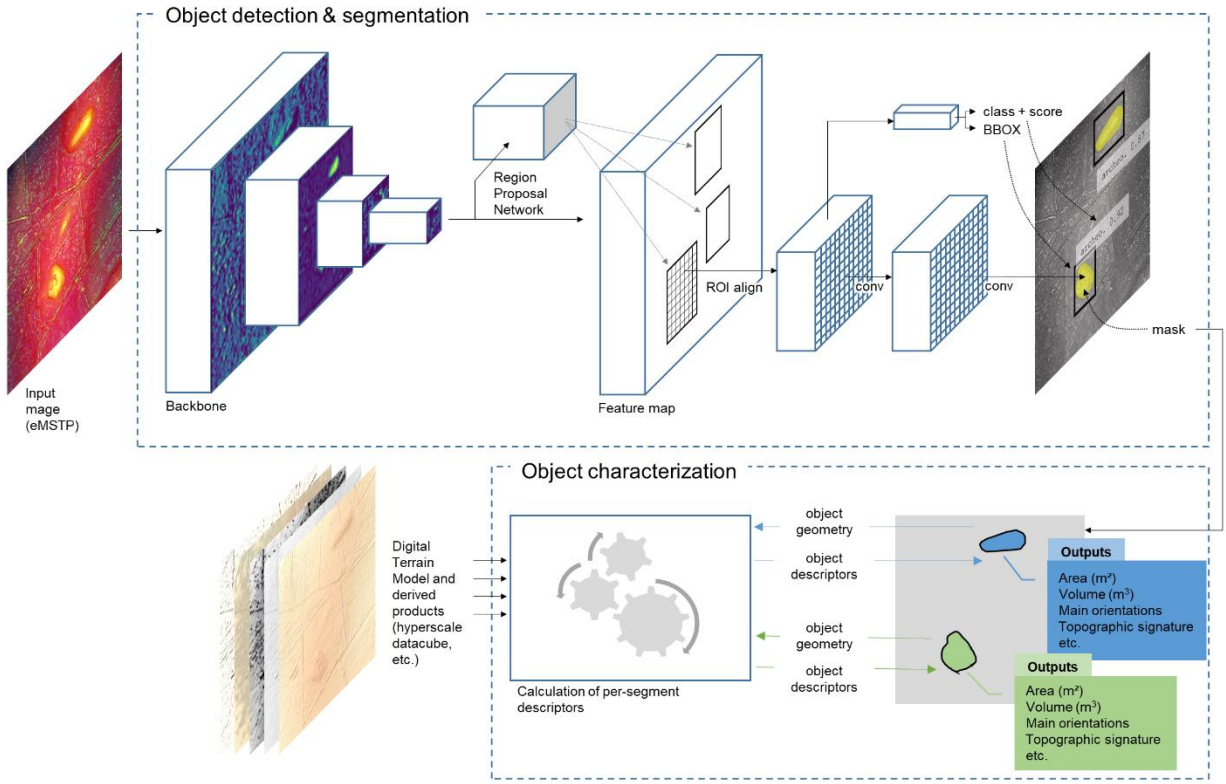

Figure 4.5. Overall workflow of (semi-)automatic object detection, segmentation, and characterization of archaeological structures. eMSTP = enhanced multiscale topographic position, ROI = region of interest, BBOX = bounding box.

4.2.3.2) (Semi-)automatic object detection and segmentation

We used the open-source implementation of Mask R-CNN developed by Matterport (Abdulla, 2017). The feature-extraction phase (backbone) was performed using the Resnet-101 deep CNN initialized with weights pre-trained on the COCO dataset (Lin et al., 2014) for the transfer-learning strategy.

To limit overfitting due to the small training dataset, data augmentation (DA) was activated in the Mask R-CNN workflow using the *imgaug* library (Jung et al., 2020). For each epoch, input images were randomly augmented with affine transformations (scaling: 80-120% of the original image size; translation: -20% to 20% of the original image position; rotation: -25° to 25° of the original image orientation). These transformations were defined within limited ranges of scaling, translation and rotation to avoid unrealistic versions of the eMSTP images. The augmentation process was applied 50% of the time to ensure that the deep CNN received both augmented and non-augmented versions of the training dataset.

A specific sampling strategy was used to assess the model's stability (varying training/validation/test draws) and sensitivity to the number of training samples (varying training size). The initial dataset of 150 images was randomly split into 110, 20 and 20 images for training,

validation and testing, respectively. This random split was performed 10 times to create 10 different experimental datasets (different draws). For each experimental dataset, the training dataset was divided into 11 sub-training datasets with 10-110 images, with an increment of 10. Given the number of experimental datasets and sub-training datasets, a total of 110 experimental configurations were available (see Appendix A.1). Each experimental configuration was checked to ensure that no leaks occurred between validation, test and training datasets. Many hyperparameters can be calibrated in Mask R-CNN. To reduce specific effects and focus on the generalized behavior of the model, only a few hyperparameters were configured. The Region Proposal Network (RPN) was configured to consider the size and aspect ratios of objects of interest by setting *RPN_ANCHOR_SCALES = [16, 32, 64, 128]* (in px) and *RPN_ANCHOR_RATIOS = [0.5, 1, 2]* (width/height ratio).

The training was performed on 60 epochs with a decaying learning rate (LR) schedule (training stage 1:20 epochs at LR 10^{-3}, training stage 2:20 epochs at LR 10^{-4}, training stage 3:20 epochs at LR 10^{-5}). To consider the variability in training size (10 -110 images, depending on the experiment), the number of iterations per epoch (*STEP_PER_EPOCH* parameter) was dynamically adjusted to the number of training images available at the beginning of each experiment (assuming a batch size of 1, and 1 image per GPU). This configuration ensured that the deep CNN observed each image (or its augmented version) only once per epoch.

The training process was set to fine-tune the head layers of the network (RPN, classifier and mask) (the other layers were frozen) to maximize use of transfer learning within the backbone network. The validation dataset was used to monitor the loss at the end of each epoch. For each experimental configuration, the model was run in inference mode to predict results from the test dataset (20 images). The inference returned a BBOX, confidence score and binary mask (or segment) for each object detected in the images of the test dataset.

Model performance was evaluated both statistically and visually. Predictions were assessed statistically per experiment by using metrics adapted to object detection and segmentation. The AP (average precision) for an IoU (intersection over union) threshold of 0.5 was used to assess each image and averaged as mAP to assess each dataset of the experimental configurations.

IoU refers to the overlapping score of the predicted mask compared to the reference data:

$$IoU = \frac{area\ of\ intersection}{area\ of\ union} \qquad \text{(eq. 4.1)}$$

AP refers to the area under the precision-recall curve, with:

$$precision = \frac{TP}{TP+FP} \qquad \text{(eq. 4.2)}$$

$$recall = \frac{TP}{TP+FN} \qquad \text{(eq. 4.3)}$$

with TP and FP and FN the true positives, false positives and false negatives, respectively.

$mAP@IoU_v$ refers to the mean APs at a IoU threshold v for a given dataset with:

$$mAP@IoU_v = \frac{1}{n}\sum_{i=1}^{n} \mathrm{AP}_i \qquad \text{(eq. 4.4)}$$

with n the number of images i for a given dataset.

Visual analysis was then performed to compare reference data and model predictions for each image for three case studies.

To assess the approach within an archaeological prospection scheme, we trained an additional deep CNN model (the deployment model) using all possible reference data (i.e. 150 images). The deployment model was applied to an independent set of images of the study area that did not contain any known archaeological structures that are topographically visible. The model was evaluated through human-interpretation and field survey.

4.2.3.3) Characterization of segmented objects

The results of (semi-)automatic detection and segmentation (i.e., predicted masks) were used to evaluate object characterization (morphological and contextual characterization). Predicted masks (polygons) were used as base units to calculate simple morphometric descriptors (Table 4.1) and extract hyperscale topographic position signatures of the segmented objects (see the *LiDAR-derived visualization image* section for details on the hyperscale datacube).

Table 4.1. Characterization metrics calculated for the objects detected.

Name	Type	Calculation
Area	Morphology	Mask area
Perimeter	Morphology	Mask perimeter
Major axis	Morphology	Orientated mask BBOX major-axis length (m)
Minor axis	Morphology	Orientated mask BBOX minor-axis length (m)
Hyperscale topographic signatures	Context	See the LiDAR-derived visualization image subsection

4.3 Results

4.3.1 Object detection and segmentation performances

4.3.1.1) Sensitivity of deep CNN to the amount of sample data

The overall performances of the deep CNN approach applied to 110 experimental datasets (i.e. 10 datasets × 11 training sizes) were measured using the mean average precision (mAP) metric. The

creation of the experimental datasets from 150 images and the evaluation metric (mAP@IoU.5) used to assess performance are described in the *Materials and methods* section.

The mAP@IoU.5 ranged from 0.29 (experiment $F_{train10}$) to 0.77 (experiment $A_{train80}$), with a mean of 0.50 and standard deviation of 0.10 (Figure 4.6a and 6b). The sensitivity analysis of the number of training images available (Figure 4.6b) showed that mean mAP@IoU.5 increased from 0.37 to 0.55 as the number of training images increased from 10 to 110, respectively. Mean mAP@IoU.5 varied greatly among datasets (Figure 4.6c), with the mean mAP@IoU.5 ranging from 0.40 (dataset E) to 0.69 (dataset A).

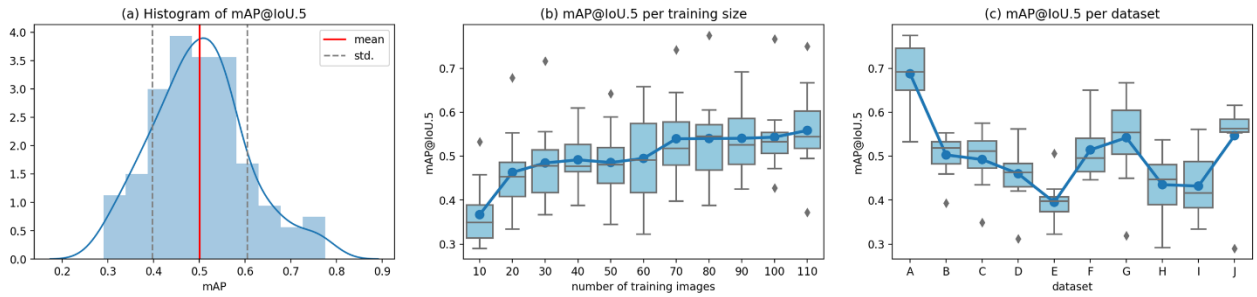

Figure 4.6. Statistical performances of the 110 models. (a) histogram of mAP values, (b) boxplots of mAP per training size and (c) boxplots of mAP per dataset. Whiskers represent 1.5 times the interquartile range.

4.3.1.2) Detailed analysis of three case studies

Predictions for object detection and segmentation compared to the reference dataset from a per-image analysis are illustrated (Figure 4.7) for three areas (Area 1, Area 2, Area 3). Models $A_{train110}$ (maximum training size) and $A_{train10}$ (minimum training size) were used as contrasting examples.

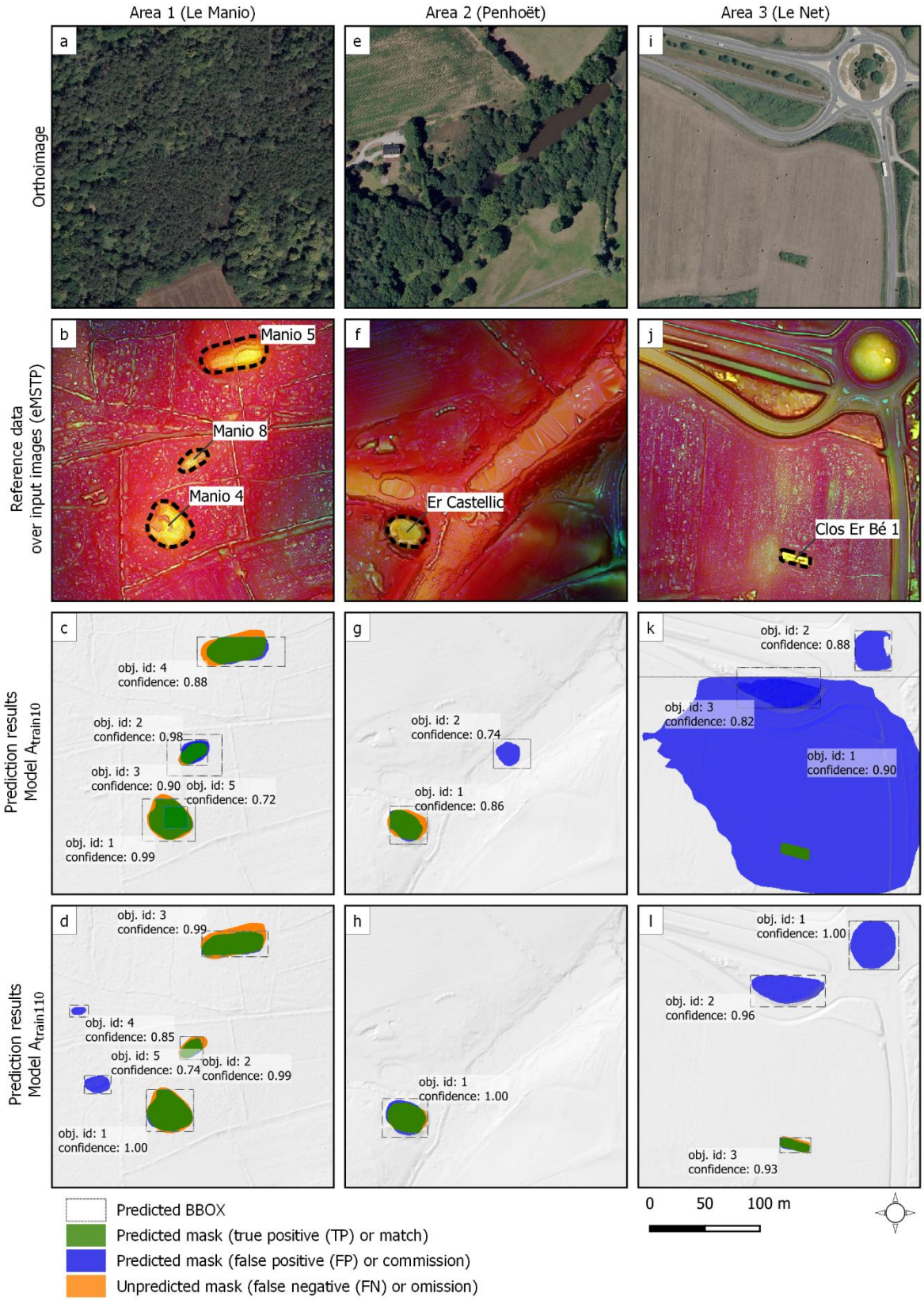
Area 1 (Le Manio)
Area 2 (Penhoët)
Area 3 (Le Net)
Orthoimage
Reference data over input images (eMSTP)
Prediction results Model $A_{train10}$
Prediction results Model $A_{train110}$
a
b
c
d
e
f
g
h
i
j
k
l
Manio 5
Manio 8
Manio 4
Er Castellic
Clos Er Bé 1
obj. id: 4 confidence: 0.88
obj. id: 2 confidence: 0.98
obj. id: 3 confidence: 0.90
obj. id: 5 confidence: 0.72
obj. id: 1 confidence: 0.99
obj. id: 2 confidence: 0.74
obj. id: 1 confidence: 0.86
obj. id: 2 confidence: 0.88
obj. id: 3 confidence: 0.82
obj. id: 1 confidence: 0.90
obj. id: 3 confidence: 0.99
obj. id: 4 confidence: 0.85
obj. id: 5 confidence: 0.74
obj. id: 2 confidence: 0.99
obj. id: 1 confidence: 1.00
obj. id: 1 confidence: 1.00
obj. id: 1 confidence: 1.00
obj. id: 2 confidence: 0.96
obj. id: 3 confidence: 0.93
0 50 100 m
Predicted BBOX
Predicted mask (true positive (TP) or match)
Predicted mask (false positive (FP) or commission)
Unpredicted mask (false negative (FN) or omission)

Figure 4.7. Detected (BBOX) and segmented (mask) objects predicted by $A_{train10}$ and $A_{train110}$ models. Results are shown for Area 1 (Le Manio), Area 2 (Penhoët) and Area 3 (Le Net), France.

4.3.1.2.a) Area 1: Le Manio, Carnac

Area 1, located at *Le Manio* (Carnac, France), has three Neolithic burial mounds under a dense canopy composed mainly of coniferous vegetation and brush undergrowth (Figure 4.7a and 7b). These archaeological structures are identified as Manio 4 (56 034 0113), Manio 5 (56 034 0114) and Manio 8 (56 034 0259) on the national archaeological map.

The low-trained model ($A_{train10}$) and high-trained model ($A_{train110}$) performed well in this area, with 3/3 matches (AP@IoU.5 = 0.92 and 1.0, respectively) (Figure 4.8). $A_{train10}$ predicted five objects (Figure 4.7c) that corresponded to three known archaeological structures. However, for the two objects with the lowest IoU values (obj. 3 (0.66) and 5 (0.31)) the predicted BBOXs influenced the predicted mask. While obj. 3 converged to a correctly adjusted segment by leveraging the segmentation phase within a BBOX larger than the target, obj. 5 resulted in an excessively small segment bounded by an excessively small predicted BBOX. $A_{train110}$ also predicted five objects (Figure 4.7d); the three with the highest confidence scores corresponded to the three known archaeological structures. The other two objects (obj. 4 and 5), which had lower confidence scores (0.85 and 0.74 respectively), were local topographic anomalies assumed to be due to recent (contemporary period) forestry operations. The quality of the predicted segments was confirmed using available archaeological documentation and in-situ photos (Figure 4.9).

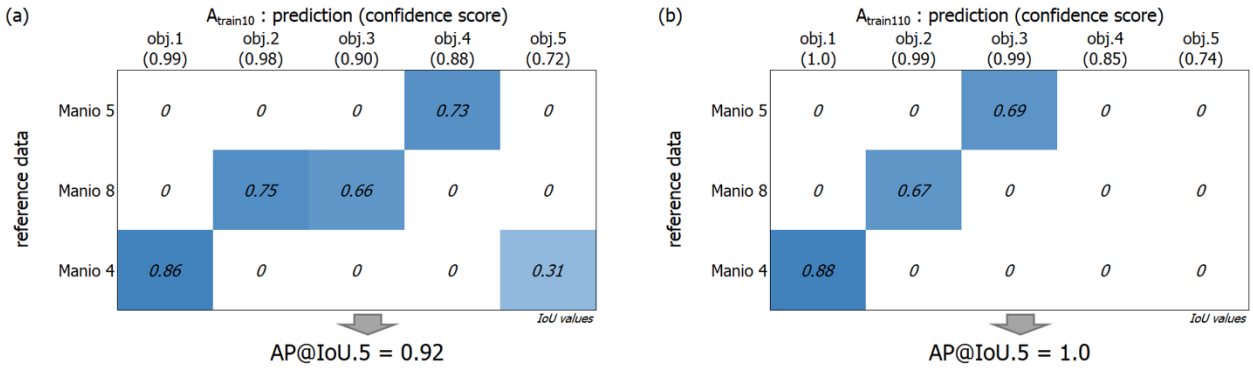

Figure 4.8. Prediction matrix for (a) $A_{train10}$ and (b) $A_{train110}$ models in Area 1 (Le Manio, France).

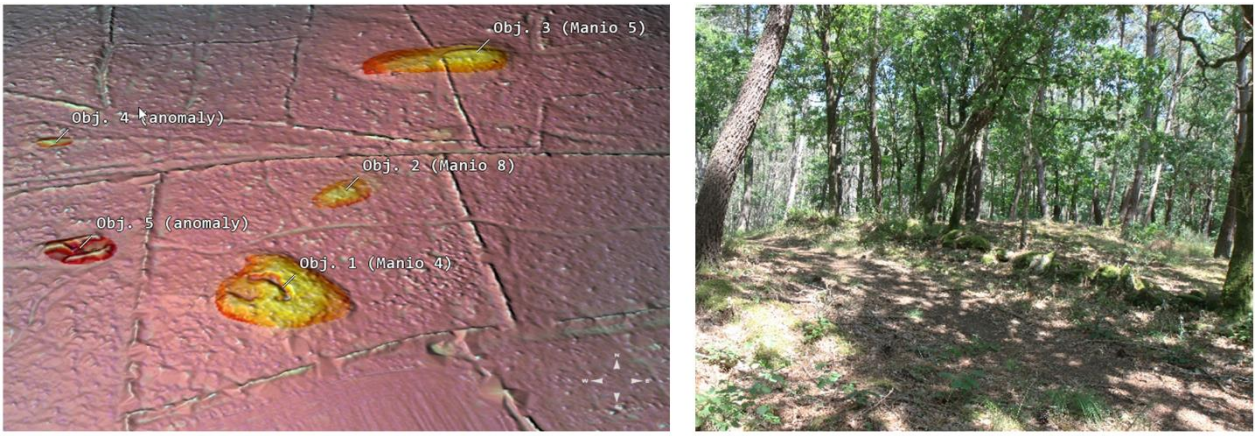

(a) (b)

Figure 4.9. Burial mounds at Le Manio (France). (a) Perspective view of the predicted masks (highlighted over an enhanced multiscale topographic position image) and corresponding archaeological structures. (b) Manio 5 viewed from the southwest.

4.3.1.2.b) Area 2: Penhoët, Crac'h

Area 2, located at Penhoët (Crac'h, France), has an archaeological structure that is considered to be a motte (Brochard, 1994; Cayot-Délandre, 1847), that dominates the valley of Le Plessis near the confluence of the Auray River. The archaeological structure, identified as *Er Castellic* (56 046 0015) on the national archaeological map, has never been excavated and it is scarcely documented.

Both the low-trained model ($A_{train10}$) and high-trained model ($A_{train110}$) were able to predict the presence of the archaeological structure (AP@IoU.5 = 1.0). $A_{train10}$ predicted two objects (Figure 4.7g); the BBOX with the highest confidence score (0.86) corresponded to the motte's location. The second BBOX (confidence score 0.74) was a false positive most likely due to an irregularity in the interpolated DTM that was visible on the enhanced multiscale topographic position (eMSTP) image on the surface of a lake.

$A_{train110}$ predicted a single object with a confidence score of 1.00 at the motte's location (Figure 4.7h). While the predicted mask (770 m²) was slightly larger than the object that had been drawn manually based on the reference data (690 m²), it represented the compact ovoid shape (Figure 4.10a) of the archaeological structure better. Topographic analysis across the predicted mask identified a visible external ditch and an internal embankment (Figure 4.10c and 10d).

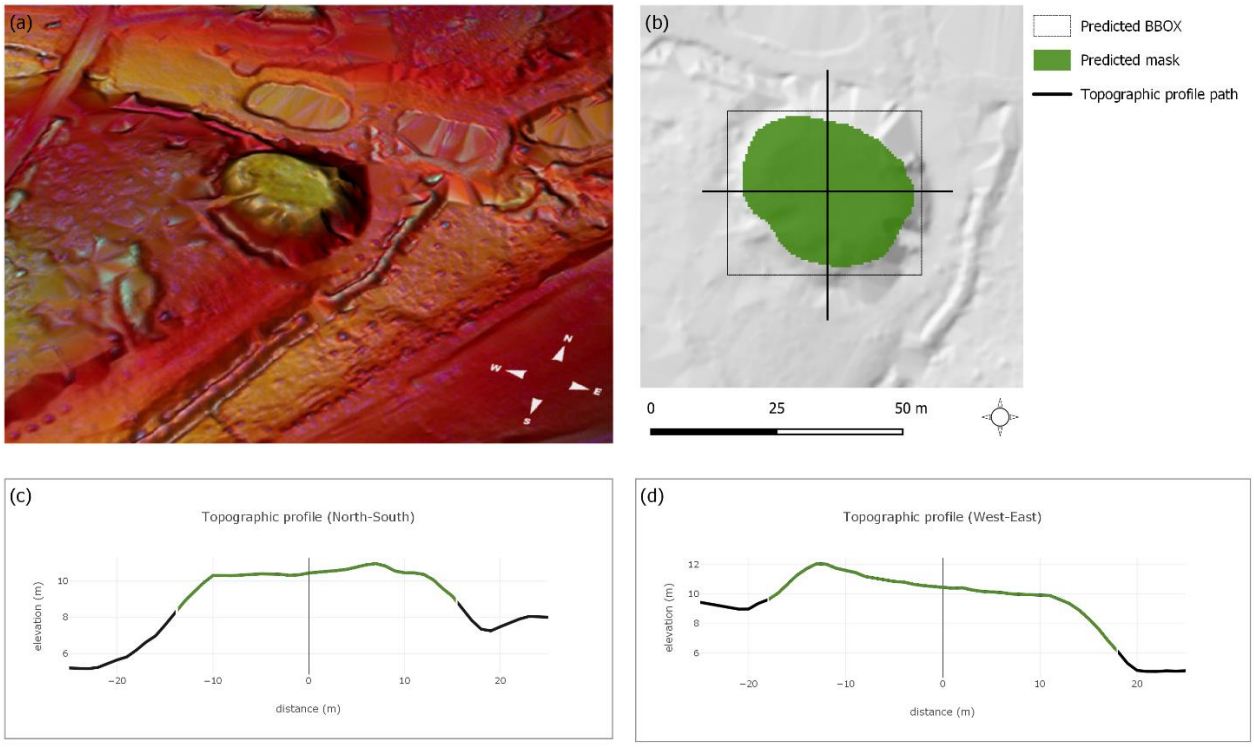

Figure 4.10. (a) Perspective view of Er Castellic (France) with enhanced multiscale topographic position image overlay, (b) 2D view of the predicted object over the hillshade DTM and (c and d) topographic profiles generated across the predicted object.

4.3.1.2.c) Area 3: Le Net, St Gildas de Rhuys

Area 3, located at Le Net (Saint Gildas de Rhuys, France), has a Neolithic passage grave 21 m long registered as a National Historic Monument since 1923 (Figure 4.11a). The site, located in an agricultural field and covered by vegetation and bushes (Figure 4.11b, 11c), is identified as Clos Er Bé 1 (56 214 0004) on the national archaeological map.

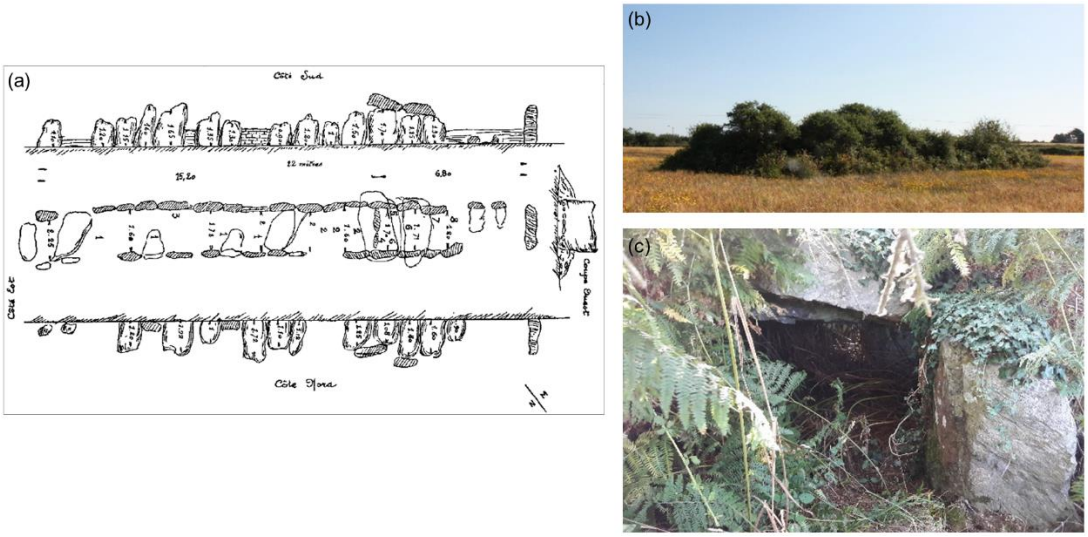

Figure 4.11. (a) Plan and cross-sectional views of the Clos Er Bé passage grave (France) (Le Rouzic et al., 1922). (b, c) Current state of the monument covered by bushes and ferns.

$A_{train10}$ predicted that the monument was contained in one (obj. 1) of the three objects detected (Figure 4.7k). However, visual analysis revealed that obj. 1 was a large (> 3 ha) irregular stain that covered most of the image. The commission error associated with this single object was 99%.

$A_{train110}$ predicted also three objects (Figure 4.7l). The passage grave was predicted (obj. 3) with a confidence of 0.93 and an IoU of 0.79, indicating that it corresponded to the footprint of the archaeological structure provided by the reference dataset. The other two objects (obj. 1 and 2), which had higher confidence scores (1.0 and 0.96, respectively), are perfect examples of false positives. Obj. 1 is a traffic roundabout with a perfectly circular mound landscape design as the central element, while obj. 2 is a recent elongated embankment that protects the bicycle lane. Both objects have topographical and morphological characteristics that resulted in the model making inaccurate predictions.

4.3.2 Object characterization: initial results

As mentioned, the (semi-)automatic process of the deep CNN provided two levels of information: (i) the location of the objects of interest (BBOX, associated with a confidence score) and (ii) a mask that describes the shape of each predicted object. The latter information was used to characterize the context and morphology of the detected and segmented objects.

This approach was applied to the archaeological site of Park Er Guren (Figure 4.12), which is located east of the Bay of Saint Jean in the commune of Crac'h. The site contains two dolmens separated by 25 m in a north-south orientation that were registered as National Historic Monuments in 1926. The model predicted the presence of two objects (Figure 4.13). Hyperscale topographic position signatures (Figure 4.14) and morphometric descriptors (Table 4.2) were calculated for the masks of both objects.

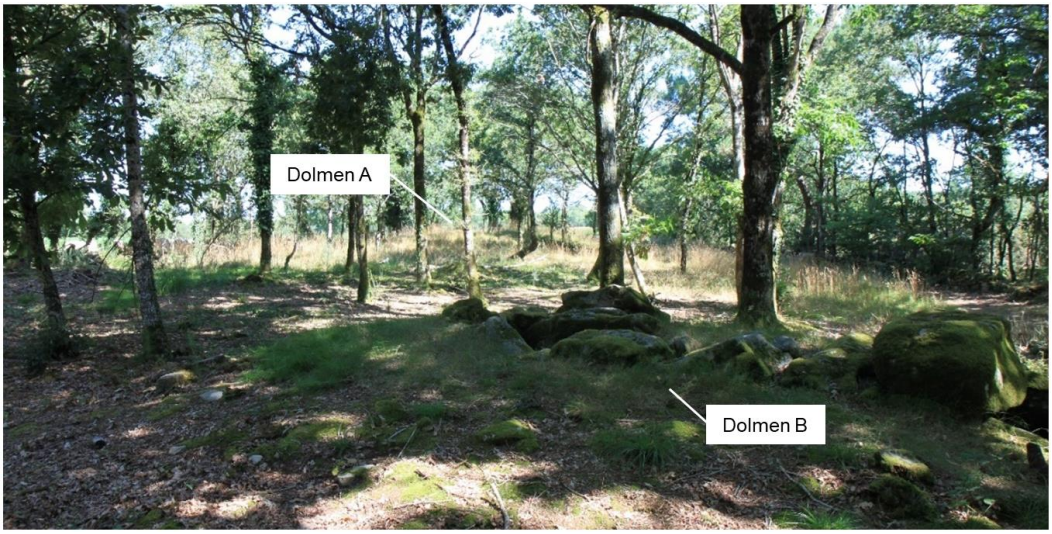

Figure 4.12. Dolmens of Park Er Guren (France), view from south. Dolmen A lies in the background, while Dolmen B lies in the foreground.

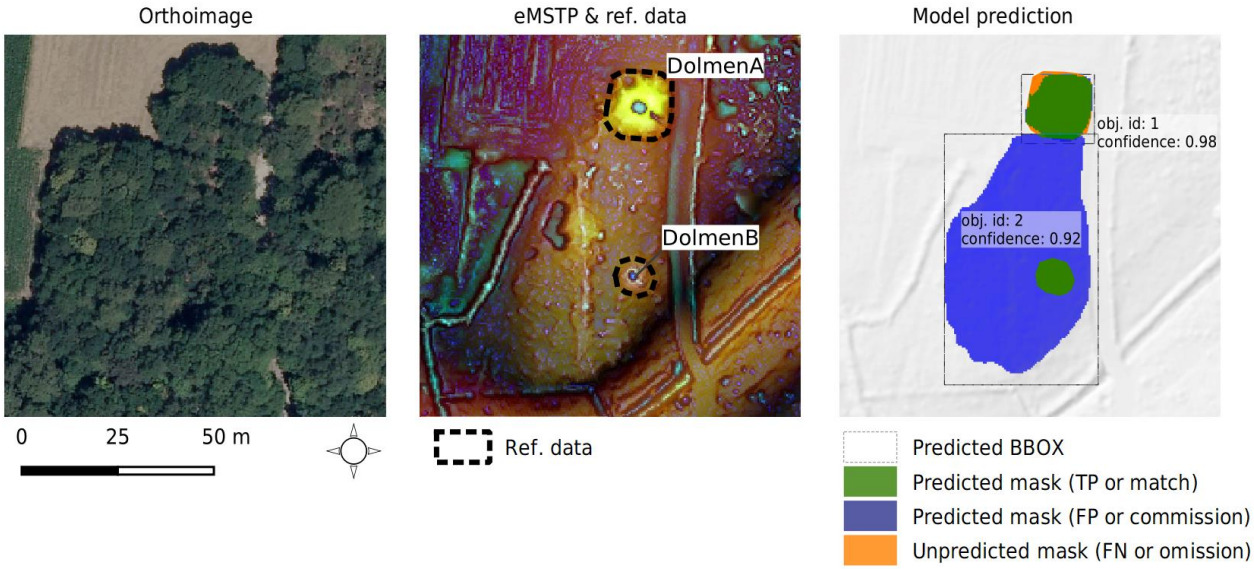

Figure 4.13. $A_{train110}$ model predictions for the area of Park Er Guren (France). eMSTP = enhanced multiscale topographic position, BBOX = bounding box, TP = true positive, FP = false positive, FN = false negative.

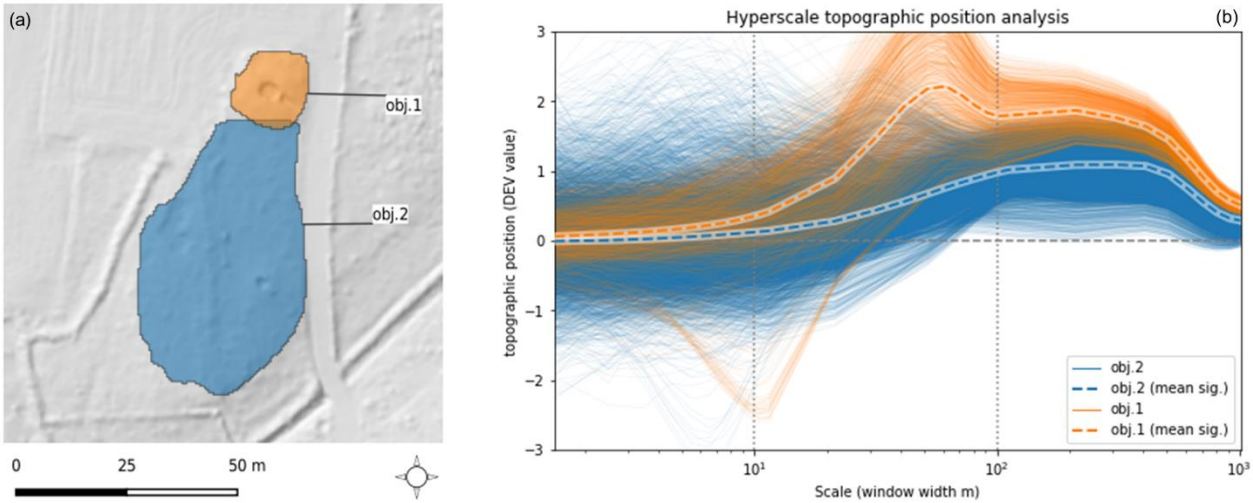

Figure 4.14. Characterization of the predicted objects for Park Er Guren (France) based on the resulting (semi-)automatic approach. (a) Object segmentation results for object 1 (orange) and 2 (blue), (b) hyperscale topographic position signatures (each corresponds to a pixel included in the object footprint). Dashed curves indicate the mean signature of each object.

Table 4.2. Hyperscale topographic position signatures and morphometric descriptors calculated for the predicted objects for Park Er Guren (France).

Object	**obj.1**	**obj.2**
Area (m²)	243	1809
Perimeter (m)	71	203
Major-axis (m)	20	64
Minor-axis (m)	16	37
Hyperscale topographic signature	Figure 4.14b	Figure 4.14b

The hyperscale topographic position signatures and morphometric descriptors were then used to provide a data-driven description of the predicted objects, which was then compared to the archaeological reference dataset and additional archaeological documentation (Gouezin, 2017; Le Rouzic, 1933) as follows:

- Object 1 was a pseudo-circular element 16-20 m in diameter composed of two main topographical units (groups of signatures). The first unit largely dominated its environment at the mesoscale (10-100 m) and, to a lesser extent, macroscale (100-1000 m). The second unit, with only few pixels, had a negative value of topographic position at the micro-/meso-scale, indicating the presence of a pit or trench. This object corresponded to Dolmen A and described its visible inner structures (e.g. corridor, central position of the chamber). The dolmen's topographically dominant position is characteristic of other Neolithic funeral monuments in the area.
- Object 2 was a large piriform element 64 m long and 37 m wide that varied greatly in topographic positions. Its mean topographic position became progressively dominant at the meso- and macro-scales, while not being the most dominating element within windows wider than 500 m. A few signatures were highly negative at the microscale, indicating the presence of local depressions within the object's footprint. The complex combination of signatures reflects the multiple topographical units in this piriform mound. The reference data did not describe this complex structure (thus making it statistically a false positive or commission error), but the object suggested an elongated tumulus associated with the dolmens. In addition to the mound, analysis of the hyperscale topographic position signatures suggested topographically visible pits that may correspond to (i) the chamber of Dolmen B and (ii) modern excavation areas visible on the western flank of the mound (Figure 4.13). Locally (micro- and meso-scales), dominating signatures highlighted the presence of the north-south oriented embankment on top of the mound.

4.3.3 Evaluation of the approach within an archaeological prospection scheme

The results of the deployment model showed predicted potential structures with confidence scores ranging from 0.5 to 1. These prediction results highlighted the pixel to object aggregation capability of the deep CNN approach, and predicted object sharing shape and size characteristics

with the reference data used to train the model. The predicted objects were visually interpreted on the eMSTP image using two additional study sites that were not included for model training, validation or testing.

4.3.3.1) Analysis on the area of Goah Leron, Carnac (France)

Objects A and B were considered as interesting structures for further field verification. Object A with a circular shape (16m diameter) and low positive elevation (less than 0.3m above surrounding terrain) showed a rough texture on the eMSTP image, typical of undergrowth vegetation under dense canopy (Figure 4.15). Object B with a pseudo-circular shape (36m diameter) and a positive elevation of 0.8m above surrounding terrain, shared the same eMSTP characteristics. It is to be noted that the presence of standing stones (not visible on the LiDAR-derived DTM) is attested between object A & object B, thus supporting the idea of the possible presence of Neolithic burial mounds nearby.

Object C was considered as a false-positive. This object corresponded to a north-south orientated terrain depression of 12m wide, 46m long and 40cm deep that shared similarities with the representation of some elongated tumulus in the eMSTP image. This was mostly due to the conversion of the topographic metric DEVs from relative to absolute values during the calculation of the eMSTP image.

Object D was also considered as a false positive. This object, which corresponded to a horse training arena with flat elevation and surrounding embankments, shared shape characteristics with reference data, but not topographic or texture characteristics.

The model did not predict any potential structure on the hill located North-East of the area (point E). While the yellow-reddish color in the eMSTP image -associated to the meso-macro dominating topographic signature- corresponded to the specific position of many tumulus in the study area, the model did not predict any object, which was probably due to the absence of local morphological anomalies.

The remaining predicted objects were isolated small mounds (4 to 6m in diameter) less than 1m high, most of them being located in open agricultural areas. While it was not possible to determine their nature only based on the interpretation of the eMSTP image further investigation would be required to identify them.

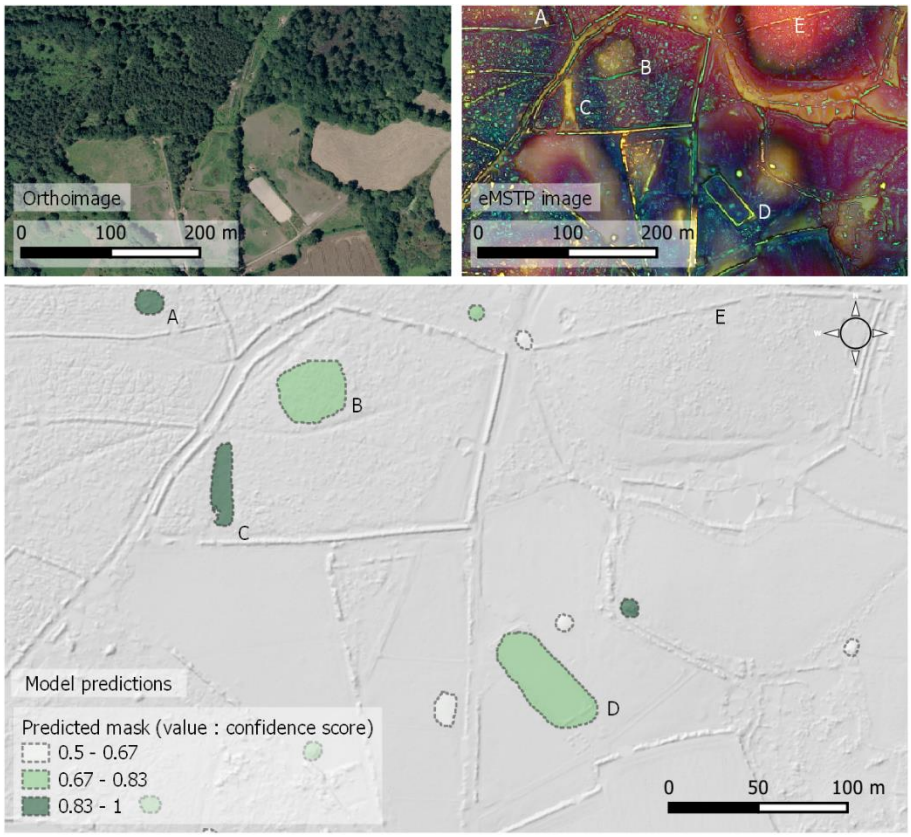

Figure 4.15: Example of prediction results outside the reference dataset, Goah Lêron area, Carnac (France). Objects A and B were considered as interesting structures for further field investigation based on human-interpretation of the eMSTP image. Objects C and D were considered as false positives. Point E highlighted the fact that no potential structure was predicted on the hill. The remaining objects (small isolated mounds) would require further investigation.

4.3.3.2) Analysis on the area of Brahen, Carnac (France)

Objects A and B were identified as archaeological entities. Object A was a circular mound (26m diameter) with positive elevation of 0.8m above the surrounding terrain (Figure 4.16). The field verification confirmed the probable archaeological nature of this structure as a tumulus, with a possible attribution to the Bronze Age based on its morphology. Object C corresponded to a dominating terrain covered by dense vegetation with a morphological anomaly on its highest position (Object B). In the field, remaining elements of a possible megalithic stone alignment were identified at this position.

Object D was considered as a false-positive. This object corresponded to a narrow ditch with east-west orientation that shared similarities with the representation of some elongated tumulus in the eMSTP image. This detection error could be due to the conversion of the topographic metric DEVs from relative to absolute values during the calculation of the eMSTP image.

The remaining predicted objects corresponded to local morphological anomalies that would require further investigation.

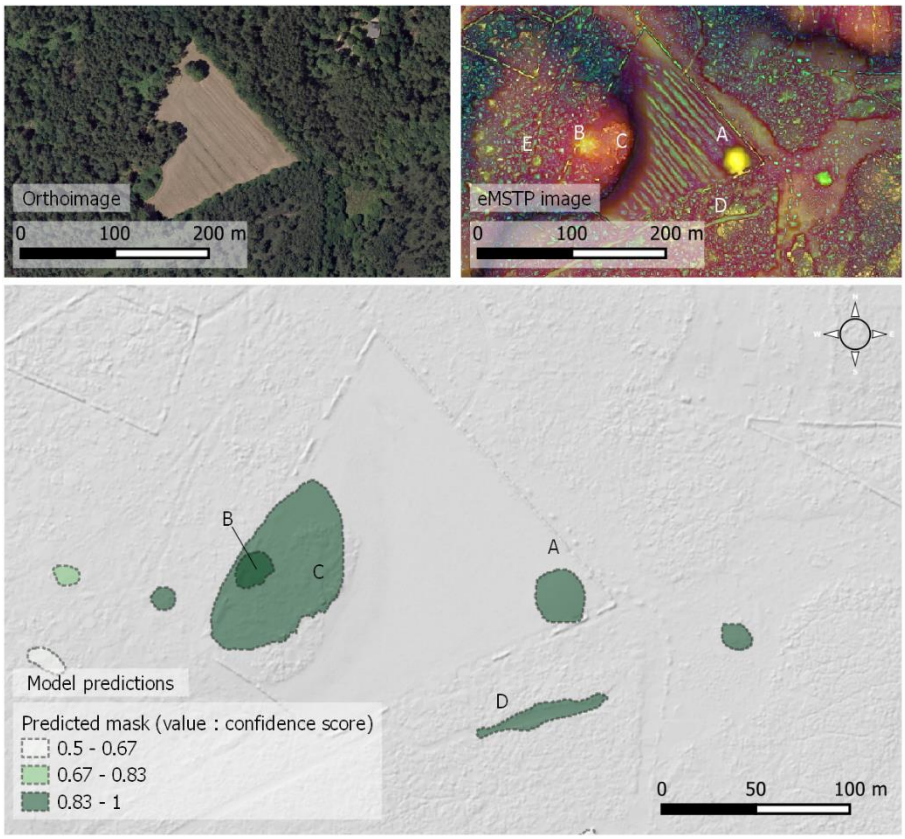

Figure 4.16: Example of prediction results outside the reference dataset, Brahen area, Carnac (France). Objects A and B corresponded to archaeological structures confirmed by field verification, object C being a dominating terrain including object B. Object D was considered as false-positive. Remaining objects were local morphological anomalies that would require further investigation.

4.4 Discussion

4.4.1 Sensitivity of the approach and generalization ability

The deep CNN approach resulted in high detection and segmentation performances (mAP up to 0.77) with relatively small training datasets. The largest training dataset contained 110 images, which is small training set for deep learning. This confirms the approach's ability to perform well in archaeological contexts in which sparse reference data are a common limitation.

Nonetheless, the model's sensitivity to the images selected for the training and test datasets (with mAP@IoU.5 varying from 0.29 (model $E_{train110}$) to 0.77 (model $A_{train110}$) for the same number of training images) raises some concerns. A previous study that focused on (semi-)automatic archaeological mapping also mentioned this sensitivity (Verschoof-van der Vaart et al., 2020).

Some of the variability is related to the metrics used to evaluate detection and segmentation performances, but the main sources of variability seem to be the images selected for model evaluation (the complexity of the test dataset) and training (whether the training dataset is representative and comprehensive) (Soroush et al., 2020) .

The deep CNN approach showed adaptability in detecting and segmenting different archaeological structures within the region. However, model training and evaluation were limited to a region that has particular topographic and archaeological characteristics. Most of the archaeological structures contained in the reference dataset have a topographically dominant position (burial mounds, hillforts, wind mills), but their local dominance is highly variable in magnitude and scale. While the trained models detected most above mean elevations (e.g. roundabout), they differed from local maximum detectors on their ability to consider the following archaeological landscape characteristics: the multiscale topographic position of the sites (maxima at specific local neighborhood or scale) and the local morphological patterns of archaeological structures. As confirmed by the results obtained using the deployment model applied on an independent set of images of the study area, these characteristics were learned during the training phase and used for prediction. This demonstrated the generalization capabilities of the approach in the geo-archaeological context of the study area.

The limits of the deep CNN approach were also identified. Beside prediction errors that were expected (e.g. roundabout), errors were also observed for objects sharing few or no similarities with the reference dataset (e.g. horse training area, large ditch). Such undesired behavior of the deep CNN models raised the question of negative training (i.e. providing the model with negative examples during training). While this was not implemented in the Mask R-CNN framework used in this study, it should be addressed in future works to improve prediction performances, for example using software frameworks that handle negative training for instance segmentation, such as Detectron2 (Wu et al., 2019).

More generally, results showed that a particular attention should be paid to the selection of training examples. The sample selection strategy is still a challenging concern especially with the hidden and non-intuitive phenomena related to deep CNN. Tools that facilitate insights into model successes and failures such as Gradient-weighted Class Activation Mapping (Grad-CAM) (Selvaraju et al., 2020) could be used to tackle such concern.

Further investigation of the multiple hyper-parameters and model configurations of deep CNN architectures would be helpful to assess the scope and limits of the approach. As an example, data augmentation (DA) was empirically used to improve model performances and generalization capabilities (Shorten & Khoshgoftaar, 2019). The evaluation of DA was not included in this study, because a comprehensive assessment would involve a full-fledged study (evaluation of performances with and without DA, and with multiple DA configurations involving various combinations of DA techniques). Although we did not perform this comprehensive evaluation, we evaluated DA effect on a single model ($A_{train110}$) trained without and with data-augmentation

using a performance test. Results showed an increase of the mAP@IoU0.5 performance from 0.64 to 0.75.

Assessing the overall generalization ability at a larger geographical scale (spatial generalization) and for more types of archaeological structures (typological generalization) would require further experiments. First, to assess spatial generalization, a pre-trained model could be used to identify topographical anomalies that have characteristics similar to those on the coast of Morbihan using the LiDAR dataset of relevant regions in the world. Second, to assess typological generalization, the model could be retrained to include new types of structures to increase the diversity of archaeological contexts assimilated by the deep CNN. These strategies would benefit from public benchmark dataset targeted to detect archaeological sites from remotely sensed data.

4.4.2 Evaluation metrics for ambiguous reference data

The results indicate that statistical assessment of the models provided an objective metric of the quality of predictions, but it did not completely capture the approach's performance because the overall mAP hides local discrepancies that could be identified only through case-by-case visual analysis of model predictions. The metrics used for object detection and segmentation were based on an overlap measurement (i.e., IoU) that was a threshold for determining a match or non-match. However, the complex relation between remotely sensed archaeological information and comprehensive archaeological information (e.g. excavation and field reports, archives) is not considered regardless of the threshold value (i.e. one or more values). The definition of reference data frequently raises issues in archaeological mapping, such as how remote sensing perceives the footprint of a known archaeological structure or diffuse footprints, such as large artificial mounds that have been eroding for thousands of years.

Similar concerns also arise for detecting undiscovered archaeological structures. A false detection by machine-learning could become a true positive after in-situ verification. Therefore, a liberal strategy (rather than a conservative strategy) is required to define the detection thresholds (related to the confidence score and overlap measurement), which allows for a certain number of false negatives. This study's examples of false-positive detections (Figure 4.7d and 7l) are representative of this intentionally liberal strategy, with topographical structures detected (i) correctly because they share characteristics with known archaeological structures and (ii) incorrectly because they are ultimately interpreted as contemporary human earthworks that are not considered of archaeological importance. Such a strategy can be justified to detect a maximum number of potential structures, as long as the prediction corresponds to a relevant response from the deep CNN considering the input examples it was trained on. Then, potential structures are interpreted based on human expertise.

These issues highlight that the current evaluation metrics, which originated from computer-vision and image-analysis domains, are only partially adapted to archaeological mapping. This could be considered in future studies such as by using fuzzy approaches.

Guyot, Alexandre. Contribution of airborne LiDAR and hyperspectral data to archaeological mapping in terrestrial and submerged environments. 2021

4.4.3 One-class approach and post-detection characterization: potential for a new paradigm for (semi-)automatic mapping in archaeology

Most approaches in machine learning-based archaeological mapping use a pre-defined nomenclature (e.g. barrows, charcoal kilns, celtic fields, burial mounds, mining pits) to consider local archaeological characteristics (e.g. site morphology, chrono-typological relation, spatial relationship). However, a standard and consensual typology appropriate for remotely sensed archaeological structures that span time and space remains a concern (Tarolli et al., 2019). Moreover, classes are often distributed unequally (i.e. datasets of archaeological structures with a lack of samples for certain classes).

We used a one-class rather than multi-class approach to address these two issues because we assumed that the deep CNN would have higher generalization abilities (i.e. depend less on target type and variety) with a one-class approach. This was confirmed by the results obtained for the *Er Castellic* motte, whose structure type was not included in the training dataset. Although this artificially elevated terrain monument was the only example of its type in the study area, it was sufficiently similar to a tumulus for the model to detect it as an object of interest. These topographical and morphological similarities with certain tumulus were mentioned in an archaeological prospection report (Brochard, 1994) and reinforced our assumption. Indeed, from a LiDAR perspective, archaeological sites of different chronologies and typologies share patterns that the deep CNN can discover and extract.

The characterization phase, based on the object-segmented mask and data-driven description, provides information that can help to identify the nature of the archaeological structures. For example, characterization of the detected objects and segmented at the *Park Er Guren* site made it possible to identify a tumulus and related dolmens. Although more examples are required to confirm this assumption, this approach provides new perspectives by inversing the common conceptual model in remote sensing archaeological mapping in which a typology of target options must be defined before (semi-)automatic detection.

4.5 Conclusion

We demonstrated potential methods that can detect and characterize archeological structures by performing object segmentation using a deep CNN approach combined with transfer learning. Our study reveals that the approach developed can be used to (semi-) automatically detect, delineate and characterize topographic anomalies. The results, compared to archaeological reference data collected from archaeological documentation, showed detection accuracy (mAP@IoU.5) up to 0.77 and provided new perspectives for archaeological documentation and interpretation through morphometric and contextual characterization via object segmentation. The one-class detection method combined with a characterization-interpretation strategy provides a new paradigm for prospecting archaeological structures in varying states of

conservation or with conflicting typologies. The application of such a deep CNN approach to large scale archaeological mapping in wider geographical and archaeological contexts still needs to be extended and assessed. Beside the necessary addition of a new set of reference data covering various geo-archaeological situations, this would also involve the development of methods for the optimal selection of training samples. It would also involve further investigation on the effectiveness of the LiDAR-derived VT as input to the automatic detection and segmentation processes. In this regards, the objective evaluation metrics provided by the deep CNN approach could be used for the benchmarking of new and existing VTs.

Guyot, Alexandre. Contribution of airborne LiDAR and hyperspectral data to archaeological mapping in terrestrial and submerged environments. 2021

Chapter 5. Objective comparison of relief visualization techniques with deep CNN for archaeology

This chapter is entirely reproduced from the peer-reviewed article published during the thesis in *Journal of Archaeological Science: Reports*.

> Guyot, A., Lennon, M., & Hubert-Moy, L. (2021). Objective comparison of relief visualization techniques with deep CNN for archaeology. *Journal of Archaeological Science: Reports*, 38, 103027. https://doi.org/10.1016/j.jasrep.2021.103027

Contents lists available at ScienceDirect

Journal of Archaeological Science: Reports

journal homepage: www.elsevier.com/locate/jasrep

Article

Objective comparison of relief visualization techniques with deep CNN for archaeology

Alexandre Guyot [1,2,*], Marc Lennon [2], and Laurence Hubert-Moy [1]

1. Laboratoire LETG - UMR 6554, Université Rennes 2, Place du recteur Henri Le Moal, 35043, Rennes, France
2. Hytech-Imaging, 115 Rue Claude Chappe, 29280, Plouzané, France

* Correspondence: alexandre.guyot@univ-rennes2.fr

Received: 14 September 2020; Accepted: 15 January 2021; Published: 03 February 2021

Abstract: Archaeology has been profoundly transformed by the advent of airborne laser scanning (ALS) technology (a.k.a airborne LiDAR). High-resolution and high-precision synoptic views of earth's topography are now available, even in densely forested environments, to identify and characterize landform patterns resulting from past human occupation. ALS-based archaeological prospection relies on digital terrain model (DTM) visualization techniques (VTs) that highlight subtle topographical changes perceived and interpreted by archaeologists. An increasing number of VTs have been developed, and they have been evaluated to date mainly based on subjective human perception. This study developed a new approach based on state-of-the-art computer-vision algorithms to benchmark VTs using objective metrics. Thirteen VTs were applied to a ALS-derived DTM, and a deep convolution neural network (deep CNN) was implemented and trained to automatically detect and segment archaeological structures from these images. Visual interpretation of the images showed that the most informative VT was e²MSTP, which combined a multiscale topographic analysis (MSTP) with a morphologically explicit image and a slope-invariant relief detrending technique. The deep CNN approach confirmed these results and

provided objective performance metrics. This study indicates that the computer vision approach opens new perspectives in the objective selection of the most suitable VT for archaeological prospection.

5.1 Introduction

In the past few decades, archaeology has been profoundly transformed by the advent of airborne laser scanning (ALS) technology (a.k.a airborne LiDAR). High-resolution and high-precision synoptic views of earth's topography are now available, even in densely forested environments, to identify and characterize landform patterns resulting from past human occupation. Common ALS-based archaeological prospection relies on digital terrain model (DTM) visualization techniques (VTs) to highlight subtle topographical changes that are visually interpreted by archaeologists (Štular et al., 2012).

Representation of the characteristics archaeological structures (e.g. size, shape, orientation, landscape context, topographic position) varies greatly among VTs (Kokalj & Hesse, 2017). However, selecting the most suitable VT for enhancing the perception of archaeological structures remains challenging. Several studies have provided valuable assessment of multiple VTs applied to ALS-derived DTM via visual comparison (Bennett et al., 2012a; Devereux et al., 2008; M. Doneus, 2013; Orengo & Petrie, 2018; Štular et al., 2012; Zakšek et al., 2011). However, this approach is limited due to the subjectivity and bias of visual interpretation (Grammer et al., 2017; Risbøl, 2013), which can influence identification and characterization decisions. To our knowledge, only one study to date has addressed this concern with an objective approach: (Mayoral et al., 2017) assessed VTs analytically based on local contrast and zonal statistics. Their approach provided useful information about the ability of VTs to perceive variations in local slope or roughness based on pre-selected topographic conditions. However, it did not address global objective assessment of VTs and did not consider an automatic-detection framework. These limitations and the growing number of available VTs (Kokalj & Somrak, 2019) increase the need to develop new objective assessment tools and methods.

The computer-vision field has also changed profoundly in recent years, especially with the development of deep convolutional neural networks (deep CNNs) to solve complex image-analysis tasks. CNN is a type of artificial neural network whose connections are roughly inspired by biological processes in the visual cortex (Hubel & Wiesel, 1962). Deep CNNs are composed of many connected layers that can learn hierarchical representations of data with multiple levels of abstraction (LeCun et al., 2015). While emerging in the 20th century, it is only in the past decade that implementation of deep CNNs resulted in ground-breaking results in image classification (Krizhevsky et al., 2012) and object detection (Girshick, 2015). For details on deep CNNs, see Goodfellow et al. (2016).

Guyot, Alexandre. Contribution of airborne LiDAR and hyperspectral data to archaeological mapping in terrestrial and submerged environments. 2021

The scientific community's increasing interest for such high-performance computer vision capability has resulted in the publication of multiple open source state-of-the art deep CNN software frameworks. Among them, Mask R-CNN, available in different open source Python implementations (Abdulla, 2017; Wu et al., 2019), is designed for object detection and instance segmentation. In deep CNN, object detection predicts the presence and location (surrounded by a bounding-box) of an object in the image, while instance segmentation adds a contour (also called "mask" or "segment") to the detected object.

The first approaches using deep CNN applied to ALS-based archeological prospection were developed to automatically detect charcoal kilns (Trier et al., 2016). They were then evaluated in different contexts and configurations to detect archaeological structures (Bonhage, 2021; Gallwey et al., 2019; Kazimi et al., 2018; Trier et al., 2018, 2021; Verschoof-van der Vaart et al., 2020; Verschoof-van der Vaart & Lambers, 2019). In these studies, a single type of input data was used (either raw elevation data or VT), which had been selected empirically based on intuition or the visual perception provided by the input data. Very few studies evaluated the use of various VTs with deep CNNs in archaeological context. Somrak et al. (2020) applied deep CNN models with different ALS-derived inputs for classifying images of ancient settlements. However, to our knowledge, no studies questioned the potential of computer-vision approaches, especially object detection and segmentation, for the objective assessment of VTs and the relation between computer-based and human-based perception.

In this study we developed a new approach that uses state-of-the-art computer-vision algorithms to benchmark VTs using objective metrics. To this end, VTs were first visually interpreted and compared to assess their ability to identify archaeological structures. Then, the same VTs were compared using a deep CNN trained for automatic detection and segmentation of archaeological structures.

First, we tested the assumption that visual representation of data, effective from the perspective of human vision, is also effective from the perspective of deep CNNs. Then, we presented the results and discussed the benefits and limits of an objective comparison of ALS-derived relief VTs using deep CNN for archaeology.

5.2 Materials and Methods

5.2.1 Study area

The study area (Figure 5.1) was located in the Morbihan department (Brittany, France), along the Atlantic coast. The region has a complex and fragmented mosaic of landscapes. The hinterland is composed of woodlands, moorlands and farmland that form a rural environment oriented to agriculture. The coastal area is also diverse, with estuaries and small islands near the intricate Gulf of Morbihan and large open, sandy areas in the Bay of Quiberon that concentrate most of the economic activities of tourism and fisheries.

The area is home to a unique megalithic heritage. Erected between the 5th and 3rd millennia BC, the Neolithic architecture (standing stones and megalithic tombs) represents an exceptional corpus of archaeological sites that are candidates for the UNESCO World Heritage List. Beyond this emblematic heritage, the coast of Morbihan includes a wide variety of archaeological sites that encompass several prehistorical and historical periods.

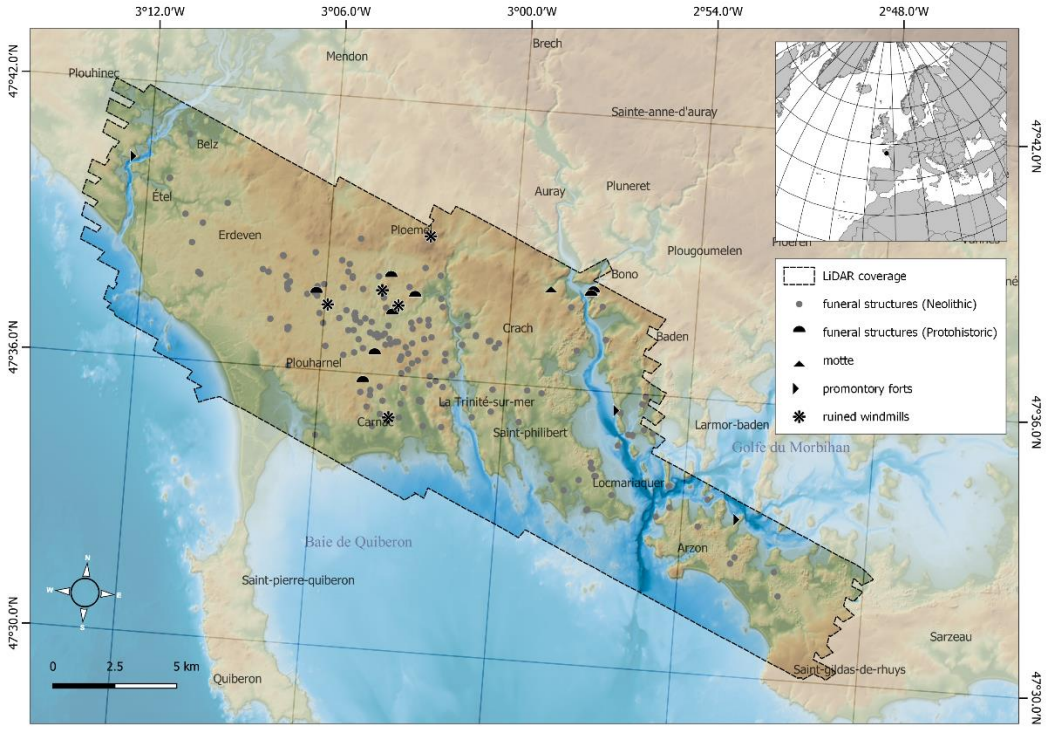

Figure 5.1. Airborne Laser Scanning (ALS) coverage of the study area with archaeological reference data used to train and test the Deep convolution neural network models

5.2.2 Dataset

5.2.2.1) Digital terrain model

The DTM was generated from a ALS point cloud collected with a fixed-wing plane using an Optech Titan ALS sensor operated over the study area in the leaf-off season in 2016. The specifications of the airborne acquisition were defined to obtain a nominal point density of 14 points/m². Ground points were filtered from the raw point cloud using LAStools (Isenburg, 2020) before being interpolated to create a Triangular Irregular Network that was rasterized onto a grid of 50 cm resolution (see Guyot et al., 2018 for processing details).

5.2.2.2) Archaeological reference data

The reference dataset consisted of 195 georeferenced polygons that represented footprints of known archaeological sites in the study area. The sites were selected from the regional archaeological reference dataset provided by Brittany's Service régional de l'archéologie. Only archaeological structures whose topographic characteristics could be perceived on the ALS-derived DTM were kept (excluding sites related only to small-object deposits and sites considered as aboveground structures with no influence on the bare-earth topography, such as standing stones).

The archaeological sites selected had diverse chronologies, morphologies and landscape contexts. Their state of conservation also varied greatly, from long-known restored monuments to unexcavated little-documented structures. The reference dataset included 195 archaeological structures (Figure 5.1): 176 funeral structures attributed to the Neolithic, 10 funeral structures attributed to protohistoric periods, 1 motte, 3 promontory forts and 5 ruined windmills. Note that the great majority of structures are elevated and there are only few depressions.

Given the highly imbalanced dataset (since Neolithic structures dominated), the annotations were intentionally grouped into a single "archaeological structure" class with no further distinction. The reference dataset was converted from a geospatial format to an annotation format (json COCO format) in which each annotation was associated with its corresponding VT tile to be input into the deep CNN architecture. Due to the spatial proximity of some archaeological sites, 150 VT images covered the 195 annotations (a mean of 1.3 annotations per image).

5.2.3 Methods

5.2.3.1) Visualization techniques of the ALS-derived terrain model

We compared 13 VTs: 12 came from archaeological prospection literature, and one (e^2MSTP) was designed during this study. All VTs were applied to the ALS-derived DTM at 50 cm resolution, with specific calculation and visualization parameters (Table 5.1) using open-source tools such as RVT software (Kokalj, 2020), WhiteboxTools (J. Lindsay, 2020) and Python blend-mode libraries (Roscheck, 2020).

Table 5.1. visualization techniques compared in the study

	Description	**References**	**Calculation parameters**	**Visualization parameters**
HS	Analytical hillshading	(Yoëli, 1967)	Sun azimuth : 315°; Sun elevation angle : 35°	Linear histogram stretch between 0 and 1
HS_PCA	PCA of multi-analytical hillshading	(Devereux et al., 2008)	Sun azimuths : 16 directions; Sun elevation angle : 35°; Number of principal components: 3	Histogram equalization with 2% cut-off

SLP	Gradient of elevation	(M. Doneus & Briese, 2006)	No parameters	Linear histogram stretch between 0 and 51°
ON	Negative topographic openness	(M. Doneus, 2013)	Number of search directions: 16; Search radius : 10 px	linear histogram stretch between 60° and 95°
OP	Positive topographic openness	(M. Doneus, 2013)	Number of search directions: 16; Search radius : 10 px	linear histogram stretch between 60° and 95°
SVF	Sky view factor	(Kokalj et al., 2011)	Number of search directions: 16; Search radius : 10 px	Linear histogram stretch between 0.64 and 1.00
LD	Local dominance	(Hesse, 2016)	Minimum radius: 10 px; Maximum radius: 20 px	Linear histogram stretch between 0.5 and 1.8
SLRM	Simple local relief model	(Hesse, 2010)	Radius for trend assessment : 20 px	Histogram equalization with 2% cut-off
RRIM	Red relief image map	Based on (Chiba et al., 2008)	Source images: openness ((OP-ON) / 2) & SLP (red-toned) Blending : addition with 70% (SLP) and 30% openness	See SLP, OP, ON
MSTP	Multiscale topographic position	(Guyot et al., 2018; J. B. Lindsay et al., 2015)	Number of |DEV| calculation : 30 ; Micro scale (Blue) : 3 to 21 px; Meso scale (Green): 23 to 203 px ; Macro scale (Red): 223 to 2023 px	linear histogram stretch between 0 to 3
e^2MSTP	enhanced MSTP	Adapted from (Guyot, Lennon, Lorho, et al., 2021)	Source images: MSTP, RRIM, SLRM. Blending : SLRM blended (screen, 25% opacity) with RRIM blended (softlight, 70% opacity) with MSTP	See MSTP, RRIM, SLRM
VAT	Visualization for Archaeological Topography	(Kokalj & Somrak, 2019)	Source images: HS, SLP, OP, SVF Blending : SVF blended (multiply, 25% opacity) with OP blended (overlay, 50% opacity) with SLP blended (luminosity, 70% opacity) with HS.	See HS, SLP, OP, SVF
VAT-HS_channels	3-band, Visualization for Archaeological Topography	(Somrak et al., 2020)	Source images: SLP, OP, SVF Combined in a 3-band RGB image (Red:	See SLP, OP, SVF

Guyot, Alexandre. Contribution of airborne LiDAR and hyperspectral data to archaeological mapping in terrestrial and submerged environments. 2021

			SLP, Green:OP, Blue: SVF)	

All VTs were normalized to 0-255 using the visualization parameters (Table 5.1) and converted to 8-bit 3-band images (RGB) to be used as input to the deep CNN. Greyscale VTs were transformed from 8-bit (0-255) single-band to 8-bit (0-255) 3-band images by duplicating the 8-bit single-band images.

The blending techniques were applied using the 3-band normalized and transformed images.

Guyot, Alexandre. Contribution of airborne LiDAR and hyperspectral data to archaeological mapping in terrestrial and submerged environments. 2021

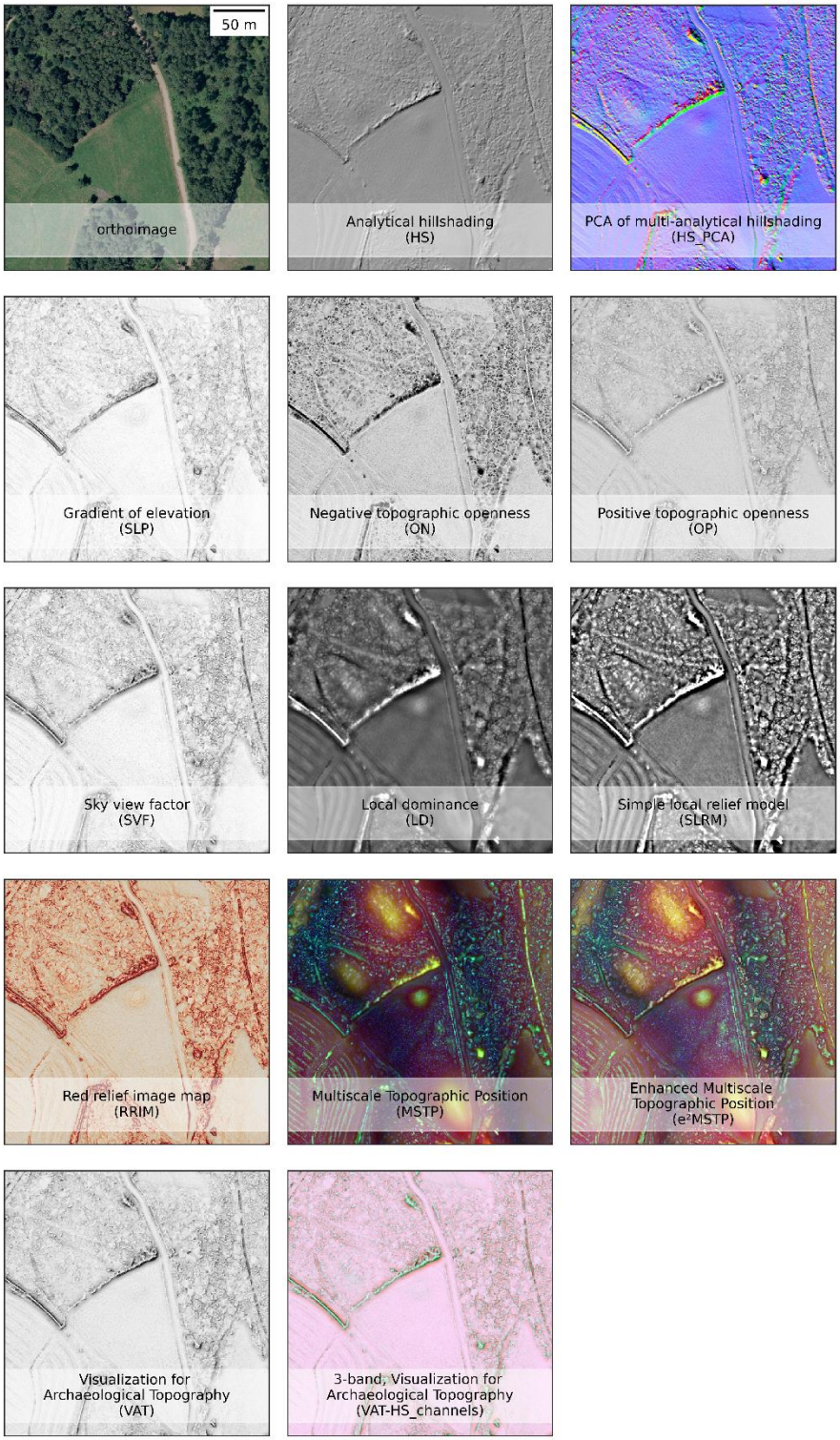

Figure 5.2. Visualization techniques applied to the Le Pusso area, Carnac (France). The area has a variety of landforms, including multiple archaeological structures.

5.2.3.1.a) Deep CNN for instance segmentation

The deep CNN was based on a Detectron2 framework (Wu et al., 2019) that implemented a Mask R-CNN architecture for instance segmentation (Figure 5.3). Mask R-CNN was chosen for its ability to perform instance segmentation by combining automatic detection and segmentation phases in sequential order. The benefit of instance segmentation for archaeological prospection is that besides automatic detection, predicted segments can be used for morphological or contextual characterization of the terrain anomalies identified.

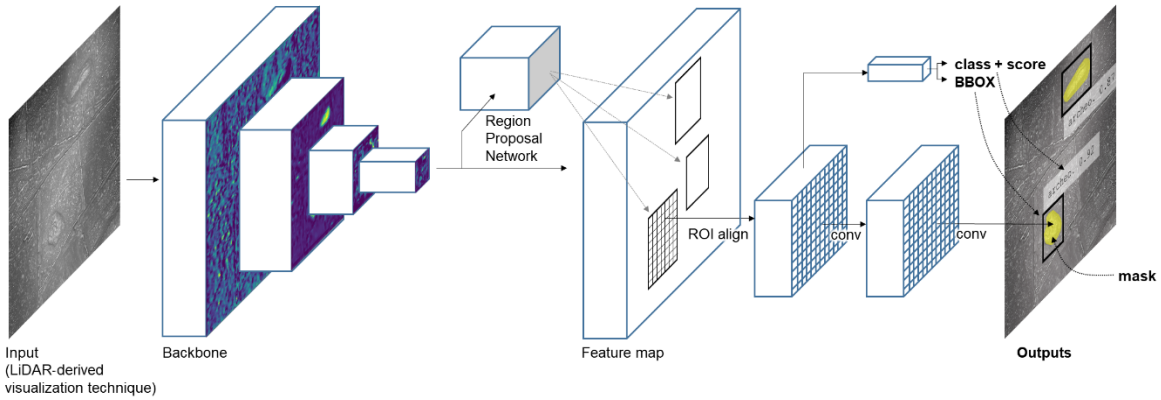

Figure 5.3. Architecture of Mask R-CNN for instance segmentation on visualization technique images

Detectron2 was configured to use a Resnet-101+FPN backbone, and training hyperparameters (Table 5.2) were predefined and remained static for all experiments.

For the transfer-learning strategy, weights of the network were initialized using a model pre-trained with a the Common Object in Context (COCO) dataset (Lin et al., 2014).

A Data augmentation technique was included in the training workflow with randomized flip, crop and rotation transformations

Table 5.2. Main hyperparameters used to train the deep convolution neural network

Hyperparameters	Value
Learning rate (LR)	BaseLR = 0.002; 100 warmup iterations then 0.1xBaseLR, 0.01xBaseLR, 0.001xBaseLR at 500, 1000 and 1500 iterations respectively
Total iterations	2000
Batch size	2
Epochs*	33 (for 120 images)
Anchors size	16, 32, 64, 128, 256, 512 px
Data augmentation	flip, crop and rotation transformations (50% probability)

*** Epochs = total iterations * batch size / total number of images**

5.2.3.1.b) Evaluation metric and cross-validation

Performances of the resulting segmentation were evaluated statistically using the Average Precision (AP) metric (Padilla et al., 2020) for an intersection over union (IoU) threshold of 0.5. This threshold value, commonly used in the literature, was justified in our study by the fuzzy nature and spatial uncertainty associated with the archaeological reference dataset (Guyot, Lennon, Lorho, et al., 2021). The metric, called AP@IoU0.5, refers to the area under the precision-recall curve.

Cross-validation was performed using a K-fold (K=5) strategy with a 80%/20% train/test split (120/30 images, respectively) to assess the performance stability of each VT (Rodriguez et al., 2010). Since model hyper-parameters were not tuned (only model parameters were fine-tuned), no model selection was performed. Therefore, a split between validation and test sets was not required.

Each VT (Figure 5.2, Figure 5.4) was visually interpreted by a human to empirically assess their performance for visual perception. The same VT configurations (visualization techniques and visualization parameters) were used as input for the deep CNN and as a basis for visual interpretation.

5.3 Results

5.3.1 VT assessment through human-based interpretation

Visually, multiscale VTs (MSTP, e²MSTP) had the best perception performances for archaeological sites with subtle positive topographic variations, regardless of their size or morphology. This result was especially evident for a levelled tumulus (example 1, Figure 5.4) whose remaining trace spreads over an area 80 m long and 50 m wide. The multiscale VTs were also, by design, the only ones that provided information about the wider topographical context (example 2, Figure 5.4), by highlighting the dominant position of the Neolithic funeral structures in the landscape. The combination of multiscale representation and local morphological information (e²MSTP) allowed for better interpretation of structured terrain; for example, terrain with pits, narrow ditches or embankments (example 2, Figure 4). Detrending techniques (LD and SLRM) were highly informative for small scale-terrain variations; however, their limits were apparent for the following geoarchaeological configurations: (1) small archaeological structures (smaller than the radius of analysis) within highly textured terrain (usually in undergrowth vegetation) and, (2) large archaeological structures (larger than the radius of analysis) considered to be the natural trend of the terrain and thus not enhanced. Terrain openness and its variants (OP, ON, SVF, RRIM) appeared to be effective for small archaeological structures, especially for small mounds (< 10 m radius) with a central pit; however, the lack of overall contextual information (such as multiscale topographic position) reduced the ability to interpret these structures. However, these

VTs were not visually informative for continuous and subtle variations that occur at a larger scale with the presence of leveled tumulus. This limitation was also observed for standard VTs, such as slope (SLP), hillshadings (HS and, to a lesser extent, HS_PCA) as well also for the combined visualization of archaeological topography (VAT and its 3-band variation VAT-HS_channels). VAT was designed to improve the recognition of small topographical features (Kokalj & Somrak, 2019). While it was informative for the visual description of small structures or local morphological characteristics, the results we obtained showed that it was not adapted for the visualization of larger subtle topographic variations or for specific topographic positions.

5.3.2 VT assessment through computer-based analysis

The AP@IoU0.5 performance results by VT (Figure 5.4) showed a minimum average of 24% (analytical hillshading to a maximum average of 65% (e^2MSTP), with per-fold individual performance extremes ranging from 19% (analytical hillshading, fold 4) to 76% (e^2MSTP, fold 5). Monochromatic VTs, such as HS (24%), OP (26%), SVF (28%) and ON (33%), had lower performances than other VTs and were thus considered less informative by the deep CNN model. VAT (the combined monochromatic VT) showed an average performance of 28%, which was higher than the performance of its components, except for SLP (38%). The VAT-HS_channels (a colored VT) showed a better average performance of 39%, confirming the value of multi-band information. However, monochromatic VTs based on terrain detrending such as SLRM (42%) and LD (48%) had higher performances than VAT_HS_channels and other colored VTs such as HS_PCA (34%), based on virtual illumination, or RRIM (41%), based on morphological representation. However, monochromatic VTs based on terrain detrending such as SLRM (42%) and LD (48%) had higher performances than VAT_HS_channels and other colored VTs such as HS_PCA (34%), based on virtual illumination, or RRIM (41%), based on morphological representation. Only the multiscale approaches, MSTP (58%) and e^2MSTP (65%), obtained performances that exceeded 50%. The e^2MSTP, based on a combination of multiscale information with morphological (RRIM) and local detrending (SLRM) representations, was an improvement over the standard MSTP version (+7%).

The statistical performance of deep CNN obtained using different VTs enabled the VTs to be ranked by the mean AP@IoU.5 value (Figure 5.4). This metric-based ranking was similar to the subjective human-based assessment presented in 3.1, thus confirming the initial assumption that visual representation of data, effective from the perspective of human vision, is also effective from the perspective of deep CNNs.

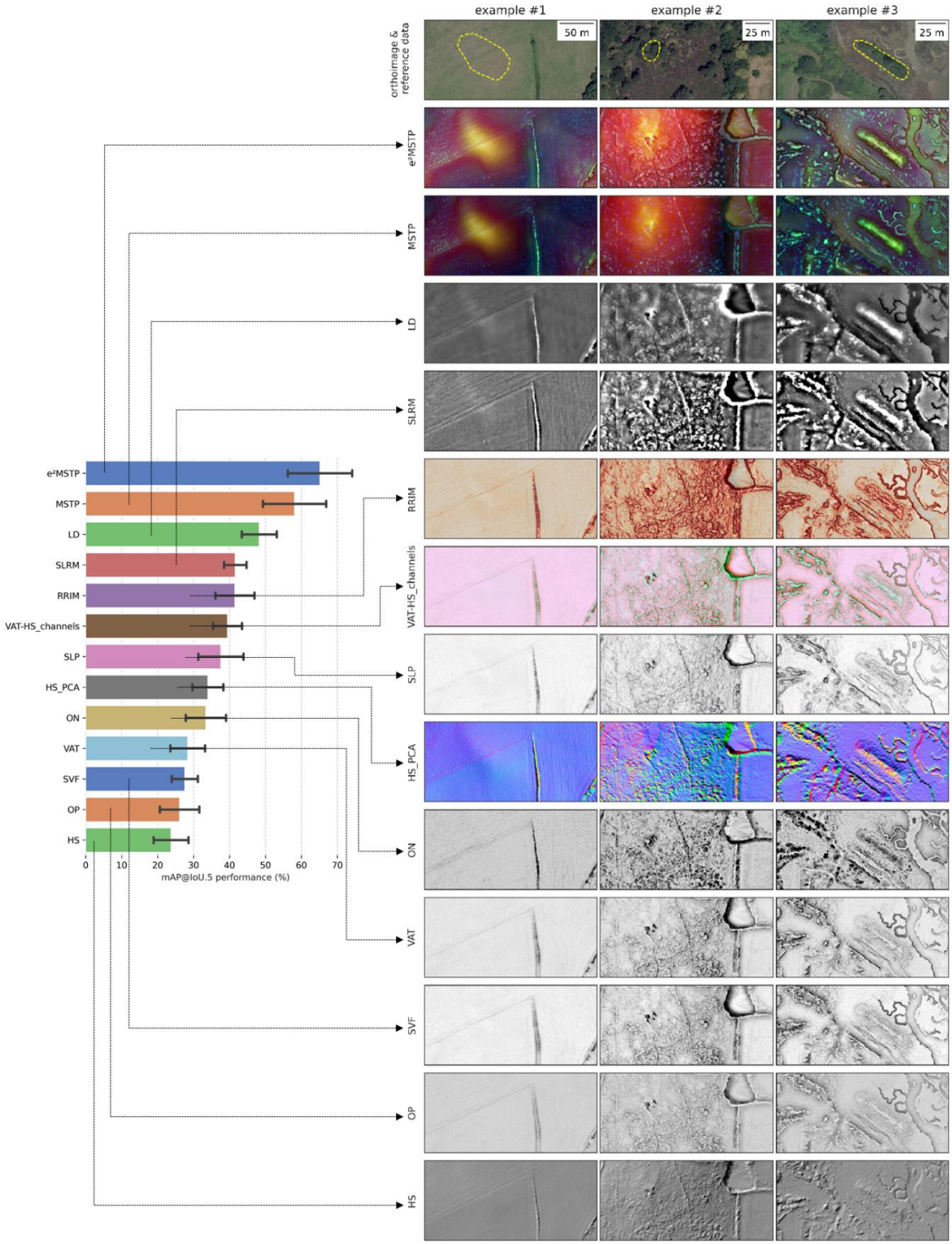

Figure 5.4. Performances of detection/segmentation using deep convolution neural network (CNN) for different visualization techniques (VTs). Visual examples of VTs with (right) the reference data and (left) mean deep CNN model performances (mAP@IoU.5) of each VT. Error bars indicate 1 standard deviation. Example 1 is a leveled Neolithic tumulus in an agricultural field. Example 2 is a megalithic complex of 3

dolmens under dense vegetation. Example 3 is a Neolithic tumulus of elongated shape in a marshland area.

5.4 Discussion

5.4.1 Towards an objective creation of suitable VTs

The best-performing VT was the e²MSTP generated using multiscale topographic analysis (MSTP) combined (via a blending technique) with a morphologically explicit image (RRIM) and a slope-invariant relief-detrending technique (SLRM). This VT was created based on empirical knowledge and iterative selection of parameters that enhance the perception of ALS-derived terrain data for archaeological prospection. The computer-vision approach shows the suitability of such VTs for identifying archaeological structures on ALS-derived terrain models in the study area. In particular, it highlights the utility of using a multiscale approach that provides contextual topographic position information and is more robust for varying structure size (Guyot et al., 2018). It also confirms the advantage of combining complementary VTs to address identified limitations of single VTs (e.g. blending morphological and detrended information with multiscale information). Nevertheless, evaluating the complementarity of VTs and selecting the optimal blending strategies to emphasis this complementarity remains a challenge. This was illustrated by the results we obtained using VAT and VAT-HS_channels. As expected, VAT showed lower performance than its 3-band variant VAT-HS_channels that is in accordance with the results of (Somrak et al., 2020) who compared these two VTs for image classification task. However, VAT-HS_channels, which was produced without blending but by simple stacking of SLP, OP and SVF, showed lower performance than SLP used as a single VT. This could be due to the visual correlation between SLP, OP and SVF. A simple stacking of correlated VTs does not necessarily generate a better performing combined image.

While evaluating all possible VT combinations was out of the scope of this study, the proposed approach could open new perspectives in the objective selection of the most suitable VT or blending parameters as the remote sensing archaeological or geomorphological community develops new ALS-derived terrain model visualizations.

5.4.2 Generalization of the benchmarking approach

The deep CNN was trained on a limited typology of archaeological remains (mostly funeral structures from the Neolithic) and within a limited geographical area. A similar approach applied to different contexts would not necessarily provide the same performances from a deep CNN perspective. It would require new training and evaluation, which may not result in the same ranking of VTs, especially if structures or landforms differ from those in our study area. However,

the approach is expected to maintain the relation between the degree of visual perception from VTs and the ability to perform segmentation automatically using Deep CNN.

This deep-CNN-based benchmarking approach has not yet been developed for diverse geographical and archaeological environments. While the available coverage of ALS data is rapidly growing (due to a decrease in the cost of acquisition and an increase in the number of open-access ALS projects supported by public funding), the availability of archaeological reference datasets remains a key issue. The collection, publication and maintenance of labelled archaeological data is not straightforward. Available inventories (e.g. the "*Carte Archéologique Nationale*" in France) are gradually addressing this issue, but the limits of large-scale archaeological references persist: many sites remain to be discovered, and for many of them, the nature and spatial extent of the archaeological structures could, paradoxically, be confirmed only by destructive archaeological excavation. The "ground truth", which serves as an essential base for all supervised remote sensing classification or detection approaches, would remain wishful thinking in the archaeological prospection domain. Thus, New paradigms based on fuzzy or partial reference datasets need to be developed.

5.4.3 Computer vision as a support for human interpretation

This study is based on the initial assumption that the deep CNN-based and human-based processes involved in image interpretation share some similarities (Brachmann et al., 2017; Geirhos et al., 2018; J. Kim et al., 2019; R. Zhang et al., 2018). The results confirmed this assumption by showing comparable VT rankings between the computer-based and human-based interpretation. In both cases, the detection performance is related to the ability of a VT to enrich the original data representation with interpretable information. However, the image data is not the only information that influence human-based interpretation.

An expert-based interpretation would include perceptions of the information included in the image, but also external information not available in the data itself (geoarchaeological knowledge of the area or skills based on experience). The computer-vison approach applied to an image cannot encompass the exhaustive aspects that influence archaeological interpretation. Therefore, the proposed approach does not aim at replacing expert-knowledge or imposing a single VT for archaeological interpretation of ALS-derived terrain model, but rather aim at proposing a significant support tool for archaeological analysis. With a high capacity of data processing, a consistent response against similar data and an interpretation bias (even if not entirely absent) that can be measured, the deep CNN approach provides a complementary tool for the identification and characterization of archaeological structures from ALS-derived relief model.

5.5 Conclusion

In this study, we demonstrated the potential of the deep CNN approach as a tool to objectively assess the utility of ALS-derived VTs in the context of archaeological prospection. We used a state-

Guyot, Alexandre. Contribution of airborne LiDAR and hyperspectral data to archaeological mapping in terrestrial and submerged environments. 2021

of-the-art open-source instance-segmentation framework to compare the performances of automatic detection and segmentation of deep CNN models with 11 different VTs used as input data. The results allowed to rank VTs by their performance from an automatic detection and segmentation point of view. This computer-based ranking was compared to a subjective human-based interpretation. Ranking outcomes were comparable and thus confirmed the assumption that the deep CNN perception was similar to the subjective perception of human-based visual interpretation. Based on this confirmation, we showed that deep CNN computer vision approach could be used to objectively assess the ability of VTs ability to enhance the perception of archaeological structures. Although the study was conducted in a limited geoarchaeological context, the approach is expected to be reproducible on different areas and different types of structures or landforms, especially because it is based on relative evaluation of the selected VTs. Moreover, by relying on a non-subjective benchmarking method, the approach developed could help design new or hybrid VTs that could be used to improve the human-based interpretation, or as inputs to the CNN for further automatic extraction tasks on large datasets.

Summary of Part II

In this part, we addressed some important concerns highlighted in the first part of the thesis, particularly on visualization techniques and (semi-)automatic detection based on LiDAR-derived terrain data in archaeological context.

More specifically, in chapter 4, we have shown that the limitation of current (semi-)automatic approaches designed for object localization, which is that they do not allow for further data-driven structure characterization of structures could be addressed by the development of deep CNN instance segmentation approaches.

Moreover, we have confirmed that such approaches can be implemented by considering the constraints (such as sparsity and ill-defined typology) affecting archaeological data. The sparse availability of sample data was for example addressed by using transfer-learning strategy adapted to the input visualization technique. The complexity or ill-defined typology was addressed by implementing a one-class strategy, which eventually appears to be conceptually in phase with the complex archaeological uncertainty only related to information of surface. Indirectly, this chapter also highlighted the importance of visualization techniques and notably the use of multiscale topographic analysis in combination with local morphological representation, first for orienting the archaeological prospection and field verifications, second to support the characterization of structures by extracting data-derived information via object segmentation at the object-level rather than the pixel-level.

In chapter 5, as a continuation of the previous chapter, we upturned the use of deep CNN segmentation approach, this time not to directly evaluate its performance for archaeological prospection (this was the purpose of chapter 4), but to provide an objective mean of comparing different VTs and their effectiveness in enhancing the perception of archaeological structures. In this experiment, the relative score of segmentation was used as benchmark tool to rank multiple VTs. The computer-based ranking appeared to be comparable to the subjective human-based ranking, and thus provided some interesting perspectives in the development and evaluation of efficient VTs and the convergence of human-based and computer-based perception for remote sensing archaeology.

The results of these studies, which demonstrate the value of combining LiDAR-terrain derived visualization techniques and computer-vision approach, should however not mask the limitations and remaining concerns regarding their wider application in operational context. These limitations include the dependence to the derived terrain model, and in our case the implicit exclusion of some above-ground archaeological features of interest such as standing stones or steles when considering under-canopy environments. They also include concerns on the bias related to a particular geo-archaeological context, and finally also encompass the difficulty in

Guyot, Alexandre. Contribution of airborne LiDAR and hyperspectral data to archaeological mapping in terrestrial and submerged environments. 2021

defining a conceptual framework or ontology shared amongst archaeologist and remote sensing specialists.

A number of perspectives stem from these first experiments and results, which are discussed in general conclusion.

Guyot, Alexandre. Contribution of airborne LiDAR and hyperspectral data to archaeological mapping in terrestrial and submerged environments. 2021

PART III. AIRBORNE HYPERSPECTRAL IMAGERY FOR MAPPING ARCHAEOLOGICAL STRUCTURES IN SUBMERGED ENVIRONMENTS

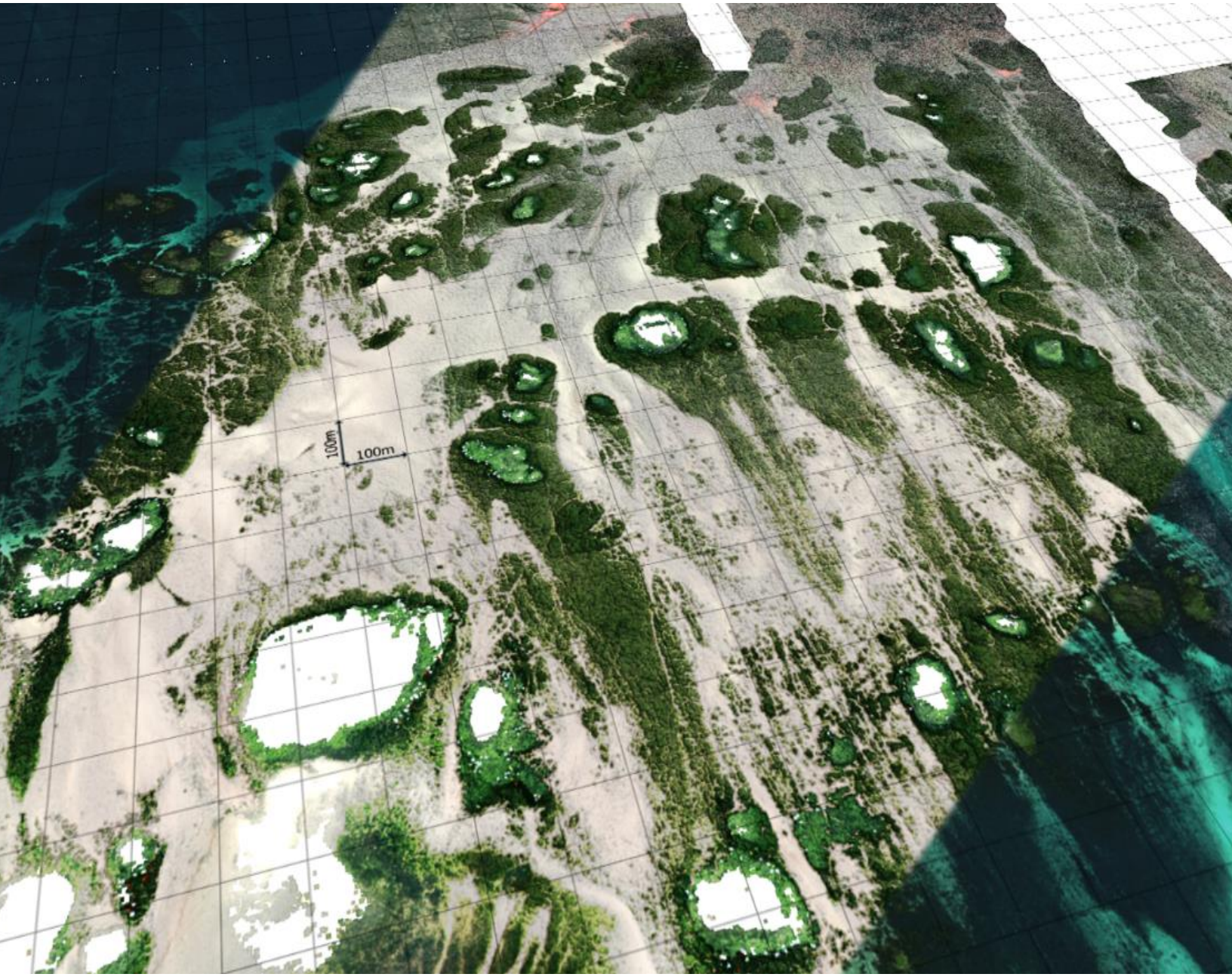

Introduction to Part III

The third part of this manuscript presents an evaluation of airborne hyperspectral data for archaeological mapping in submerged context. The evaluation was carried out using hyperspectral VNIR imagery covering the megalithic site of Er Lannic located in the study site of Carnac and Gulf of Morbihan, and the study site of the Molène archipelago. This part is developed in two complementary chapters.

In Chapter 6, the objective is to assess the use of airborne hyperspectral imagery, as a first attempt to visualize and map submerged archaeological structures in shallow waters. The main questions addressed in the chapter are: (i) Can submerged archaeological structures be identified using AHI? (ii) How can they be detected automatically and characterized spatially and spectrally?

Chapter 7 is a complementary study that aims at enlarging the application scope of airborne hyperspectral imagery not only for the documentation of existing submerged archaeological structures, but also for large-scale archaeological prospection in coastal shallow water environments. The main questions addressed in the chapter are: (i) Similarly to the previous chapter, can submerged archaeological structures be identified using AHI? With this second case study, we implicitly pose the question in a different geo-archaeological context (ii) Can AHI be used not only to map known structures but also to support large-scale prospection? (iii) And more generally, can AHI be used to visualize large-scale submerged landscape?

Chapter 6. AIRBORNE HYPERSPECTRAL IMAGING FOR SUBMERGED ARCHAEOLOGICAL MAPPING IN SHALLOW WATER ENVIRONMENTS

This chapter is entirely reproduced from the peer-reviewed article published during the thesis in *Remote Sensing*, which was integrated in the special issue *Archaeological Remote Sensing in the 21st Century: (Re)Defining Practice and Theory* (D. Cowley et al., 2021).

> Guyot, A., Lennon, M., Thomas, N., Gueguen, S., Petit, T., Lorho, T., Cassen, S., & Hubert-Moy, L. (2019). Airborne Hyperspectral Imaging for Submerged Archaeological Mapping in Shallow Water Environments. *Remote Sensing*, 11(19), 2237. https://doi.org/10.3390/rs11192237

remote sensing

MDPI

Article

Airborne hyperspectral imaging for submerged archaeological mapping in shallow water environments

Alexandre Guyot [1,2,*], Marc Lennon [2], Nicolas Thomas [2], Simon Gueguen [2], Tristan Petit [2], Thierry Lorho [3], Serge Cassen [4] and Laurence Hubert-Moy [1]

1. Laboratoire LETG - UMR 6554, Université Rennes 2, Place du recteur Henri Le Moal, 35043, Rennes, France
2. Hytech-Imaging, 115 Rue Claude Chappe, 29280, Plouzané, France
3. DRAC Bretagne, Service régional de l'archéologie, Avenue Charles Foulon, 35700, Rennes, France
4. Laboratoire LARA - UMR6566, Université de Nantes, Chemin la Censive du Tertre, 44312, Nantes, France

* Correspondence: alexandre.guyot@univ-rennes2.fr

Received: 23 August 2019; Accepted: 23 September 2019; Published: 25 September 2019

Abstract: Nearshore areas around the world contain a wide variety of archeological structures, including prehistoric remains submerged by sea level rise during the Holocene glacial retreat. While natural processes, such as erosion, rising sea level, and exceptional climatic events have always threatened the integrity of this submerged cultural heritage, the importance of protecting them is becoming increasingly critical with the expanding effects of global climate change and human activities. Aerial archaeology, as a non-invasive technique, contributes greatly to documentation of archaeological remains. In an underwater context, the difficulty of crossing the water column to reach the bottom and its potential archaeological information usually requires active remote sensing technologies such as airborne LiDAR bathymetry or ship-borne acoustic soundings. More recently, airborne hyperspectral passive sensors have shown potential for

accessing water-bottom information in shallow water environments. While hyperspectral imagery has been assessed in terrestrial continental archaeological contexts, this study brings new perspectives for documenting submerged archaeological structures using airborne hyperspectral remote sensing. Airborne hyperspectral data were recorded in the Visible Near Infra-Red (VNIR) spectral range (400–1000 nm) over the submerged megalithic site of Er Lannic (Morbihan, France). The method used to process these data included (i) visualization of submerged anomalous features using a minimum noise fraction transform, (ii) automatic detection of these features using Isolation Forest and the Reed–Xiaoli detector and (iii) morphological and spectral analysis of archaeological structures from water-depth and water-bottom reflectance derived from the inversion of a radiative transfer model of the water column. The results, compared to archaeological reference data collected from in-situ archaeological surveys, showed for the first time the potential of airborne hyperspectral imagery for archaeological mapping in complex shallow water environments.

6.1 Introduction

Whether of natural (e.g., erosion, rising sea level and exceptional climatic events) or human (e.g., urbanization, agriculture, and pollution) origin, threats to archaeological heritage are increasingly significant (Daire et al., 2012; Reeder-Myers, 2015). Documenting and monitoring archaeological sites is consequently increasingly becoming a crucial aspect of conserving cultural heritage. In an underwater context, documenting archaeological remains requires mapping seabed details to interpret various forms of past human traces (Costa, 2019; Guzinski et al., 2016; Singh et al., 2000). While much underwater archaeological research has been oriented to shipwrecks (Costa, 2019; Ruppe & Barstad, 2013; Westley et al., 2019), nearshore areas contain a wide variety of ancient structures, including prehistoric remains submerged by the sea rise initiated 15,000 years ago by the Holocene glacial retreat. On a global scale, the now-submerged landscapes that were once attractive terrestrial habitats for prehistoric human occupation are estimated to cover ca. 20 million km^2 (Harff et al., 2016).

In the last few decades, active remote sensing methods have successfully detected and recorded submerged archaeological sites in deep and shallow water. From the water surface, multibeam echo sounders (MBES) installed on hydrographic vessels or USV (unmanned surface vehicles) are used for archaeological applications. Despite high costs of operation and relatively low spatial coverage per time unit, MBES remain the preferred solution for seabed prospection, especially in deep water (Plets et al., 2011). In coastal shallow waters, however, rock outcrops and rough sea conditions can reduce the potential area of operation due to safety issues, and multipath acoustic propagation interference also decreases the quality of acoustic measurements (Xu & Xu, 2017). More recently, underwater hyperspectral imagers have also shown considerable potential for underwater archaeological surveys (Ødegård et al., 2018); however, their use is limited to in-situ observations and low spatial coverage. Airborne LiDAR bathymetry (ALB) has gained great

interest for underwater archaeological mapping (M. Doneus et al., 2013, 2015; Shih et al., 2014). When operated in topo-bathy mode, it can cover the intertidal zone and provide seamless representation of terrestrial and submerged topography. ALB has drawbacks, however, including relatively high deployment costs and difficulty in retrieving reliable depth measurements in very shallow water (Bachmann et al., 2009; Yang et al., 2007).

In comparison, passive remote sensing data, such as multispectral or hyperspectral airborne and spatial imagery, have so far focused almost exclusively on terrestrial archaeological contexts. Airborne hyperspectral instruments measure, for a large number of pixels (millions) and wavelengths (tens to hundreds), the radiation (spectral radiance) received at the sensor. The data they collect are generally presented in the form of a data cube (2 spatial dimensions × 1 spectral dimension). Depending on sensor characteristics, the spectral dimension covers specific wavelength ranges, such as the Visible Near Infra-Red (VNIR) range, corresponding to wavelengths of 400–1000 nm. Due to its ability to acquire highly detailed spectral information, airborne hyperspectral imagery (AHI) has been used for various types of earth observation: land-cover/land-use mapping (Adam et al., 2010; Roessner et al., 2001), target detection (D. Manolakis et al., 2003), geology (van der Meer et al., 2012) and coastal mapping (Dekker et al., 2011). For archaeological applications, airborne hyperspectral data have been greatly valuable for terrestrial mapping (Aqdus et al., 2012; Cavalli et al., 2013, 2007; Cerra et al., 2018; M. Doneus et al., 2014; Emmolo et al., 2004; Savage et al., 2012; Traviglia, 2006a, 2006b; G. J. Verhoeven, 2017), but to our knowledge, no studies have yet assessed AHI in a submerged context. Using it for underwater mapping requires addressing challenges related to the complexity of (i) the data (including high dimensionality and signal-to-noise ratio), (ii) the object of study (degraded and partially documented structures) and (iii) the environment, especially the complex light-matter interactions in water, affected by multiple environmental factors such as water constituents, surface conditions and benthic composition.

Thus, the aim of this study was to evaluate the potential of AHI for detecting and documenting submerged sites in coastal archeology. The questions addressed are (a) can submerged archaeological structures be visible using AHI? (b) Can they be detected automatically? (c) Can they be characterized spatially and spectrally?

6.2 Materials and Methods

6.2.1 Study Area

The Gulf of Morbihan (France) has one of the most important architectural heritages of megaliths in the world. Due to their density and exceptional character, these Neolithic monuments, built from the 5th to 3rd millennia BC, are candidates for the UNESCO World Heritage List. One of the most emblematic sites in this region is the islet of Er Lannic and its two semicircular stone monuments.

The islet of Er Lannic, 80 ha in size, lies between the island of Gavrinis (with an imposing tumulus and abundant Neolithic engravings), 300 m to the north, and the Point of Penbert, on the Rhuys peninsula, 500 m to the south (Figure 6.1). The islet borders the main channel of the Gulf of Morbihan, which has one of the strongest tidal currents in Europe.

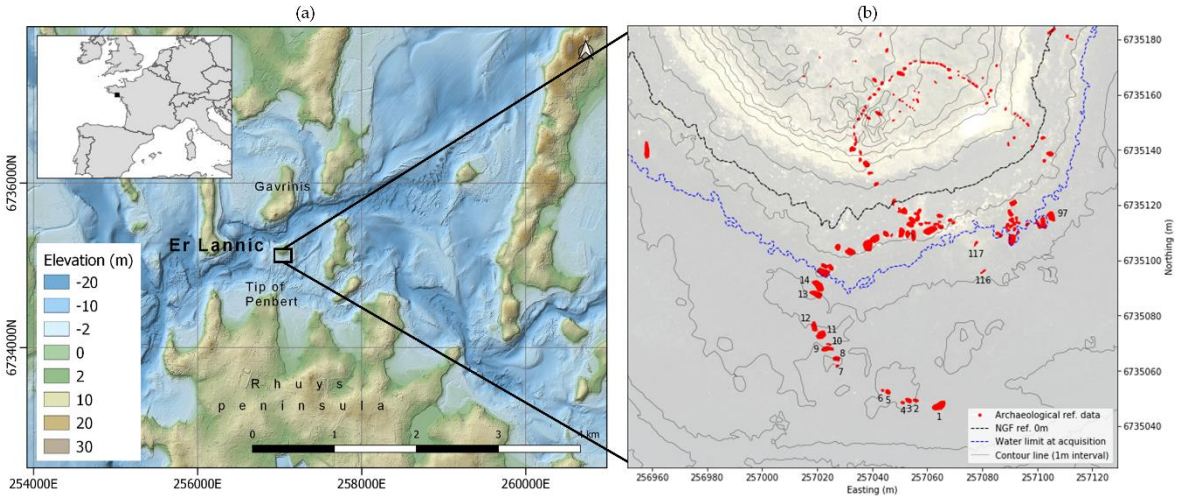

*Figure 6.1. (**a**) Location of the study area (Er Lannic islet, Morbihan, France), (**b**) the archaeological reference data (submerged steles are numbered).*

The two semicircular stone monuments, each 50–60 m wide, are located on the southern end of Er Lannic. After its construction by Neolithic humans, the site was submerged due to the rise in sea level during the post-glacial marine transgression (Baltzer et al., 2015). The coastline of the Gulf of Morbihan is estimated to have been ca. 5 m below the current sea level during the Neolithic period (Baltzer et al., 2015). The megalithic site of Er Lannic (Figure 6.2) was first mentioned in 1866 by archaeologist G. de Closmadeuc (de Closmadeuc, 1867). Initially, only the terrestrial part of the monument was discovered and identified as a complete stone circle. The submerged structures were then revealed to archaeologists several years later by an extremely low tide. The first site map, depicting two adjacent stone circles, was drawn in 1882 (de Closmadeuc, 1882). Since then, several archaeological operations have been performed on site to complement and improve the site map. However, the strong tidal current and rock outcrops at the sea surface complicate surveys of the subtidal rocky platform, preventing any MBES surveys by boat. Despite the scientific interest of the site, few underwater measurements have been taken. The most recent documented underwater surveys were performed in the early 1990s (Gouezin, 1991) using traditional topographic techniques with a theodolite and a leveling rod, the latter being held in shallow water by divers during each measurement.

Figure 6.2. Megalithic monument of Er Lannic.

6.2.2 Airborne Hyperspectral Data

The study was based on AHI acquired by Hytech Imaging (Plouzané, France) with a NEO HySpex VNIR-1600 push broom sensor (Table 6.1). The sensor was coupled with an IMAR iTrace-RT-F200 system and an OmniSTAR L1/L2 GNSS antenna to measure position and orientation.

Table 6.1. Characteristics of the HySpex Visible Near Infra-Red (VNIR)-1600 sensor.

Spectral range	Spatial pixels	Spectral resolution	Spectral sampling	Number of bands	FOV across track	Pixel FOV across/along track	Coding
0.4–1.0 µm	1600	4.5 FWHM	3.7 nm	160	17°	0.18 mrad/ 0.36 mrad	12 bits

The aerial survey was performed on 14 September 2018 at an altitude of ca. 1200 m to obtain a ground sampling distance of 50 cm (Table 6.2).

Table 6.2. Parameters of the aerial survey.

Flight altitude	Ground sampling distance	Swath	Integration time	Viewing angle	Solar zenith angle
1200 m	50 cm	352 m	10.1 ms	16.75°	16.75°

During the survey, images were collected in clear sky and calm sea conditions (preconditions to reduce sun-glint effects and solar irradiance variation). Er Lannic was overflown at 13:00 UTC, corresponding to low-tide conditions (tide coefficient of 85).

6.2.3 Bathymetric Reference Data

The reference bathymetric data used for this study are based on the Litto3D project (Litto3D, 2019; Pastol, 2011) of the French Naval Hydrographic and Oceanographic Office (Shom) and the French

National Geographic Institute (IGN). This project produced a seamless, high-resolution topographic and bathymetric model of French coastal areas using multiple survey techniques (Topographic LiDAR, ALB, MBES). For the Gulf of Morbihan, the Litto3D data consist of three complementary, locally overlapping surveys:

- ALB (SHOALS-1000T) by Shom (2005):
    - Topographic and bathymetric modes: spot spacing 2 and 5 m, altitude 900 and 400 m, absolute planimetric accuracy < 1.5 and < 2.8 m, and absolute vertical accuracy < 0.3 and < 0.5 m, respectively
- MBES by Shom (2003) and IFREMER (2013)

Shom/IGN provided the data as a merged 3D point cloud with source identifiers (Figure 6.3a). Each point is defined as XYZ coordinates in Lambert93 system using the RGF93 geodetic system (EPSG: 2154) and NGF/IGN69 height reference for elevation. The merged point cloud was converted to a raster of 1 m resolution using Triangulated Irregular Networks interpolation (Figure 6.3b).

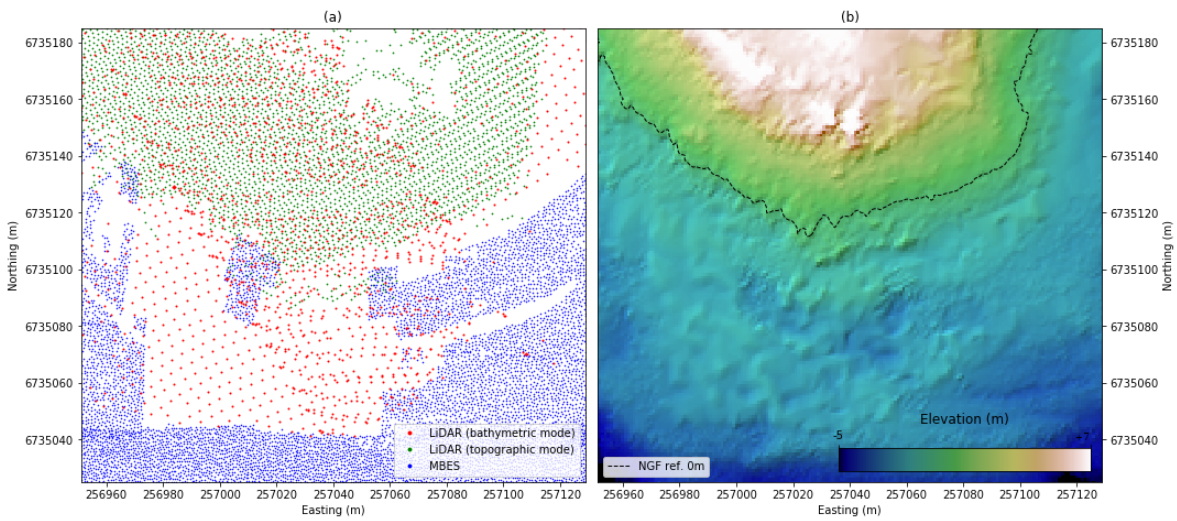

*Figure 6.3. Litto3D bathymetric reference data (**a**) point cloud and (**b**) 1 m resolution raster.*

6.2.4 Archaeological Reference Data

Archaeological reference data for this study came from a georeferenced 2D map (Figure 6.1b) of each stone (or stele) of the site recorded by archaeologists from 1990-2018 (Cassen et al., 2018; Cassen, Grimaud, et al., 2019; Cassen, Grimault, et al., 2019). The Regional Archaeological Service of Brittany (DRAC/SRA) currently uses this map. The map is projected in the Lambert93 system using the RGF93 geodetic system (EPSG: 2154).

Spatially, the northernmost semicircular stone monument, composed of ca. 60 steles—collapsed or erect—is entirely visible at lowest astronomical tide. The second semicircular stone monument,

composed of 29 steles, is submerged and sits on the shore platform 2-3 m below mean sea level. Additional steles are also present at the junction of the semicircles, near a granite outcrop north of the second semicircle, and at isolated points away from the semicircles. The steles, most of them metamorphic orthogneiss, vary in projected horizontal area from < 0.5-11 m².

For identification purposes, steles are numbered from 1-201 (Cassen et al., 2018) (i.e., $Stl_{\#1}$ to $Stl_{\#201}$). Based on the tide and sea conditions when the images were acquired, 17 steles ($Stl_{\#1}$ to $Stl_{\#14}$, $Stl_{\#97}$, $Stl_{\#116}$ and $Stl_{\#117}$) were located beyond the shoreline, of which 15 were completely submerged and 2 ($Stl_{\#1}$ and $Stl_{\#14}$) were partially submerged.

6.2.5 Dimensionality Reduction and Visualization

Dimensionality reduction techniques concentrate information by projecting the original data, with high dimensionality, into a lower dimensional space. Its objective is to decrease computational burden (i.e., reduce the number of bands), remove spectrally redundant information or noise and highlight informative spectral variation in the imagery. For remote sensing hyperspectral data, for which interband correlation is high and noise omnipresent, dimensionality reduction algorithms are used to enhance visual interpretation or as pre-processing before other procedures, such as classification (Traviglia, 2006b). These algorithms include Principal Component Analysis (PCA) and Minimum Noise Fraction (MNF) (Green et al., 1988). PCA projects data into a new subspace where the projected components maximize the variance of the data under the constraint that each component is orthogonal to its preceding component. PCA can thus reduce dimensionality of the data while conserving the maximum amount of information. When applied to hyperspectral imagery, however, PCA is not the most suitable method, notably because of its limitation with noisy observations. MNF is a linear transformation based on two sequential PCA rotations. The first rotation decorrelates and scales the noise using a noise covariance matrix calculated by estimating local noise using the difference between adjacent pixels. The result is a hyperspectral data cube in which noise has unit variance and no band-to-band correlation (white noise). The second rotation performs a PCA on the noise-whitened data cube to separate noise from data and thus maximize the signal-to-noise ratio (SNR).

6.2.6 Unsupervised Anomaly Detection

In the machine learning field, unsupervised learning is the task of identifying structures or relationships in the input data without prior knowledge by mean of reference or labelled data. Since submerged archaeological structures might be undescribed in nature, degraded or covered (with sediments, vegetation or biofilm), archaeological prospection using remote sensing data usually seeks anomalies rather than looking for known signatures (Aqdus et al., 2012; Traviglia, 2006a) . Unsupervised anomaly-detection techniques are adapted to these conditions, since they require no predefined target characteristics and try to separate common observations from unusual observations. Doing the latter requires two main assumptions: anomalies are (i) spectrally different from the surrounding background and (2) represent a minority of pixels in an

image (low occurrence). Existing unsupervised anomaly-detection algorithms include the Reed–Xiaoli detector (RXD) and associated variants, and the Isolation Forest (IF) algorithm.

RXD, developed by Reed & Yu (1990), is based on a statistical distance (Mahalanobis distance) calculated between the observation (a pixel) and the image background. Global RXD relies on a pre-calculated background at the image level, while local RXD (LRXD) is based on a local background estimated using a sliding window that can have inner and outer sizes to adapt to specific anomaly sizes.

IF, developed by Liu et al. (2008), is based on the widely used Random Forest classification algorithm. IF combines multiple weak decision trees to calculate an anomaly score that reflects how much an observation differs from other observations. Each tree is created recursively by randomly selecting a feature and an associated random threshold value. Each observation is passed through the tree and compared to each node (feature and threshold) until it can be isolated from other observations (reaching an external node). The shorter an observation's path in the tree, the higher is its anomaly score. The final anomaly score equals the mean score of all trees.

6.2.7 Radiative Transfer Model over Shallow Water

Over optically shallow water (inland or coastal waters whose bottom is visible from the surface), total radiance measured by the remote sensor includes contributions from the atmosphere, the water surface, the water column and the water bottom. Hyperspectral remote sensing uses this radiative relationship to characterize the water column and water bottom physically. The radiative transfer model of Lee (Z. Lee et al., 1999) calculates subsurface remote sensing reflectance R_{rs}^{-} as:

$$R_{rs}^{-} = R_{rs}^{\infty}\left(1 - A_1 e^{-(K_d + k_{uW})Z}\right) + A_2 R_{rs}^{B} e^{-(K_d + k_{uB})Z} \qquad \text{(eq. 6.1)}$$

where R_{rs}^{∞} is the remote sensing reflectance for optically deep water; K_d, k_{uW}, k_{uB} are diffuse coefficients related to downwelling irradiance, upwelling radiance of the water column, and upwelling radiance from bottom reflection, respectively; A_1 and A_2 are constants; R_{rs}^{B} is the bottom reflectance and Z is the bottom depth.

Equation 1 verifies that for $Z \to \infty$, $R_{rs}^{-} \to R_{rs}^{\infty}$, and for $Z \to 0$, $R_{rs}^{-} \to R_{rs}^{B}$. This semi-analytical model is then inversed to retrieve the parameters (including R_{rs}^{B} and Z) that minimize the difference between the observed and modeled spectra (Sicot et al., 2015).

This radiative-transfer–based method, unlike empirical approaches, has the advantage of not requiring prior bathymetric data (existing elevation model or in-situ measurements) for the inversion process and derivation of bottom depth (Dekker et al., 2011).

6.3 Methodology

6.3.1 Workflow

The methodology developed and the associated workflow (Figure 6.4) were organized in subsections corresponding to the research questions of this study.

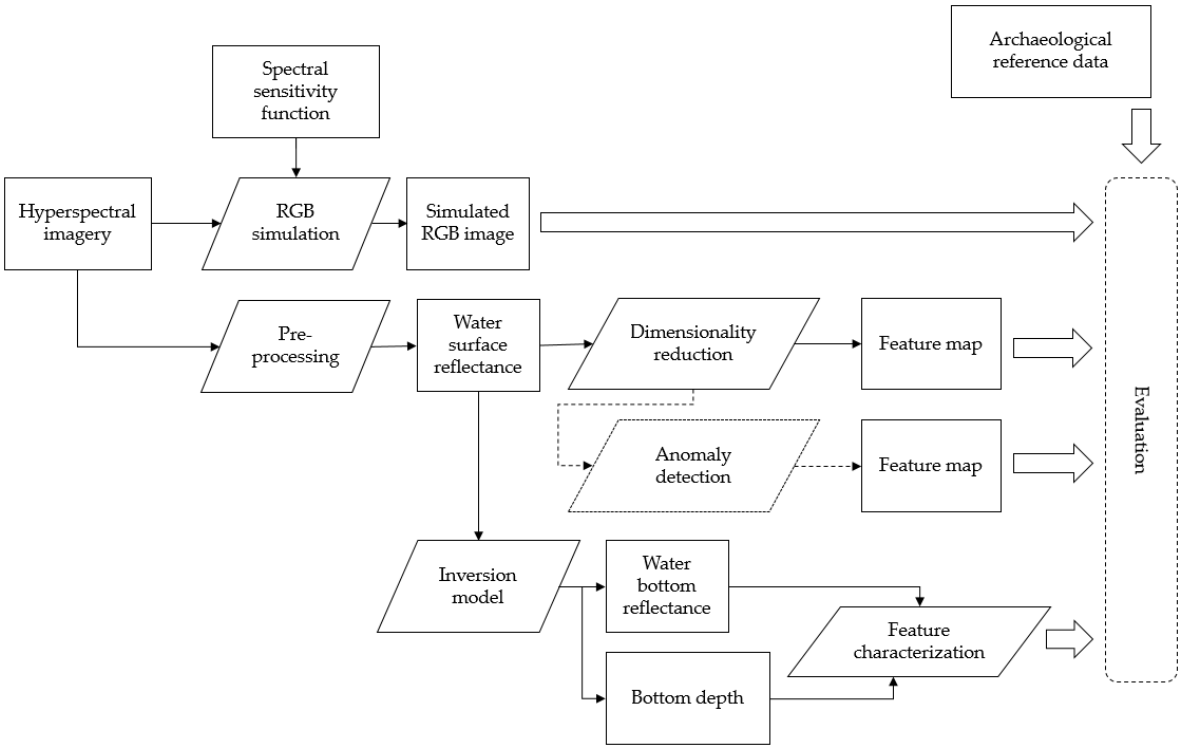

Figure 6.4. Diagram of the method developed.

6.3.2 Pre-processing

The hyperspectral images were processed from level 0 (raw) to level1b (radiometrically and geometrically calibrated) using the HYPIP (HYPperspectral Image Preprocessing) chain of Hytech-imaging that includes ATCOR/PARGE software applications (ReSe Applications, Wil, Switzerland) to obtain georeferenced images in spectral radiance ($W.m^{-2}.sr^{-1}.\mu m^{-1}$). Surface reflectance was then obtained by performing atmospheric corrections in a two-step process: (i) atmospheric corrections using ATCOR-4 software and (ii) empirical adjustment of each spectrum by applying coefficients (gain and bias) calculated per spectral band by linear regression between surface reflectance data and the reflectance signature of pre-calibrated targets (tarps) positioned near the area of interest and overflown during the survey. The resulting hyperspectral products (at-sensor radiance, surface reflectance) were then spatially subset to a 2048 px × 2048 px tile (representing an area of ca. 1 km²), encompassing the area of interest of Er Lannic islet.

6.3.3 Simulation of True-color Image

The initial hypothesis of the study was that VNIR AHI carries information valuable for visualizing submerged archaeological structures. To evaluate the contribution of hyperspectral data compared to that of traditional true-color photography, a red-green-blue (RGB) image was simulated using the spectra sensitivity response (Figure 6.5) of a digital single-lens reflex camera (DSLR Canon EOS 10D) and the hyperspectral cube.

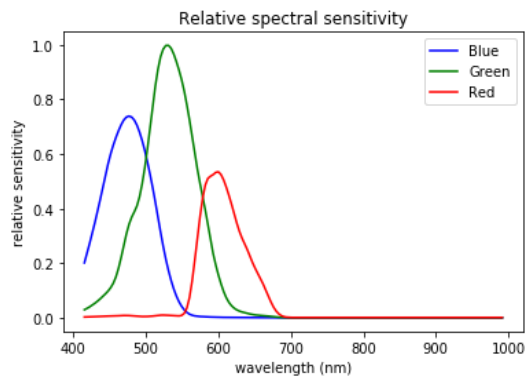

Figure 6.5. Relative spectral sensitivity function of a Canon 10D digital single-lens reflex camera used to simulate a true-color red-green-blue (RGB) image from the hyperspectral imagery.

Red, green and blue bands of the simulated image were produced by convolution products (Equations 6.2, 6.3 and 6.4, respectively):

$$Red_{sim} = \sum_{\lambda 400}^{\lambda 700} RSS_r(\lambda) * L(\lambda)^s_{tot.} \quad \text{(eq. 6.2)}$$

$$Green_{sim} = \sum_{\lambda 400}^{\lambda 700} RSS_g(\lambda) * L(\lambda)^s_{tot.} \quad \text{(eq. 6.3)}$$

$$Blue_{sim} = \sum_{\lambda 400}^{\lambda 700} RSS_b(\lambda) * L(\lambda)^s_{tot.} \quad \text{(eq. 6.4)}$$

where $L(\lambda)^s_{tot.}$ is the at-sensor radiance from hyperspectral imagery, and $RSS_r(\lambda), RSS_g(\lambda),\ and\ RSS_b(\lambda)$ are relative spectral sensitivity functions of the red, green and blue channel, respectively, of the DSLR (Zhao (2019) citing Zhao et al. (2009)).

The contrast/brightness of the simulated RGB image was then adjusted using gamma correction ($\gamma = 0.4$) to improve visualization (Maini & Aggarwal, 2010).

6.3.4 Dimensionality Reduction Using MNF (Minimum Noise Fraction) transform

MNF transform was then applied to the reflectance hyperspectral images. Full spectral information from 400–1000 nm wavelengths was kept for the MNF decomposition. Noise was

estimated by (i) selecting a homogeneously dark area of the image and (ii) extracting the noise covariance matrix from it using the shift difference method (i.e., the processed pixel minus its top-right neighbor). This procedure respectively exploits the facts that (i) signal variation in a homogeneously dark area of an image is due primarily to environmental and instrumental noise and (ii) the signal at any point in the image is strongly correlated with the signal at neighboring pixels, while noise is not or only weakly spatially correlated (Green et al., 1988).

Given the site context and to allow for continuous visual interpretation of terrestrial and submerged structures (including rock outcrops or emerging steles), the MNF transform was applied to the entire subset of the imagery, including terrestrial and submerged areas. Only MNF components with a SNR ≥ 5 were conserved. The resulting components were visualized individually and in multiple pseudo-colored images (combining three components selected to highlight spectral and spatial variation in the data) to enhance visualization of submerged features. The results were compared to (i) the synthetically created true-color image and (ii) the georeferenced archaeological reference data identifying each stele.

6.3.5 Automatic Anomaly Detection

LRXD and IF unsupervised anomaly-detection algorithms were used to identify submerged anomalies automatically and compare them to the known archaeological reference data. The algorithms were applied to the MNF results calculated from the surface reflectance image. LRXD was applied to the MNF subset within a sliding window of 30 px × 30 px (outer window) and 15 px × 15 px (inner window). The IF model was trained with 100 decision trees, 100 randomly drawn observations and 10 randomly drawn features to train each tree.

For both algorithms, results were evaluated visually and statistically. Visually, the anomaly score map was compared to the georeferenced archaeological reference data. Statistically, the receiver operating characteristic (ROC) curve was calculated to illustrate the trade-off between the true positive rate and false positive rate at different score thresholds. Accuracy was assessed by calculating a normalized confusion matrix of the binary classification with a threshold defined from the ROC curve. Statistical evaluation was limited to the submerged area to focus on submerged anomalies.

6.3.6 Depth and Bottom Reflectance Estimation

Before inverting the radiative transfer model, a mask for the water was applied using the normalized difference water index (NDWI) (McFeeters, 1996):

$$NDWI = \frac{R(\lambda_{550}) + R(\lambda_{850})}{R(\lambda_{550}) - R(\lambda_{850})} \quad \text{(eq. 6.5)}$$

where $R(\lambda_{550})$ and $R(\lambda_{850})$ are the pixel reflectance values in the green and near-infrared areas of the spectrum, respectively.

To reduce variability due to noise, reflectance was extracted using the median values within ± 20 nm of each central wavelength (550 or 850 nm).

The semi-analytical radiative-transfer model, as seen in equation (6.1) was inverted using SWIM (Shallow Water mappIng using optical reMote sensor(s)) (Lennon et al., 2013; Sicot et al., 2015) to estimate bottom reflectance (R_{rs}^{b}), bottom depth (Z) and water column parameters ($C_{cdom}, C_{phy}, C_{NAP}$) from the observed subsurface reflectance (R_{rs}^{-}). The inversion problem is solved by minimizing a least square cost function representing distance between the observed subsurface reflectance and the modelled subsurface reflectance. Optimization was performed using the Levenberg-Marquardt. For each pixel, the algorithm converged to a solution for a vector of parameters ($R_{rs}^{b}, Z, C_{cdom}, C_{phy}, C_{NAP}$). R_{rs}^{b} and Z were used subsequently for further analysis. No external data (in-situ depth measurements or existing elevation model) was used for refining the bottom-depth estimation.

The bottom depth in raster format was post-processed using a median filter of 5 × 5 px to reduce the salt-and-pepper noise that can decrease interpretability for archaeological purposes. The data were then corrected for the tidal effect using tide information available from Shom and converted from the hydrographic reference to the terrestrial height reference NGF/IGN69 using the RAM product (maritime altimetric reference values) provided by Shom. The results were compared to the archaeological reference data as well as to the Litto3D continuous topo-bathymetric reference dataset collected from MBES and ALB by Shom/IGN on the Gulf or Morbihan.

6.4 Results

6.4.1 Analysis of the Simulated RGB Image

The northernmost and terrestrial semicircle of Er Lannic was visible on the RGB image, as were the locations of archaeological structures (individually for large steles and linear shapes for groups of smaller steles) (Figure 6.6b,c). Bright colors of on-shore steles and shadows projected by standing steles facilitated visualization and interpretation. On the submerged part of the site, large terrestrial steles on the upper intertidal platform were apparent, but the continuity of the submerged semicircle was difficult to perceive without prior knowledge of the site or the reference archaeological data. Effects of the water surface were visible at the southern tip of the semicircle and corresponded to the presence of an emerging stele ($Stl_{\#1}$).

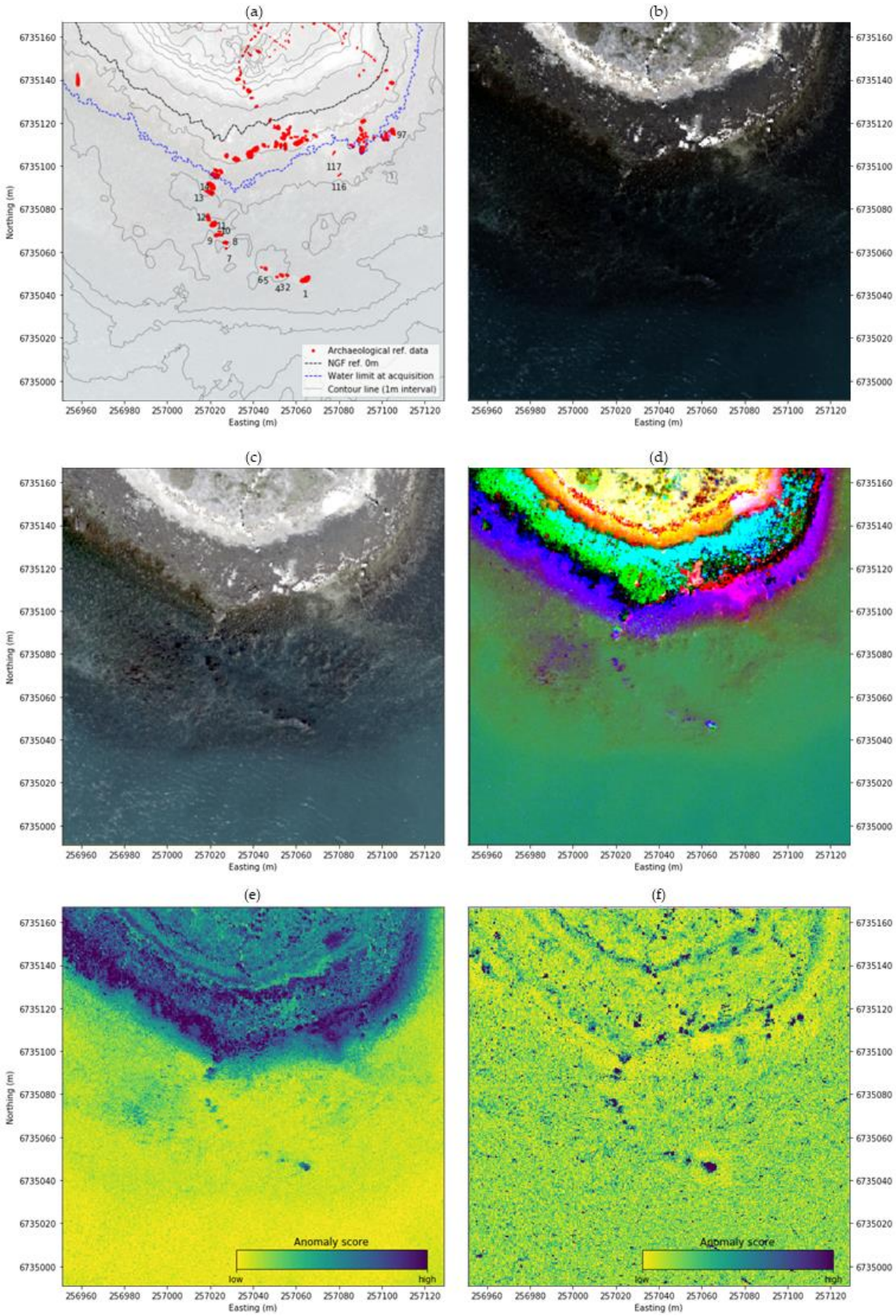
(a)
(b)
(c)
(d)
(e)
(f)
Northing (m)
Easting (m)
Archaeological ref. data
NGF ref. 0m
Water limit at acquisition
Contour line (1m interval)
Anomaly score
low
high

*Figure 6.6. (**a**) Archaeological reference map of the study site (submerged steles are numbered). True-color (RGB) images simulated from hyperspectral data and spectral sensitivity functions (**b**) without and (**c**) with gamma correction (γ=0.4). (**d**) Minimum noise fraction pseudo-color image with bands Red=9, Green=3 and Blue=4. (**e**) Anomaly score calculated using the Isolation Forest (IF) algorithm. (**f**) Anomaly score calculated using the local Reed–Xiaoli detector (LRXD) algorithm.*

According to the MNF components extracted from AHI, the hyperspectral data did not greatly improve visualization or description of the northernmost semicircle (Figure 6.7). However, the variability in the ground spectral signature near the steles highlighted many natural ground features (e.g., sands, granitic rocks, dry algae, grass). On intertidal and submerged platforms, the presence of features (local variations in MNF) through the water-column was visually confirmed, especially from MNF components 3, 4, 5, 8, 9, 12 and 13. Local variations were visually interpreted to identify the presence of the submerged semicircle.

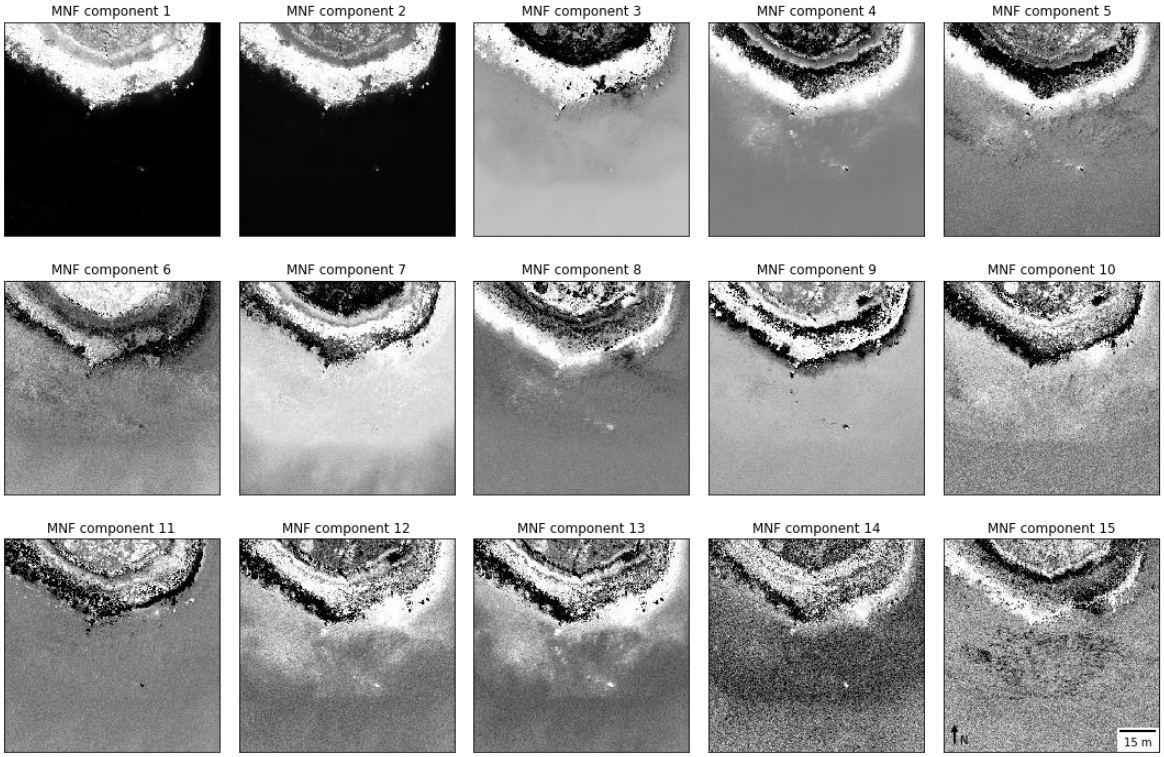

Figure 6.7. Minimum noise fraction (MNF) components 1–15 (signal-to-noise ratio ≥ 5) calculated from surface reflectance.

The pseudo-color image, created from visual selection of components 3 (green), 4 (blue) and 9 (red) of the MNF, confirmed the identification of submerged anomalies corresponding to the submerged steles ($Stl_{\#1}$ to $Stl_{\#14}$, $Stl_{\#97}$, $Stl_{\#116}$ and $Stl_{\#117}$) (Figure 6.6d).

6.4.2 Automatic Detection of Archeological Structures

According to IF, the most anomalous pixels were located mainly on-shore due to the high variability in spectral signatures (Figure 6.6e). Submerged archaeological structures had lower scores (i.e., less anomalous than on-shore structures) but were clearly visible and spatially defined due to their difference with the background (common observations). In contrast, structures at the land/water interface were not clearly defined due to little difference in the anomaly score.

Results obtained with the LRXD algorithm emphasized the location and shape of each submerged structure (Figure 6.6f). While LRXD is subject to impulse noise due to anomalous single-pixel observations, the spatial pattern of the submerged monuments was clearly distinguishable as a whole and as individual steles.

Comparing statistical results of the submerged area (at the time of acquisition) of the IF and LRXD methods, IF performed better than LRXD because LRXD (i) tended to enlarge anomalies spatially and (ii) generated a higher false positive rate (0.16, vs. 0.08 for IF) because it detected more anomalies on the submerged area (Table 6.3, Figure 6.8).

Table 6.3. Normalized confusion matrix for Isolation Forest (IF) and local Reed–Xiaoli detector (LRXD) anomaly detection of submerged structures.

	Predicted label "standard"	**Predicted label "anomaly"**
True label "standard"	0.92 (IF) 0.84 (LRXD)	0.08 (IF) 0.16 (LRXD)
True label "anomaly"	0.12 (IF) 0.27 (LRXD)	0.88 (IF) 0.73 (LRXD)

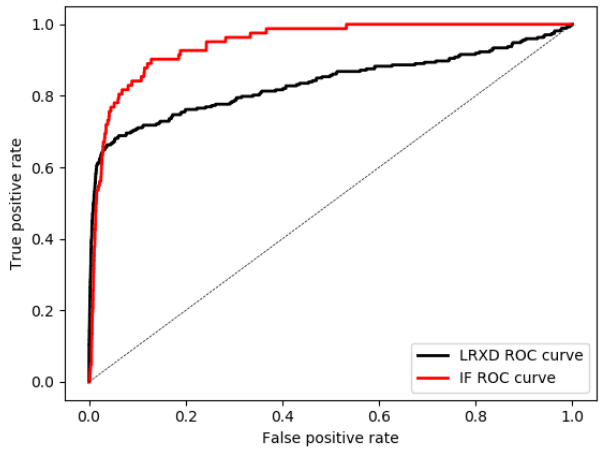

Figure 6.8. Receiver operating characteristic (ROC) curves for Isolation Forest (IF) and local Reed–Xiaoli detector (LRXD) anomaly detection calculated for the submerged structures.

6.4.3 Characterization of Archeological Structures

6.4.3.1) Morphological Characterization

The Bathymetric Digital Elevation Model (DEM) derived from AHI showed topographic variations corresponding to the submerged steles. An adapted view (using slope and colored-ramp overlay blending and 0.1 m contour lines) of the estimated water bottom highlighted the features (local maxima) and provided an initial morphological description (shape, area). On the submerged semicircle, 10 features on the DEM were interpreted as archaeological structures (Figure 6.9). Eight of these features (denoted *F#*) were associated with single steles (*F#1*: $Stl_{\#1}$, *F#3*: $Stl_{\#5}$, *F#4*: $Stl_{\#6}$, *F#5*: $Stl_{\#8}$, *F#6*: $Stl_{\#9}$, *F#7*: $Stl_{\#11}$, *F#8*: $Stl_{\#12}$, *F#10*: $Stl_{\#116}$), while the other two were associated with aggregations of multiple steles (*F#2*: $Stl_{\#2}$, $Stl_{\#3}$, $Stl_{\#4}$; *F#9*: $Stl_{\#13}$, $Stl_{\#14}$) since individual DEM signals for them were not apparent. Submerged steles $Stl_{\#7}$, $Stl_{\#10}$ and $Stl_{\#117}$ were not identified from the AHI-derived water-bottom morphology.

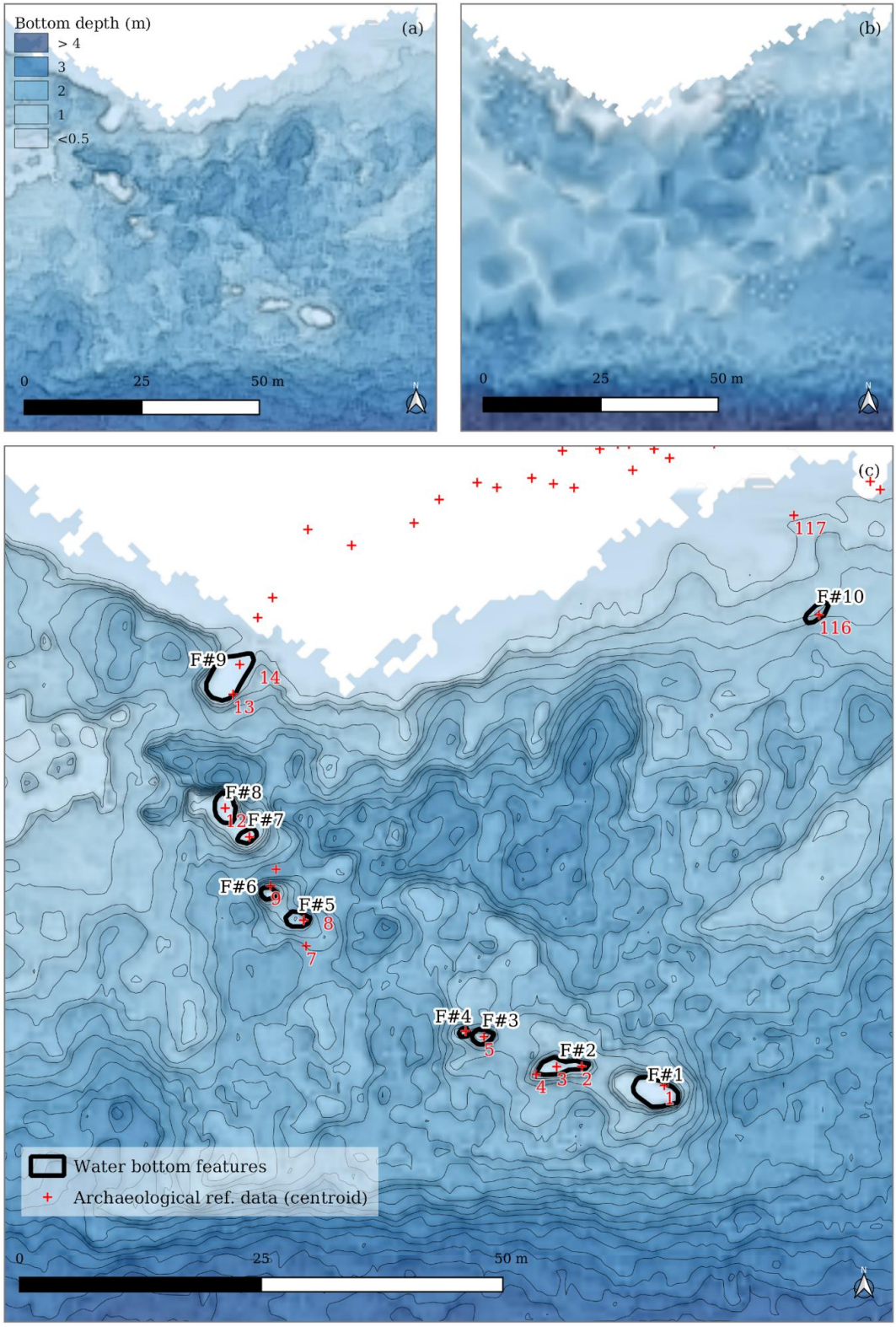

*Figure 6.9. (**a**) Bottom depth estimated from airborne hyperspectral imagery (AHI), (**b**) Litto3D bathymetric data (Shom/IGN) and (**c**) Bottom depth estimated from AHI with extraction of visible water-*

bottom features (local maxima) from 0.1 m contour lines. Archaeological reference data (stele centroids) are shown in red.

The area of the features extracted (2D projected horizontal area) were then compared to those of the archaeological reference data (Table 6.4). Linear regression between the two indicated relatively good agreement ($R^2 = 0.72$).

Table 6.4. Area of airborne hyperspectral imagery-derived water-bottom features compared those of steles from archaeological reference data. Coefficient of determination $R^2 = 0.72$.

Feature ID ($\boldsymbol{Feat_{\#n}}$)	**Feature area (m²)**	**Stele IDs ($\boldsymbol{Stl_{\#n}}$)**	**Stele area (m²)**
1	10.3	$Stl_{\#1}$	9.8
2	5.8	$Stl_{\#2}$, $Stl_{\#3}$, $Stl_{\#4}$	4.7 (1.4, 2.4, 0.9)
3	2.5	$Stl_{\#5}$	2.1
4	0.7	$Stl_{\#6}$	0.5
5	4.0	$Stl_{\#8}$	9.0
6	1.5	$Stl_{\#9}$	4.8
7	2.0	$Stl_{\#11}$	6.9
8	5.1	$Stl_{\#12}$	4.7
9	15.1	$Stl_{\#13}, Stl_{\#14}$	16.1 (6.9, 9.2)
10	2.8	$Stl_{\#116}$	0.7

Visualization of a path profile of bottom depth along the submerged semicircle (Figure 6.10) allowed AHI-derived bathymetry and Litto3D reference bathymetry to be compared. AHI-derived bathymetry described water-bottom morphology in more detail, and the presence of local maxima at the location of known archaeological structures confirmed its ability to visualize submerged structures and, to some extent, describe their morphological characteristics (i.e., shape, depth, and area).

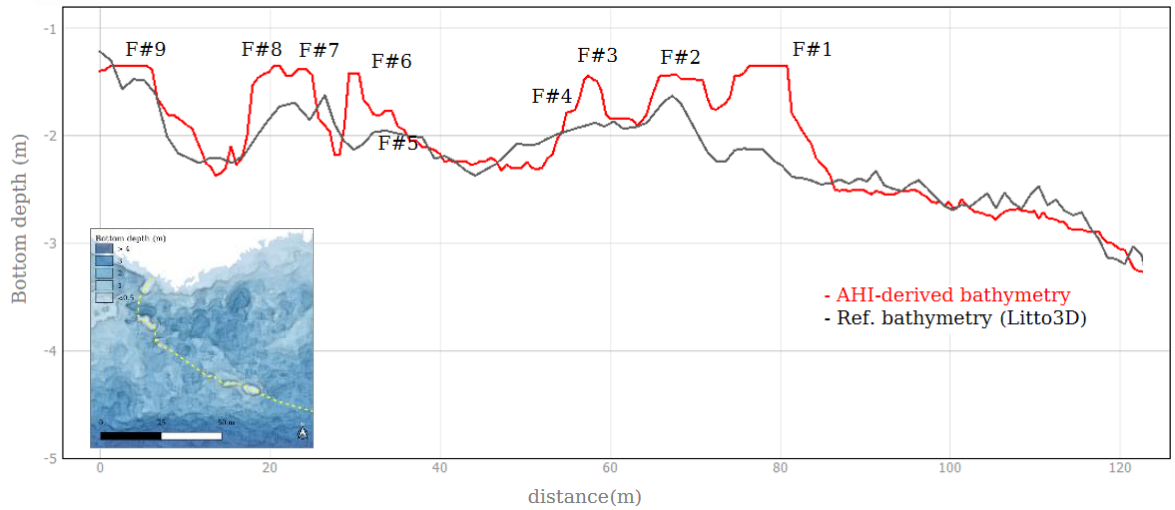

Figure 6.10. Path profile of bottom depth estimated from airborne hyperspectral imagery (AHI) and reference Litto3D (Shom/IGN) bathymetric data over the submerged structures.

6.4.3.2) Spectral Characterization of the Archeological Structures

Spectral signatures (bottom reflectance) selected on the submerged semicircle (Figure 6.11a) had a low amplitude of estimated reflectance (< 1%) due to low reflectivity of the water bottom. It also revealed green (around 580nm) and red-edge (increase in spectral reflectance from 650–720 nm) peaks on the submerged features, which reflected the presence of vegetation in plant-based biofilm (i.e., micro-algae) or macro-algae on the steles. In-situ observations (Figure 6.11b) confirmed the presence and the diversity of macro-algae (green and brown) on the steles.

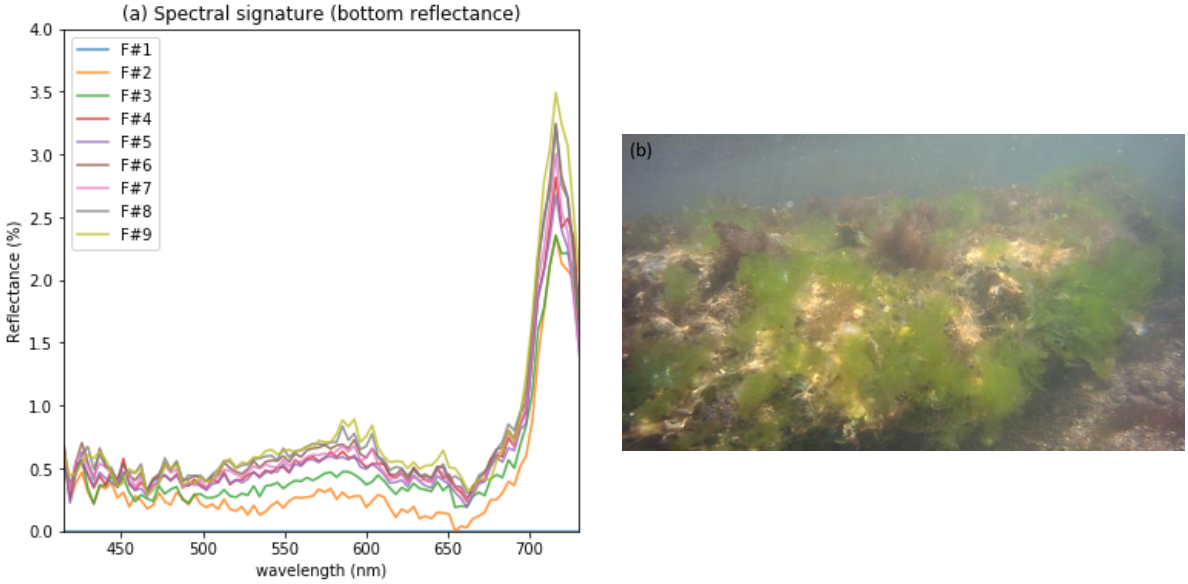

*Figure 6.11. (**a**) Spectral signatures of bottom reflectance showing archaeological structures and (**b**) photograph of a permanently submerged stele of Er Lannic covered by green and brown algae.*

6.5 Discussion and Perspectives

6.5.1 AHI: Potential for Application to Underwater Archaeology

Until recently, ALB was considered the only aerial remote sensing technique that could collect high-resolution data in very shallow water (Lecours et al., 2016). Development of AHI for shallow water mapping, first in academic contexts and more recently towards operational usages, shows that passive remote sensing is becoming a potential alternative for estimating bathymetry and describing water-bottom morphology and benthic cover types at a fine scale (meter or sub-meter resolution) (Bajjouk et al., 2019; Dekker et al., 2011). The present study opens new perspectives for underwater cultural heritage monitoring and archaeological prospection. Benefits of AHI for these applications include lower survey costs than those of ALB (J. Gao, 2009) and high spectral and spatial description. However, AHI also has drawbacks. As AHI is an optical remote sensing system (such as ALB), the efficiency of AHI for accessing water bottom information depends on environmental factors such as turbidity, water surface condition and sea state, bottom depth and bottom reflectance. Moreover, as a passive optical system, the quality of the data is also dependent on the illumination conditions and cloud cover (Göritz et al., 2018). While additional investigations are required to determine the dependency of the proposed approach on these environmental variables, the management of AHI surveys for archaeological mapping in a shallow water environment remains a sensitive aspect of the workflow.

6.5.2 Data Uncertainty and Statistical Results

The statistical results for unsupervised detection of anomalies were influenced by uncertainties in the context and input data. Since the target structures we sought had areas of 0.5–10 m^2, they were represented by clusters of a few pixels in the image (spatial resolution: 50 cm). Given this resolution, the sensor's point spread function and the uncertainty in horizontal precision (usually 1-2 pixels), the probability of having local/spatial discrepancies between the collected data and the reference data was relatively high. Another source of uncertainty was the reference archaeological data. Like for other archaeological reference data, a "ground truth" map is limited by at least two factors. The first is the measurement itself: every spatial measurement is inaccurate (as it never exactly matches with the true value which remains undefined), especially for archaeological sites of limited accessibility (i.e., partially or entirely submerged), and the uncertainty in location can be high. The second is the exhaustiveness of the reference data, which is never guaranteed. Since the reference map of an archaeological site evolves with methods and techniques, it should be considered a "current state of knowledge" rather than a "ground truth". Since we did not consider any of these sources of uncertainty, the results must be analyzed with care. They should not be considered a baseline for similar approaches in different archaeological contexts, but rather a baseline for comparing novel anomaly-detection methods in the same experimental conditions.

6.5.3 From Anomaly to Archaeological Structure

As shown in this study, morphological and spectral characterization of submerged archaeological structures can be complex. The weak reflectance (and consequently low SNR) in water conditions, combined with the continuous presence of vegetation (micro- or macro-algae) on submerged mineral structures, limited the ability to distinguish between archaeological and natural structures spectrally. Thus, the use of the term "morphological or spectral characterization" could be an inappropriate description of hyperspectral remote sensing if it is assumed to provide information similar to that from in-situ archaeological analysis. Considering the information provided by remote sensing to be a faithful description of archaeological structures is premature. Instead, the information provided by AHI should be considered a proxy or surrogate description of archaeological structures. For example, archaeologists consider that algae covering steles are not part of the archaeological structures (in fact, algae are regularly removed from the steles of Er Lannic that are accessible at low tide). Therefore, the morphological or spectral descriptors of submerged features extracted from remote sensing data describe not only archaeological structures but the natural environment that surrounds them (their envelope). Nevertheless, a first characterization of the bottom spectral properties is a valuable information offered by AHI and an advantage over ALB for which the backscattering intensity of a single wavelength signal is less adapted for the description of benthic composition (Pan et al., 2016).

6.5.4 Perspectives and Future Research Directions

This study was an initial approach to demonstrate the potential of hyperspectral imagery for prospecting and monitoring submerged archaeological structures in shallow water environments. It opens new perspectives. First, from an archaeological perspective, the study focused on a known archaeological site built during the Neolithic period. The archaeological potential in coastal shallow water environment, for example in Brittany, is important and a major challenge from a scientific perspective and with regard to cultural heritage management. Our objective is to broaden this study to prospect or monitor archaeological sites of different chrono-typologies.

Second, from a remote sensing and data-analysis perspective, we intend to continue research on unsupervised and supervised anomaly detection. For archaeological prospection, anomaly detection is a key challenge for identifying structures for which only partial knowledge usually exists. Indeed, the state of conservation and surface condition of archaeological structures, especially in water conditions, is *a priori* undefined, and the expected characteristics that reference typologies provide, although informative, can mislead prospections for predefined morphological structures that differ from the complex in-situ situation. To address this limitation, our future research will aim to go further in the use of unsupervised or self-supervised anomaly detection algorithms, including deep-learning techniques such as convolutional autoencoders in 2D (spatial) or 3D (spatial/spectral), to extract informative patterns from the hyperspectral cube for application to archaeology.

6.6 Conclusion

We demonstrated AHI's potential for submerged archaeological prospection and monitoring in shallow water environments. While AHI is regularly used for terrestrial archaeology, its use has not yet been assessed for underwater archaeology. By taking advantage of the high-resolution spatial and spectral characteristics of AHI data, the study showed that AHI passive remote sensing could be a valuable alternative to active remote sensing techniques for mapping submerged archaeological structures. The study was performed on the megalithic site of Er Lannic in Morbihan (France), composed of two semicircles of steles, one of which lay on the water bottom 2–3 m below the mean sea level. The method was divided into three steps: (i) visualize submerged structures, (ii) detect submerged anomalies automatically and (iii) characterize the features identified by estimating their morphological and spectral characteristics. The results showed that hyperspectral data can collect underwater information necessary for archaeological mapping. This information was extracted from AHI either by data-driven analysis (dimensionality reduction/anomaly detection) or by estimating physical parameters such as water depth and bottom reflectance by the inversion of a radiative transfer model. Comparing the information extracted to archaeological and bathymetric reference data confirmed AHI's potential for archaeological prospection and monitoring. Although this study focused on a single archaeological site (i.e., chrono-typology), the approach will be further explored to assess its application to a wider range of structures and archaeological and environmental contexts. Future research will also assess unsupervised or self-supervised machine-learning techniques to reduce dimensionality and detect submerged anomalies in hyperspectral images.

Guyot, Alexandre. Contribution of airborne LiDAR and hyperspectral data to archaeological mapping in terrestrial and submerged environments. 2021

Chapter 7. Airborne hyperspectral imagery for archaeological prospection of submerged landscapes. A case study of the stone tidal fishweirs of the Molène archipelago, France

This chapter is entirely reproduced from the article currently submitted for review in *Archaeological prospection*:

> Guyot, A., Lennon, M., Stephan, P., Péres, T., Hascoet, M., Gandois, H., Daire, M-Y., Hubert-Moy, L. Airborne hyperspectral imagery for archaeological prospection of submerged landscapes. A case study of the stone tidal fishweirs of the Molène archipelago, France. (Manuscript submitted for publication)

Article

Airborne hyperspectral imagery for archaeological prospection of submerged landscapes. A case study of the stone tidal fishweirs of the Molène archipelago, France

Alexandre Guyot[1,2,*] , Marc Lennon[2], Pierre Stéphan[3], Thibaut Péres[1], Marie Hascoët[4], Henri Gandois[5], Marie-Yvane Daire[5], Laurence Hubert-Moy[1]

1. Université Rennes 2, Laboratoire LETG - UMR6554, Rennes, France
2. Hytech-Imaging, 115 Rue Claude Chappe, 29280, Plouzané, France
3. CNRS, Laboratoire LETG - UMR6554, Plouzané, France
4. Parc naturel marin d'Iroise, Office français de la biodiversité, Le Conquet, France
5. CNRS, Laboratoire CReAAH - UMR6566, Rennes, France

* Correspondence: alexandre.guyot@univ-rennes2.fr

Submitted: 11/10/2021

Abstract: Effects of Climate change and human pressure on the coastal zone are increasing, which presents serious challenges for the protection of submerged archaeological sites. Cartographic mapping of this submerged cultural heritage and landscape is necessary to address these challenges. While active acoustic and optical remote -sensing data are regularly used to document the seafloor, they face challenges, such as limited accessibility of the shallow water zone, high costs of deployment, low spatial resolution and limitation of the spatial extent that can be surveyed. In this study, we assessed the use of airborne hyperspectral imagery (AHI) as innovative data for large -scale representation of submerged landscapes, and specifically its application to archaeological documentation and prospection of stone tidal fishweirs of the

Molène archipelago (France). Two information -extraction approaches, one data-driven and one physics-based, were used and assessed for the identification and characterization of known submerged fishweirs using AHI data. these approaches were then used to create input visualization images for large-scale remotely sensed archaeological prospection. The results showed that AHI was able to identify 89% of the known fishweirs, thus reaching higher identification performance than traditional prospection methods used on the same area. Moreover, AHI-derived data led to visual identification and characterization of 28 anomalies at depths of 0-6.8 m below chart datum. An underwater survey of three of them confirmed that they were submerged archaeological structures. This study demonstrates for the first time that AHI can be considered as a new tool for mapping submerged landscapes at a largescale to manage underwater cultural heritage in shallow waters.

7.1 Introduction

7.1.1 Coastal archaeology: underwater cultural heritage at risk

Effects of Climate change and human pressure on the coastal zone are increasing, which presents serious challenges for the protection of submerged archaeological sites. According to Flemming (2020), 80% of known submerged sites in Europe are less than 5 m deep. As mentioned in the latest report of the International Committee on the Underwater Cultural Heritage (Hafner et al., 2020), shallow coastal waters are thus the areas of most concern and vulnerability for underwater cultural heritage. archaeological research in foreshore and nearshore areas not only highlights past societies' relations to the sea, but also helps understand chronologically related sites on the hinterland (Billard et al., 2019). Submerged archaeological evidence is also a proxy for estimating the rise in sealevel that has occurred since the last glacial maximum period ca. 20,000 years ago (G. Bailey et al., 2020). As such, submerged cultural heritage provides a unique source of information for understanding long-term landscape and environmental dynamics in coastal areas.

A multidisciplinary research approach is becoming crucial to address the challenges that submerged archaeology faces. Specifically, remote sensing and mapping of submerged landscapes can provide useful tools (Missiaen et al., 2017) to (i) extend existing documentation of archaeological sites and (ii) create new sources of information to support and orient archaeological prospection to enrich the body of knowledge of sites and generate preservation plans.

7.1.2 Archaeology of fishweirs

Throughout the world, human communities settled on the coast have exploited marine resources such as shellfish, fish and seaweed. In areas with a large tidal range, coastal societies have relied on the daily ebb and flow of the sea to trap fish in fixed structures made of stone or wood located on the foreshore (Connaway, 2007). At high tide, fish enter a trapping area and are then unable to escape as the water progressively recedes. Depending on the morphology of the tidal fishweir,

fish are then caught by nets within the temporary pond or forced into a narrow exit (the sluice), where they are captured (Langouët & Daire, 2009).

In France, along the coasts of the Atlantic Ocean and English channel, nearly 800 fishweirs have been identified (Billard & Daire, 2019). In Brittany, intertidal and subtidal archaeological prospections have supplemented the observation and inventory of these monumental but often poorly preserved archaeological structures (Daire & Langouet, 2008; Daire & Langouët, 2010; Gandois et al., 2018; Stéphan, Gandois, et al., 2019). The diversity of fishweir structures observed has led to the development of a morpho-typology (Figure 7.1). This classification, based on more than 400 known remains of fishweir structures, differentiates the structures by shape (L: linear, C: curvilinear, S: snakelike) and construction context (A: single wall between two natural rock outcrops, B: multiple walls connect several rock outcrops, C: two walls converge, D: one wall next to the coastline).

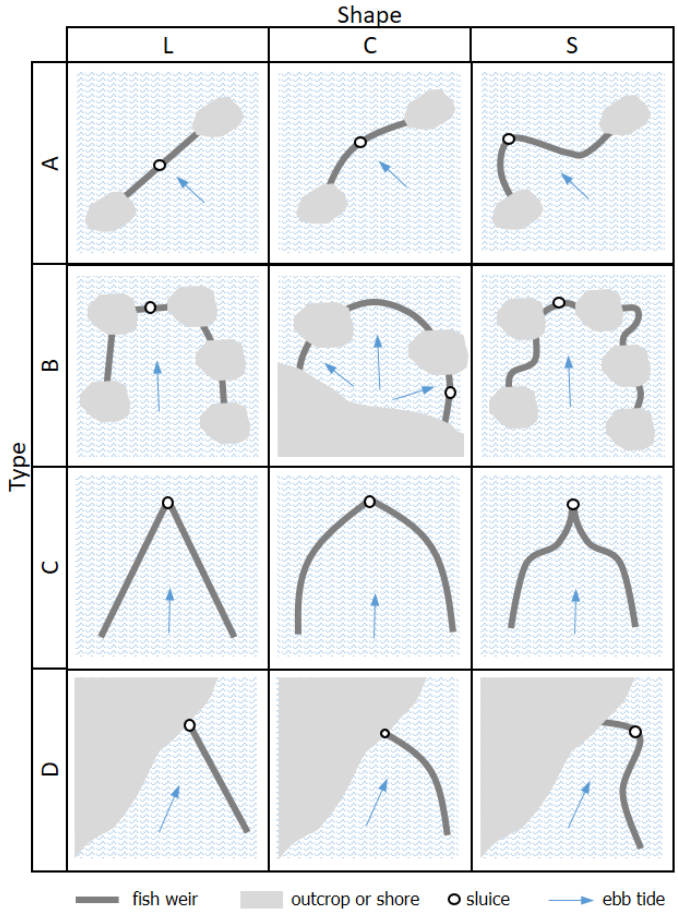

Figure 7.1. Fishweir morpho-typology as a function of construction context (A: single wall between two natural rock outcrops, B: multiple walls connect several rock outcrops, C: two walls converge walls, D: one wall next to the coastline) and shape (L: linear, C: curvilinear, S: snakelike). Adapted from Langouët & Daire (2009)

Although direct dating of stone fisheries remains challenging due to the lack of organic material for radiocarbon measurements, Daire and Langouët (2011) developed a dating method based on the elevation of the fishweir and its relation to the history of sealevel change. With recent updating of this history (Stéphan & Goslin, 2014), the method has been used to provide dating information on fishweirs (Pailler et al. 2014; Gandois et al. 2018). The morpho-typology and dating information collected raises questions about the construction and use of these fishweirs, but also about the change in paleo-landscapes since the Holocene (Stéphan, Gandois, et al., 2019). Whether to preserve cultural heritage or enrich archaeological knowledge, it is necessary to improve identification and description of fishweirs using mapping techniques.

7.1.3 Mapping the seafloor

technical and scientific advances in the past 20 years have contributed greatly to archaeological research on the continental shelf (G. N. Bailey & Flemming, 2008; Sturt et al., 2018). Large-scale prospection of the seafloor has been made possible mainly by hydrographic survey techniques, such as ship-based acoustic systems (e.g. multibeam echosounders (MBES), side -scan sonars). However, the coastal seafloor, referred to as the "white ribbon" (Kotilainen & Kaskela, 2017; Leon et al., 2013), is not wellknown due to a lack of synoptic and high-resolution data. Indeed, large-scale mapping of submerged coastal landscapes remains a challenge for subsurface sensors, especially because it is constrained to areas of safe navigation with sufficient depth (Bowens, 2009; Menna et al., 2018).

In this context, airborne sensors have been useful for mapping submerged archaeological sites. For example, the use of airborne LiDAR bathymetry (ALB) and topo-bathymetry (ALTB), as active remote -sensing sensors, for underwater archaeological surveys has been assessed in a variety of geoarchaeological contexts. ALB was used as an alternative to sonar surveying to identify shipwrecks in the South China Sea atoll, which has dangerous shoals (Shih et al., 2014). Doneus et al. (2015) assessed the ability of ALTB in an inland lake in Austria and a coastal area of Croatia to provide archaeological information on a Neolithic lake-dwelling and a submerged Roman harbor, respectively. More recently, a similar approach, based on analysis of an ALTB -derived digital terrain model, was used to re-assess the interpretation of the Roman site complex at Vizula (Croatia) on the Adriatic coast (N. Doneus et al., 2020). Recent studies have also used unmanned aerial vehicle (UAV)-based imagery to represent large-scale submerged landscapes by combining visual information on the seabed with water height (Agrafiotis et al., 2019; Papakonstantinou et al., 2019). These approaches, however, based on photogrammetry, were limited to areas with excellent through-water visibility and a sufficiently textured sea bottom to allow for 3D reconstruction of structure based on motion and multi-view stereo processing pipelines.

In parallel, decades of advances in optical remote -sensing of coastal waters have led to the emergence of hyperspectral imagery (HSI) and especially airborne hyperspectral imagery (AHI) as an improved source of information for seafloor mapping, including estimates of water height and water -bottom types (Dekker et al., 2011; Kutser et al., 2020). As light travels through the water

column, absorption and scattering phenomena progressively attenuate its intensity, and the degree of attenuation depends on the wavelength of light. AHI in the visible and near-infrared (VNIR) range of the electromagnetic spectrum (400-1000 nm) allows for (i) visualization of variation in spatial/spectral data caused by light interacting with the water bottom and (ii) estimation of physical characteristics of the scene by using physical radiative -transfer models (Figure 7.2).

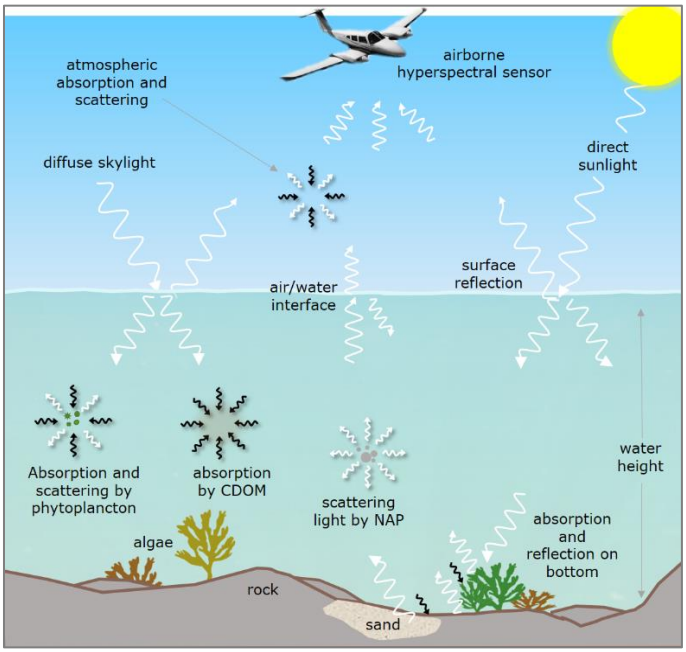

Figure 7.2. Diagram of radiative transfer in shallow water (adapted from Bertels et al. (2008) and Petit (2017)). CDOM: colored dissolved organic matter, NAP: non-algal particles

In this context, semi-analytic radiative -transfer models, such as the Lee model (Z. Lee et al., 1998) have been developed as a simplified model of interactions between light and matter in shallow waters. By inverting the model, this physics-based approach estimates water height and water-bottom reflectance from water-surface reflectance (Z. Lee et al., 1999). Initially used in environmental applications such as habitat mapping (Bajjouk et al., 2019; Bertels et al., 2008), the utility of this approach for mapping a submerged megalithic site in shallow water (Guyot, Lennon, Thomas, et al., 2019) was recently assessed . Like other optical passive remote -sensing techniques, it is limited to the depths that natural light can reach, but it shows an interesting capacity to document submerged archaeological structures spectrally and morphologically. To date, however, it has been used to document only one megalithic site and has been limited to site-scale mapping.

In this study, we assessed the use of AHI as innovative data for large -scale representation of submerged landscapes, and specifically its application to archaeological documentation and prospection of stone tidal fishweirs of the Molène archipelago (France). We assessed the utility of

AHI data for (i) visualizing large-scale submerged landscapes, (ii) documenting inventoried fishweirs and (iii) prospecting for unknown archaeological structures.

7.2 Study Area

The Molène archipelago is located in the Iroise Sea and starts five nautical miles off the west coast of Brittany, France (Figure 7.3). It is composed of a string of islands and islets that emerge from an underwater shelf covering more than 150 km², with a depth that rarely exceeds 10 m.

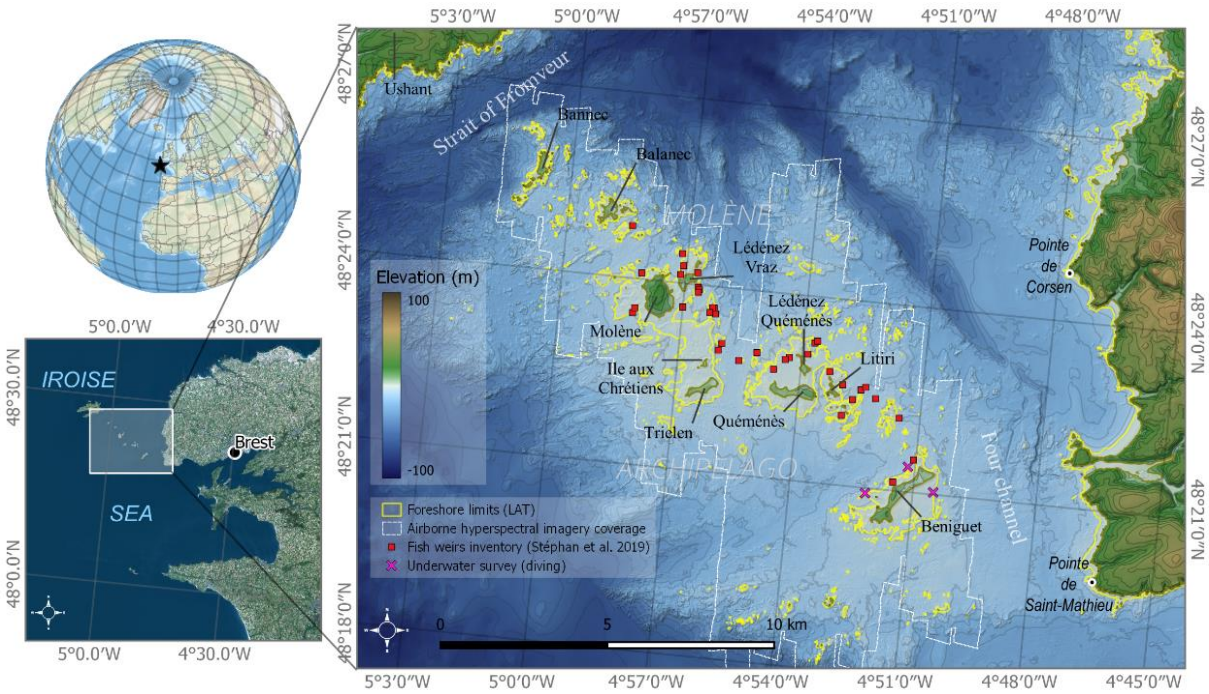

Figure 7.3. Location and composition of the Molène archipelago

The Molène archipelago includes nine main islands, aligned along a northwest to southeast axis: Bannec, Balanec, Molène, Trielen, Ile aux Chrétiens, Quéménès, Litiry, Morgol and Béniguet. A dozen Additional islets complete the terrestrial part of the archipelago. The land area above the highest astronomical tide covers 2.5 km². With a tidal range of up to 7.9 m, the emerged area – including the foreshore – increases to 16.5 km² at the lowest astronomical tide.

Paleogeographic reconstructions have shown that the plateau, now separated from the continent by the Four channel, was connected to the mainland during the last glacial maximum (ca. 18,000 cal BP). It was then progressively submerged during the post-glacial transgression as the sealevel rose (Hallégouët, 1982). From the Neolithic period to the present, the landscape gradually evolved from a continuous foreshore area that covered the plateau at low tide to the landscape known today (Stéphan, Gandois, et al., 2019). Evidence of human occupation on the archipelago extends

back at least to the Neolithic period (5th millennium BCE), with the erection of Megalithic structures (Pailler et al., 2014). The geographical context of the archipelago implied a strong relationship between its inhabitants and the sea. This relation is attested by the many fishweirs on the archipelago, most of which are now constantly submerged. While dating such mineral submerged human-made structures remains a challenge (Gandois et al., 2018), some of them could have been built by the Neolithic population based on estimates of the Holocene sealevel (Stéphan et al. 2019). development of new prospection methods in shallow waters would increase the knowledge of these structures and likely help discover new ones.

7.3 Materials and methods

7.3.1 Airborne hyperspectral imagery

AHI was collected by Hytech-Imaging with a NEO HySpex VNIR-1600 pushbroom sensor. The sensor operates in the 400-1000 nm spectral range, acquired in 160 bands, with a spectral resolution of 4.5 nm FHWM (full width at half maximum). With a field of view of 34° and acquisition at 1200 m above ground level, each flight line covered a swath of ca. 700 m and represented a ground sampling distance of 1 m. Associated with the sensor, an IMAR iTrace-RT-F200 inertial measurement and global positioning /global navigation satellite system with an OmniSTAR L1/L2 antenna was used to provide position and orientation information. The airborne survey was performed on 8 May 2020 during low-tide conditions with a tide coefficient of 108, representing a total area of 125 km².

Hyperspectral images were radiometrically calibrated and geometrically corrected using the HYPIP (HYPperspectral Image Preprocessing) processing chain developed by Hytech-Imaging, and including ATCOR/PARGE software (ReSe Applications GmbH). Georeferenced flight lines in at-sensor spectral radiance ($W.m^{-2}.sr^{-1}.\mu m^{-1}$) were converted to bottom-of-atmosphere (or surface) reflectance values using a two-step process: (i) atmospheric corrections using ATCOR-4 software and (ii) empirical line adjustment using linear regressions between pixel -reflectance spectra and reflectance spectra of pre-calibrated targets (i.e. tarps) placed in the study area during the survey.

7.3.2 Reference data

7.3.2.1) In situ spectroscopy

In situ spectroscopy was performed using a GER-1500 handheld spectrometer operating in the VNIR spectral range. Several targets in the intertidal area, including different substrate types (rock, sand) and algae (brown, red and green algae) were measured and used as spectral references to create a spectral library of six endmembers (Figure 7.4). This spectral library was used for the physics-based approach.

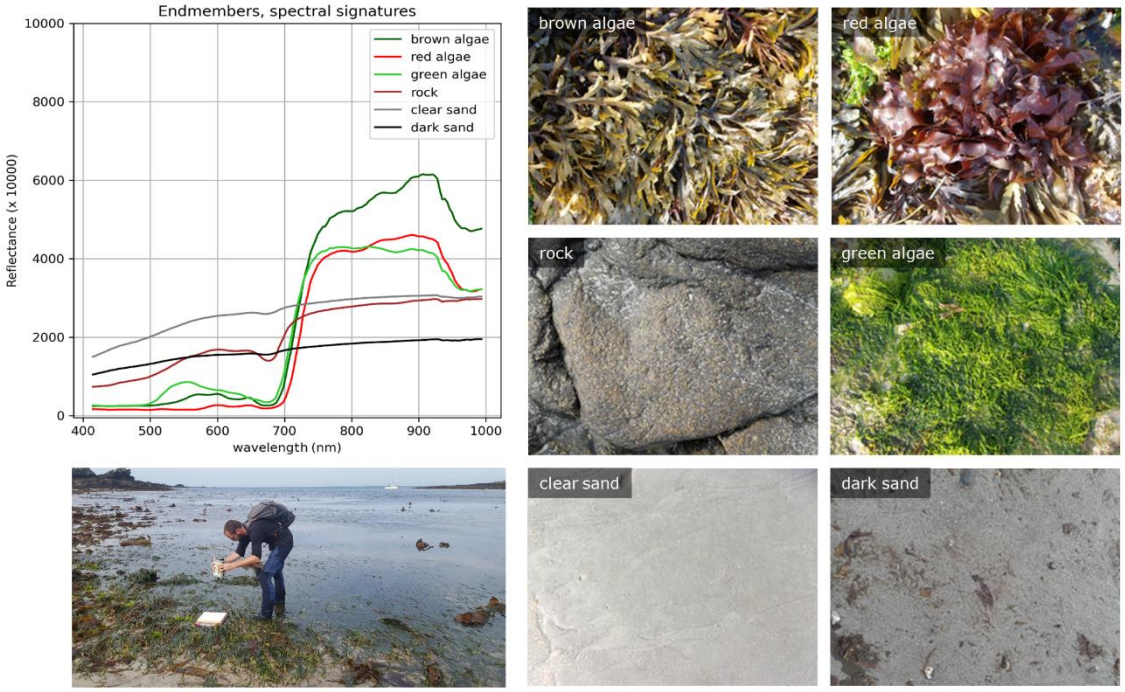

Figure 7.4. Spectral library measured using a handheld spectrometer on the foreshore area in and near the study area

7.3.2.2) Litto3D® topo-bathymetric data

topo-bathymetric reference data were used in this study to evaluate and compare the bathymetry -derived AHI data. The data came from the Litto3D® project (Louvart & Grateau, 2005), operated by the French Naval Hydrographic and Oceanographic Office (Shom) and the French National Geographic Institute (IGN). This project produces a seamless, high-resolution topographic and bathymetric model of French coastal areas using multiple survey techniques (i.e. ALB, ALTB and MBES). Shom/IGN provided the data as a merged 1 m resolution raster in the Lambert93 system using the RGF93 geodetic system (EPSG: 2154) and the NGF/IGN69 height reference for elevation. When required for comparison, NGF/IGN69 elevations (French topographic datum) were converted to Shom chart datum (French hydrographic datum) using the latest Référence Altimétrique Marine (RAM) provided by Shom. For the harbor of Molène, the difference between chart datum and NGF/IGN69 was -3.841 m.

7.3.2.3) Fishweir inventory

The fishweir inventory of was used as a reference to assess the results(Stéphan, Gandois, et al., 2019). elaborated using a variety of sources, including *in situ* observation, airborne prospection, ALB and MBES, it lists 36 fishweirs or related sea-bottom anomalies. Although only a few of them have been confirmed by *in situ* archaeological observations or dives, the geographic position (i.e. latitude, longitude and depth), length and width of each one is described.

7.3.3 Data processing

the processing workflow consisted of two approaches, a data-driven approach and a physics-based approach, to extract underwater information from AHI (Figure 7.5).

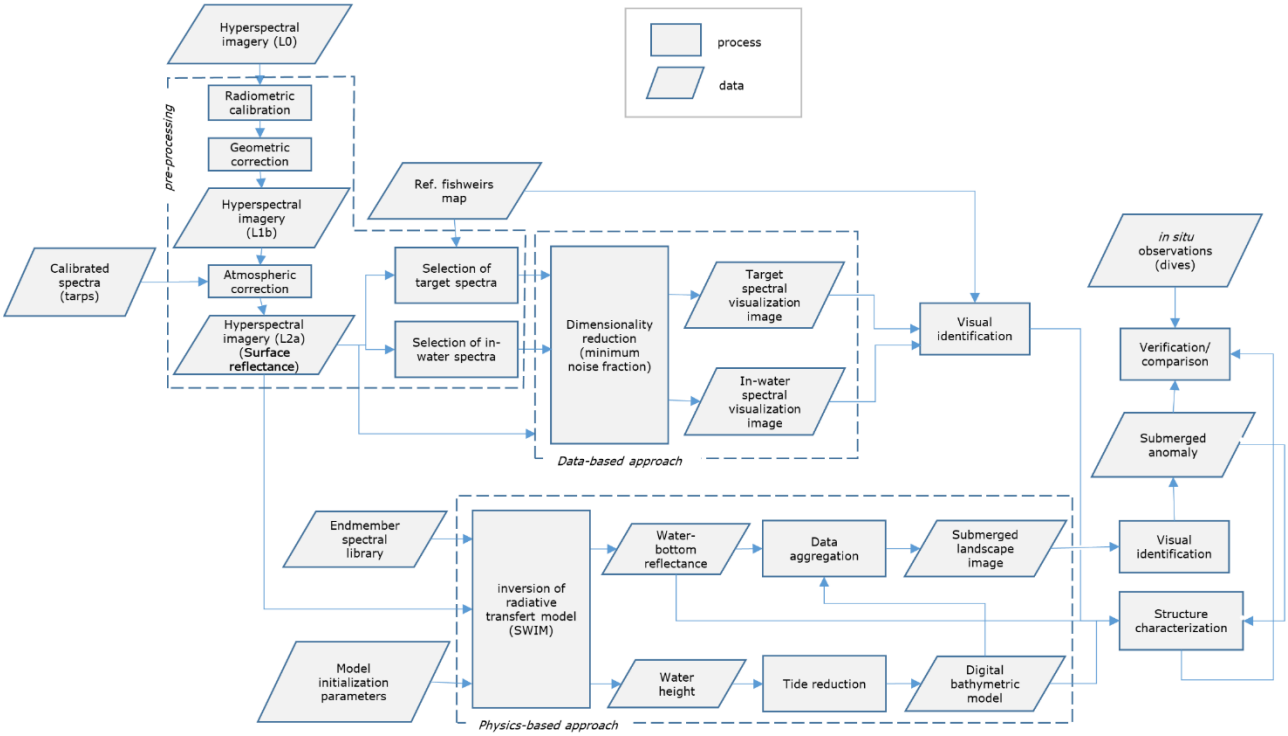

Figure 7.5. Processing workflow

7.3.3.1) The data-driven approach

The data-driven approach assumes that the water -surface -reflectance data contain the water-bottom information sought. Thus, we looked for small spatial/spectral variations in the signal that could be related to water-bottom variations.

Given the signal-to-noise ratio of water -surface reflectance and the large number of spectral bands, the small spectral/spatial variations were extracted using a minimum -noise -fraction (MNF) transformation (Green et al., 1988). Two MNF transformations were performed using different sampling strategies to calculate the noise and data statistics required to reduce dimensionality:

- An “in-water model”, based on all water pixels of a shallow -water area northwest of Molène island. This sampling strategy was used to model the overall data variability of shallow -water areas, and thus to create an MNF projection specialized for them.

- A "target model", based on pixels selected around the 36 structures inventoried in the reference dataset. Pixels were selected using a 100 m buffer around the polylines that represented the fishweirs. This sampling strategy was used to model the data variability of expected targets (fishweirs) and their environments, and thus to create an MNF projection specialized for them.

The noise and data statistics were calculated from the sampled spectra and limited to the range of 480-780 nm due to signal absorption by water. The first three components of each MNF transformation were kept to generate a color-composite RGB image to visualize spatial/spectral variations of the submerged areas.

7.3.3.2) The physics-based approach

7.3.3.2.a) Inversion of a radiative-transfer model

The physics-based approach is based on inverting the semi-analytical radiative-transfer model of Lee et al. (1998). This model mathematically describes the relation between physical parameters of the water column (i.e. water components, water height and water -bottom reflectance) and the observed subsurface remote -sensing reflectance R_{rs}^{-} at wavelength λ (eq. 7.1):

$$R_{rs}^{-}(\lambda) = \underbrace{R_{rs}^{\infty}(\lambda)\left(1 - A_0 e^{-(K_d(\lambda)+k_{uW}(\lambda))Z}\right)}_{\text{water column contribution}} + \underbrace{A_1 \rho(\lambda).\, e^{-(K_d(\lambda)+k_{uB}(\lambda))Z}}_{\text{water bottom contribution}} \qquad \text{(eq. 7.1)}$$

where $R_{rs}^{\infty}(\lambda)$ is the remote -sensing reflectance for optically deep water; K_d, k_{uW}, k_{uB} are diffuse coefficients related to downwelling irradiance, upwelling radiance of the water column and upwelling radiance from bottom reflection, respectively; A_0 and A_1 are constants; ρ is the water -bottom reflectance and Z is the water height.

The diffuse coefficients K_d, k_{uW}, k_{uB} are related to the total absorption (a) and backscattering coefficients (b_b) at different wavelengths (λ), which are defined, using a series of semi-analytical relationships (Z. Lee et al., 1998, 1999), to the concentration of optically active components in the water column : phytoplankton, non-algal particles and colored-dissolved matter. Thus, subsurface reflectance at a given wavelength (R_{rs}^{-}) is a function of five elements inferred during the inversion (eq. 7.2):

$$R_{rs}^{-} = f(K_d, k_{uW}, k_{uB}, Z, x) \qquad \text{(eq. 7.2)}$$

where x is the vector of abundance for the six endmembers Figure 7.4(), grouped in a matrix (E). These endmembers are used to model bottom reflectance as a support for the inversion (Sicot et al., 2015), using a linear mixing model (eq. 7.3):

$$\rho = x.E \qquad \text{(eq. 7.3)}$$

The model was inverted using SWIM (Shallow Water mappIng using optical reMote sensor(s)) (Lennon et al., 2013), developed by Hytech-Imaging. As input, the remote -sensing water -surface reflectance (R_{rs}^{+}) was first corrected for specular reflection at the water surface (sun glint) by

subtracting sun -glint reflectance, estimated as the mean reflectance ($\overline{R_{rs}^{+}}$) in the range of 850-950 nm, from $R_{rs}^{+}(\lambda)$ (eq. 7.4).

$$R_{rs\_sgc}^{+} = R_{rs}^{+} - \overline{R_{rs}^{+}}\left(\lambda_{[850,950]}\right) \qquad \text{(eq. 7.4)}$$

$R_{rs\_sgc}^{+}$ was then transformed to subsurface reflectance (R_{rs}^{-}) via air/water -interface correction using the equation of Lee et al. (1999) (eq. 7.5).

$$R_{rs}^{-} = \frac{R_{rs\_sgc}^{+}}{0.5 + 1.5R_{rs\_sgc}^{+}} \qquad \text{(eq. 7.5)}$$

Starting with pre-defined initialization parameters, for each pixel, SWIM compared measured in -water subsurface and bottom -reflectance spectra to modeled in -water subsurface and bottom -reflectance spectra. Using a gradient -descent algorithm, the difference between them was minimized (in the least -squares sense) until it converged to a per-pixel set of optimum parameters. Upon convergence, the optimization algorithms provided, for each above -water pixel of the hyperspectral image, an estimate of water -column parameters Z, K_d, k_{uW} and k_{uB}. water height (Z) was kept for further post-processing. water-bottom reflectance (ρ) was calculated analytically from eq. 7.1, rewritten as eq. 7.6, and the estimated water -column parameters:

$$\rho = \frac{R_{rs}^{-} - R_{rs}^{\infty}\left(1 - A_0 e^{-(K_d + k_{uW})Z}\right)}{A_1} e^{-(K_d + k_{uB})Z} \qquad \text{(eq. 7.6)}$$

7.3.3.2.b) Post-processing

The resulting water-height and water-bottom -reflectance images were then post-processed:

- The water -height image was filtered spatially using a 3×3 median filter. Water height was then corrected for local tide elevation using the FES2014 model (Carrere et al., 2015) using the Python-based tidal prediction software pyTMD (Sutterley, 2021). Tidal corrections were applied per flight line using the associated acquisition time and central geographic coordinates. Finally, the data were converted from the hydrographic datum to the topographic datum NGF/IGN69 using the RAM product of Shom. The result was one AHI-derived bathymetric digital elevation model (DEM) per flightline.

- The water -bottom -reflectance image estimated by model inversion was successively filtered spectrally and spatially to reduced noise effects. Spectra were smoothed using the Savitzky-Golay method (Savitzky & Golay, 1964), based on least-square smoothing using local polynomial fitting. Smoothing parameters were defined empirically with local windows 7 bands wide and a polynomial order of 3. Spatial smoothing was performed using a 3×3 kernel to detect local outliers (>2 standard deviations) and replace them with the inlier local mean spectrum. The result was one AHI-derived water-bottom -reflectance image (Rb) per flightline.

The AHI-derived bathymetric DEM and AHI-derived Rb per flightline were then mosaicked to create two seamless products that covered the study area. The mosaicking strategy used scan-angle information associated with each pixel of the flightline. When flightlines overlapped, the pixel information kept for the mosaic was that acquired with the smallest absolute scanangle (i.e. closest to the nadir). This strategy was chosen to use fewer pixels from on the edges of flight lines, which often experience stronger sensor and surface effects.

These two layers of information were then used in a GIS environment (QGIS) to produce (i) a water-corrected submerged -landscape mosaic for visualization and prospection from visual aggregation (overlay) of the AHI-derived bathymetric DEM and AHI-derived R_b mosaics and (ii) spectral and morphological information layers to characterize structures and anomalies by analyzing spectral signatures and generating topographical profiles.

7.3.4 Evaluation of the approaches developed

7.3.4.1) Documenting inventoried fishweirs

First, the data-driven and physics-based approaches were assessed and compared to estimate their ability to visually identify the fishweirs inventoried in the reference dataset. morphological and spectral characterization using the physics-based approach was demonstrated on a known structure, the Gored Ar Litiri Vraz, inventoried by Daire and Langouët (2010) and included in the fishweir inventory.

7.3.4.2) Prospecting for unknown fishweirs

The approaches developed were applied to perform remote -sensing-based archaeological prospection on the Molène archipelago and identify anomalies that other prospection techniques had not previously identified.

An underwater survey was performed with the support of the National Marine Protected Area staff (Parc Naturel Marin d'Iroise) to evaluate the results of this AHI-based prospection. This survey was performed on 19 July 2021 near the island of Béniguet (Figure 7.3), on an area that included three identified anomalies selected for their differing contexts and morphological characteristics. We selected three anomalies based on the material and human resources available for this initial assessment.

Before the survey, all georeferenced data layers (i.e. anomaly positions, and data-driven and physics-based visualization results) were downloaded onto a GNSS-enabled mobile tablet using QGIS/Qfield open-source applications (QField, 2021; QGIS, 2021).

During the survey, the following *in situ* protocol was followed for each anomaly: (i) the boat was positioned at the GPS coordinates of the anomaly; (ii) the anomaly and its expected characteristics (i.e. depth, size, orientation and context) was visualized on the mobile tablet before the dive

(Figure 7.6a); (iii) three divers investigated the anomaly for 25-40 minutes (Figure 7.6b,c) and (iv) underwater videos were recorded using a GoPro® camera.

Figure 7.6. (a) Visualization of the anomaly and its expected characteristics (i.e. depth, size, orientation and context) on georeferenced data layers loaded onto a GNSS-enabled mobile tablet using QGIS/Qfield applications. (b) Underwater view of a diver at work. (c) Diver in action near anomaly 7.4.3"b" (images used with permission, © Yannis Turpin/OFB).

The survey was performed in good weather and sea conditions: Low wind speed, high solar irradiance and underwater visibility of ca. 10 m. Nevertheless, a high density of macro-algae (especially kelp) in summer reduced access to and interpretability of the seafloor.

For this study, the two main objectives of the underwater survey were to (i) confirm whether or not seabed structures consistent with the identified anomalies were present and (ii) collect information (observations and videos) to understand relations between remote -sensing data and field observations, and thus to provide insights for further archaeological interpretation.7.4.3

7.4 Results

7.4.1 Analysis of results of the data-driven approach

Fishweirs inventoried in the reference dataset were located by interpreting the "in-water" and "target" spectral visualization images (Figure 7.7). Of the 36 reference structures on the Molène archipelago, 32 (89%) were visible on the spectral visualization image.

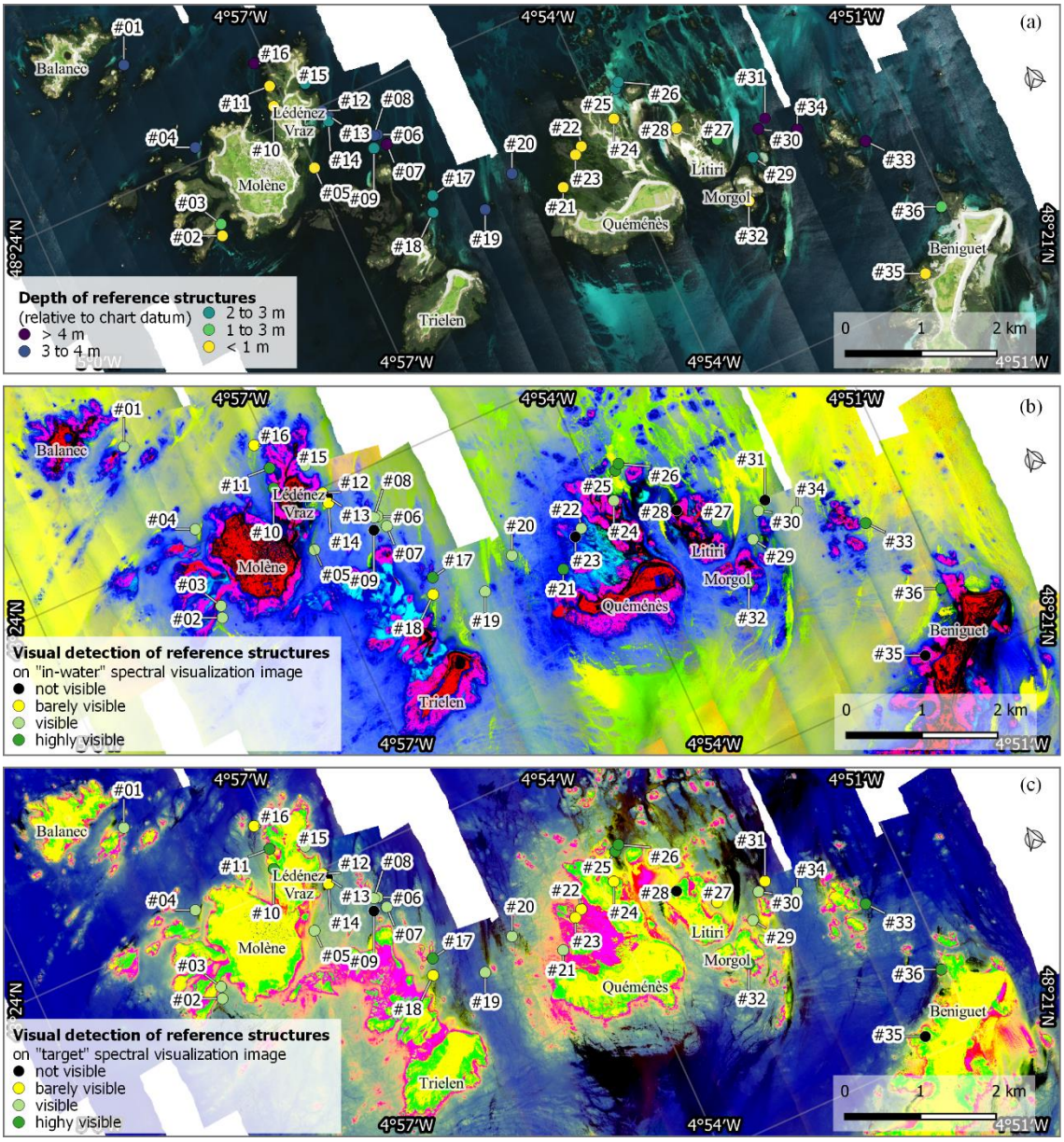

Figure 7.7. Visualization of Molène archipelago using hyperspectral imagery and a data-driven approach. (a) Above -water image, which is a true-color RGB visualization of water -surface reflectance (red: 620 nm, green: 570 nm, blue: 495 nm), (b) "in-water" spectral visualizations, (c) "target" spectral

visualizations. The inventoried fishweirs were located and numbered according to the list of Stéphan et al. (2019).

The ability to detect each structure on spectral visualizations was assigned one of four perception levels: not visible, barely visible, visible and highly visible. The four structures (11%) that were not visible were positioned relatively high (mean depth of 0.9 m) on the foreshore (Table 7.1), which was emerged when the images were acquired, which indicates that either the spectral visualization sampling strategy was not adapted to emerged areas or that the structures could not be differentiated spectrally from their environment (i.e. under a continuous and mono-specific algae cover). visible structures became more difficult to detect as water depth increased. Combining results of the two spectral visualizations, the mean depth ranged from 1.6 m for highly visible structures (25% of the reference structures) to 2.6 m for visible structures (47%) and 3.0 m for barely visible structures (17%).

Table 7.1. The number and mean depth (in parentheses, from hydrographic datum) of reference structures as a function of their degree of visibility on the "target" and "in-water" spectral visualizations.

Type of spectral visualization	**Not visible**	**Barely visible**	**Visible**	**Highly visible**
target	4 *(0.9 m)*	9 *(2.3 m)*	15 *(2.8 m)*	8 *(1.8 m)*
In-water	6 *(1.4 m)*	4 *(3.3 m)*	17 *(2.6 m)*	9 *(1.6 m)*
target or in-water	4 *(0.9 m)*	6 *(3.0 m)*	17 *(2.6 m)*	9 *(1.6 m)*

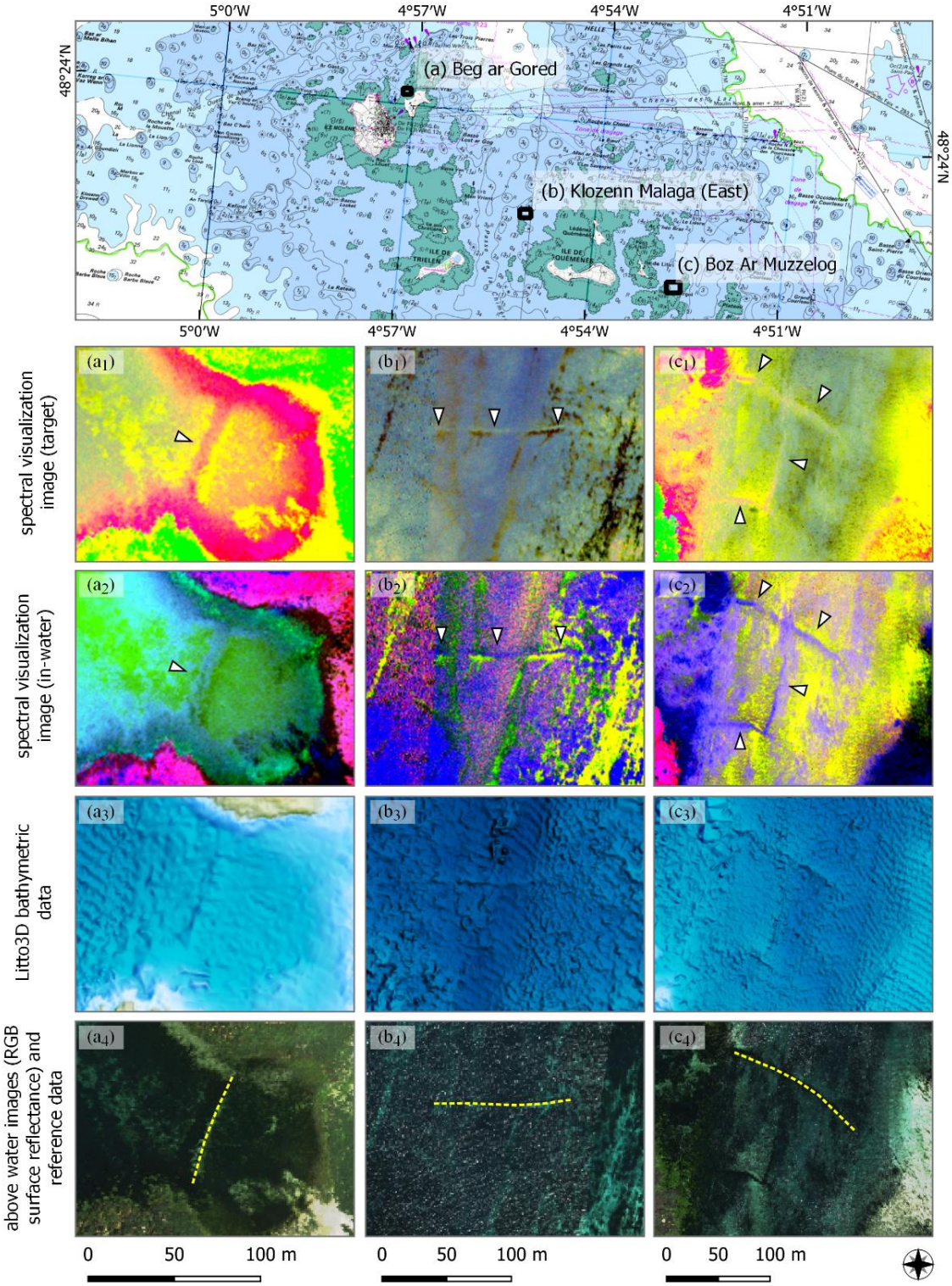

Figure 7.8. Data-driven visualization results for three fishweirs in the reference dataset of Stéphan et al. (2019). Letters a,b,c correspond to Beg Ar Gored, Klozenn Malaga (East) and Boz Ar Muzzelog, respectively. Index numbers (1,2,3,4) correspond to "target" spectral visualization, "in-water" spectral visualization, Litto3D® topo-bathymetric reference data and above -water images, respectively. Spectral

visualizations are color-composite images of the first three components (red: 1st , green: 2nd , blue: 3rd) of minimum -noise -fraction transformations. Above -water images are true-color RGB visualizations of water -surface reflectance (red: 620 nm, green: 570 nm, blue: 495 nm) (Source of above map background: Scan Littoral IGN/Géobretagne).

The spectral visualizations showed local linear patterns associated with the presence of fishweirs (Figure 7.8). However, local color variations depended on environmental parameters that influenced water -surface spectral information (i.e. surface conditions, depth, water -column composition and bottom reflectance). Although the data-driven approach does not estimate or infer these parameters, some characteristics of the reference structures could be determined by interpreting images. These characteristics included measurements of 2D morphological information (i.e. length, width) of the structure (as visible on the spectral visualizations). They also included information on uniformity based on identifying spectral continuities or discontinuities along the structures. Thus, Klozenn Malaga East (Figure 7.8b_1, b_2) showed some spectral discontinuities that were also visible on the topo-bathymetric reference data (local decrease in elevation). They could have been caused by degradation of the structure, which would require *in situ* confirmation. The spectral visualizations also showed some contextual characteristics of the structures, which helped interpret the structures and classify them according to the morpho-typology of Langouët and Daire 2009 (Figure 7.1). Thus, the visualization of Beg ar Gored (Figure 7.8a_1) indicated a structure, built perpendicular to facing rocky outcrops, that closed a sea cove (i.e. type AL). Klozenn Malaga East (Figure 7.8b_1, b_2) showed no particular connectivity with the shore; thus, it could be a type C. Boz Ar Muzzelog (Figure 7.8c_2) showed connectivity with the rocky shore east of Morgol, which indicated a construction strategy in relation to the island and a fishweir of type D. Its morphology was also more complex, including the crossing of linear features and sharp turns along its southern edge. This complexity was not clearly visible in the topo-bathymetric reference data; thus, it will require further investigation, including underwater observations.

7.4.2 Analysis of results of the physics-based approach

7.4.2.1) Identification of reference structures

The submerged -landscape mosaic image generated by overlaying the AHI-derived Rb mosaic on the AHI-derived bathymetric DEM mosaic (Figure 7.9) highlighted the complexity of benthic habitats and landforms. It is a synoptic visualization of the shallow water area with a virtual removal of the water column. The submerged landscape contained two informative components – bottom topography and bottom reflectance – that allowed for interpretation of the landscape context and identification of local anomalies.

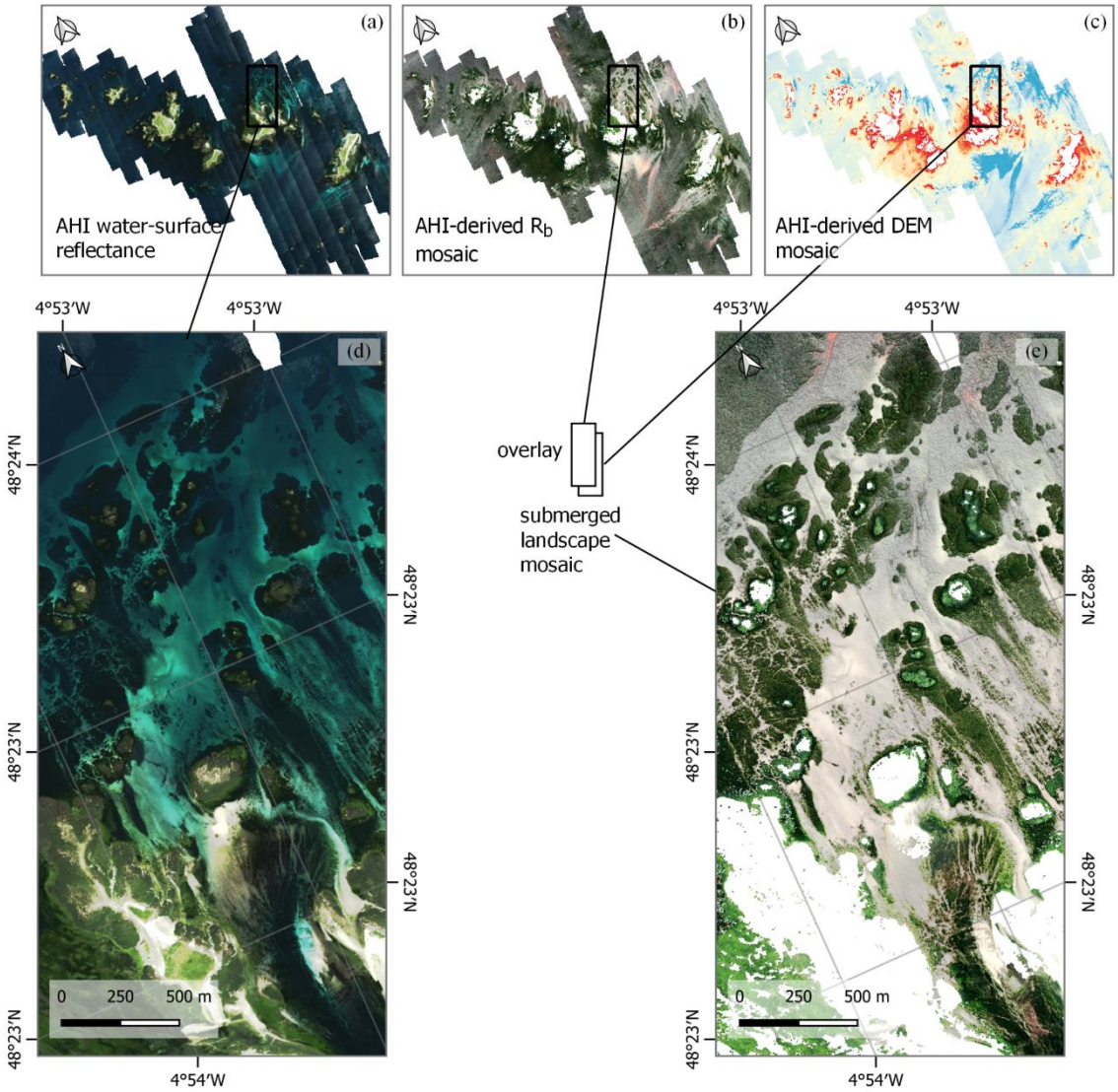

Figure 7.9. Visualization of the submerged landscape north of Lénédès Quéménès in the Molène archipelago: (a) RGB visualization of water -surface reflectance (red: 620 nm, green: 570 nm, blue: 495 nm); (b) RGB visualization of the water -bottom reflectance mosaic (red: 620 nm, green: 570 nm, blue: 495 nm) derived from the hyperspectral data; (c) Digital bathymetric model mosaic derived from the hyperspectral data; (d) close-up of the RGB visualization of water -surface reflectance; (e) close-up of the submerged -landscape mosaic image overlaying (b) and (c) as hillshaded terrain. white patches on the submerged -landscape mosaic corresponded to areas above the water level (land).

of the 36 reference structures inventoried on the Molène archipelago, 26 (72%) were visible on the submerged -landscape mosaic image, 17 percentage points fewer than those using data-driven approach.

Most reference fishweirs were identified on seafloor that had both vegetation and mineral elements (77% of the fishweirs detected) (Table 7.2), because stone fishweirs are often covered by

dense algae, and contrast between fishweirs and the surrounding environment facilitates identification of structures in the image. Fishweirs became more difficult to identify as mean water depth increased; it ranged from 1.2 m for highly visible structures (14% of the reference structures) to 2.5 m for visible structures (31%) and 3.5 m for barely visible structures (28%).The structures that were not visible (28%) were positioned relatively high (mean depth of 1.3 m) on the foreshore (including one above water at the time of acquisition, and thus excluded from the submerged -landscape mosaic image).

Table 7.2. Number and mean depth (in parentheses, from chart datum) of the reference structures according to their degree of visibility on the submerged -landscape mosaic image and the type of the water bottom (mineral, vegetation, both).

Water bottom	**Not visible**	**Barely visible**	**Visible**	**Highly visible**	**Total**
vegetation	4	4	2	-	10
mineral	1	-	-	-	1
mixed bottom	4	6	9	5	24
Excluded (above water)	1	-	-	-	1
Total	10 *(1.1 m)*	10 *(3.5 m)*	11 *(2.5 m)*	5 *(1.2 m)*	

7.4.2.2) Toward characterization of fishweirs

Gored Ar Litiri Vraz, located on the eastern shore of the Litiri islet, is a stone fishweir of type AC (Daire & Langouët, 2010). The structure was identified as #27 in Stéphan et al. (2019). Its characteristics were taken as baseline from the reference dataset (Table 7.3).

Table 7.3. Characteristics of the Gored Ar Litiri Vraz fishweir

XY Local coordinates (Lambert 93 / RGF93	**Length**	**Width**	**Height**	**Depth (chart datum ref.)**
117308 m, 6837640 m	325 m	5 m	unknown	1.77 m

Although considered "barely visible" in the "target" spectral visualization, *Gored Ar Litiri Vraz* was considered "visible" by the data-driven and physics-based approaches.

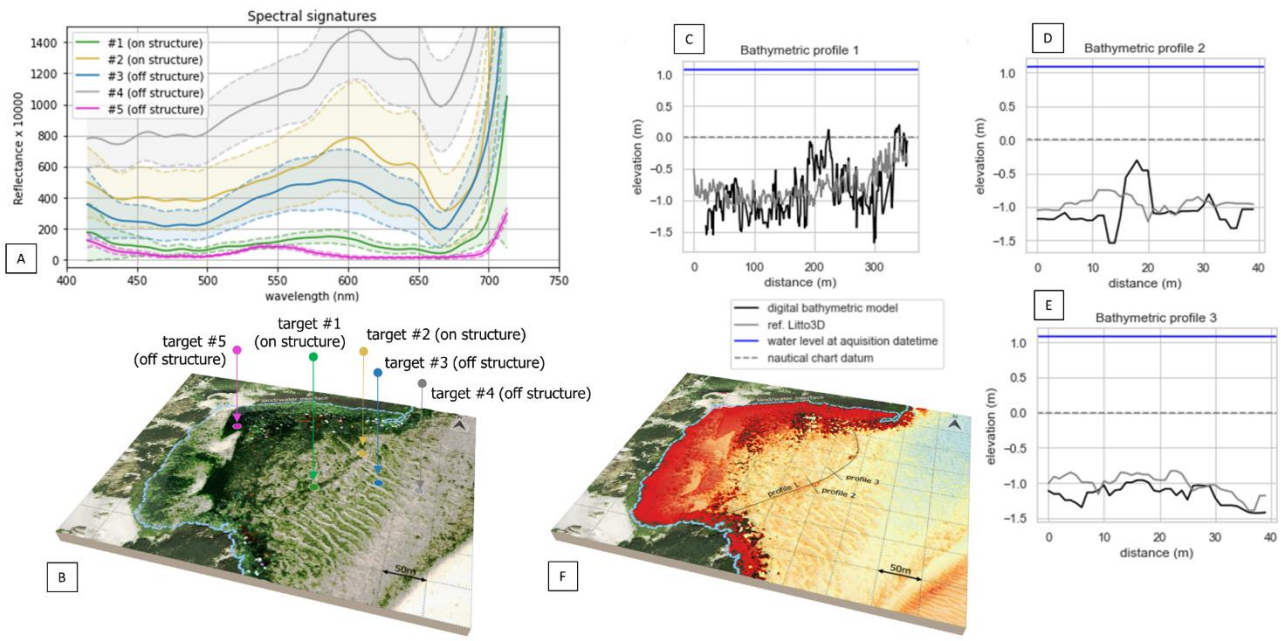

Figure 7.10. Bottom -reflectance spectral signatures (left: A, B) and topographic profiles (right: C, D, E) extracted from hyperspectral derived information for the characterization of the Gored Ar Litiri Vraz *fishweir.*

The spectral signatures (Figure 7.10A) of five targets selected on the water -bottom reflectance image (Figure 7.10B) differed greatly in amplitude and shape, especially in the 500-670 nm wavelength range. Targets #1 and #2 were selected on the fishweir, while targets #3, #4 and #5 were selected off of it. While no distinction between on- and off -structure signatures was interpreted, the spectral shape and low spectral variability of targets #1 and #5 indicated the presence of dense macroalgal cover. The peak reflectance in the visible range of the spectrum was centered around 580 nm for target #1 and 550 nm for target #5, which could indicate a stronger presence of green algae on target #5. Targets #2, #3 and #4 had higher amplitude spectra (5-15% maximum reflectance), which indicates a mineral contribution with a reduction in macroalgal cover. However, absorption bands around 630 nm and 670 nm are characteristic of chlorophyll C and chlorophyll A, respectively (Uhl et al., 2016), which indicates the presence of benthic microalgae.

Three bathymetric profiles (Figure 7.10C, D, E) were extracted from the bathymetric DEM (Figure 7.10F). The longitudinal profile (profile 1) followed the curvilinear structure from north to south over a distance of 318 m (Figure 7.10C). The estimated bathymetry varied from -1.68 m to 0.20 m (mean of -0.86 m, standard deviation of 0.41 m). The root mean square difference from the topo-bathymetric reference dataset was 0.20 m. Although the high length:height ratio did not facilitate interpretation of the profile or its comparison with the topo-bathymetric reference dataset, a feature with higher elevation (0.5 m above the mean) was identified ca. 190-210 m away. This feature corresponded to dense vegetation cover identified in the Rb image. The transverse profile 2 (Figure 7.10D) taken across this feature indicated that it was 5 m wide and 0.5 m high. While

this width corresponded to information in the reference dataset, further investigation is required to confirm whether its height corresponded to the algal canopy or the aboveground stone structure.

7.4.3 Prospection of shallow-water -bottom anomalies

7.4.3.1) Detection and characterization of potential fishweirs

To supplement the mapping and characterization of inventoried fishweirs in the study area, remote -sensing -based archaeological prospection was performed using the hyperspectral data on the Molène archipelago.

A total of 28 new anomalies, whose contexts and morphologies suggested potential human-made underwater structures, were visually identified and characterized from the data-driven and physics-based visualization results, and three of them were selected for initial assessment of the approach (Figure 7.11).

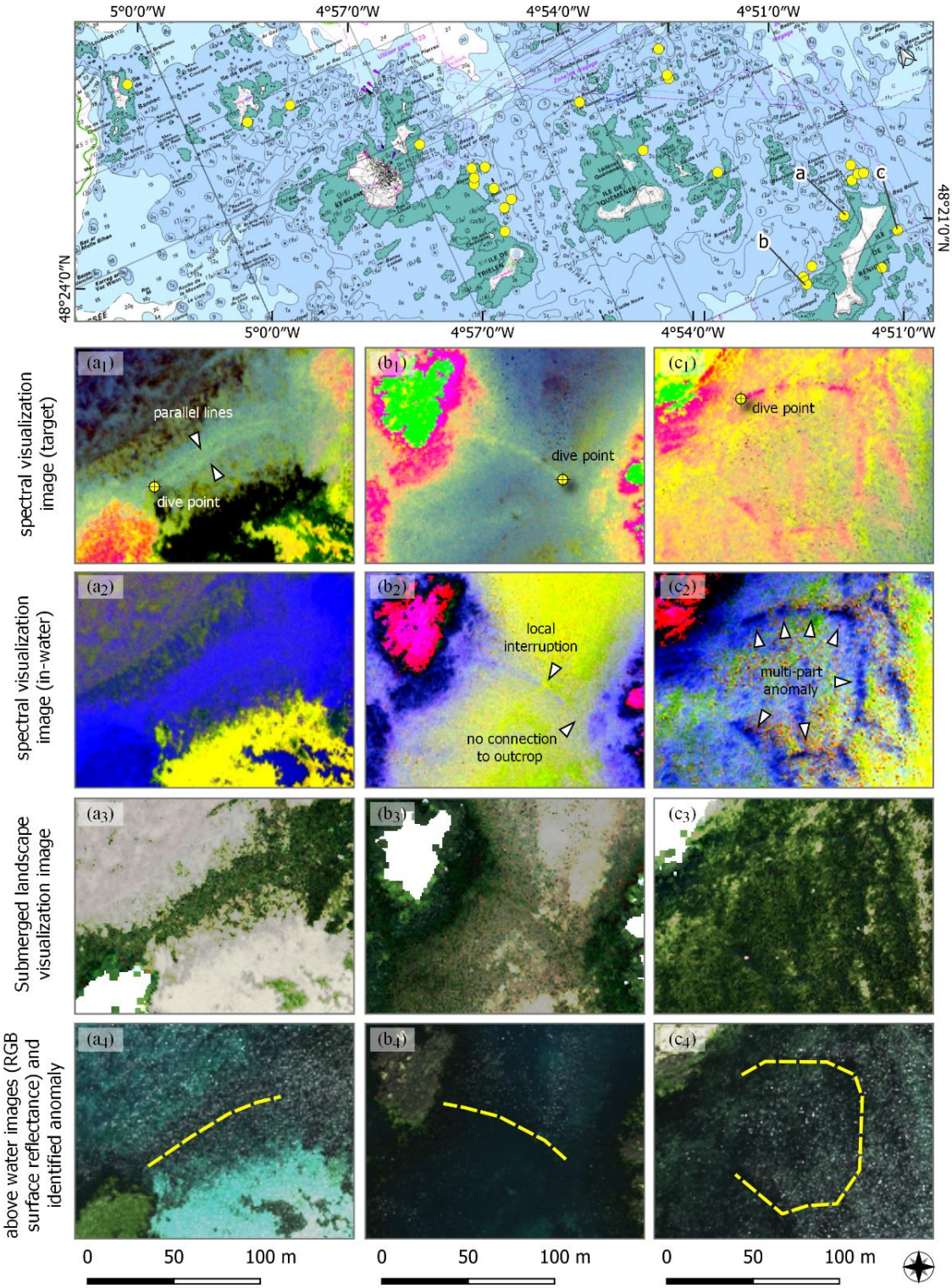

Figure 7.11. Location of the 28 anomalies (top) and data-driven as well as physics-based visualization results for the three anomalies that were verified by underwater surveys (a,b,c). Index numbers (1,2,3,4) are for "target" spectral visualizations, "in-water" spectral visualizations, submerged -landscape mosaic

images and interpreted anomalies overlain on water images , respectively (Source of "top map" background: Scan Littoral IGN/Géobretagne).

The hyperspectral-based interpretations that were conducted are depicted here for the 3 selected anomalies:

- Anomaly "a" (Figure 7.11a$_{1-4}$) was a quasi-straight linear anomaly 90 m long located northwest of Béniguet. Because it connected two rocky outcrops and closed a small sea cove, it may have been a fishweir of type AL or AC. The anomaly was located below chart datum (-1.7 m). On the "target" visualization (Figure 7.11a1), the anomaly appeared as two parallel lines. The gap between the two lines was ca. 2 pixels (2 m), and the anomaly was ca. 8 pixels wide. Although fishweirs of double stone lines have been inventoried (Langouët & Daire, 2009), this gap seemed too wide for two facing walls of a single linear fishweir structure.
- Anomaly "b" (Figure 7.11b$_{1-4}$) was a curvilinear anomaly 90 m long located West of Béniguet. It was located below chart datum (-1 m) and connected to a rocky outcrop on its western end. While it was not clear whether it was connected on its eastern end, a small outcrop there suggested this possibility. Given its morphology and geographical context, the anomaly may have been a fishweir of type AC or DC. Local discontinuity in the curve observed in the "in-water" visualization (Figure 7.11b$_2$) may be the location of the sluice if the structure were confirmed to be a fishweir.
- Anomaly "c" (Figure 7.11c$_{1-4}$) was a multipart pseudo-circular anomaly 80 m in diameter located northeast of Béniguet. It did not correspond to any morphology of known fishweirs, but its spatial arrangement suggested a non-natural feature. The anomaly was located below chart datum (-0.6 m).

7.4.3.2) Underwater observations

Underwater observations and videos of these anomalies confirmed the presence of three archaeological structures on the seafloor. At sea, GNSS positioning of the boat helped to locate the structures. Before each dive, visualization of the anomalies and their expected characteristics derived from hyperspectral data helped to identify them.

- Dive observations of anomaly "a": The dive started at the western tip of the anomaly (Figure 7.11a$_1$), where it is attached to a rocky outcrop that emerges at lowtide. A large linear structure was quickly identified on the seafloor. It is a stone structure, ca. 1.5 m wide and of variable height (up to 0.7 m), covered mainly with redalgae and golden kelp (*Laminaria ochroleuca*). Large flat edge-mounted stone blocks (up to 1 m in diameter) lie on the longitudinal axis of the structure, similar to previously documented fishweirs (Gandois et al., 2018). The structure was followed for a length of ca. 30 m. No double stone lines were visible during the dive, but underwater video-frames taken along the longitudinal axis showed a large difference in reflectivity (Figure 7.12a) between the

structure (lowreflectivity due to the algal cover) and its surroundings on both sides (highreflectivity due to the dominance of coarse sand and gravel covered by the seaweed Saccorhiza polyschides). This difference could explain the appearance of double lines for this anomaly; the structure would thus be the central line inbetween.

- Dive observations of anomaly "b": The dive started at the eastern tip of the anomaly (Figure 7.11b1). The linear structure on the seafloor was rapidly identified as a stone structure lying on coarse sand and gravel. Its morphology appears similar to that of anomaly "a", although more disturbed, with large edge-mounted stone blocks lying regularly along the longitudinal axis (Figure 7.12c,d). The structure is colonized by kelp, especially *Laminaria digitata* and *Laminaria hyperborea.* The local discontinuity ca. 15 m from the starting point was identified. Before and after it, the structure appears to have different stonework, with edge-mounted stone blocks on the transversal axis. This anomaly would be the sluice of the fishweir, but it needs to be confirmed by additional investigation.
- Dive observations of anomaly "c": The dive started at the northwestern tip of the pseudo-circular anomaly (Figure 7.11c1). A structure standing out from its surroundings was identified at the given position. Dense kelp cover (especially *S. polyschides*) made underwater interpretation difficult, but stone structures that rise from a coarse sand bottom were observed. The first sub-structure, ca. 2 m wide and 10 m long, is composed of large edge-mounted stone blocks positioned longitudinally on each side of the structure, with smaller blocks or rubble between them (Figure 7.12d). After several m of void, another degraded structure was seen (ca. 1 m wide , 2 m long and 0.5 m high). It is composed of flat stones arranged in horizontal layers. An activerisk of degradation was identified at this site due to large kelp clamped onto moveable stoneblocks that could be dragged away during storms, which may explain the discontinuous nature of the structure. This apparently non-natural structure must be investigated further to determine its nature.

Figure 7.12. Underwater video-frame extractions during survey dives of three anomalies identified by airborne hyperspectral imagery. (a) Wide-scale view of the stone structure covered by redalgae and surrounded by golden kelp on Anomaly "a". (b and c) Close-up view of edge-mounted stone blocks of anomaly "b". (d) Perspective view of the edge-mounted stone blocks positioned longitudinally on each side of the structure of anomaly "c". (Images used with permission, © Yannis Turpin, Jean-André Prat, Livier Schweyer/OFB)

7.5 Discussion

7.5.1 The data-driven approach

The data-driven approach developed used MNF dimensionality reduction to emphasize spatial/spectral variations related to the presence of submerged structures. The sampling strategy (target and in-water) was defined to cover a variety of local situations and adapt the data projection accordingly. MNF was chosen for its computational efficiency and ability to segregate noise from signals, thus making it easy to apply to real airborne hyperspectral data of large spatial extent.

Since MNF is a linear dimensionality reduction technique, non-linear relations in the data may not appear in the resulting image. Non-linear techniques such as UMAP (McInnes et al., 2018) and T-SNE (Pouyet et al., 2018) could be used to address this limitation. However, they were not

applied in this study due to the large amount of computational resources required (thus limiting their application to local examples).

Data-driven approaches, which depend on the sampling strategy, also lack standardization. In this study, the reduced components (bands) were empirically selected as the first three bands of the MNF to standardize visualization of the entire study area. Modifying the data -sampling strategy would influence the spectral visualization directly, thus decreasing the ability to compare study areas or types of data acquisition. Moreover, the first three components (visible as RGB) are only a partial or compressed representation of the signal. However, combining the visualization of more than three components remains a challenge since it increases the number of visualizations and thus limits its operational use for human-based interpretation.

Despite these limitations and the lack of physical interpretability, the data-driven approach identified 89% of the inventoried fishweirs. It was thus considered a more relevant combination of data/approach for visualizing submerged structures than those previously used to create the reference inventory (Stéphan, Gandois, et al., 2019)(MBES and ALB together represented 80%, while airborne prospection represented 22%).

7.5.2 The physics-based approach

The physics-based approach overcame limitations of physical interpretability by estimating physical characteristics of the scene, especially water height and water -bottom reflectance. Combining these outputs provided a valuable source of information for representing water-free submerged landscapes. While the physics-based approach had lower identification performance overall (72%) than the data-driven approach (89%), it allowed for extraction of morphological and spectral characteristics of structures and surrounding environment.

To date, combining AHI data and the physics-based approach was not yet considered by coastal archaeologists to prospect large submerged landscapes. This study confirmed that AHI provides valuable data for this application. Nevertheless, inferring consistent water -column and water -bottom reflectance from an airborne sensing signal is a complex concern with several challenges. One challenge is related to inversion of the semi-analytical model, especially its parametrization, including the design of the water -bottom model used as a support for the inversion and the initialization parameters. Another challenge concerns the direct model itself, which remains a simplified representation of complex interactions of light and matter in the water column and with the water bottom. For example, Lee's model assumes that the composition of the water column remains constant vertically and that the bottom surface has an isotropic (Lambertian) character. These assumptions do not hold in reality, but they are one way to represent the complex reality. A third major challenge is related to the pre-processing steps, including atmospheric correction, sunlight removal and water/air interface correction. These steps, which are also based on models, imply to take into account a certain level of uncertainty in the process of converting at-sensor data to seafloor information. The definition of the uncertainty level at each step of the

signal processing chain and its propagation from raw data to output information is an important challenge for the earth-observation research community, and several studies (Gillis et al., 2018; Sicot et al., 2021; Thomas et al., 2021; Thompson et al., 2019) have paved the way to a better characterization of errors throughout the hyperspectral data value chain.

the data-driven approach yielded smaller spatial/spectral variations than the physics-based approach when used to detect fishweirs. This indicated that some of these small variations were probably not conserved (or emphasized) during radiative -transfer -model inversion. Identifying the characteristics of such variations could help determine the reason for the loss (e.g. direct model, inversion, water -bottom model, pre- or post-processing steps) and improve the utility of the estimated water -bottom signature and bathymetric model. This kind of investigation could be facilitated by acquiring *in situ* underwater spectral signatures (underwater VNIR spectrometry). While the methods of this approach lie beyond the scope of this study, they could be applied to assess further the robustness of estimated water -bottom reflectance as a physical signal.

7.5.3 Complementarities of data-driven and physics-based approaches

As discussed, data-driven and physics-based approaches each have advantages and disadvantages for mapping submerged archaeological landscapes. In operational conditions, the two approaches complemented each other well. The data-driven approach can be applied rapidly without considering the complex interactions of light and matter between the sensor and the targeted seafloor area. It showed interesting results for visualizing small spectral/spatial variations that helped identify underwater anomalies. Moreover, the synoptic perception and interpretation of the submerged landscape was provided mainly by the physics-based approach, via its original visualization of combined bathymetry and water -bottom reflectance. Using both approaches together as visual aids for *in situ* verification was valuable for archaeological prospection in shallow waters. This complementarity provides interesting perspectives for developing both approaches independently and in combination.

7.5.4 Information provided by the spectral dimension

Active optical (ALB or ALTB) and acoustic (MBES) sensors traditionally used for hydrographic surveys essentially collect data based on range (distance) measurements. In contrast, as a passive optical sensor, AHI collects data based on spectral measurements.

The remains of stone tidal fishweirs are usually low and narrow linear structures. The combined effects of degradation and sedimentation reveal structures a few tens of cm high above the sea bottom (locally up to 1 m, with edge-mounted stones only a few cm thick) and only a few m wide. These structural characteristics influence the bottom topography in a tenuous and fragmented way, which makes it difficult to identify them from bathymetric data. These variations in water height are also difficult to measure spectrally; however, variation in the type of bottom (e.g. soft substrate vs. macro-algae-colonized stone, two different macro-algae covers) cause perceptible

spectral variations. for example, AHI-derived information led to identification of anomalies "b" and "c" (both confirmed with underwater observations), which were partially or completely imperceptible in the topo-bathymetric reference data (Figure 7.13). This performance highlights the utility of information provided by AHI in the context of identifying partially preserved or degraded submerged structures.

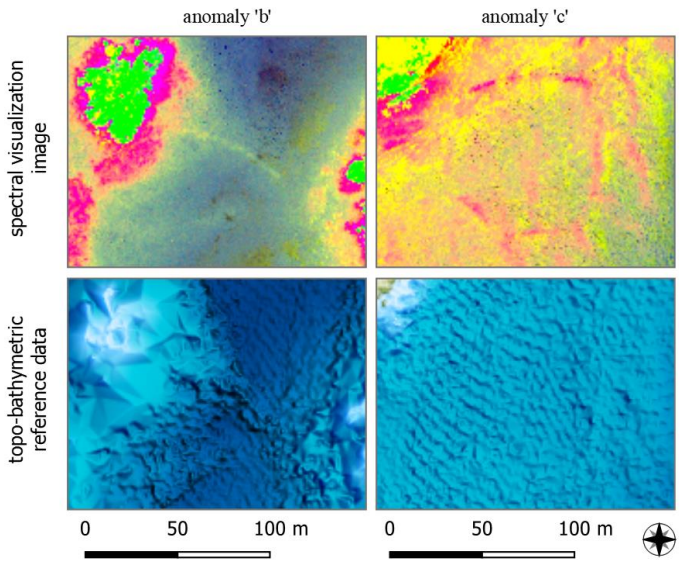

Figure 7.13. Comparison of observed anomalies "b" and "c" using (top) AHI-derived spectral visualization images and (bottom) topo-bathymetric reference data.

7.5.5 Hyperspectral imagery as a new tool for mapping submerged landscapes

To our knowledge, previous studies have not addressed the representation of large-scale submerged landscapes using both bathymetry and bottom spectral information. While some coastal archaeology studies have stressed the importance of developing non-destructive remote -sensing methods for mapping underwater landscapes (G. N. Bailey & Flemming, 2008; Benjamin et al., 2019; Bowens, 2009; Jöns et al., 2019; Menna et al., 2018; Wickham-Jones, 2018), to date, AHI has not been considered as a source of information to document submerged archaeological landscapes. As shown in the present study, AHI can be applied operationally to manage underwater cultural heritage in shallow waters due to its ability to capture small variations in light transmission through the water column and its relatively low-cost (i.e. there can be a factor more than 10 between the cost of a VNIR AHI survey and a ALB survey).

Despite some limitations (e.g. low water turbidity, low-reflective seafloor, shallow depth) inherent to using optical remote -sensing data to map shallow waters, AHI appeared to be optimal in this study for generating visualizations that combined relief and seafloor spectra to cover the "whiteribbon" (Leon et al., 2013).

Following the example of methods currently being developed for Airborne LiDAR archaeological prospection on land (Guyot, Lennon, Lorho, et al., 2021), future studies could focus on

(semi-)automatic detection and characterization of structures from AHI-derived data in submerged contexts, for example using object-based image segmentation with state-of-the-art deep convolutional neural networks.

The increasing development of spaceborne, airborne and handheld hyperspectral sensors (Behmann et al., 2018; Jia et al., 2020; Ødegård et al., 2018; Transon et al., 2018; Zhong et al., 2018) should also provide new perspectives on multiscale and multi-temporal approaches applied to coastal archaeology and submerged landscapes in the near future.

7.6 Conclusion

underwater archaeological heritage is facing increasing threats of natural and human origins. The need for mapping information for the seafloor is becoming a critical challenge, especially in shallow -water environments that lack high-resolution synoptic data. In this study, we demonstrated that AHI could provide unique information to identify and characterize submerged fishweirs and more generally map submerged landscapes. To assess the potential of AHI in this context, two approaches were developed. First, a data-driven approach for visualizing submerged structures by using minimum -noise -fraction transformations adapted to targeting underwater or infratidal fishweirs was applied to water -surface reflectance imagery. Second, a physics-based approach based on inverting a shallow -water radiative -transfer model was used to estimate bathymetric and water -bottom reflectance data that were then combined to develop a large-scale visualization of the submerged landscape. The results showed that AHI-derived information was more comprehensive than that from bathymetric LiDAR, acoustic sounding or standard airborne imagery for identifying inventoried fishweirs of the Molène archipelago. The two approaches were then applied to perform archaeological prospection by identifying and characterizing AHI-derived seafloor anomalies not previously identified. Diving operations on three of them confirmed the presence of underwater structures whose characteristics were associated with human structures and remains of ancient fishweirs. These results open multiple perspectives to further improve and strengthen application of AHI for mapping submerged archaeological landscapes. In the context of the Molène archipelago, the identification of new fishweirs and the remaining potential of AHI-derived anomalies also raise questions about these structures, the past-societies that built them and the conservation effort necessary to protect such unique cultural heritage.

Summary of Part III

In this third part, we have attempted to address the important concerns of archaeological mapping in submerged area by questioning the fact that AHI could be a pertinent data for accessing sea-bottom spatial/spectral information in archaeological context. To our knowledge, the evaluation of AHI in underwater archaeological context was never performed before and we were able to demonstrate the potential of this airborne passive optic data in two different case studies and we raised some of its limits and domain of applicability.

More specifically, in chapter 6, we have shown that AHI could be a relevant source of data for the documentation of inventoried submerged small-scale structures (megalithic *stèles* of Er Lannic) laying in the first few meters of water depth. We particularly identified that the visualization of the structures was made possible by data-driven approach based on the reduction of dimensionality of the hyperspectral surface reflectance datacube, and that local (Reed-Xiaoli detector) and global (Isolation Forest) anomaly detection algorithms, could be used to help identifying the structures of interest from a AHI derived color-composite image. We also demonstrated that a first morphological and spectral characterization of individual *stèle* could be considered by mobilizing a physics-based approach (i.e. using the inversion of a shallow water radiative transfer model for bathymetry and bottom surface reflectance).

In chapter 7, as a complementary approach to the previous chapter, we evaluated AHI in a different geo-archaeological context: the stone tidal fish-weirs of the Molène archipelago. Data-driven and physics based approach were also developed and extended to demonstrate that AHI, for this study, was a relevant source of data (compared to traditional sources such as aerial photography and bathymetric measurements) to map submerged structures in shallow waters (up to 5m deep). For the data-driven approach, two different sampling strategies (in-water and target sampling) were used for guiding the MNF dimensionality reduction and visualization of spectral/spatial anomalies which confirmed the potential of AHI for visualizing known submerged structures (89% of fish-weirs were perceived). The physics-based approach, by estimating the bathymetry and the bottom reflectance which were overlaid to form a submerged landscape visualization image, showed a reduced capacity to reveal the submerged structures (72% of fish weirs were perceived). However, it offered the ability to physically characterize the structures and their environment. More importantly, the approaches appeared to be complementary and were assessed together in a prospection campaign at the scale of the archipelago (126 km² of imagery). The initial results of this campaign, that includes *in situ* verifications by diving operations, have so far confirmed the identification of 3 underwater structures previously unknown.

The results of these studies, which demonstrate the potential of AHI as an innovative source of data for archaeological prospection in submerged coastal area, should however not mask the limitations and obstacles to a wider use of AHI in operational context, including the dependence

Guyot, Alexandre. Contribution of airborne LiDAR and hyperspectral data to archaeological mapping in terrestrial and submerged environments. 2021

to local conditions from a meteo-oceanical point of view (turbidity, sea surface conditions, illumination conditions) and from a geographical point of view (coastal topography and nature of the sea-bottom).

A number of perspectives stem from these first experiments and results, which are discussed in general conclusion.

Guyot, Alexandre. Contribution of airborne LiDAR and hyperspectral data to archaeological mapping in terrestrial and submerged environments. 2021

General conclusion & perspectives

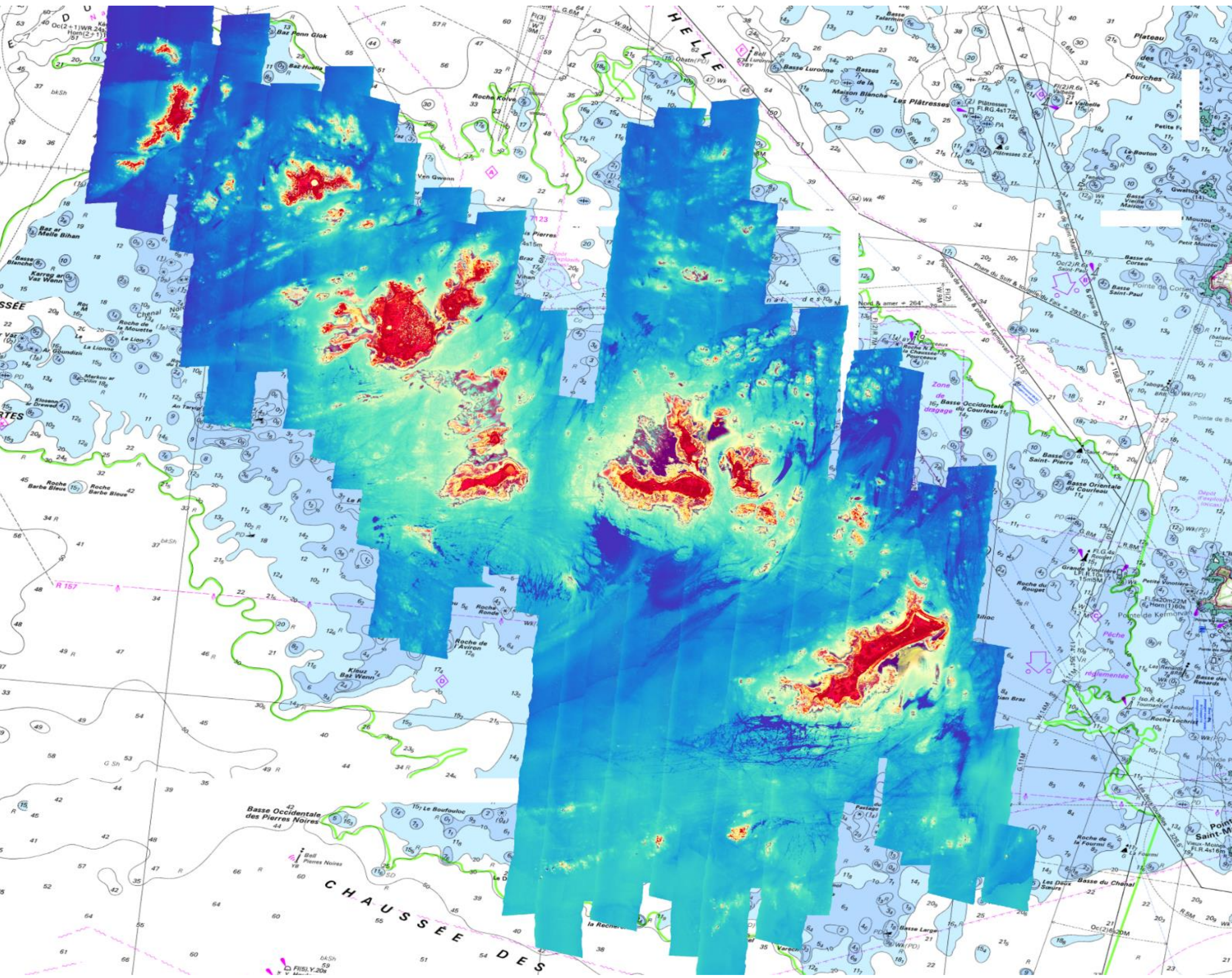

General conclusion & perspectives

The objective of this thesis was to assess the contribution of airborne LiDAR and hyperspectral remote sensing data for archaeological mapping in terrestrial and submerged environments.

In the first part of this thesis, we exposed the stakes of archaeological mapping and the current challenges posed by remote sensing applied to archaeological mapping. In the last decades, global environmental and social changes have affected the archaeological heritage at an increasing pace. In the meantime, remote sensing has proven to be an important tool participating in the inventory and preservation of this heritage by supporting archaeological research through the inclusion of unique spatial information. In this context, airborne LiDAR and airborne hyperspectral data have played essential roles. However, despite their respective contributions, airborne LiDAR and hyperspectral data did not reveal all their value for the detection and characterization of archaeological structures, especially in landscapes where archaeological prospection is limited, such as in shallow waters or woodlands. Accordingly, we hypothesized that the perception and characterization of archaeological landscapes and structures from LiDAR and hyperspectral data can be improved and extended by combining innovative data visualization techniques and computer-vision algorithms.

To support this idea, we developed two main research themes based on airborne remote sensing data collected in the region of Brittany:

- The first theme, developed in Part 2, based on airborne LiDAR data acquired over the area of Carnac and the Gulf of Morbihan, presented the assessment of multiscale topographic analysis and (semi-)automatic object segmentation applied to LiDAR-derived terrain data in the context of archaeological mapping in woodland-dominated landscape. In particular, we showed that state-of-the-art image analysis methods, such as deep convolutional neural networks, could be used with LiDAR-derived terrain data to not only detect but also segment (delineate) potential archaeological features in complex woodland environments. We also showed that such algorithms reached their best performance (mAP@IoU = 0.77) when multiscale topographic analysis was used to generate the input images. These results (i) confirmed the potential of deep CNN for detecting/segmenting and thus characterizing heterogeneous archaeological features from LiDAR-data in complex landscape, and (ii) illustrated the interest in using such computer-vision method to objectively assess the efficiency of different LiDAR-derived terrain visualization techniques.

  Beyond statistical results, these outcomes led to new insights on the use of (semi-)automatic approach on LiDAR data in archaeological context. First, even in sparse sample data application (in the magnitude of hundred samples), we confirmed that deep-learning can successfully be applied by leveraging a transfer learning strategy and adapted

inputs formats. Second, we demonstrated that the complex and disputed concern of defining archaeological typologies from remote sensing data could be deferred to the post-detection phase by implementing a one-class strategy. The instance segmentation can support this strategy by providing post-detection morphological or spectral characteristics at the anomaly level. Third, we confirmed that multiscale topographic information can provide contextual information for the detection and characterization of archaeological structures, and when combined (by merging techniques) with local morphological information (such as red-relief image map and local-relief model) can provide a highly efficient visualization technique (named here as e^2MSTP) adapted to both computer-based and human-based perception. The design of improved versions of such visualization techniques could furthermore be facilitated by the objective assessment capability of deep convolutional neural networks.

From an operational point of view, outside this thesis, the method was implemented in a large-scale diachronic archaeological prospection scheme on the area of Carnac and the Gulf of Morbihan (see reports Guyot et al., 2019, 2020, 2021) with the support of the SRA-Bretagne. Out of 73 verified anomalies, the confrontation of remote sensing-based prospection with terrain-based verification has, so far, resulted in the confirmation and declaration of 24 new archaeological entities (33%) in the *carte archéologique*. 22 anomalies (30%) were of undetermined nature (further investigation required), 7 anomalies were already inventoried but with imprecise geo-position information, and only 20 anomalies (20%) were considered as either considered as natural or recent man-made topographic anomalies.

- The second theme, developed in Part 3, based on airborne hyperspectral data acquired over (i) the gulf of Morbihan with the submerged megalithic structure of Er Lannic, and (ii) the Molène archipelago, presented the potential of airborne spectro-imagery for the documentation of inventoried underwater archaeological remains, but also provided unique sea-floor information to support large-scale archaeological prospections in coastal shallow waters. In particular, we showed that airborne hyperspectral imagery which was, to our knowledge and until now, not identified as a potential source of information for submerged archaeological prospection, appeared as efficient data for this challenging context. In particular, we showed that subtle spectral/spatial information could be extracted from water surface reflectance data to map and document inventoried submerged metric-scale megalithic structures with higher spatial details than traditional hydrographic methods such as acoustic sounding or bathymetric LiDAR. Furthermore, the potential of airborne hyperspectral information extraction from data-driven and physics-based approaches was further assessed in a different geo-archaeological context. The results, on the Molène archipelago, confirmed AHI as a relevant source of data (89%

Guyot, Alexandre. Contribution of airborne LiDAR and hyperspectral data to archaeological mapping in terrestrial and submerged environments. 2021

of structures perceived) compared to traditional sources such as aerial photography and bathymetric measurements (respectively 22% and 80% of structures perceived).

Beyond statistical results, these outcomes led to new insights on the use of airborne hyperspectral data for archaeological mapping in submerged context. Notably, we demonstrated that spatial/spectral visualizations, either based on synthetic composite images or on image of estimated physical parameters such as water depth and water-bottom reflectance, offered complementary information for perceiving subtle water-bottom variations (variations in morphology and/or in nature). This effectively confirmed the suitability of AHI for mapping submerged structures at local scale, but also for providing an innovative and unique way of representing submerged archaeological landscape for large-scale mapping of coastal environment.

From an operational point of view, the developed method is currently implemented and evaluated in a large-scale archaeological prospection campaign in shallow waters in the Molène archipelago. The initial results presented in chapter 7 will be complemented by underwater situ verifications planned for the coming months.

The use of remote sensing and computer-based information extraction implies different sources of uncertainties. Remote sensing for archaeological mapping is for example subject to uncertainties and errors at all levels of workflow: from measurements uncertainties, model uncertainties, human interpretation bias or pareidolia. Remote sensing can therefore not be a strategy on its own, isolated from archaeological ground. Nevertheless, through the two main developed themes, we demonstrated how LiDAR and hyperspectral remote sensing data could enhance the perception of a territory, from subtle local structures to wide landscapes. These data and methods provide often unprecedented points of view on topographic or spectral characteristics of the observed surfaces, in a synoptic manner thanks to the spatial continuity of information. This unprecedented capacity to represent a territory raises questions about the perception of these data and their relationship to the so-called “ground truth”. On several occasions during this thesis, during field campaigns, we have been confronted with the shift in perception or interpretation between an indeterminate structure, clearly visible on remote sensing data but illegible or difficult to perceive in the field. Hyperspectral imagery visualizations on intertidal or subtidal areas, or LiDAR data visualizations under dense forest cover are the most prominent examples of this "shift". Even in the field of remote sensing, this paradigm is relatively recent (related to the advent of very high-resolution synoptic data combined with beyond-visible information). Questioning the position of remote sensing beyond the traditional opposition of desk-based vs field-based approach is therefore becoming crucial in Earth-related science such as archaeology. Rather than systematically confronting remote sensing data on the one hand and field data on the other, we advocate a better integration of the two approaches in a scheme where neither of them can be dissociated from the other.

Guyot, Alexandre. Contribution of airborne LiDAR and hyperspectral data to archaeological mapping in terrestrial and submerged environments. 2021

To promote this integration and as perspective of this thesis, different themes, arising from the contributions and limitations highlighted in this work, could be developed on methodological and thematic aspects of remote sensing for archaeological mapping.

From a methodological point of view

The perspectives include the use of vectors and sensors developed for acquiring data of increased spatial or spectral resolution. UAV-born LiDAR and hyperspectral sensors are progressively being developed. The miniaturization of sensors, often at the expense of optical quality, is opening new perspectives to further reduce the gap between remote sensing and field measurements. This is particularly exemplified in hyperspectral imagery for which UAV-based image-spectroscopy - little affected by atmospheric effect due to low-altitude operation- can provide spectral measurements at centimetric resolution (similar to field spectroscopy) alongside a spatial contextualization. While large-scale coverage remains limited for UAV (limited to areas ranging from few hectares to few km^2), such highly defined spectral-spatial information could facilitate the development of spectro-imagery analysis (such as spectra unmixing) at larger scale and larger spatial resolution.

Perspectives also arise for data analysis, especially on the visualization and automatic detection phase. For data visualization, this particularly implies to evaluate non-linear dimensionality reduction techniques (such as UMAP or deep auto-encoders), that could be applied to hyperspectral data as well as applied to the results of the hyperscale topographic analysis of LiDAR-derived terrain data, to enhance the perception of subtle non-linear relations in spectral or topographic signatures.

For automatic detection, facilitating insights into deep-learning model successes and failures is an important concern in the computer vision community. While visual explanation tools such as Grad-CAM (Gradient-weighted Class Activation Mapping) could be implemented to tackle this concern, the sensitivity of a deep-learning model to the quality and representativeness of sample data remains an important constraint, especially for application domain, such as archaeology, with sparse or uncertain reference data. Another possible way would be to use self-supervised learning approaches (Jing & Tian, 2020) developed for solving complex recognition tasks without the need for labeled data. The (semi-)automatic capability of segmentation should remain a key point for future developments, as it provides the object-based framework for further morphological, spectral and contextual information.

The above perspectives primarily stand for LiDAR remote sensing, but they can also be projected on hyperspectral remote sensing. While implementing deep-learning approach on hyperspectral-derived data was not done for this thesis, it appears as a natural outlook for including (semi-)automatic detection and characterization capabilities in the context of archaeological mapping in shallow waters. This transposition of data-driven analysis should however not be performed without considering the limitations of the actual data-driven and physics-based approaches which, in itself, represents a large area of research. On this aspect, the study initiated

Guyot, Alexandre. Contribution of airborne LiDAR and hyperspectral data to archaeological mapping in terrestrial and submerged environments. 2021

on the Molène archipelago has raised questions regarding the inversion of the radiative transfer model. To better evaluate the physics-based results and their limitations, a campaign of underwater field spectral spectroscopy is currently being intended in 2022. The objective is to create an underwater spectral library for (i) improving and assessing the inversion of the radiative transfer model, (ii) accessing *in situ* measurements to characterize archaeological and natural submerged structures.

Based on the results of this thesis, an evaluation of LiDAR topo-bathymetry seems also interesting to conduct. This assessment could for example be performed in comparing topo-bathymetry LiDAR data with hyperspectral data (notably the AHI-derived bathymetry estimation), for example on the submerged site of Er Lannic. The complementarity of these two types of remote sensing data (passive and active) could also be assessed through the implementation of data-fusion at different levels: at model-level, for example with the integration of LiDAR bathymetry forcing in the radiative transfer model to improve the estimation of background reflectance, or at raw or derived-data level. The assessment of topographic and spectral continuity at the land-sea interface could also be one of the objectives of such study.

In open-field areas, the fusion of airborne LiDAR and hyperspectral was not directly addressed in this thesis, but their complementarity was experimented (see report Guyot et al. (2020) p.37-39). Topographic and spectral characteristics extracted using respectively LiDAR and hyperspectral data, were combined to facilitate the perception and interpretation in the field. This complementarity provides interesting perspectives for identifying and documenting subtle anomalies in open areas and could be further assessed, notably based on advanced data-fusion methods (Frati et al., 2021; H. Wang & Glennie, 2015).

As a more general point of view, the integration of remote sensing within archaeological fieldwork is progressing rapidly but an important remaining concern is the generalization of research methodology -including those developed in this thesis- in wider (and therefore heterogeneous) geo-archaeological contexts. So far, despite an increasing number of publications on that matter, such concern is still pending and dependent on two major constraints: (i) the lack of large coverage of open-access LiDAR and hyperspectral data, (ii) the absence of site-level reference open-access archaeological data in different geo-archaeological contexts. The first constrain is progressively being relaxed for airborne LiDAR data with national-scale acquisition programs being publicly available (such as in the United Kingdom, the Netherlands or the United States). In France, the LiDAR HD program[19] initiated by the *Institut Géographique National* in 2021 (and expected to be completed in 2025) is a real opportunity for large-scale development of LiDAR-based archaeology.

Considering the framework of this thesis that was limited to airborne LiDAR and hyperspectral data, a large number of various remote sensing vectors and sensors could also be assessed for the

[19] https://www.ign.fr/lidar-hd-vers-une-nouvelle-cartographie-3d-du-territoire

detection and characterization of archaeological structures. Broadening the spatial domain with the use of satellites and drones, and expanding the spectral domain with the use of data collected in the short-wave infrared, the thermal infra-red and the radiowave domains would be a logical continuation of the research undertaken. In such a large context, assessing the application of methods developed during this thesis (such as multiscale visualizations and (semi)automatic detection) on various remote sensing data (such as thermal imagery) is one example of identified perspectives.

From a thematic point of view

Although the relationship between remote sensing data and the chronology of structures remains a complex subject for which the surface measurement done using optical remote sensing often remains insufficient to initiate an archaeological interpretation, the diachronic prospection of a territory or landscape seems conceptually more in phase with the methods of remote observation.

The themes of development that we have initiated with the (semi-)automatic object segmentation open up perspectives to support approaches of site/site and site/anomaly comparison. Object-segmentation could further be applied to characterize archaeological structures, notably on their morphological and spectral aspects but also on their contextual and topological aspects (relationship of sites/anomalies between them). Such strategy, close to spatial modeling approaches, could rely on the remote sensing spatial and spectral descriptors to support typo-morphological or chrono-typological interpretations. These approaches could, for example, be based on, or even complement, those currently developed for the typological classification of the Iron Age enclosures in Brittany (Leroux et al., 1999).

Specific approaches per geo-archaeological context could also be developed. For example, in foreshore areas -where the concerns of preservation of natural heritage and cultural heritage of natural habitats echo each other- intermediate results have highlighted the contribution of topographic and spectral information for mapping and field interpretation. Although these "blind" surveys have not yet led to specific investigation, the large datasets collected (especially field spectroscopy and hyperspectral imagery on Molène and Gulf of Morbihan) should make it possible to initiate targeted programs in which the methodologies proposed in the framework of this thesis -and whose development are continuing- could be rapidly mobilized for the assessment of data/methods as a support for particular foreshore archaeological questions (port sites, ship-wrecks).

These perspectives illustrate the importance of developing research approaches based on multi-disciplinary collaborations, in which all parties (research labs, national and local authorities, private companies, citizens) share their experience and knowledge for a better understanding of our past and for the protection of this archaeological heritage to be transmitted to future generations. The region of Brittany, with 2470 km length of coastline, an exceptional cultural heritage and an active pole of research in archaeology as well as in geospatial field, both in

Guyot, Alexandre. Contribution of airborne LiDAR and hyperspectral data to archaeological mapping in terrestrial and submerged environments. 2021

academic and industry, stands as an ideal place to continue the challenging quest initiated during this thesis.

Guyot, Alexandre. Contribution of airborne LiDAR and hyperspectral data to archaeological mapping in terrestrial and submerged environments. 2021

REFERENCES

Abdulla, W. (2017). *Matterport/Mask_RCNN: Mask R-CNN for object detection and instance segmentation on Keras and TensorFlow*. https://github.com/matterport/Mask_RCNN

Adam, E., Mutanga, O., & Rugege, D. (2010). Multispectral and hyperspectral remote sensing for identification and mapping of wetland vegetation: A review. *Wetlands Ecology and Management*, *18*(3), 281–296. https://doi.org/10.1007/s11273-009-9169-z

Agache, R. (1999). L'art de l'archéologie aérienne et ses pièges. La prospection à basse altitude est-elle un jeu? Un art? Une science? *Revue archéologique de Picardie*, *17*(1), 39–47. https://doi.org/10.3406/pica.1999.2087

Agapiou, A., Alexakis, D. D., Lysandrou, V., Sarris, A., Cuca, B., Themistocleous, K., & Hadjimitsis, D. G. (2015). Impact of urban sprawl to cultural heritage monuments: The case study of Paphos area in Cyprus. *Journal of Cultural Heritage*, *16*(5), 671–680. https://doi.org/10.1016/j.culher.2014.12.006

Agapiou, A., Hadjimitsis, D. G., & Alexakis, D. D. (2012). Evaluation of Broadband and Narrowband Vegetation Indices for the Identification of Archaeological Crop Marks. *Remote Sensing*, *4*(12), 3892–3919. https://doi.org/10.3390/rs4123892

Agapiou, A., Hadjimitsis, D. G., Georgopoulos, A., Sarris, A., & Alexakis, D. D. (2012). Towards an Archaeological Index: Identification of the Spectral Regions of Stress Vegetation due to Buried Archaeological Remains. In M. Ioannides, D. Fritsch, J. Leissner, R. Davies, F. Remondino, & R. Caffo (Eds.), *Progress in Cultural Heritage Preservation* (pp. 129–138). Springer. https://doi.org/10.1007/978-3-642-34234-9_13

Agapiou, A., Hadjimitsis, D. G., Sarris, A., Georgopoulos, A., & Alexakis, D. D. (2013). Optimum temporal and spectral window for monitoring crop marks over archaeological remains in the Mediterranean region. *Journal of Archaeological Science*, *40*(3), 1479–1492. https://doi.org/10.1016/j.jas.2012.10.036

Agapiou, A., Hadjimitsis, D. G., Sarris, A., Georgopoulos, A., & Alexakis, D. D. (2012). Linear Spectral Unmixing for the Detection of Neolithic Settlements in the Thessalian Plain, central Greece. *Advances in Geoscience*, 21–24.

Agrafiotis, P., Skarlatos, D., Georgopoulos, A., & Karantzalos, K. (2019). Shallow Water Bathymetry Mapping from UAV Imagery Based on Machine Learning. *ISPRS - International Archives of the Photogrammetry, Remote Sensing and Spatial Information Sciences*, *XLII-2/W10*, 9–16. https://doi.org/10.5194/isprs-archives-XLII-2-W10-9-2019

Agudo, P., Pajas, J., Pérez-Cabello, F., Redón, J., & Lebrón, B. (2018). The Potential of Drones and Sensors to Enhance Detection of Archaeological Cropmarks: A Comparative Study Between Multi-Spectral and Thermal Imagery. *Drones*, *2*(3), 29. https://doi.org/10.3390/drones2030029

Ahokas, E., Kaartinen, H., & Hyyppä, J. (2003). A quality assessment of airborne laser scanner data. *International Archives of Photogrammetry and Remote Sensing*, *34*(part 3), W13. http://www.isprs.org/proceedings/xxxiv/3-W13/papers/Ahokas_ALSDD2003.pdf

Alexakis, D., Sarris, A., Astaras, T., & Albanakis, K. (2009). Detection of Neolithic Settlements in Thessaly (Greece) Through Multispectral and Hyperspectral Satellite Imagery. *Sensors*, *9*(2), 1167–1187. https://doi.org/10.3390/s90201167

Allouis, T., Bailly, J.-S., Pastol, Y., & Le Roux, C. (2010). Utilisation conjointe de trains d'ondes LiDAR vert et infrarouge pour la bathymétrie des eaux de très faible profondeurs. *Revue Française de Photogrammétrie et de Télédétection*, *191*, 52–61. https://hal.archives-ouvertes.fr/hal-00581299

Anderson, K., Hancock, S., Disney, M., & Gaston, K. J. (2016). Is waveform worth it? A comparison of LiDAR approaches for vegetation and landscape characterization. *Remote Sensing in Ecology and Conservation*, *2*(1), 5–15. https://doi.org/10.1002/rse2.8

Aqdus, S. A., Drummond, J., & Hanson, W. S. (2008). Discovering archaeological cropmarks: A hyperspectral approach. *Int. Arch. Photogramm. Remote Sens. Spat. Inf. Sci*, *37*, 361–365.

Aqdus, S. A., Hanson, W. S., & Drummond, J. (2012). The potential of hyperspectral and multi-spectral imagery to enhance archaeological cropmark detection: A comparative study. *Journal of Archaeological Science*, *39*(7), 1915–1924. https://doi.org/10.1016/j.jas.2012.01.034

Asner, G. P., Vaughn, N. R., Balzotti, C., Brodrick, P. G., & Heckler, J. (2020). High-Resolution Reef Bathymetry and Coral Habitat Complexity from Airborne Imaging Spectroscopy. *Remote Sensing*, *12*(2), 310. https://doi.org/10.3390/rs12020310

Atzberger, C., Wess, M., Doneus, M., & Verhoeven, G. (2014). ARCTIS — A MATLAB® Toolbox for Archaeological Imaging Spectroscopy. *Remote Sensing*, *6*(9), 8617–8638. https://doi.org/10.3390/rs6098617

Axelsson, P. (2000). DEM generation from laser scanner data using adaptive TIN models. In D. Fritsch & M. Molenaar (Eds.), *International Archives of Photogrammetry and Remote Sensing* (pp. 110–117).

Bachmann, C. M., Nichols, C. R., & Montes, M. J. (2009). Airborne Remote Sensing of Trafficability in the Coastal Zone. *NRL Review*, 223–228.

Bahn, P. (2014). *The History of Archaeology: An Introduction*. Routledge.

Bailey, G., Galanidou, N., Peeters, H., Jöns, H., & Mennenga, M. (2020). The Archaeology of Europe's Drowned Landscapes: Introduction and Overview. In G. Bailey, N. Galanidou, H. Peeters, H. Jöns, & M. Mennenga (Eds.), *The Archaeology of Europe's Drowned Landscapes* (Vol. 35, pp. 1–23). Springer International Publishing. https://doi.org/10.1007/978-3-030-37367-2_1

Bailey, G. N., & Flemming, N. C. (2008). Archaeology of the continental shelf: Marine resources, submerged landscapes and underwater archaeology. *Quaternary Science Reviews*, *27*(23), 2153–2165. https://doi.org/10.1016/j.quascirev.2008.08.012

Bajjouk, T., Mouquet, P., Ropert, M., Quod, J.-P., Hoarau, L., Bigot, L., Le Dantec, N., Delacourt, C., & Populus, J. (2019). Detection of changes in shallow coral reefs status: Towards a spatial approach using hyperspectral and multispectral data. *Ecological Indicators*, *96*, 174–191. https://doi.org/10.1016/j.ecolind.2018.08.052

Ballevre, M., Bosse, V., Dabard, M.-P., Ducassou, C., Fourcade, S., Paquette, J.-L., Peucat, J.-J., & Pitra, P. (2013). Histoire géologique du Massif armoricain: Actualité de la recherche. *Bulletin de La Société Géologique et Minéralogique de Bretagne*, *500*, 5–96.

Balsa-Barreiro, J. (2012). Airborne light detection and ranging (LiDAR) point density analysis. *Scientific Research and Essays*, *7*(33). https://doi.org/10.5897/SRE12.278

Baltsavias, E. P. (1999). Airborne laser scanning: Basic relations and formulas. *ISPRS Journal of Photogrammetry and Remote Sensing*, *54*(2–3), 199–214.

Baltzer, A., Cassen, S., Walter-Simonnet, A.-V., Clouet, H., Lorin, A., & Tessier, B. (2015). Variations du niveau marin Holocène en Baie de Quiberon (Bretagne sud): Marqueurs archéologiques et sédimentologiques. *Quaternaire*, *vol. 26/2*, 105–115. https://doi.org/10.4000/quaternaire.7201

Baradez, J. (1949). *Fossatum Africae, Recherches aériennes sur l'organisation des confins sahariens à l'époque romaine*. Arts et Métiers Graphiques.

Barker, P. (2002). *Techniques of archaeological excavation* (3. ed., Repr). Routledge.

Bassani, C., Cavalli, R. M., Goffredo, R., Palombo, A., Pascucci, S., & Pignatti, S. (2009). Specific spectral bands for different land cover contexts to improve the efficiency of remote sensing archaeological prospection: The Arpi case study. *Journal of Cultural Heritage*, *10*, e41–e48. https://doi.org/10.1016/j.culher.2009.09.002

Baswaraj, D., Govardhan, A., & Premchand, P. (2012). Active Contours and Image Segmentation: The Current State Of the Art. *Global Journal of Computer Science and Technology*.

Behmann, J., Acebron, K., Emin, D., Bennertz, S., Matsubara, S., Thomas, S., Bohnenkamp, D., Kuska, M. T., Jussila, J., Salo, H., Mahlein, A.-K., & Rascher, U. (2018). Specim IQ: Evaluation of a New, Miniaturized Handheld Hyperspectral Camera and Its Application for Plant Phenotyping and Disease Detection. *Sensors*, *18*(2), 441. https://doi.org/10.3390/s18020441

Bellman, R., & Kalaba, R. (1961). Reduction of Dimensionality, Dynamic Programming, and Control Processes. *Journal of Basic Engineering*, *83*(1), 82–84. https://doi.org/10.1115/1.3658896

Bello, S. A., Yu, S., Wang, C., Adam, J. M., & Li, J. (2020). Review: Deep Learning on 3D Point Clouds. *Remote Sensing*, *12*(11), 1729. https://doi.org/10.3390/rs12111729

Benjamin, J., McCarthy, J., Wiseman, C., Bevin, S., Kowlessar, J., Astrup, P. M., Naumann, J., & Hacker, J. (2019). Integrating Aerial and Underwater Data for Archaeology: Digital Maritime Landscapes in 3D. In J. K. McCarthy, J. Benjamin, T. Winton, & W. van Duivenvoorde (Eds.), *3D Recording and Interpretation for Maritime Archaeology* (Vol. 31, pp. 211–231). Springer International Publishing. https://doi.org/10.1007/978-3-030-03635-5_14

Bennett, R., Welham, K., Hill, R. a., & Ford, A. (2012a). A Comparison of Visualization Techniques for Models Created from Airborne Laser Scanned Data: A Comparison of Visualization Techniques for ALS Data. *Archaeological Prospection*, *19*(1), 41–48. https://doi.org/10.1002/arp.1414

Bennett, R., Welham, K., Hill, R. A., & Ford, A. (2013). Airborne spectral imagery for archaeological prospection in grassland environments—An evaluation of performance. *Antiquity*, *87*(335), 220–236. https://doi.org/10.1017/S0003598X00048730

Bennett, R., Welham, K., Hill, R. A., & Ford, A. L. J. (2012b). The Application of Vegetation Indices for the Prospection of Archaeological Features in Grass-dominated Environments: Application of Vegetation Indices in Grass-dominated Environments. *Archaeological Prospection*, *19*(3), 209–218. https://doi.org/10.1002/arp.1429

Bertels, L., Vanderstraete, T., Van Coillie, S., Knaeps, E., Sterckx, S., Goossens, R., & Deronde, B. (2008). Mapping of coral reefs using hyperspectral CASI data; a case study: Fordata, Tanimbar, Indonesia. *International Journal of Remote Sensing*, *29*(8), 2359–2391. https://doi.org/10.1080/01431160701408469

Bewley, R. H. (2003). Aerial survey for archaeology. *The Photogrammetric Record*, *18*(104), 273–292. http://onlinelibrary.wiley.com/doi/10.1046/j.0031-868X.2003.00023.x/full

Bewley, R. H., Crutchley, S. P., & Shell, C. A. (2005). New light on an ancient landscape: Lidar survey in the Stonehenge World Heritage Site. *Antiquity*, *79*(305), 636–647. https://doi.org/10.1017/S0003598X00114577

Billard, C., & Daire, M.-Y. (2019). L'émergence d'une archéologie des installations de pêche de l'estran: Les barrages à poissons. *Les Nouvelles de l'archéologie*, *156*, 21–27. https://doi.org/10.4000/nda.6376

Billard, C., Daire, M.-Y., Dupont, C., Hulot, O., & Marchand, G. (2019). L'estran: Un espace fantasmé. *Les nouvelles de l'archéologie*, *156*, 5–6. http://journals.openedition.org.distant.bu.univ-rennes2.fr/nda/6131

Billard, C., Daire, M.-Y., & Martin, C. (2020). France: Submerged Prehistory on Atlantic and Mediterranean Coasts. In G. Bailey, N. Galanidou, H. Peeters, H. Jöns, & M. Mennenga (Eds.), *The Archaeology of Europe's Drowned Landscapes* (Vol. 35, pp. 249–280). Springer International Publishing. https://doi.org/10.1007/978-3-030-37367-2_12

Bioucas-Dias, J. M., Plaza, A., Dobigeon, N., Parente, M., Du, Q., Gader, P., & Chanussot, J. (2012). Hyperspectral Unmixing Overview: Geometrical, Statistical, and Sparse Regression-Based Approaches. *IEEE Journal of Selected Topics in Applied Earth Observations and Remote Sensing*, *5*(2), 354–379. https://doi.org/10.1109/JSTARS.2012.2194696

Blaschke, T. (2010). Object based image analysis for remote sensing. *ISPRS Journal of Photogrammetry and Remote Sensing*, *65*(1), 2–16. https://doi.org/10.1016/j.isprsjprs.2009.06.004

Blomley, R., Weinmann, M., Leitloff, J., & Jutzi, B. (2014). Shape distribution features for point cloud analysis & a geometric histogram approach on multiple scales. *ISPRS Annals of Photogrammetry, Remote Sensing and Spatial Information Sciences*, *II–3*, 9–16. https://doi.org/10.5194/isprsannals-II-3-9-2014

Blythe Bowman Proulx. (2013). Archaeological Site Looting in "Glocal" Perspective: Nature, Scope, and Frequency. *American Journal of Archaeology*, *117*(1), 111. https://doi.org/10.3764/aja.117.1.0111

Bonhage, A. (2021). A modified Mask region-based convolutional neural network approach for the automated detection of archaeological sites on high-resolution light detection and ranging-derived digital elevation models in the North German Lowland. *Archaeological Prospection*. https://doi.org/10.1002/arp.1806

Borghys, D., Kåsen, I., Achard, V., & Perneel, C. (2012). Hyperspectral Anomaly Detection: Comparative Evaluation in Scenes with Diverse Complexity. *Journal of Electrical and Computer Engineering*, *2012*, e162106. https://doi.org/10.1155/2012/162106

Bowens, A. (Ed.). (2009). *Underwater archaeology: The NAS guide to principles and practice* (2nd ed). Blackwell Pub.

Brachmann, A., Barth, E., & Redies, C. (2017). Using CNN Features to Better Understand What Makes Visual Artworks Special. *Frontiers in Psychology*, *8*. https://doi.org/10.3389/fpsyg.2017.00830

Brando, V. E., Anstee, J. M., Wettle, M., Dekker, A. G., Phinn, S. R., & Roelfsema, C. (2009). A physics based retrieval and quality assessment of bathymetry from suboptimal hyperspectral data. *Remote Sensing of Environment*, *113*(4), 755–770. https://doi.org/10.1016/j.rse.2008.12.003

Brassel, K. (1974). A Model for Automatic Hill-Shading. *The American Cartographer*, *1*(1), 15–27. https://doi.org/10.1559/152304074784107818

Breiman, L. (2001). Random forests. *Machine Learning*, *45*(1), 5–32. http://www.springerlink.com/index/U0P06167N6173512.pdf

Briard, J. (1984). *Les tumulus d'Armorique*. Picard.

Briese, C. (2014). Extraction of Digital Terrain Models. In G. Vosselman & H. G. Maas (Eds.), *Airborne and Terrestrial Laser Scanning*. Whittles Publishing.

Brochard, E. (1994). *Les Fortifications de terre du Comté de Vannes*. Drac SRA Bretagne. http://bibliotheque.numerique.sra-bretagne.fr/files/original/8cb583797aa8aff38bd9960c154771ff.pdf

Brock, J. C., Wright, C. W., Sallenger, A. H., Krabill, W. B., & Swift, R. N. (2002). Basis and Methods of NASA Airborne Topographic Mapper Lidar Surveys for Coastal Studies. *Journal of Coastal Research*, *18*(1), 1–13. https://www.jstor.org/stable/4299049

Brodu, N., & Lague, D. (2012). 3D terrestrial lidar data classification of complex natural scenes using a multi-scale dimensionality criterion: Applications in geomorphology. *ISPRS Journal of Photogrammetry and Remote Sensing*, *68*, 121–134. https://doi.org/10.1016/j.isprsjprs.2012.01.006

Burke, S., Cox, P., Daly, C., Downes, J., Gomez-Ferrer Bayo, A., Flores-Roman, M., Lefèvre, R.-A., Markham, A., Megarry, W., Odiaua, I., Potts, A., & Rockman, M. (2019). *L'avenir de notre passé: Engager le patrimoine culturel dans l'action pour le climat.* (I. ICOMOS, Ed.). ICOMOS (Conseil international des monuments et des sites). http://openarchive.icomos.org/id/eprint/2452/

Campana, S. (2007). *From space to place or from site to landscape? Mind the gap*.

Carman, J. (2014). Legislation in Archaeology: Overview and Introduction. In C. Smith (Ed.), *Encyclopedia of Global Archaeology* (pp. 4469–4484). Springer. https://doi.org/10.1007/978-1-4419-0465-2_276

Carrere, L., Lyard, F., Cancet, M., & Guillot, A. (2015). *FES 2014, a new tidal model on the global ocean with enhanced accuracy in shallow seas and in the Arctic region*. *17*, 5481. http://adsabs.harvard.edu/abs/2015EGUGA..17.5481C

Carrilho, A. C., Galo, M., & Santos, R. C. (2018). Statistical Outlier Detection Method For Airborne Lidar Data. *The International Archives of the Photogrammetry, Remote Sensing and Spatial Information Sciences*, *XLII–1*, 87–92. https://doi.org/10.5194/isprs-archives-XLII-1-87-2018

Caspari, G., & Crespo, P. (2019). Convolutional neural networks for archaeological site detection – Finding "princely" tombs. *Journal of Archaeological Science*, *110*, 104998. https://doi.org/10.1016/j.jas.2019.104998

Cassen, S., Grimaud, V., Boujot, C., Chaigneau, C., Collado, E., De Jersey, P., Querré, G., Vigier, E., & Vourc'h, M. (2019). *Quelques résultats 2018 du PCR " Corpus des signes gravés*

néolithiques en Bretagne .” 16–17. https://hal-univ-rennes1.archives-ouvertes.fr/hal-02148425

Cassen, S., Grimaud, V., Christine Boujot, Olivier Celo, Cyrille Chaigneau, Emmanuelle Collado, Mikaël Guiavarc'h, Céline Jardiné, Philip de Jersey, Christian Obeltz, Guirec Querré, Bettina Schulz-Paulsson, Dominique Sellier, Emmanuelle Vigier, & Marie Vourc'h. (2018). *Corpus des signes gravés Néolithiques* (Programme Collectif de Recherche). Université de Nantes.

Cassen, S., Grimault, V., & Obeltz, C. (2019). Architectures monumentales néolithiques submergées en Morbihan. *Les nouvelles de l'archéologie*, *156*, 60–66. https://doi.org/10.4000/nda.7021

Cavalli, Licciardi, G. A., & Chanussot, J. (2013). Detection of Anomalies Produced by Buried Archaeological Structures Using Nonlinear Principal Component Analysis Applied to Airborne Hyperspectral Image. *IEEE Journal of Selected Topics in Applied Earth Observations and Remote Sensing*, *6*(2), 659–669. https://doi.org/10.1109/JSTARS.2012.2227301

Cavalli, R. M., Colosi, F., Palombo, A., Pignatti, S., & Poscolieri, M. (2007). Remote hyperspectral imagery as a support to archaeological prospection. *Journal of Cultural Heritage*, *8*(3), 272–283. https://doi.org/10.1016/j.culher.2007.03.003

Cavalli, R. M., Pascucci, S., & Pignatti, S. (2009). Optimal spectral domain selection for maximizing archaeological signatures: Italy case studies. *Sensors (Basel, Switzerland)*, *9*(3), 1754–1767. https://doi.org/10.3390/s90301754

Cayot-Délandre, M. (1847). *Le Morbihan, son histoire et ses monuments*. éditions Cauderan. https://books.googleusercontent.com/books/content?req=AKW5Qacnoh0xHvCNXt9h876h-Fr6fLy3wAM1lWbOon9Wg5ow2UNrUdsazGd-HIO3CQ7nfcdOQ_-Wnk89j3Um0ral5JvWJrTSWo-pfECGNeYeiRKKB65fjaggLJlJGeoP_rMruSRQ8Sem_GY8In-IChC5djilUJvb20lSvJjkLwoZku5APLye2beHI5tBjsaJKrcNtX4jTMwlmVDhm-iu1igQCFTWSokm3cY3QE4_YfGBzjYfdSO-

51RIFDgSDAMHEUz2Pm_ZcGk0Szgx4X1FofdlSJN_D1zPxkz4UjWe_7AKYrBgNuVwkc0

Cerra, D., Agapiou, A., Cavalli, R. M., & Sarris, A. (2018). An Objective Assessment of Hyperspectral Indicators for the Detection of Buried Archaeological Relics. *Remote Sensing*, *10*(4), 500. https://doi.org/10.3390/rs10040500

Chaillou, A., & Thomas, J. (2007). L'application Patriarche. *Les nouvelles de l'archéologie*, *107*, 52–57. https://doi.org/10.4000/nda.498

Challis, K., Forlin, P., & Kincey, M. (2011). A Generic Toolkit for the Visualization of Archaeological Features on Airborne LiDAR Elevation Data. *Archaeological Prospection*, *18*(4), 279–289. https://doi.org/10.1002/arp.421

Chase, A. F., Chase, D. Z., Weishampel, J. F., Drake, J. B., Shrestha, R. L., Slatton, K. C., Awe, J. J., & Carter, W. E. (2011). Airborne LiDAR, archaeology, and the ancient Maya landscape at Caracol, Belize. *Journal of Archaeological Science*, *38*(2), 387–398. https://doi.org/10.1016/j.jas.2010.09.018

Chauve, A., Vega, C., Durrieu, S., Bretar, F., Allouis, T., Deseilligny, M. P., & Puech, W. (2009). Advanced full-waveform lidar data echo detection: Assessing quality of derived terrain and tree height models in an alpine coniferous forest. *International Journal of Remote Sensing*, *30*(19), 5211–5228. https://doi.org/10.1080/01431160903023009

Chehata, N., Guo, L., & Mallet, C. (2009, September). Airborne LiDAR Feature Selection For Urban Classification Using Random Forests. *Laserscanning*. https://hal.archives-ouvertes.fr/hal-02384719

Chein-I Chang & Shao-Shan Chiang. (2002). Anomaly detection and classification for hyperspectral imagery. *IEEE Transactions on Geoscience and Remote Sensing*, *40*(6), 1314–1325. https://doi.org/10.1109/TGRS.2002.800280

Chen, Q., Gong, P., Baldocchi, D., & Xie, G. (2007). Filtering airborne laser scanning data with morphological methods. *Photogrammetric Engineering & Remote Sensing*, *73*(2), 175–185.

Chen, Y., Ji, Y., Zhou, J., Chen, X., & Shen, W. (2012). Computation of signal-to-noise ratio of airborne hyperspectral imaging spectrometer. *2012 International Conference on Systems and Informatics (ICSAI2012)*, 1046–1049. https://doi.org/10.1109/ICSAI.2012.6223191

Chen, Z., Gao, B., & Devereux, B. (2017). State-of-the-Art: DTM Generation Using Airborne LIDAR Data. *Sensors*, *17*(1), 150. https://doi.org/10.3390/s17010150

Chevallier, R. (1964). Colloque international d'archéologie aérienne. *Annales. Histoire, Sciences Sociales*, *19*(4), 750–754. https://doi.org/10.3406/ahess.1964.421208

Chiba, T., Kaneta, S., & Suzuki, Y. (2008). Red relief image map: New visualization method for three dimensional data. In J. CHEN, J. JIANG, & W. KAINZ (Eds.), *Proceedings of the XXIth ISPRS Congress* (Vol. 37, pp. 1071–1076). ISPRS Archives. http://www.isprs.org/proceedings/XXXVII/congress/2_pdf/11_ThS-6/08.pdf

Clarke, D. L. (1968). *Analytical Archaeology*. Methuen & Co. Ltd.

Collin, A., Archambault, P., & Long, B. (2008). Mapping the Shallow Water Seabed Habitat With the SHOALS. *IEEE Transactions on Geoscience and Remote Sensing*, *46*(10), 2947–2955. https://doi.org/10.1109/TGRS.2008.920020

Conel, J., Green, R., Vane, G., Bruegge, C., Alley, R., & Curtiss, B. (1987). AIS-2 radiometry and a comparison of methods for the recovery of ground reflectance. *Undefined*. https://www.semanticscholar.org/paper/AIS-2-radiometry-and-a-comparison-of-methods-for-of-Conel-Green/5132ce352166d39d5f21caf51d87739f193d8de7

Connaway, J. M. (2007). *Fishweirs: A world perspective with emphasis on the fishweirs of Mississippi*. Mississippi Dept. of Archives and History.

Corns, A., & Shaw, R. (2009). High resolution 3-dimensional documentation of archaeological monuments & landscapes using airborne LiDAR. *Journal of Cultural Heritage*, *10*, e72–e77. https://doi.org/10.1016/j.culher.2009.09.003

Costa, E. (2019). The progress of survey techniques in underwater sites: The case study of Cape Stoba shipwreck. *ISPRS - International Archives of the Photogrammetry, Remote Sensing and*

Spatial Information Sciences, *XLII-2/W10*, 69–75. https://doi.org/10.5194/isprs-archives-XLII-2-W10-69-2019

Cousseau, F. (2016). *Archéologie du bâti mégalithique dans l'ouest de la France* [Unpublished thesis (PhD)]. Université Rennes 1.

Cover, T. M., Thomas, J. A., & others. (1991). Entropy, relative entropy and mutual information. *Elements of Information Theory*, *2*(1), 12–13.

Cowley, D., Verhoeven, G., & Traviglia, A. (2021). Editorial for Special Issue: "Archaeological Remote Sensing in the 21st Century: (Re)Defining Practice and Theory." *Remote Sensing*, *13*(8), 1431. https://doi.org/10.3390/rs13081431

Crawford, O. G. S. (1923). Air Survey and Archaeology. *The Geographical Journal*, *61*(5), 342. https://doi.org/10.2307/1781831

Crow, F. C. (1984). Summed-area tables for texture mapping. *ACM SIGGRAPH Computer Graphics*, *18*(3), 207–212. http://dl.acm.org/citation.cfm?id=808600

Cunliffe, E. (2014). Archaeological Site Damage in the Cycle of War and Peace: A Syrian Case Study. *Journal of Eastern Mediterranean Archaeology & Heritage Studies*, *2*(3), 229–247. https://doi.org/10.5325/jeasmedarcherstu.2.3.0229

Dabas, M., Delétang, H., Ferdière, A., & Jung, C. (2006). *La prospection*. Editions Errance. https://www.amazon.com/prospection-Michel-Dabas/dp/2877723283?SubscriptionId=AKIAIOBINVZYXZQZ2U3A&tag=chimbori05-20&linkCode=xm2&camp=2025&creative=165953&creativeASIN=2877723283

Daire, M.-Y. (1992). Un aspect méthodologique original de la prospection aérienne à travers l'exemple du nord du Finistère. *Revue Archéologique de l'Ouest*, *9*(1), 187–190. https://doi.org/10.3406/rao.1992.990

Daire, M.-Y., & Langouet, L. (2008). *Les pêcheries de Bretagne Archéologie et Histoire des pêcheries d'estran: Vol. N°AE*. CeRAA. https://hal-univ-rennes1.archives-ouvertes.fr/hal-02343379

Daire, M.-Y., & Langouët, L. (2010). Les anciens pièges à poissons des côtes de Bretagne: Un patrimoine au rythme des marées.. In *Les anciens pièges à poissons des côtes de Bretagne un*

patrimoine au rythme des marées... Centre Régional d'Archéologie d'Alet (Ce.R.A.A.) Association Manche Atlantique pour la recherche archéologique dans les îles (A.M.A.R.A.I.).

Daire, M.-Y., & Langouët, L. (2011). Dater les anciennes pêcheries par les niveaux marins approche méthodologique et perspectives géoarchéologiques: Le Bas Léon, nord Finistère, Bretagne. *Norois*, *220*, 69–93. https://doi.org/10.4000/norois.3680

Daire, M.-Y., Lopez-Romero, E., Proust, J.-N., Regnauld, H., Pian, S., & Shi, B. (2012). Coastal Changes and Cultural Heritage (1): Assessment of the Vulnerability of the Coastal Heritage in Western France. *The Journal of Island and Coastal Archaeology*, *7*(2), 168–182. https://doi.org/10.1080/15564894.2011.652340

Daly, P., & Evans, T. L. (Eds.). (2005). *Digital Archaeology* (1st edition). Routledge. https://doi.org/10.4324/9780203005262

Dassié, J. (1978). *Manuel d'archéologie aérienne*. Éditions Technip.

Davis, D. (2021). Theoretical Repositioning of Automated Remote Sensing Archaeology: Shifting from Features to Ephemeral Landscapes. *Journal of Computer Applications in Archaeology*, *4*(1), 94–109. https://doi.org/10.5334/jcaa.72

Davis, D. S. (2019). Object-based image analysis: A review of developments and future directions of automated feature detection in landscape archaeology. *Archaeological Prospection*, *26*(2), 155–163. https://doi.org/10.1002/arp.1730

Davis, D. S., Buffa, D. C., & Wrobleski, A. C. (2020). Assessing the Utility of Open-Access Bathymetric Data for Shipwreck Detection in the United States. *Heritage*, *3*(2), 364–383. https://doi.org/10.3390/heritage3020022

Davis, D. S., Sanger, M. C., & Lipo, C. P. (2019). Automated mound detection using lidar and object-based image analysis in Beaufort County, South Carolina. *Southeastern Archaeology*, *38*(1), 23–37. https://doi.org/10.1080/0734578X.2018.1482186

Dawson, T., Hambly, J., Kelley, A., Lees, W., & Miller, S. (2020). Coastal heritage, global climate change, public engagement, and citizen science. *Proceedings of the National Academy of*

Sciences of the United States of America, *117*(15), 8280–8286. https://doi.org/10.1073/pnas.1912246117

de Closmadeuc, G. (1867). Découverte d'un cromlec'h dans l'île d'El Lanic (Morbihan). *Bulletin de La Société Polymathique Du Morbihan*, 28–30.

de Closmadeuc, G. (1882). Le cromlech d'Er Lanic et le Golfe du Morbihan à l'époque dite Celtique. *Bulletin de La Société Polymathique Du Morbihan*, 8–24.

Deckers, P., Lewis, M., & Thomas, S. (2016). Between Two Places: Archaeology and Metal-detecting in Europe. *Open Archaeology*, *2*(1). https://doi.org/10.1515/opar-2016-0031

Dekker, A. G., Phinn, S. R., Anstee, J., Bissett, P., Brando, V. E., Casey, B., Fearns, P., Hedley, J., Klonowski, W., Lee, Z. P., Lynch, M., Lyons, M., Mobley, C., & Roelfsema, C. (2011). Intercomparison of shallow water bathymetry, hydro-optics, and benthos mapping techniques in Australian and Caribbean coastal environments: Intercomparison of shallow water mapping methods. *Limnology and Oceanography: Methods*, *9*(9), 396–425. https://doi.org/10.4319/lom.2011.9.396

Demoule, J.-P. (Ed.). (2007). *L'archéologie préventive dans le monde: Apports de l'archéologie préventive à la connaissance du passé*. Découverte.

Demoule, J.-P., Giligny, F., Lehoërff, A., & Schnapp, A. (2020). *Guide des méthodes de l'archéologie* (Quatriéme édition). La Découverte.

Denham, T. (2017). Landscape Archaeology. In A. S. Gilbert (Ed.), *Encyclopedia of Geoarchaeology* (pp. 464–468). Springer Netherlands. https://doi.org/10.1007/978-1-4020-4409-0_168

Devereux, B. J., Amable, G. S., & Crow, P. (2008). Visualisation of LiDAR terrain models for archaeological feature detection. *Antiquity*, *82*(316), 470–479. https://doi.org/10.1017/S0003598X00096952

Devereux, B. J., Amable, G. S., Crow, P., & Cliff, A. D. (2005). The potential of airborne lidar for detection of archaeological features under woodland canopies. *Antiquity*, *79*(305), 648–660. https://doi.org/10.1017/S0003598X00114589

Dobigeon, N., Altmann, Y., Brun, N., & Moussaoui, S. (2016). Linear and Nonlinear Unmixing in Hyperspectral Imaging. In C. Ruckebusch (Ed.), *Data Handling in Science and Technology* (Vol. 30, pp. 185–224). Elsevier. https://doi.org/10.1016/B978-0-444-63638-6.00006-1

Domínguez-Rodrigo, M., Fernández-López, S., & Alcalá, L. (2011). How Can Taphonomy Be Defined in the XXI Century? *Journal of Taphonomy*, *9*(1), 13.

Doneus, M. (2013). Openness as Visualization Technique for Interpretative Mapping of Airborne Lidar Derived Digital Terrain Models. *Remote Sensing*, *5*(12), 6427–6442. https://doi.org/10.3390/rs5126427

Doneus, M., & Briese, C. (2006). Full-waveform airborne laser scanning as a tool for archaeological reconnaissance. *BAR International Series*, *1568*, 99. http://www.academia.edu/download/1927702/Doneus_Briese_ROME.pdf

Doneus, M., & Briese, C. (2011). Airborne Laser Scanning in forested areas–potential and limitations of an archaeological prospection technique. *Remote Sensing for Archaeological Heritage Management*, *3*, 59–76.

Doneus, M., Briese, C., Fera, M., & Janner, M. (2008). Archaeological prospection of forested areas using full-waveform airborne laser scanning. *Journal of Archaeological Science*, *35*(4), 882–893. https://doi.org/10.1016/j.jas.2007.06.013

Doneus, M., Doneus, N., Briese, C., Pregesbauer, M., Mandlburger, G., & Verhoeven, G. (2013). Airborne laser bathymetry – detecting and recording submerged archaeological sites from the air. *Journal of Archaeological Science*, *40*(4), 2136–2151. https://doi.org/10.1016/j.jas.2012.12.021

Doneus, M., Mandlburger, G., & Doneus, N. (2020). Archaeological Ground Point Filtering of Airborne Laser Scan Derived Point-Clouds in a Difficult Mediterranean Environment. *Journal of Computer Applications in Archaeology*, *3*(1), 92–108. https://doi.org/10.5334/jcaa.44

Doneus, M., Miholjek, I., Mandlburger, G., Doneus, N., Verhoeven, G., Briese, Ch., & Pregesbauer, M. (2015). Airborne laser bathymetry for documentation of submerged archaeological sites in shallow water. *ISPRS - International Archives of the Photogrammetry, Remote Sensing and*

Spatial Information Sciences, *XL-5/W5*, 99–107. https://doi.org/10.5194/isprsarchives-XL-5-W5-99-2015

Doneus, M., Verhoeven, G., Atzberger, C., Wess, M., & Ruš, M. (2014). New ways to extract archaeological information from hyperspectral pixels. *Journal of Archaeological Science*, *52*, 84–96. https://doi.org/10.1016/j.jas.2014.08.023

Doneus, N., Miholjek, I., Džin, K., Doneus, M., Dugonjić, P., & Schiel, H. (2020). Archaeological Prospection of Coastal and Submerged Settlement Sites. Re-Evaluation of the Roman Site Complex of Vižula, Croatia. *Archaeologia Austriaca*, *104*, 253–281. https://doi.org/10.1553/archaeologia104s253

Donoghue, D., & Shennan, I. (1988). The application of remote sensing to environmental archaeology. *Geoarchaeology*, *3*(4), 275–285.

D'Orazio, T., Palumbo, F., & Guaragnella, C. (2012). Archaeological trace extraction by a local directional active contour approach. *Pattern Recognition*, *45*(9), 3427–3438. https://doi.org/10.1016/j.patcog.2012.03.003

Dorigo, W. A., Zurita-Milla, R., de Wit, A. J. W., Brazile, J., Singh, R., & Schaepman, M. E. (2007). A review on reflective remote sensing and data assimilation techniques for enhanced agroecosystem modeling. *International Journal of Applied Earth Observation and Geoinformation*, *9*(2), 165–193. https://doi.org/10.1016/j.jag.2006.05.003

Du Châtellier, P. (1902). *Les monuments mégalithiques des îles du Finistère de Béniguet à Ouessant*. Impr. nationale.

Dubayah, R. O., & Drake, J. B. (2000). Lidar Remote Sensing for Forestry. *Journal of Forestry*, *98*(6), 44–46. https://doi.org/10.1093/jof/98.6.44

Edis, J., Macleod, D., & Bewley, R. (1989). An archaeologist's guide to classification of cropmarks and soilmarks. *Antiquity*, *63*(238), 112–126. https://doi.org/10.1017/S0003598X00075621

Efremov, I. A. (1940). Taphonomy: A new branch of paleontology. *Pan American Geologist*, *74*, 81–93.

Egloff, B. (2008). Archaeological heritage management, climate change and world heritage in the 21st century. *Heritage at Risk*, 200–202.

Ehrhold, A., Le Gall, B., Stéphan, P., Suanez, S., Houlgatte, E., Jean-Pierre, M., & Laëtitia, M. (2017). *Atlas de l'archipel de Molène: Géologie, géomorphologie et sédimentologie*.

Eilers, P. H. C. (2003). A Perfect Smoother. *Analytical Chemistry*, *75*(14), 3631–3636. https://doi.org/10.1021/ac034173t

Elachi, C. (2007). Foreword. In J. Wiseman & F. El-Baz (Eds.), *Remote sensing in archaeology* (pp. ix–x). Springer.

Elia, R. J. (1997). Looting, collecting, and the destruction of archaeological resources. *Nonrenewable Resources*, *6*(2), 85–98. https://doi.org/10.1007/BF02803807

Elmqvist, M., Jungert, E., Lantz, F., Persson, A., & Soderman, U. (2001). Terrain modelling and analysis using laser scanner data. *International Archives of Photogrammetry Remote Sensing and Spatial Information Sciences*, *34*(3/W4), 219–226.

Emmolo, D., Franco, V., Brutto, M. L., Orlando, P., & Villa, B. (2004). *Hyperspectral techniques and GIS for archaeological investigation*.

Evans, A. M., Firth, A., & Staniforth, M. (2009). Old and New Threats to Submerged Cultural Landscapes: Fishing, Farming and Energy Development. *Conservation and Management of Archaeological Sites*, *11*(1), 43–53. https://doi.org/10.1179/135050309X12508566208407

Evans, D. (2016). Airborne laser scanning as a method for exploring long-term socio-ecological dynamics in Cambodia. *Journal of Archaeological Science*, *74*, 164–175. https://doi.org/10.1016/j.jas.2016.05.009

Evans, D. H., Fletcher, R. J., Pottier, C., Chevance, J.-B., Soutif, D., Tan, B. S., Im, S., Ea, D., Tin, T., Kim, S., & others. (2013). Uncovering archaeological landscapes at Angkor using lidar. *Proceedings of the National Academy of Sciences*, *110*(31), 12595–12600. https://doi.org/10.1073/pnas.1306539110

Evans, J. S., & Hudak, A. T. (2007). A Multiscale Curvature Algorithm for Classifying Discrete Return LiDAR in Forested Environments. *IEEE Transactions on Geoscience and Remote Sensing*, *45*(4), 1029–1038. https://doi.org/10.1109/TGRS.2006.890412

Felzenszwalb, P. F., & Huttenlocher, D. P. (2004). Efficient Graph-Based Image Segmentation. *International Journal of Computer Vision*, *59*(2), 167–181. https://doi.org/10.1023/B:VISI.0000022288.19776.77

Fernandez-Diaz, J., Carter, W., Glennie, C., Shrestha, R., Pan, Z., Ekhtari, N., Singhania, A., Hauser, D., & Sartori, M. (2016). Capability Assessment and Performance Metrics for the Titan Multispectral Mapping Lidar. *Remote Sensing*, *8*(11), 936. https://doi.org/10.3390/rs8110936

Fernandez-Diaz, J., Carter, W., Shrestha, R., & Glennie, C. (2014). Now You See It… Now You Don't: Understanding Airborne Mapping LiDAR Collection and Data Product Generation for Archaeological Research in Mesoamerica. *Remote Sensing*, *6*(10), 9951–10001. https://doi.org/10.3390/rs6109951

Feygels, V., Kopilevich, Y., Kim, M., LaRocque, P., Pe'eri, S., & Philpot, W. (2019). *Chapter 4: Basic Concepts and System Design*. https://ecommons.cornell.edu/handle/1813/66303

Figorito, B., & Tarantino, E. (2014). Semi-automatic detection of linear archaeological traces from orthorectified aerial images. *Int. J. Appl. Earth Obs. Geoinformation*. https://doi.org/10.1016/j.jag.2013.04.005

Fisher, C. T., Cohen, A. S., Fernández-Diaz, J. C., & Leisz, S. J. (2017). The application of airborne mapping LiDAR for the documentation of ancient cities and regions in tropical regions. *Quaternary International*, *448*, 129–138. https://doi.org/10.1016/j.quaint.2016.08.050

Flatman, J. (2009). Conserving Marine Cultural Heritage: Threats, Risks and Future Priorities. *Conservation and Management of Archaeological Sites*, *11*(1), 5–8. https://doi.org/10.1179/135050309X12508566208245

Guyot, Alexandre. Contribution of airborne LiDAR and hyperspectral data to archaeological mapping in terrestrial and submerged environments. 2021

Flemming, N. C. (2020). Global experience in locating submerged prehistoric sites and their relevance to research on the American continental shelves. *The Journal of Island and Coastal Archaeology*, 1–24. https://doi.org/10.1080/15564894.2020.1781712

Fontaine, S., Sauvage, C., Dégez, D., Hulot, O., & Lima, C. (2017, September 28). Évaluations archéologiques en contexte sous-marin offshore: Un nouveau protocole. *2éme Séminaire Scientifique et Technique de l'Inrap : Le Diagnostic Comme Outil de Recherche*. https://doi.org/10.34692/MGWC-1081

Frati, G., Launeau, P., Robin, M., Giraud, M., Juigner, M., Debaine, F., & Michon, C. (2021). Coastal Sand Dunes Monitoring by Low Vegetation Cover Classification and Digital Elevation Model Improvement Using Synchronized Hyperspectral and Full-Waveform LiDAR Remote Sensing. *Remote Sensing*, *13*(1), 29. https://doi.org/10.3390/rs13010029

Freeland, T., Heung, B., Burley, D. V., Clark, G., & Knudby, A. (2016). Automated feature extraction for prospection and analysis of monumental earthworks from aerial LiDAR in the Kingdom of Tonga. *Journal of Archaeological Science*, *69*, 64–74. https://doi.org/10.1016/j.jas.2016.04.011

Friedman, J. H., & Tukey, J. W. (1974). A Projection Pursuit Algorithm for Exploratory Data Analysis. *IEEE Transactions on Computers*, *C–23*(9), 881–890. https://doi.org/10.1109/T-C.1974.224051

Fromentin, F., Lauzanne, S., & Ropars, A. (2006). L'inventaire archéologique national. In M. Dabas, H. Delétang, A. Ferdière, C. Jung, & W. H. Zimmermann, *La prospection* (pp. 8–12). Editions Errance.

Frost, R. (2004). Underwater Cultural Heritage Protection. In *Australian Year Book of International Law* (Vol. 23, pp. 25–50).

Galles, R. (1862). Les fouilles du mont Saint-Michel en Carnac. *Bulletin de La Société Polymathique Du Morbihan*, *6*, 7–18.

Gallwey, Eyre, Tonkins, & Coggan. (2019). Bringing Lunar LiDAR Back Down to Earth: Mapping Our Industrial Heritage through Deep Transfer Learning. *Remote Sensing*, *11*(17), 1994. https://doi.org/10.3390/rs11171994

Gandois, H., & Stéphan, P. (2015). Les barrages de pêcheries de l'archipel de Molène (mer d'Iroise, Finistère). *Bulletin de l'A.M.A.R.A.I.*, *28*, 45–76. https://hal.archives-ouvertes.fr/hal-01274912

Gandois, H., Stéphan, P., Cuisnier, D., Gladu, Y., Lallement, F., & Priol, H. (2013). *Rapport sur les prospections sous-marines et sur la zone d'estran en mer d'Iroise* (Rapport d'opération OA-1746). DRASSM.

Gandois, H., Stéphan, P., Cuisnier, D., Hulot, O., Ehrhold, A., Paul, M., Dantec, N. L., & Franzetti, M. (2018). The Stone Tidal Fish Weirs of the Molène Archipelago, Iroise Sea, Brittany, Western France: A long-term tradition with early megalithic origins: THE MEGALITHIC STONE TIDAL WEIRS OF THE MOLÈNE ARCHIPELAGO. *International Journal of Nautical Archaeology*, *47*(1), 5–27. https://doi.org/10.1111/1095-9270.12277

Gao, B.-C., Montes, M. J., Davis, C. O., & Goetz, A. F. H. (2009). Atmospheric correction algorithms for hyperspectral remote sensing data of land and ocean. *Remote Sensing of Environment*, *113*, S17–S24. https://doi.org/10.1016/j.rse.2007.12.015

Gao, J. (2009). Bathymetric mapping by means of remote sensing: Methods, accuracy and limitations. *Progress in Physical Geography: Earth and Environment*, *33*(1), 103–116. https://doi.org/10.1177/0309133309105657

Gao, L., Zhao, B., Jia, X., Liao, W., & Zhang, B. (2017). Optimized Kernel Minimum Noise Fraction Transformation for Hyperspectral Image Classification. *Remote Sensing*, *9*(6), 548. https://doi.org/10.3390/rs9060548

Gautier, M., Guigon, P., & Leroux, G. (2019). Archéologie aérienne: Les révélations d'Armorique. *Archéologia*, *582*, 54. https://hal-univ-rennes1.archives-ouvertes.fr/hal-02397596

Gautier, M., Guigon, P., Leroux, G., Batt, M., Blanchet, S., Desfonds, A., Jean, S., Le Goff, E., Millet, M., Hervé, S., Bouvet, J.-P., Garcia, D., Menez, Y., & Bréart, B. (2019). *Les moissons du ciel: 30 années d'archéologie aérienne : au dessus du Massif armoricain*.

Gaydarska, B. (2014). Spatial Analysis in Field Archaeology. In C. Smith (Ed.), *Encyclopedia of Global Archaeology* (pp. 6976–6980). Springer New York. https://doi.org/10.1007/978-1-4419-0465-2_219

Geirhos, R., Janssen, D. H. J., Schütt, H. H., Rauber, J., Bethge, M., & Wichmann, F. A. (2018). Comparing deep neural networks against humans: Object recognition when the signal gets weaker. *ArXiv:1706.06969 [Cs, q-Bio, Stat]*. http://arxiv.org/abs/1706.06969

Georges-Leroy, M. (2010). Airborne laser scanning for the management of archaeological sites in Lorraine (France). In D. C. Cowley (Ed.), *Remote Sensing for Archaeological Heritage Management Proceedings of the 11th EAC Heritage Management Symposium* (pp. 229–234). EAC. https://hal.archives-ouvertes.fr/hal-00637775

Georges-Leroy, M., Bock, J., Dambrine, É., & Dupouey, J.-L. (2011). Apport du lidar à la connaissance de l'histoire de l'occupation du sol en forêt de Haye. *ArcheoSciences. Revue d'archéométrie*, *35*, 117–129. https://doi.org/10.4000/archeosciences.3015

Ghamisi, P., Plaza, J., Chen, Y., Li, J., & Plaza, A. J. (2017). Advanced Spectral Classifiers for Hyperspectral Images: A review. *IEEE Geoscience and Remote Sensing Magazine*, *5*(1), 8–32. https://doi.org/10.1109/MGRS.2016.2616418

Gillis, D. B., Bowles, J. H., Montes, M. J., & Moses, W. J. (2018). Propagation of sensor noise in oceanic hyperspectral remote sensing. *Optics Express*, *26*(18), A818–A831. https://doi.org/10.1364/OE.26.00A818

Girshick, R. (2015). Fast r-cnn. *Proceedings of the IEEE International Conference on Computer Vision*, 1440–1448. https://doi.org/10.1109/ICCV.2015.169

Glenn, N. F., Streutker, D. R., Chadwick, D. J., Thackray, G. D., & Dorsch, S. J. (2006). Analysis of LiDAR-derived topographic information for characterizing and differentiating landslide

morphology and activity. *Geomorphology*, *73*(1–2), 131–148. https://doi.org/10.1016/j.geomorph.2005.07.006

Glennie, C. (2007). Rigorous 3D error analysis of kinematic scanning LIDAR systems. *Journal of Applied Geodesy*, *1*(3). https://doi.org/10.1515/jag.2007.017

Głomb, P., & Romaszewski, M. (2020). Anomaly detection in hyperspectral remote sensing images. In P. C. Pandey, P. K. Srivastava, H. Balzter, B. Bhattacharya, & G. P. Petropoulos (Eds.), *Hyperspectral Remote Sensing* (pp. 45–66). Elsevier. https://doi.org/10.1016/B978-0-08-102894-0.00004-8

Goodfellow, I., Bengio, Y., & Courville, A. (2016). *Deep Learning*. MIT Press.

Göritz, A., Berger, S. A., Gege, P., Grossart, H.-P., Nejstgaard, J. C., Riedel, S., Röttgers, R., & Utschig, C. (2018). Retrieval of Water Constituents from Hyperspectral In-Situ Measurements under Variable Cloud Cover—A Case Study at Lake Stechlin (Germany). *Remote Sensing*, *10*(2), 181. https://doi.org/10.3390/rs10020181

Gouezin, P. (1991). *Le site mégalithique d'Er Lannic* (Rapport Scientifique) [Rapport Scientifique]. http://ns2014576.ovh.net/files/original/cfbab36dafcd84d23c17ce7af1d267ee.pdf

Gouezin, P. (2017). *Structures funéraires et pierres dressées. Analyses architecturales et spatiales. Mégalithes du département du Morbihan* [Unpublished thesis (PhD)]. Université Rennes 1.

Grammer, B., Draganits, E., Gretscher, M., & Muss, U. (2017). LiDAR-guided Archaeological Survey of a Mediterranean Landscape: Lessons from the Ancient Greek Polis of Kolophon (Ionia, Western Anatolia). *Archaeological Prospection*, *24*(4), 311–333. https://doi.org/10.1002/arp.1572

Green, A. A., Berman, M., Switzer, P., & Craig, M. D. (1988). A transformation for ordering multispectral data in terms of image quality with implications for noise removal. *IEEE Transactions on Geoscience and Remote Sensing*, *26*(1), 65–74. https://doi.org/10.1109/36.3001

Guilcher, A. (1959). L'archipel de Molène (Finistère). Etude morphologique. *Revue de Géographie Physique et de Géologie Dynamique*, *2*, 81–86.

Guyot, A., Hubert-Moy, L., & Lorho, T. (2018). Detecting Neolithic Burial Mounds from LiDAR-Derived Elevation Data Using a Multi-Scale Approach and Machine Learning Techniques. *Remote Sensing*, *10*(2), 225. https://doi.org/10.3390/rs10020225

Guyot, A., Lennon, M., & Hubert-Moy, L. (2019). *Rapport 2018 de prospection archéologique diachronique par télédétection, zone Unesco: Carnac, Baie de Quiberon et Golfe du Morbihan* (No. RAP03683). Service régional de l'archéologie de Bretagne. http://bibliotheque.numerique.sra-bretagne.fr/items/show/3789

Guyot, A., Lennon, M., & Hubert-Moy, L. (2020). *Rapport 2019 de prospection archéologique diachronique par télédétection, zone Unesco: Carnac et Rives du Morbihan* (No. RAP03986). Service régional de l'archéologie de Bretagne. http://bibliotheque.numerique.sra-bretagne.fr/items/show/4108

Guyot, A., Lennon, M., & Hubert-Moy, L. (2021). *Rapport 2020 de prospection archéologique diachronique par télédétection, zone Unesco: Carnac et Rives du Morbihan* (No. RAP04008). Service régional de l'archéologie de Bretagne. http://bibliotheque.numerique.sra-bretagne.fr/items/show/4133

Guyot, A., Lennon, M., Lorho, T., & Hubert-Moy, L. (2021). Combined Detection and Segmentation of Archeological Structures from LiDAR Data Using a Deep Learning Approach. *Journal of Computer Applications in Archaeology*, *4*(1), 1–19. https://doi.org/10.5334/jcaa.64

Guyot, A., Lennon, M., Thomas, N., Gueguen, S., Petit, T., Lorho, T., Cassen, S., & Hubert-Moy, L. (2019). Airborne Hyperspectral Imaging for Submerged Archaeological Mapping in Shallow Water Environments. *Remote Sensing*, *11*(19), 2237. https://doi.org/10.3390/rs11192237

Guzinski, R., Spondylis, E., Michalis, M., Tusa, S., Brancato, G., Minno, L., & Hansen, L. B. (2016). Exploring the Utility of Bathymetry Maps Derived With Multispectral Satellite Observations in the Field of Underwater Archaeology. *Open Archaeology*, *2*(1), (1). https://doi.org/10.1515/opar-2016-0018

Hafner, A., Öniz, H., Semaan, L., & Underwood, C. (2020). *Heritage at Risk: Special Edition 2020: Heritage Under Water at Risk: Threats, Challenges and Solutions* (p. 2018) [Rapports Techniques]. International Council on Monuments and Sites. http://openarchive.icomos.org/id/eprint/2488/

Hallégouët, B. (1982). *Géomorphologie de l'archipel de Molène*. *15*(110), 83–97.

Hampton, J. N. (1974). An Experiment In Multispectral Air Photography For Archaeological Research. *The Photogrammetric Record*, *8*(43), 37–64. https://doi.org/10.1111/j.1477-9730.1974.tb01226.x

Hampton, J. N., Palmer, R., & Clark, A. J. (1977). Implications of Aerial Photography for Archaeology: Geophysical and Chemical Assessment of Air Photograph Sites. *Archaeological Journal*, *134*(1), 157–193. https://doi.org/10.1080/00665983.1977.11078434

Han, T., & Goodenough, D. G. (2008). Investigation of Nonlinearity in Hyperspectral Imagery Using Surrogate Data Methods. *IEEE Transactions on Geoscience and Remote Sensing*, *46*(10), 2840–2847. https://doi.org/10.1109/TGRS.2008.2002952

Harff, J., Bailey, G. N., & Lüth, F. (2016). Geology and archaeology: Submerged landscapes of the continental shelf: an introduction. *Geological Society, London, Special Publications*, *411*(1), 1–8. https://doi.org/10.1144/SP411.13

He, K., Gkioxari, G., Dollar, P., & Girshick, R. (2017). Mask R-CNN. *Proceedings of the IEEE International Conference on Computer Vision (ICCV)*, 2961–2969.

Hearst, M. A., Dumais, S. T., Osuna, E., Platt, J., & Scholkopf, B. (1998). Support vector machines. *IEEE Intelligent Systems and Their Applications*, *13*(4), 18–28. https://doi.org/10.1109/5254.708428

Hedley, J. D., Roelfsema, C. M., Phinn, S. R., & Mumby, P. J. (2012). Environmental and Sensor Limitations in Optical Remote Sensing of Coral Reefs: Implications for Monitoring and Sensor Design. *Remote Sensing*, *4*(1), 271–302. https://doi.org/10.3390/rs4010271

Hesse, R. (2010). LiDAR-derived Local Relief Models—A new tool for archaeological prospection. *Archaeological Prospection*, *17*(2), 67–72. https://doi.org/10.1002/arp.374

Hesse, R. (2016). *Visualisierung hochauflösender Digitaler Geländemodelle mit LiVT* [Pdf]. https://doi.org/10.17171/3-34-7

Hickman, G. D., & Hogg, J. E. (1969). Application of an airborne pulsed laser for near shore bathymetric measurements. *Remote Sensing of Environment*, *1*(1), 47–58. https://doi.org/10.1016/S0034-4257(69)90088-1

Hoeser, T., & Kuenzer, C. (2020). Object Detection and Image Segmentation with Deep Learning on Earth Observation Data: A Review-Part I: Evolution and Recent Trends. *Remote Sensing*, *12*(10), 1667. https://doi.org/10.3390/rs12101667

Hofton, M. A., Rocchio, L. E., Blair, J. B., & Dubayah, R. (2002). Validation of Vegetation Canopy Lidar sub-canopy topography measurements for a dense tropical forest. *Journal of Geodynamics*, *34*(3), 491–502. https://doi.org/10.1016/S0264-3707(02)00046-7

Holtorf, C. (2020). An archaeology for the future: From developing contract archaeology to imagining post-corona archaeology. *Post-Classical Archaeologies*, *10*, 57–72.

Høye, G., Løke, T., & Fridman, A. (2015). Method for quantifying image quality in push-broom hyperspectral cameras. *Optical Engineering*, *54*(5), 053102. https://doi.org/10.1117/1.OE.54.5.053102

Hubel, D. H., & Wiesel, T. N. (1962). Receptive fields, binocular interaction and functional architecture in the cat's visual cortex. *The Journal of Physiology*, *160*(1), 106–154. https://doi.org/10.1113/jphysiol.1962.sp006837

Huete, A. R. (1988). A soil-adjusted vegetation index (SAVI). *Remote Sensing of Environment*, *25*(3), 295–309. https://doi.org/10.1016/0034-4257(88)90106-X

Hughes, G. (1968). On the mean accuracy of statistical pattern recognizers. *IEEE Transactions on Information Theory*, *14*(1), 55–63. https://doi.org/10.1109/TIT.1968.1054102

Inomata, T., Triadan, D., Vázquez López, V. A., Fernandez-Diaz, J. C., Omori, T., Méndez Bauer, M. B., García Hernández, M., Beach, T., Cagnato, C., Aoyama, K., & Nasu, H. (2020). Monumental architecture at Aguada Fénix and the rise of Maya civilization. *Nature*, *582*(7813), 530–533. https://doi.org/10.1038/s41586-020-2343-4

Isenburg, M. (2020). *LasTools: Efficient LiDAR Processing Software* (Version 170322) [Computer software]. Rapidlasso. http://lastools.org

Jay, S., Guillaume, M., Minghelli, A., Deville, Y., Chami, M., Lafrance, B., & Serfaty, V. (2017). Hyperspectral remote sensing of shallow waters: Considering environmental noise and bottom intra-class variability for modeling and inversion of water reflectance. *Remote Sensing of Environment*, *200*, 352–367. https://doi.org/10.1016/j.rse.2017.08.020

Jia, J., Wang, Y., Chen, J., Guo, R., Shu, R., & Wang, J. (2020). Status and application of advanced airborne hyperspectral imaging technology: A review. *Infrared Physics & Technology*, *104*, 103115. https://doi.org/10.1016/j.infrared.2019.103115

Jing, L., & Tian, Y. (2020). Self-supervised visual feature learning with deep neural networks: A survey. *IEEE Transactions on Pattern Analysis and Machine Intelligence*.

Jöns, H., Galanidou, N., Mennenga, M., Bailey, G., & Peeters, H. (2019). *The Archaeology of Europe's Drowned Landscapes*. Springer.

Jung, A. B., Wada, K., Crall, J., Tanaka, S., Graving, J., Reinders, C., Yadav, S., Banerjee, J., Vecsei, G., Kraft, A., Rui, Z., Borovec, J., Vallentin, C., Zhydenko, S., Pfeiffer, K., Cook, B., Fernández, I., De Rainville, F.-M., Weng, C.-H., … others. (2020). *Imgaug*. https://github.com/aleju/imgaug

Jutzi, B., & Stilla, U. (2005). Measuring and processing the waveform of laser pulses. *Optical*, *3*, 194–203.

Kabir, S., Leigh, L., & Helder, D. (2020). Vicarious Methodologies to Assess and Improve the Quality of the Optical Remote Sensing Images: A Critical Review. *Remote Sensing*, *12*(24), 4029. https://doi.org/10.3390/rs12244029

Kashani, A., Olsen, M., Parrish, C., & Wilson, N. (2015). A Review of LIDAR Radiometric Processing: From Ad Hoc Intensity Correction to Rigorous Radiometric Calibration. *Sensors*, *15*(11), 28099–28128. https://doi.org/10.3390/s151128099

Kaufman, Y. J., & Tanre, D. (1992). Atmospherically resistant vegetation index (ARVI) for EOS-MODIS. *IEEE Transactions on Geoscience and Remote Sensing*, *30*(2), 261–270. https://doi.org/10.1109/36.134076

Kay, S. M. (1998). *Fundamentals of Statistical Signal Processing: Detection theory*. Prentice-Hall PTR.

Kazimi, B., Thiemann, F., Malek, K., Sester, M., & Khoshelham, K. (2018). Deep Learning for Archaeological Object Detection in Airborne Laser Scanning Data. *Proceedings of the 2nd Workshop On Computing Techniques For Spatio-Temporal Data in Archaeology And Cultural Heritage*, 15. https://doi.org/10.4230/LIPIcs.COARCH.2018

Kazimi, B., Thiemann, F., & Sester, M. (2019). Object Instance Segmentation in Digital Terrain Models. In M. Vento & G. Percannella (Eds.), *Computer Analysis of Images and Patterns* (Vol. 11679, pp. 488–495). Springer International Publishing. https://doi.org/10.1007/978-3-030-29891-3_43

Kazimi, B., Thiemann, F., & Sester, M. (2020). Detection Of Terrain Structures in Airborne Laser Scanning Data Using Deep Learning. *ISPRS Annals of Photogrammetry, Remote Sensing and Spatial Information Sciences*, *V-2–2020*, 493–500. https://doi.org/10.5194/isprs-annals-V-2-2020-493-2020

Keshava, N. (2003). A survey of spectral unmixing algorithms. *Lincoln Laboratory Journal*, *14*(1), 55–78.

Khan, A., Sohail, A., Zahoora, U., & Qureshi, A. S. (2020). A survey of the recent architectures of deep convolutional neural networks. *Artificial Intelligence Review*, *53*(8), 5455–5516. https://doi.org/10.1007/s10462-020-09825-6

Khan, S., Aragão, L., & Iriarte, J. (2017). A UAV–lidar system to map Amazonian rainforest and its ancient landscape transformations. *International Journal of Remote Sensing*, *38*(8–10), 2313–2330. https://doi.org/10.1080/01431161.2017.1295486

Kim, J., Nguyen, A., & Lee, S. (2019). Deep CNN-Based Blind Image Quality Predictor. *IEEE Transactions on Neural Networks and Learning Systems*, *30*(1), 11–24. https://doi.org/10.1109/TNNLS.2018.2829819

Kim, M., Kopilevich, Y., Feygels, V., Park, J. Y., & Wozencraft, J. (2016). Modeling of Airborne Bathymetric Lidar Waveforms. *Journal of Coastal Research*, *76*, 18–30. https://doi.org/10.2112/SI76-003

Kluiving, S. J., & Guttmann-Bond, E. (Eds.). (2012). *Landscape Archaeology between Art and Science: From a Multi- to an Interdisciplinary Approach*. Amsterdam University Press. https://doi.org/10.26530/OAPEN_419690

Kokalj, Ž. (2020). *Relief Visualization Toolbox (RVT)*. https://iaps.zrc-sazu.si/en/rvt#v

Kokalj, Ž., & Hesse, R. (2017). *Airborne laser scanning raster data visualization a guide to good practice*. Založba ZRC. http://zalozba.zrc-sazu.si/p/P14

Kokalj, Ž., & Mast, J. (2021). Space lidar for archaeology? Reanalyzing GEDI data for detection of ancient Maya buildings. *Journal of Archaeological Science: Reports*, *36*, 102811. https://doi.org/10.1016/j.jasrep.2021.102811

Kokalj, Ž., & Somrak, M. (2019). Why Not a Single Image? Combining Visualizations to Facilitate Fieldwork and On-Screen Mapping. *Remote Sensing*, *11*(7), 747. https://doi.org/10.3390/rs11070747

Kokalj, Ž., Zakšek, K., & Oštir, K. (2011). Application of sky-view factor for the visualisation of historic landscape features in lidar-derived relief models. *Antiquity*, *85*(327), 263–273. https://www.cambridge.org/core/journals/antiquity/article/application-of-sky-view-factor-for-the-visualisation-of-historic-landscape-features-in-lidar-derived-relief-models/653F5AE9086CE2028974934C3BBDC104

Kokalj, Ž., Zakšek, K., & Oštir, K. (2013). Visualizations of lidar derived relief models. In R. Opitz & D. Cowley, *Interpreting archaeological topography: Airborne laser scanning, 3D data and ground observation* (Vol. 5, pp. 100–114). Oxbow Books: Oxford, UK.

Kotilainen, A. T., & Kaskela, A. M. (2017). Comparison of airborne LiDAR and shipboard acoustic data in complex shallow water environments: Filling in the white ribbon zone. *Marine Geology*, *385*, 250–259. https://doi.org/10.1016/j.margeo.2017.02.005

Kramer, M. A. (1991). Nonlinear principal component analysis using autoassociative neural networks. *AIChE Journal*, *37*(2), 233–243. https://doi.org/10.1002/aic.690370209

Kraus, K., & Pfeifer, N. (1998). Determination of terrain models in wooded areas with airborne laser scanner data. *ISPRS Journal of Photogrammetry and Remote Sensing*, *53*(4), 193–203. https://doi.org/10.1016/S0924-2716(98)00009-4

Krizhevsky, A., Sutskever, I., & Hinton, G. E. (2012). ImageNet Classification with Deep Convolutional Neural Networks. In F. Pereira, C. J. C. Burges, L. Bottou, & K. Q. Weinberger (Eds.), *Advances in Neural Information Processing Systems 25* (pp. 1097–1105). Curran Associates, Inc. http://papers.nips.cc/paper/4824-imagenet-classification-with-deep-convolutional-neural-networks.pdf

Kutser, T., Hedley, J., Giardino, C., Roelfsema, C., & Brando, V. E. (2020). Remote sensing of shallow waters – A 50 year retrospective and future directions. *Remote Sensing of Environment*, *240*, 111619. https://doi.org/10.1016/j.rse.2019.111619

Kutut, V., Lepkova, N., & Zrobek, S. (2021). Immovable Cultural Heritage Usage Modes: Theoretical Approach. *EUROPEAN RESEARCH STUDIES JOURNAL*, *XXIV*(Special Issue 1), 1136–1151. https://doi.org/10.35808/ersj/2092

Kwong, J. D., Messinger, D. W., & Middleton, W. D. (2009). *Hyperspectral clustering and unmixing for studying the ecology of state formation and complex societies* (S. S. Shen & P. E. Lewis, Eds.; p. 74570E). https://doi.org/10.1117/12.826354

Lague, D., & Feldmann, B. (2020). Topo-bathymetric airborne LiDAR for fluvial-geomorphology analysis. In *Developments in Earth Surface Processes* (Vol. 23, pp. 25–54). Elsevier. https://doi.org/10.1016/B978-0-444-64177-9.00002-3

Lambeck, K., Rouby, H., Purcell, A., Sun, Y., & Sambridge, M. (2014). Sea level and global ice volumes from the Last Glacial Maximum to the Holocene. *Proceedings of the National Academy of Sciences*, *111*(43), 15296–15303. https://doi.org/10.1073/pnas.1411762111

Lambers, K., Verschoof-van der Vaart, W., & Bourgeois, Q. (2019). Integrating Remote Sensing, Machine Learning, and Citizen Science in Dutch Archaeological Prospection. *Remote Sensing*, *11*(7), 794. https://doi.org/10.3390/rs11070794

Lane, P. J. (2011). Future Urban Growth and Archaeological Heritage Management: Some Implications for Research Activity in Africa. *Conservation and Management of Archaeological Sites*, *13*(2–3), 134–159. https://doi.org/10.1179/175355211X13179154165980

Langouët, L., & Daire, M.-Y. (2009). Ancient Maritime Fish-Traps of Brittany (France): A Reappraisal of the Relationship Between Human and Coastal Environment During the Holocene. *Journal of Maritime Archaeology*, *4*(2), 131. https://doi.org/10.1007/s11457-009-9053-2

Lasaponara, R., & Masini, N. (Eds.). (2012). *Satellite remote sensing: A new tool for archaeology*. Springer.

Lasaponara, R., Masini, N., Pecci, A., Perciante, F., Pozzi Escot, D., Rizzo, E., Scavone, M., & Sileo, M. (2017). Qualitative evaluation of COSMO SkyMed in the detection of earthen archaeological remains: The case of Pachamacac (Peru). *Journal of Cultural Heritage*, *23*, 55–62. https://doi.org/10.1016/j.culher.2015.12.010

Lato, M. J., Diederichs, M. S., & Hutchinson, D. J. (2010). Bias Correction for View-limited Lidar Scanning of Rock Outcrops for Structural Characterization. *Rock Mechanics and Rock Engineering*, *43*(5), 615–628. https://doi.org/10.1007/s00603-010-0086-5

Launeau, P., Giraud, M., Robin, M., & Baltzer, A. (2019). Full-Waveform LiDAR Fast Analysis of a Moderately Turbid Bay in Western France. *Remote Sensing*, *11*(2), 117. https://doi.org/10.3390/rs11020117

Le Rouzic, Z. (1933). Morphologie et chronologie des sépultures préhistoriques du Morbihan. *L'Anthropologie*, *3–4*, 225–265.

Le Rouzic, Z., Péquard, S.-J., & Péquard, M. (1922). Carnac (Morbihan), Fouilles faites dans la région. Allée couverte du Net, dite « Er-Bé (la. Tombe), Commune de Saint-Gildas de Rhuis. *Revue Antropologique*, 183–189.

Lecours, V., Dolan, M. F. J., Micallef, A., & Lucieer, V. L. (2016). A review of marine geomorphometry, the quantitative study of the seafloor. *Hydrology and Earth System Sciences*, *20*(8), 3207–3244. https://doi.org/10.5194/hess-20-3207-2016

Lecroere, T. (2016). "There Is None So Blind as Those Who Won't See": Metal Detecting and Archaeology in France. *Open Archaeology*, *2*(1). https://doi.org/10.1515/opar-2016-0014

LeCun, Y., Bengio, Y., & Hinton, G. (2015). Deep learning. *Nature*, *521*(7553), 436–444. https://doi.org/10.1038/nature14539

LeCun, Y., Boser, B., Denker, J. S., Henderson, D., Howard, R. E., Hubbard, W., & Jackel, L. D. (1989). Backpropagation Applied to Handwritten Zip Code Recognition. *Neural Computation*, *1*(4), 541–551. https://doi.org/10.1162/neco.1989.1.4.541

Lee, K. S., Cohen, W. B., Kennedy, R. E., Maiersperger, T. K., & Gower, S. T. (2004). Hyperspectral versus multispectral data for estimating leaf area index in four different biomes. *Remote Sensing of Environment*, *91*(3–4), 508–520. https://doi.org/10.1016/j.rse.2004.04.010

Lee, Z., & Carder, K. L. (2001). *Hyperspectral remote sensing of shallow water environments: A review* (R. J. Frouin, H. Kawamura, & M. Kishino, Eds.; pp. 83–94). https://doi.org/10.1117/12.411661

Lee, Z., Carder, K. L., Mobley, C. D., Steward, R. G., & Patch, J. S. (1998). Hyperspectral remote sensing for shallow waters I A semianalytical model. *Applied Optics*, *37*(27), 6329. https://doi.org/10.1364/AO.37.006329

Lee, Z., Carder, K. L., Mobley, C. D., Steward, R. G., & Patch, J. S. (1999). Hyperspectral remote sensing for shallow waters: 2 Deriving bottom depths and water properties by optimization. *Applied Optics*, *38*(18), 3831. https://doi.org/10.1364/AO.38.003831

Lenhard, K., Baumgartner, A., & Schwarzmaier, T. (2015). Independent Laboratory Characterization of NEO HySpex Imaging Spectrometers VNIR-1600 and SWIR-320m-e. *IEEE Transactions on Geoscience and Remote Sensing*, *53*(4), 1828–1841. https://doi.org/10.1109/TGRS.2014.2349737

Lennon, M., Sicot, G., Thomas, N., Smet, S., Taillandier, C., Corman, D., Watremez, P., & Gauthiez, F. (2013). SWIM : un outil de cartographie de la zone de petits fonds à partir de données de télédétection optique Colloque Carhamb'ar, Cartographie des habitats marins benthiques: De l'acquisition à la restitution, Brest, 26-28 Mars 2013. *Cartographie des habitats marins benthiques : de l'acquisition à la restitution*, 42–46.

Leon, J. X., Phinn, S. R., Hamylton, S., & Saunders, M. I. (2013). Filling the 'white ribbon' – a multisource seamless digital elevation model for Lizard Island, northern Great Barrier Reef. *International Journal of Remote Sensing*, *34*(18), 6337–6354. https://doi.org/10.1080/01431161.2013.800659

Leroux, G., Gautier, M., Meuret, J.-C., & Naas, P. (1999). *Enclos gaulois et gallo-romains en Armorique: De la prospection aérienne à la fouille entre Blavet et Mayenne*. Association pour la diffusion des recherches archéologiques dans l'Ouest de la France.

Liao, X., Zhang, Y., Su, F., Yue, H., Ding, Z., & Liu, J. (2018). UAVs surpassing satellites and aircraft in remote sensing over China. *International Journal of Remote Sensing*, *39*(21), 7138–7153. https://doi.org/10.1080/01431161.2018.1515511

Lillesand, T. M., Kiefer, R. W., & Chipman, J. W. (2015). *Remote sensing and image interpretation* (Seventh edition). John Wiley & Sons, Inc.

Lin, T.-Y., Maire, M., Belongie, S., Hays, J., Perona, P., Ramanan, D., Dollár, P., & Zitnick, C. L. (2014). Microsoft COCO: Common Objects in Context. In D. Fleet, T. Pajdla, B. Schiele, & T. Tuytelaars (Eds.), *Computer Vision – ECCV 2014* (pp. 740–755). Springer International Publishing. https://doi.org/10.1007/978-3-319-10602-1_48

Lindenthal, S. M., Ussyshkin, V. R., Wang, J. G., & Pokorny, M. (2012). Airborne lidar: A fully-automated self-calibration procedure. *The International Archives of the Photogrammetry, Remote Sensing and Spatial Information Sciences*, *XXXVIII-5/W12*, 73–78. https://doi.org/10.5194/isprsarchives-XXXVIII-5-W12-73-2011

Lindsay, J. (2020). *WhiteboxTools* (1.4.0) [Computer software]. https://jblindsay.github.io/ghrg/WhiteboxTools/index.html

Lindsay, J. B., Cockburn, J. M. H., & Russell, H. A. J. (2015). An integral image approach to performing multi-scale topographic position analysis. *Geomorphology*, *245*, 51–61. https://doi.org/10.1016/j.geomorph.2015.05.025

Linford, N. (2006). The application of geophysical methods to archaeological prospection. *Reports on Progress in Physics*, *69*(7), 2205–2257. https://doi.org/10.1088/0034-4885/69/7/R04

Litto3D. (2019). *Litto3D terre mer altimétrie bathymétrie interface terre-mer levé lidar*. https://diffusion.shom.fr/pro/risques/l3d-mar-morbihan-2015.html

Liu, F. T., Ting, K. M., & Zhou, Z.-H. (2008). Isolation Forest. *2008 Eighth IEEE International Conference on Data Mining*, 413–422. https://doi.org/10.1109/ICDM.2008.17

Liu, P. (2015). A survey of remote-sensing big data. *Frontiers in Environmental Science*, *3*. https://doi.org/10.3389/fenvs.2015.00045

Louchard, E. M., Reid, R. P., Stephens, C. F., Davis, C. O., Leathers, R. A., Downes, T. V., & Maffione, R. (2002). Derivative analysis of absorption features in hyperspectral remote sensing data of carbonate sediments. *Optics Express*, *10*(26), 1573–1584. https://doi.org/10.1364/OE.10.001573

Louvart, L., & Grateau, C. (2005). The Litto3D project. *Europe Oceans 2005*, 1244-1251 Vol. 2. https://doi.org/10.1109/OCEANSE.2005.1513237

Lubbock, J. (1865). *Pre-Historic Times: As illustrated by ancient remains and the manners and customs of modern savages* (Vol. 8). Williams and Norgate.

Lucas, G. (2001). Destruction and the Rhetoric of Excavation. *Norwegian Archaeological Review*, *34*(1), 35–46. https://doi.org/10.1080/00293650119347

Luo, G., Chen, G., Tian, L., Qin, K., & Qian, S.-E. (2016). Minimum Noise Fraction versus Principal Component Analysis as a Preprocessing Step for Hyperspectral Imagery Denoising. *Canadian Journal of Remote Sensing*, *42*(2), 106–116. https://doi.org/10.1080/07038992.2016.1160772

Luo, L., Wang, X., Guo, H., Lasaponara, R., Zong, X., Masini, N., Wang, G., Shi, P., Khatteli, H., Chen, F., Tariq, S., Shao, J., Bachagha, N., Yang, R., & Yao, Y. (2019). Airborne and

spaceborne remote sensing for archaeological and cultural heritage applications: A review of the century (1907–2017). *Remote Sensing of Environment*, *232*, 111280. https://doi.org/10.1016/j.rse.2019.111280

Lyman, R. (2010). What Taphonomy Is, What it Isn't, and Why Taphonomists Should Care about the Difference. *Journal of Taphonomy*, *8*, 1–16.

Lyzenga, D. R. (1981). Remote sensing of bottom reflectance and water attenuation parameters in shallow water using aircraft and Landsat data. *International Journal of Remote Sensing*, *2*(1), 71–82. https://doi.org/10.1080/01431168108948342

Ma, L., Liu, Y., Zhang, X., Ye, Y., Yin, G., & Johnson, B. A. (2019). Deep learning in remote sensing applications: A meta-analysis and review. *ISPRS Journal of Photogrammetry and Remote Sensing*, *152*, 166–177. https://doi.org/10.1016/j.isprsjprs.2019.04.015

Maini, R., & Aggarwal, H. (2010). A Comprehensive Review of Image Enhancement Techniques. *ArXiv:1003.4053 [Cs]*. http://arxiv.org/abs/1003.4053

Mallet, C., & Bretar, F. (2009). Full-waveform topographic lidar: State-of-the-art. *ISPRS Journal of Photogrammetry and Remote Sensing*, *64*(1), 1–16. https://doi.org/10.1016/j.isprsjprs.2008.09.007

Mandelbrot, B. B. (1982). *The fractal geometry of nature* (Vol. 1). WH freeman.

Mandlburger, G., Pfennigbauer, M., Steinbacher, F., & Pfeifer, N. (2011). *Airborne Hydrographic LiDAR Mapping-Potential of a new technique for capturing shallow water bodies*. 2416–2422. https://doi.org/10.36334/modsim.2011.e14.mandlburger

Manolakis, D. G., Lockwood, R. B., & Cooley, T. W. (2016). *Hyperspectral imaging remote sensing: Physics, sensors, and algorithms*. Cambridge University Press.

Manolakis, D., Marden, D., & Shaw, G. A. (2003). *Hyperspectral Image Processing for Automatic Target Detection Applications*. *14*(1), 39.

Marchand, G. (2020). Mesolithic networks of Atlantic France: The two faces of Brittany (7th and 6th millennia cal BC). In *Coastal Landscapes of the Mesolithic* (pp. 202–226). Routledge.

Marshall, M., Thenkabail, P., Biggs, T., & Post, K. (2016). Hyperspectral narrowband and multispectral broadband indices for remote sensing of crop evapotranspiration and its components (transpiration and soil evaporation). *Agricultural and Forest Meteorology*, *218–219*, 122–134. https://doi.org/10.1016/j.agrformet.2015.12.025

Masini, N., Lasaponara, R., Rizzo, E., & Orefici, G. (2012). Integrated Remote Sensing Approach in Cahuachi (Peru): Studies and Results of the ITACA Mission (2007–2010). In R. Lasaponara & N. Masini (Eds.), *Satellite Remote Sensing* (Vol. 16, pp. 307–344). Springer Netherlands. https://doi.org/10.1007/978-90-481-8801-7_14

Mayoral, A., Toumazet, J.-P., Simon, F.-X., Vautier, F., & Peiry, J.-L. (2017). The Highest Gradient Model: A New Method for Analytical Assessment of the Efficiency of LiDAR-Derived Visualization Techniques for Landform Detection and Mapping. *Remote Sensing*, *9*(2), 120. https://doi.org/10.3390/rs9020120

McFeeters, S. K. (1996). The use of the Normalized Difference Water Index (NDWI) in the delineation of open water features. *International Journal of Remote Sensing*, *17*(7), 1425–1432. https://doi.org/10.1080/01431169608948714

McInnes, L., Healy, J., & Melville, J. (2018). UMAP: Uniform Manifold Approximation and Projection for Dimension Reduction. *ArXiv:1802.03426 [Cs, Stat]*. http://arxiv.org/abs/1802.03426

McManamon, F. P., Stout, A., & Barnes, J. A. (Eds.). (2008). Introduction: Contemporary Archaeological Resource Management and the 'Liberals' Dilemma. In *Managing Archaeological Resources*. Routledge.

Mehendale, N., & Neoge, S. (2020). Review on Lidar Technology. *SSRN Electronic Journal*. https://doi.org/10.2139/ssrn.3604309

Meng, X., Currit, N., & Zhao, K. (2010). Ground Filtering Algorithms for Airborne LiDAR Data: A Review of Critical Issues. *Remote Sensing*, *2*(3), 833–860. https://doi.org/10.3390/rs2030833

Menna, F., Agrafiotis, P., & Georgopoulos, A. (2018). State of the art and applications in archaeological underwater 3D recording and mapping. *Journal of Cultural Heritage*, *33*, 231–248. https://doi.org/10.1016/j.culher.2018.02.017

Migoń, P. (2013). Cultural Heritage and Natural Hazards. In P. T. Bobrowsky (Ed.), *Encyclopedia of Natural Hazards* (pp. 135–140). Springer Netherlands. https://doi.org/10.1007/978-1-4020-4399-4_82

Missiaen, T., Sakellariou, D., & Flemming, N. C. (2017). Survey Strategies and Techniques in Underwater Geoarchaeological Research: An Overview with Emphasis on Prehistoric Sites. In G. N. Bailey, J. Harff, & D. Sakellariou (Eds.), *Under the Sea: Archaeology and Palaeolandscapes of the Continental Shelf* (Vol. 20, pp. 21–37). Springer International Publishing. https://doi.org/10.1007/978-3-319-53160-1_2

Mobley, C. D. (1999, December 20). *Estimation of the remote-sensing reflectance from above-surface measurements*. https://www.osapublishing.org/abstract.cfm?URI=ao-38-36-7442

Mobley, C. D., & Mobley, C. D. (1994). *Light and water: Radiative transfer in natural waters*. Academic press.

Mohan, B. K., & Porwal, A. (2015). Hyperspectral image processing and analysis. *Current Science*, *108*(5), 833–841. https://www.jstor.org/stable/24216512

Mohri, M., Rostamizadeh, A., & Talwalkar, A. (2012). *Foundations of machine learning*. MIT Press.

Molines, N. (1992). Le chopper de l'île Molène et le chopper de l'île Ilur. *Bulletin d'Information de l'Association Manche Atlantique Pour La Recherche Archéologique Dans Les Iles*, *5*, 19–23.

Montealegre, A. L., Lamelas, M. T., & de la Riva, J. (2015). A Comparison of Open-Source LiDAR Filtering Algorithms in a Mediterranean Forest Environment. *IEEE Journal of Selected Topics in Applied Earth Observations and Remote Sensing*, *8*(8), 4072–4085. https://doi.org/10.1109/JSTARS.2015.2436974

Naudinot, N., Bourdier, C., Laforge, M., Paris, C., Bellot-Gurlet, L., Beyries, S., Thery-Parisot, I., & Le Goffic, M. (2017). Divergence in the evolution of Paleolithic symbolic and technological

systems: The shining bull and engraved tablets of Rocher de l'Impératrice. *PLOS ONE*, *12*(3), e0173037. https://doi.org/10.1371/journal.pone.0173037

Nicolas, C., Pailler, Y., Stephan, P., Pierson, J., Aubry, L., Le Gall, B., Lacombe, V., & Rolet, J. (2021). La carte et le territoire: La dalle gravée du Bronze ancien de Saint-Bélec (Leuhan, Finistère). *Bulletin de La Société Préhistorique Française*, *118*(1), 99–146.

Nicu, I. C. (2020). Natural Hazards Versus Cultural Heritage. In C. Smith (Ed.), *Encyclopedia of Global Archaeology* (pp. 7641–7652). Springer International Publishing. https://doi.org/10.1007/978-3-030-30018-0_3185

Niculiță, M. (2020). Geomorphometric Methods for Burial Mound Recognition and Extraction from High-Resolution LiDAR DEMs. *Sensors*, *20*(4), 1192. https://doi.org/10.3390/s20041192

Noble, G., Lamont, P., & Masson-Maclean, E. (2019). Assessing the ploughzone: The impact of cultivation on artefact survival and the cost/benefits of topsoil stripping prior to excavation. *Journal of Archaeological Science: Reports*, *23*, 549–558. https://doi.org/10.1016/j.jasrep.2018.11.015

Ødegård, Ø., Mogstad, A. A., Johnsen, G., Sørensen, A. J., & Ludvigsen, M. (2018). Underwater hyperspectral imaging: A new tool for marine archaeology. *Applied Optics*, *57*(12), 3214. https://doi.org/10.1364/AO.57.003214

Olsen, B., Shanks, M., Webmoor, T., & Witmore, C. (2012). *Archaeology: The Discipline of Things*. University of California Press. https://doi.org/10.1525/9780520954007

O'Mahony, N., Campbell, S., Carvalho, A., Harapanahalli, S., Hernandez, G. V., Krpalkova, L., Riordan, D., & Walsh, J. (2020). Deep Learning vs. Traditional Computer Vision. In K. Arai & S. Kapoor (Eds.), *Advances in Computer Vision* (pp. 128–144). Springer International Publishing. https://doi.org/10.1007/978-3-030-17795-9_10

Opitz, R. (2016). Airborne Laserscanning in Archaeology: Maturing Methods and Democratizing Applications. In M. Forte & S. Campana (Eds.), *Digital Methods and Remote Sensing in*

Archaeology (pp. 35–50). Springer International Publishing. http://link.springer.com/10.1007/978-3-319-40658-9_2

Opitz, R., & Herrmann, J. (2018). Recent Trends and Long-standing Problems in Archaeological Remote Sensing. *Journal of Computer Applications in Archaeology*, *1*(1), 19–41. https://doi.org/10.5334/jcaa.11

Opitz, R., & Nuninger, L. (2013). *Point cloud metrics for separating standing archaeological remains and low vegetation in ALS data*. http://www.int-arch-photogramm-remote-sens-spatial-inf-sci.net/XL-5-W2/459/2013/isprsarchives-XL-5-W2-459-2013.pdf

Opitz, R. S., & Cowley, D. (Eds.). (2013). *Interpreting archaeological topography: Airborne laser scanning, 3D data and ground observation*. Oxbow Books.

Oppelt, N. (2012). Hyperspectral classification approaches for intertidal macroalgae habitat mapping: A case study in Heligoland. *Optical Engineering*, *51*(11), 111703. https://doi.org/10.1117/1.OE.51.11.111703

Orengo, H. A., & Petrie, C. A. (2018). Multi-scale relief model (MSRM): A new algorithm for the visualization of subtle topographic change of variable size in digital elevation models. *Earth Surface Processes and Landforms*, *43*(6), 1361–1369. https://doi.org/10.1002/esp.4317

Ouellette, W., & Getinet, W. (2016). Remote sensing for Marine Spatial Planning and Integrated Coastal Areas Management: Achievements, challenges, opportunities and future prospects. *Remote Sensing Applications: Society and Environment*, *4*, 138–157. https://doi.org/10.1016/j.rsase.2016.07.003

Padilla, R., Netto, S. L., & Silva, E. A. B. da. (2020). A Survey on Performance Metrics for Object-Detection Algorithms. *2020 International Conference on Systems, Signals and Image Processing (IWSSIP)*, 237–242. https://doi.org/10.1109/IWSSIP48289.2020.9145130

Pailler, Y., & Nicolas, C. (2019). *Une maison sous les dunes: Beg ar Loued, île Molène, Finistère. Identité et adaptation des groupes humains en mer d'Iroise à la transition des IIIe–IIe millénaires avant notre ère*. Sidestone press.

Pailler, Y., & Sparfel, Y. (2001). Patrimoine archéologique de l'archipel de Molène: Nouvelle approche. *Penn Ar Bed*, *182*, 13–26.

Pailler, Y., Stéphan, P., with contributions by, Gandois, H., Nicolas, C., Sparfel, Y., Tresset, A., Donnart, K., Dréano, Y., Fichaut, B., Suanez, S., Dupont, C., Audouard, L., Marcoux, N., Mougne, C., Salanova, L., Sellami, F., & Dietsch-Sellami, M.-F. (2014). Landscape Evolution and Human Settlement in the Iroise Sea (Brittany, France) during the Neolithic and Bronze Age. *Proceedings of the Prehistoric Society*, *80*, 105–139. https://doi.org/10.1017/ppr.2014.9

Palumbo, G. (2000). Threats and Challenges to the Archaeological Heritage in the Mediterranean. In J.-M. Teutonico & G. Palumbo (Eds.), *Management Planning for Archaeological Sites*. The Getty Conservation Institute. https://www.academia.edu/22030896/Threats_and_Challenges_to_the_Archaeological_Heritage_in_the_Mediterranean

Pan, Z., Glennie, C., Fernandez-Diaz, J. C., & Starek, M. (2016). Comparison of bathymetry and seagrass mapping with hyperspectral imagery and airborne bathymetric lidar in a shallow estuarine environment. *International Journal of Remote Sensing*, *37*(3), 516–536. https://doi.org/10.1080/01431161.2015.1131869

Pandey, P. C., Srivastava, P. K., Balzter, H., Bhattacharya, B., & Petropoulos, G. P. (Eds.). (2020). *Hyperspectral remote sensing: Theory and applications*. Elsevier.

Papakonstantinou, A., Kavroudakis, D., Kourtzellis, Y., Chtenellis, M., Kopsachilis, V., Topouzelis, K., & Vaitis, M. (2019). Mapping Cultural Heritage in Coastal Areas with UAS: The Case Study of Lesvos Island. *Heritage*, *2*(2), 1404–1422. https://doi.org/10.3390/heritage2020089

Parcak, S. H. (2009). *Satellite remote sensing for archaeology*. Routledge.

Parcak, S. H. (2017). GIS, Remote Sensing, and Landscape Archaeology. In *GIS, Remote Sensing, and Landscape Archaeology* (Vol. 1). Oxford University Press. https://doi.org/10.1093/oxfordhb/9780199935413.013.11

Pascucci, S., Cavalli, R. M., Palombo, A., & Pignatti, S. (2010). Suitability of CASI and ATM airborne remote sensing data for archaeological subsurface structure detection under different land cover: The Arpi case study (Italy). *Journal of Geophysics and Engineering*, *7*(2), 183–189. https://doi.org/10.1088/1742-2132/7/2/S04

Pastol, Y. (2011). Use of Airborne LIDAR Bathymetry for Coastal Hydrographic Surveying: The French Experience. *Journal of Coastal Research*, *62*, 6–18. https://doi.org/10.2112/SI_62_2

Pearsall, D. M. (2008). *Encyclopedia of Archaeology*. Academic Press/Elsevier.

Pearson, K. (1901). On lines and planes of closest fit to systems of points in space. *The London, Edinburgh, and Dublin Philosophical Magazine and Journal of Science*, *2*(11), 559–572. https://doi.org/10.1080/14786440109462720

Pentek, Q. (2020). *Contribution à la génération de cartes 3D-couleur de milieux naturels à partir de données d'un système multicapteur pour drone* [Phdthesis, Université Montpellier]. https://tel.archives-ouvertes.fr/tel-03215906

Petit, T. (2017). *Caractérisation des fonds marins et estimation bathymétrique par inversion de modèle de transfert radiatif: Application à l'imagerie hyperspectrale en milieu corallien* [Unpublished PhD]. Université de Bretagne occidentale - Brest.

Petit, T., Bajjouk, T., Mouquet, P., Rochette, S., Vozel, B., & Delacourt, C. (2017). Hyperspectral remote sensing of coral reefs by semi-analytical model inversion – Comparison of different inversion setups. *Remote Sensing of Environment*, *190*, 348–365. https://doi.org/10.1016/j.rse.2017.01.004

Philpot, W. D. (1989). Bathymetric mapping with passive multispectral imagery. *Applied Optics*, *28*(8), 1569. https://doi.org/10.1364/AO.28.001569

Pingel, T. J., Clarke, K. C., & McBride, W. A. (2013). An improved simple morphological filter for the terrain classification of airborne LIDAR data. *ISPRS Journal of Photogrammetry and Remote Sensing*, *77*, 21–30. https://doi.org/10.1016/j.isprsjprs.2012.12.002

Pingel, T. J., Clarke, K., & Ford, A. (2015). Bonemapping: A LiDAR processing and visualization technique in support of archaeology under the canopy. *Cartography and Geographic Information Science*, *42*(sup1), 18–26. https://doi.org/10.1080/15230406.2015.1059171

Plets, R., Quinn, R., Forsythe, W., Westley, K., Bell, T., Benetti, S., McGrath, F., & Robinson, R. (2011). Using Multibeam Echo-Sounder Data to Identify Shipwreck Sites: Archaeological assessment of the Joint Irish Bathymetric Survey data: USING MULTIBEAM ECHO-SOUNDER DATA TO IDENTIFY SHIPWRECK SITES. *International Journal of Nautical Archaeology*, *40*(1), 87–98. https://doi.org/10.1111/j.1095-9270.2010.00271.x

Podobnikar, T., & Vrečko, A. (2012). Digital Elevation Model from the Best Results of Different Filtering of a LiDAR Point Cloud: High Quality DEM from LiDAR Data. *Transactions in GIS*, *16*(5), 603–617. https://doi.org/10.1111/j.1467-9671.2012.01335.x

Poidebard, A. (1928). Reconnaissance aérienne au ledja et au ṣafa (mai 1927). *Syria*, *9*(2), 114–123. https://www.jstor.org/stable/4389802

Poirier, N., Baleux, F., & Calastrenc, C. (2020). The mapping of forested archaeological sites using UAV LiDaR. A feedback from a south-west France experiment in settlement & landscape archaeology. *Archéologies Numériques*, *4*(2). https://doi.org/10.21494/ISTE.OP.2020.0556

Poirier, N., Hautefeuille, F., & Calastrenc, C. (2014). *L'utilisation des micro-drones pour la prospection archéologique à basse altitude*. 13.

Pouyet, E., Rohani, N., Katsaggelos, A. K., Cossairt, O., & Walton, M. (2018). Innovative data reduction and visualization strategy for hyperspectral imaging datasets using t-SNE approach. *Pure and Applied Chemistry*, *90*(3), 493–506. https://doi.org/10.1515/pac-2017-0907

QField. (2021). *QField—Efficient field work built for QGIS* (1.9.6) [Computer software]. OPENGIS.ch. https://qfield.org/

QGIS. (2021). *QGIS Geographic Information System.* (3.18) [Computer software]. QGIS Association. http://www.qgis.org

Racetin, I., & Krtalić, A. (2021). Systematic Review of Anomaly Detection in Hyperspectral Remote Sensing Applications. *Applied Sciences*, *11*(11), 4878. https://doi.org/10.3390/app11114878

Rączkowski, W. (2020). Power and/or Penury of Visualizations: Some Thoughts on Remote Sensing Data and Products in Archaeology. *Remote Sensing*, *12*(18), 2996. https://doi.org/10.3390/rs12182996

Rasti, B., Scheunders, P., Ghamisi, P., Licciardi, G., & Chanussot, J. (2018). Noise Reduction in Hyperspectral Imagery: Overview and Application. *Remote Sensing*, *10*(3), 482. https://doi.org/10.3390/rs10030482

Ravankhah, M., de Wit, R., Argyriou, A. V., Chliaoutakis, A., Revez, M. J., Birkmann, J., Žuvela-Aloise, M., Sarris, A., Tzigounaki, A., & Giapitsoglou, K. (2019). Integrated Assessment of Natural Hazards, Including Climate Change's Influences, for Cultural Heritage Sites: The Case of the Historic Centre of Rethymno in Greece. *International Journal of Disaster Risk Science*, *10*(3), 343–361. https://doi.org/10.1007/s13753-019-00235-z

Ravon, A.-L. (2017). *Originalité et développement du Paléolithique inférieur à l'extrémité occidentale de l'Eurasie: Le Colombanien de Menez-Dregan (Plouhinec, Finistère)* [Phdthesis, Université Rennes 1]. https://tel.archives-ouvertes.fr/tel-01646855

Reed, I. S., & Yu, X. (1990). Adaptive multiple-band CFAR detection of an optical pattern with unknown spectral distribution. *IEEE Transactions on Acoustics, Speech, and Signal Processing*, *38*(10), 1760–1770. https://doi.org/10.1109/29.60107

Reeder-Myers, L. A. (2015). Cultural Heritage at Risk in the Twenty-First Century: A Vulnerability Assessment of Coastal Archaeological Sites in the United States. *The Journal of Island and Coastal Archaeology*, *10*(3), 436–445. https://doi.org/10.1080/15564894.2015.1008074

Reeves, D. M. (1936). Aerial Photography and Archaeology. *American Antiquity*, *2*(2), 102–107. https://doi.org/10.2307/275881

Rejas, J. G., Burillo, F., Bonatti, J., & Martinez, R. (2013). Anomaly detection using remote sensing for the archaeological heritage registration. *2013 Digital Heritage International Congress (DigitalHeritage)*, 193–196. https://doi.org/10.1109/DigitalHeritage.2013.6743731

Ren, H. C., Yan, Q., Liu, Z. J., Zuo, Z. Q., Xu, Q. Q., Li, F. F., & Song, C. (2016). Study on analysis from sources of error for Airborne LIDAR. *IOP Conference Series: Earth and Environmental Science*, *46*, 012030. https://doi.org/10.1088/1755-1315/46/1/012030

Renfrew, C., & Bahn, P. G. (2016). *Archaeology: Theories, Methods, and Practice* (Seventh edition revised&updated). Thames & Hudson.

Rick, T. C., & Sandweiss, D. H. (2020). Archaeology, climate, and global change in the Age of Humans. *Proceedings of the National Academy of Sciences*, *117*(15), 8250–8253.

Riley, D. N. (1944). The Technique of Air-Archaeology. *Archaeological Journal*, *101*(1), 1–16. https://doi.org/10.1080/00665983.1944.10853775

Riley, D. N. (1985). Review of Air Photo Interpretation for Archaeologists [Review of *Review of Air Photo Interpretation for Archaeologists*, by D. R. Wilson]. *Britannia*, *16*, 357–358. https://doi.org/10.2307/526435

Risbøl, O. (2013). Cultivating the "wilderness"-how lidar can improve archaeological landscape understanding. *Interpreting Archaeological Topography: 3D Data, Visualisation and Observation; Opitz, RS, Cowley, DC, Eds*, 51–62.

Roberts, D. (1985). Calibration of airborne imaging spectrometer data to percent reflectance using field spectral measurements. *19. International Symposium on Remote Sensing of Environment*, 679–688.

Rodriguez, J. D., Perez, A., & Lozano, J. A. (2010). Sensitivity Analysis of k-Fold Cross Validation in Prediction Error Estimation. *IEEE Transactions on Pattern Analysis and Machine Intelligence*, *32*(3), 569–575. https://doi.org/10.1109/TPAMI.2009.187

Roessner, S., Segl, K., Heiden, U., & Kaufmann, H. (2001). Automated differentiation of urban surfaces based on airborne hyperspectral imagery. *IEEE Transactions on Geoscience and Remote Sensing*, *39*(7), 1525–1532. https://doi.org/10.1109/36.934082

Rogass, C., Mielke, C., Scheffler, D., Boesche, N. K., Lausch, A., Lubitz, C., Brell, M., Spengler, D., Eisele, A., Segl, K., & Guanter, L. (2014). Reduction of Uncorrelated Striping Noise—

Applications for Hyperspectral Pushbroom Acquisitions. *Remote Sensing*, *6*(11), 11082–11106. https://doi.org/10.3390/rs61111082

Roscheck, F. (2020). *blend-modes: Image processing blend modes* (2.1.0) [Python]. https://github.com/flrs/blend_modes

Roth, R., & Thompson, J. (2008). Practical application of multiple pulse in air (MPiA) Lidar in large-area surveys. *The International Archives of the Photogrammetry, Remote Sensing and Spatial Information Sciences*, *37*, 183–188.

Rouse, J., Haas, R. H., Schell, J. A., & Deering, D. (1973). *Monitoring vegetation systems in the great plains with ERTS*.

Ruppe, C. V., & Barstad, J. F. (2013). *International Handbook of Underwater Archaeology.* Springer. http://public.eblib.com/choice/publicfullrecord.aspx?p=5575544

Rusu, R. B., & Cousins, S. (2011, May 9). 3D is here: Point Cloud Library (PCL). *IEEE International Conference on Robotics and Automation (ICRA)*.

Sadr, K. (2019). Kweneng: A Newly Discovered Pre-Colonial Capital Near Johannesburg. *Journal of African Archaeology*, *17*(1), 1–22. https://doi.org/10.1163/21915784-20190001

Savage, S. H., Levy, T. E., & Jones, I. W. (2012). Prospects and problems in the use of hyperspectral imagery for archaeological remote sensing: A case study from the Faynan copper mining district, Jordan. *Journal of Archaeological Science*, *39*(2), 407–420. https://www.academia.edu/3046620/Prospects_and_Problems_in_the_Use_of_Hyperspectral_Imagery_for_Archaeological_Remote_Sensing_A_Case_Study_from_the_Faynan_Copper_Mining_District_Jordan

Savitzky, A., & Golay, M. J. E. (1964). Smoothing and Differentiation of Data by Simplified Least Squares Procedures. *Analytical Chemistry*, *36*(8), 1627–1639. https://doi.org/10.1021/ac60214a047

Schaber, G. G., & Gumerman, G. J. (1969). Infrared scanning images: An archeological application. *Science*, *164*(3880), 712–713. USGS Publications Warehouse. http://pubs.er.usgs.gov/publication/70010063

Schaer, P., Skaloud, J., Landtwing, S., & Legat, K. (2007). Accuracy estimation for laser point cloud including scanning geometry. *Mobile Mapping Symposium 2007, Padova, CONF*.

Schiffer, M. B. (1987). *Formation processes of the archaeological record* (1st ed). University of New Mexico Press.

Schlapfer, D., Nieke, J., & Itten, K. I. (2007). Spatial PSF Nonuniformity Effects in Airborne Pushbroom Imaging Spectrometry Data. *IEEE Transactions on Geoscience and Remote Sensing*, *45*(2), 458–468. https://doi.org/10.1109/TGRS.2006.886182

Schmohl, S., & Sörgel, U. (2019). ALS Point Cloud Classification with Convolutional Neural Networks. *University of Stuttgart, Institute for Photogrammetry*. https://www.ifp.uni-stuttgart.de/en/research/remote_sensing/als_point_cloud_classification/

Schneider, A., Takla, M., Nicolay, A., Raab, A., & Raab, T. (2015). A Template-matching Approach Combining Morphometric Variables for Automated Mapping of Charcoal Kiln Sites: Automated Mapping of Charcoal Kiln Sites. *Archaeological Prospection*, *22*(1), 45–62. https://doi.org/10.1002/arp.1497

Schölkopf, B., Smola, A., & Müller, K.-R. (1998). Nonlinear Component Analysis as a Kernel Eigenvalue Problem. *Neural Computation*, *10*(5), 1299–1319. https://doi.org/10.1162/089976698300017467

Schulz Paulsson, B. (2019). Radiocarbon dates and Bayesian modeling support maritime diffusion model for megaliths in Europe. *Proceedings of the National Academy of Sciences*, *116*(9), 3460–3465. https://doi.org/10.1073/pnas.1813268116

Seibert, J. (2006). Introduction. In E. C. Robertson, J. D. Seibert, D. C. Fernandez, & M. U. Zender (Eds.), *Space and Spatial Analysis in Archaeology* (pp. xiii–xxiv). University of Calgary Press; JSTOR. https://doi.org/10.2307/j.ctv6gqr9h.5

Seitsonen, O., & Ikäheimo, J. (2021). Detecting Archaeological Features with Airborne Laser Scanning in the Alpine Tundra of Sápmi, Northern Finland. *Remote Sensing*, *13*(8), 1599. https://doi.org/10.3390/rs13081599

Selvaraju, R. R., Cogswell, M., Das, A., Vedantam, R., Parikh, D., & Batra, D. (2020). Grad-CAM: Visual Explanations from Deep Networks via Gradient-Based Localization. *International Journal of Computer Vision*, *128*(2), 336–359. https://doi.org/10.1007/s11263-019-01228-7

Sesana, E., Gagnon, A. S., Ciantelli, C., Cassar, J., & Hughes, J. J. (2021). Climate change impacts on cultural heritage: A literature review. *WIREs Climate Change*, *12*(4), e710. https://doi.org/10.1002/wcc.710

Sevara, C., Pregesbauer, M., Doneus, M., Verhoeven, G., & Trinks, I. (2016). Pixel versus object—A comparison of strategies for the semi-automated mapping of archaeological features using airborne laser scanning data. *Journal of Archaeological Science: Reports*, *5*, 485–498. https://doi.org/10.1016/j.jasrep.2015.12.023

Shih, P. T.-Y., Chen, Y.-H., & Chen, J.-C. (2014). Historic Shipwreck Study in Dongsha Atoll with Bathymetric LiDAR. *Archaeological Prospection*, *21*(2), 139–146. https://doi.org/10.1002/arp.1466

Shorten, C., & Khoshgoftaar, T. M. (2019). A survey on Image Data Augmentation for Deep Learning. *Journal of Big Data*, *6*(1), 60. https://doi.org/10.1186/s40537-019-0197-0

Siart, C., Forbriger, M., & Bubenzer, O. (2018). Digital Geoarchaeology: Bridging the Gap Between Archaeology, Geosciences and Computer Sciences. In C. Siart, M. Forbriger, & O. Bubenzer (Eds.), *Digital Geoarchaeology* (pp. 1–7). Springer International Publishing. https://doi.org/10.1007/978-3-319-25316-9_1

Sicot, G., Ghannami, M. A., Lennon, M., Thomas, N., & Loyer, S. (2021). Likelihood Ratio Statistic for Inferring the Uncertainty of Satellite Derived Bathymetry. *2021 11th Workshop on Hyperspectral Imaging and Signal Processing: Evolution in Remote Sensing (WHISPERS)*, 1–5. https://doi.org/10.1109/WHISPERS52202.2021.9484053

Sicot, G., Lennon, M., Corman, D., & Gauthiez, F. (2015). Estimation of the sea bottom spectral reflectance in shallow water with hyperspectral data. *Geoscience and Remote Sensing Symposium (IGARSS), 2015 IEEE International*, 2311–2314.

Singh, H., Adams, J., Mindell, D., & Foley, B. (2000). Imaging Underwater for Archaeology. *Journal of Field Archaeology*, *27*(3), 319–328. https://doi.org/10.1179/jfa.2000.27.3.319

Sithole, G., & Vosselman, G. (2004). Experimental comparison of filter algorithms for bare-Earth extraction from airborne laser scanning point clouds. *ISPRS Journal of Photogrammetry and Remote Sensing*, *59*(1), 85–101. https://doi.org/10.1016/j.isprsjprs.2004.05.004

Sithole, G., & Vosselman, G. (2005). Filtering of airborne laser scanner data based on segmented point clouds. *International Archives of Photogrammetry, Remote Sensing and Spatial Information Sciences*, *36*(part 3), W19.

Solecki, R. S. (1957). Practical Aerial Photography for Archaeologists. *American Antiquity*, *22*(4), 337–351. https://doi.org/10.2307/276132

Somrak, M., Džeroski, S., & Kokalj, Ž. (2020). Learning to Classify Structures in ALS-Derived Visualizations of Ancient Maya Settlements with CNN. *Remote Sensing*, *12*(14), 2215. https://doi.org/10.3390/rs12142215

Soroush, M., Mehrtash, A., Khazraee, E., & Ur, J. A. (2020). Deep Learning in Archaeological Remote Sensing: Automated Qanat Detection in the Kurdistan Region of Iraq. *Remote Sensing*, *12*(3), 500. https://doi.org/10.3390/rs12030500

Star, J. L., Estes, J. E., & McGwire, K. C. (1997). *Integration of geographic information systems and remote sensing* (Vol. 5). Cambridge University Press.

Stein, J. K. (2001). A Review of Site Formation Processes and Their Relevance to Geoarchaeology. In P. Goldberg, V. T. Holliday, & C. R. Ferring (Eds.), *Earth Sciences and Archaeology* (pp. 37–51). Springer US. https://doi.org/10.1007/978-1-4615-1183-0_2

Stéphan, P. (2019). Évolutions morphologiques et indices d'occupation humaine au Pléistocène et à l'Holocène le long des côtes françaises de la Manche et de l'Atlantique. *Les nouvelles de l'archéologie*, *156*, 53–59. https://doi.org/10.4000/nda.6996

Stéphan, P., Fichaut, B., Suanez, S. S., Aoustin, D., & Marguerie, D. (2019). Changements paléogéographiques dans l'archipel de Molène, du Néolithique à aujourd'hui. In Y. Pailler & C. Nicolas (Eds.), *Une maison sous les dunes: Beg Ar Loued, île Molène, Finistère. Identité et*

adaptation des groupes humains en mer d'Iroise entre les IIIe et IIe millénaires avant notre ère (pp. 83–121). Sidestone Press. https://hal.archives-ouvertes.fr/hal-01861285

Stéphan, P., Gandois, H., Ehrhold, A., Le Dantec, N., Franzetti, M., Pailler, Y., Baltzer, A., & Jouet, G. (2019). De l'usage de certaines pêcheries à l'âge du Bronze ancien dans l'archipel de Molène. In Y. Pailler & C. Nicolas (Eds.), *Une maison sous les dunes: Beg Ar Loued, île Molène, Finistère. Identité et adaptation des groupes humains en Mer d'Iroise à la transition IIIe-IIe millénaire avant notre ère* (pp. 109–123). Sidestone Press. https://hal.archives-ouvertes.fr/hal-01861274

Stéphan, P., & Goslin, J. (2014). Évolution du niveau marin relatif à l'Holocène le long des côtes françaises de l'Atlantique et de la Manche: Réactualisation des données par la méthode des « sea-level index points ». *Quaternaire*, *vol. 25/4*, 295–312. https://doi.org/10.4000/quaternaire.7269

Stéphan, P., Pailler, Y., Tresset, A., & Gandois, H. (2013). Changements paléogéographiques de l'archipel de Molène (Finistère, Bretagne, France): Implications sur les peuplements humains du Néolithique à l'Age du Bronze. *Ancient Maritime Communities and the Relationship between People and Environment along the European Atlantic Coasts, Proceedings of the HOMER 2011 Conference, Vannes, 28 Sept.-1er Oct. 2011*. https://www.academia.edu/5419331/St%C3%A9phan_P_Pailler_Y_Tresset_A_Gandois_H_2013_Changements_pal%C3%A9og%C3%A9ographiques_de_l_archipel_de_Mol%C3%A8ne_Finist%C3%A8re_Bretagne_France_implications_sur_les_peuplements_humains_du_N%C3%A9olithique_%C3%A0_l_Age_du_Bronze

Štular, B., Kokalj, Ž., Oštir, K., & Nuninger, L. (2012). Visualization of lidar-derived relief models for detection of archaeological features. *Journal of Archaeological Science*, *39*(11), 3354–3360. https://doi.org/10.1016/j.jas.2012.05.029

Štular, B., & Lozić, E. (2020). Comparison of Filters for Archaeology-Specific Ground Extraction from Airborne LiDAR Point Clouds. *Remote Sensing*, *12*(18), 3025. https://doi.org/10.3390/rs12183025

Štular, B., Lozić, E., & Eichert, S. (2021a). *Interpolation of Airborne LiDAR Data for Archaeology*. https://hal.archives-ouvertes.fr/hal-03196185

Štular, B., Lozić, E., & Eichert, S. (2021b). Airborne LiDAR-Derived Digital Elevation Model for Archaeology. *Remote Sensing*, *13*(9), 1855. https://doi.org/10.3390/rs13091855

Stumpf, R. P., Holderied, K., & Sinclair, M. (2003). Determination of water depth with high-resolution satellite imagery over variable bottom types. *Limnology and Oceanography*, *48*(1part2), 547–556. https://doi.org/10.4319/lo.2003.48.1_part_2.0547

Sturt, F., Flemming, N. C., Carabias, D., Jöns, H., & Adams, J. (2018). The next frontiers in research on submerged prehistoric sites and landscapes on the continental shelf. *Proceedings of the Geologists' Association*, *129*(5), 654–683. https://doi.org/10.1016/j.pgeola.2018.04.008

Sutterley, T. (2021). *pyTMD: Tide Model Driver to read OTIS, GOT and FES formatted tidal solutions and make tidal predictions* (1.0.3.0) [Python]. https://github.com/tsutterley/pyTMD

Tabbagh, A. (2018). La prospection: Évolution de la sous-discipline, évolution du métier. *ArchéoSciences*, *42*, 103–108. https://doi.org/10.4000/archeosciences.5440

Talsky, G., Mayring, L., & Kreuzer, H. (1978). High-Resolution, Higher-Order UV/VIS Derivative Spectrophotometry. *Angewandte Chemie International Edition in English*, *17*(11), 785–799. https://doi.org/10.1002/anie.197807853

Tan, S.-Y. (2016). Developments in Hyperspectral Sensing. In J. N. Pelton, S. Madry, & S. Camacho-Lara (Eds.), *Handbook of Satellite Applications* (pp. 1–21). Springer New York. https://doi.org/10.1007/978-1-4614-6423-5_101-1

Tapete, D., & Cigna, F. (2019). Detection of Archaeological Looting from Space: Methods, Achievements and Challenges. *Remote Sensing*, *11*(20), 2389. https://doi.org/10.3390/rs11202389

Tapete, D., Cigna, F., & Donoghue, D. N. M. (2016). 'Looting marks' in space-borne SAR imagery: Measuring rates of archaeological looting in Apamea (Syria) with TerraSAR-X Staring Spotlight. *Remote Sensing of Environment*, *178*, 42–58. https://doi.org/10.1016/j.rse.2016.02.055

Tarolli, P., Cao, W., Sofia, G., Evans, D., & Ellis, E. C. (2019). From features to fingerprints: A general diagnostic framework for anthropogenic geomorphology. *Progress in Physical Geography: Earth and Environment*, *43*(1), 95–128. https://doi.org/10.1177/0309133318825284

Thabeng, O. L., Adam, E., & Merlo, S. (2019). Spectral Discrimination of Archaeological Sites Previously Occupied by Farming Communities Using In Situ Hyperspectral Data. *Journal of Spectroscopy*, *2019*, 1–21. https://doi.org/10.1155/2019/5158465

Thomas, N., Lennon, M., Danilo, C., Sicot, G., Ali Ghannami, M., & Loyer, S. (2021). A Method for Propagating Uncertainties of the Top of Atmosphere Sentinel-2 Measurements to Bottom of Atmosphere Reflectance for Aquatic Applications. *2021 11th Workshop on Hyperspectral Imaging and Signal Processing: Evolution in Remote Sensing (WHISPERS)*, 1–5. https://doi.org/10.1109/WHISPERS52202.2021.9484050

Thompson, D. R., Cawse-Nicholson, K., Erickson, Z., Fichot, C. G., Frankenberg, C., Gao, B.-C., Gierach, M. M., Green, R. O., Jensen, D., Natraj, V., & Thompson, A. (2019). A unified approach to estimate land and water reflectances with uncertainties for coastal imaging spectroscopy. *Remote Sensing of Environment*, *231*, 111198. https://doi.org/10.1016/j.rse.2019.05.017

Toth, C. K., Csanyi, N., Grejner-brzezinska, D. A., Toth, C. K., Csanyi, N., Grejner-brzezinska, D. A., Words, K., Toth, C. K., Csanyi, N., & Grejner-brzezinska, D. A. (2002). Automating the calibration of airborne multisensor imaging systems. *Proc. ACSM-ASPRS Annual Conference*. FIG XXII International Congress, Washington, D.C. USA.

Toumazet, J.-P., Vautier, F., Roussel, E., & Dousteyssier, B. (2017). Automatic detection of complex archaeological grazing structures using airborne laser scanning data. *Journal of Archaeological Science: Reports*, *12*, 569–579. https://doi.org/10.1016/j.jasrep.2017.03.012

Transon, J., D'Andrimont, R., Maugnard, A., & Defourny, P. (2018). Survey of Hyperspectral Earth Observation Applications from Space in the Sentinel-2 Context. *Remote Sensing*, *10*(2), 157. https://doi.org/10.3390/rs10020157

Traviglia, A. (2006a). Archaeological usability of hyperspectral images: Successes and failures of image processing techniques. *BAR International Series*, *1568*, 123.

Traviglia, A. (2006b). MIVIS hyperspectral sensors for the detection and GIS supported interpretation of subsoil archaeological sites. *Proceedings of the 34th Conference on Digital Discovery: Exploring New Frontiers in Human Heritage, CAA*.

Traviglia, A., & Torsello, A. (2017). Landscape Pattern Detection in Archaeological Remote Sensing. *Geosciences*, *7*(4), 128. https://doi.org/10.3390/geosciences7040128

Trier, Ø. D., Cowley, D. C., & Waldeland, A. U. (2018). Using deep neural networks on airborne laser scanning data: Results from a case study of semi-automatic mapping of archaeological topography on Arran, Scotland. *Archaeological Prospection*, *26*(2), 165–175. https://doi.org/10.1002/arp.1731

Trier, Ø. D., & Pilø, L. H. (2012). Automatic Detection of Pit Structures in Airborne Laser Scanning Data: Automatic detection of pits in ALS data. *Archaeological Prospection*, *19*(2), 103–121. https://doi.org/10.1002/arp.1421

Trier, Ø. D., Reksten, J. H., & Løseth, K. (2021). Automated mapping of cultural heritage in Norway from airborne lidar data using faster R-CNN. *International Journal of Applied Earth Observation and Geoinformation*, *95*, 102241. https://doi.org/10.1016/j.jag.2020.102241

Trier, Ø. D., Salberg, A.-B., & Holger Pilø, L. (2016). Semi-automatic mapping of charcoal kilns from airborne laser scanning data using deep learning. *CAA2016 : Oceans of Data*, 221–232.

Tsai, F., & Philpot, W. (1998). Derivative Analysis of Hyperspectral Data. *Remote Sensing of Environment*, *66*(1), 41–51. https://doi.org/10.1016/S0034-4257(98)00032-7

Tzvetkov, J. (2018). Relief visualization techniques using free and open source GIS tools. *Polish Cartographical Review*, *50*(2), 61–71. https://doi.org/10.2478/pcr-2018-0004

Uhl, F., Bartsch, I., & Oppelt, N. (2016). Submerged Kelp Detection with Hyperspectral Data. *Remote Sensing*, *8*(6), 487. https://doi.org/10.3390/rs8060487

Ussyshkin, V., Boba, M., & Sitar, M. (2008). Performance characterization of an airborne lidar system: Bridging system specifications and expected performance. *The International Archives of the Photogrammetry, Remote Sensing and Spatial Information Sciences*, *37*, 177–182.

Vaiphasa, C. (2006). Consideration of smoothing techniques for hyperspectral remote sensing. *ISPRS Journal of Photogrammetry and Remote Sensing*, *60*(2), 91–99. https://doi.org/10.1016/j.isprsjprs.2005.11.002

van der Meer, F. D., van der Werff, H. M. A., van Ruitenbeek, F. J. A., Hecker, C. A., Bakker, W. H., Noomen, M. F., van der Meijde, M., Carranza, E. J. M., Smeth, J. B. de, & Woldai, T. (2012). Multi- and hyperspectral geologic remote sensing: A review. *International Journal of Applied Earth Observation and Geoinformation*, *14*(1), 112–128. https://doi.org/10.1016/j.jag.2011.08.002

VanValkenburgh, P., & Dufton, J. A. (2020). Big Archaeology: Horizons and Blindspots. *Journal of Field Archaeology*, *45*(sup1), S1–S7. https://doi.org/10.1080/00934690.2020.1714307

Verhagen, P. (2012). Biting off more than we can chew? The current and future role of digital techniques in landscape archaeology. In *Landscape Archaeology between Art and Science* (pp. 309–320). Amsterdam University Press.

Verhoeven, G., & De Vliegher, B. M. (2004). Oblique aerial photography in a GIS environment for geo-archaeological research - A case study: The Potenza Valley survey. In R. Goossens (Ed.), *Remote Sensing in Transition* (pp. 427–434). Millpress Science Publishers. http://www.webofscience.com/wos/alldb/full-record/WOS:000189495100061

Verhoeven, G. J. (2017). Are We There Yet? A Review and Assessment of Archaeological Passive Airborne Optical Imaging Approaches in the Light of Landscape Archaeology. *Geosciences*, *7*(3), 86. https://doi.org/10.3390/geosciences7030086

Verhoeven, G., & Sevara, C. (2016). Trying to Break New Ground in Aerial Archaeology. *Remote Sensing*, *8*(11), 918. https://doi.org/10.3390/rs8110918

Verschoof-van der Vaart, W. B., & Lambers, K. (2019). Learning to Look at LiDAR: The Use of R-CNN in the Automated Detection of Archaeological Objects in LiDAR Data from the

Netherlands. *Journal of Computer Applications in Archaeology*, *2*(1), 31–40. https://doi.org/10.5334/jcaa.32

Verschoof-van der Vaart, W. B., Lambers, K., Kowalczyk, W., & Bourgeois, Q. P. J. (2020). Combining Deep Learning and Location-Based Ranking for Large-Scale Archaeological Prospection of LiDAR Data from The Netherlands. *ISPRS International Journal of Geo-Information*, *9*(5), 293. https://doi.org/10.3390/ijgi9050293

Vosselman, G. (2000). Slope based filtering of laser altimetry data. *International Archives of Photogrammetry and Remote Sensing*, *33*(B3/2; PART 3), 935–942.

Vosselman, G., & Maas, H. G. (2014). *Airborne and Terrestrial Laser Scanning*. Whittles Publishing.

Wagner, W., Ullrich, A., Melzer, T., Briese, C., & Kraus, K. (2004). From single-pulse to full-waveform airborne laser scanners: Potential and practical challenges. *International Archives of Photogrammetry, Remote Sensing and Spatial Information Sciences*, *35*, 201–206.

Wallach, E. (2019). Inference from absence: The case of archaeology. *Palgrave Communications*, *5*(1), 1–10. https://doi.org/10.1057/s41599-019-0307-9

Wandsnider, L. (1996). Describing and comparing archaeological spatial structures. *Journal of Archaeological Method and Theory*, *3*(4), 319–384.

Wang, C., Li, Q., Liu, Y., Wu, G., Liu, P., & Ding, X. (2015). A comparison of waveform processing algorithms for single-wavelength LiDAR bathymetry. *ISPRS Journal of Photogrammetry and Remote Sensing*, *101*, 22–35.

Wang, H., & Glennie, C. (2015). Fusion of waveform LiDAR data and hyperspectral imagery for land cover classification. *ISPRS Journal of Photogrammetry and Remote Sensing*, *108*, 1–11. https://doi.org/10.1016/j.isprsjprs.2015.05.012

Wang, J., Ma, Y., Zhang, L., Gao, R. X., & Wu, D. (2018). Deep learning for smart manufacturing: Methods and applications. *Journal of Manufacturing Systems*, *48*, 144–156. https://doi.org/10.1016/j.jmsy.2018.01.003

Wang, J.-J. (2015). Flood risk maps to cultural heritage: Measures and process. *Journal of Cultural Heritage*, *16*(2), 210–220. https://doi.org/10.1016/j.culher.2014.03.002

Wang, X., Lasaponara, R., Luo, L., Chen, F., Wan, H., Yang, R., & Zhen, J. (2020). Digital Heritage. In H. Guo, M. F. Goodchild, & A. Annoni (Eds.), *Manual of Digital Earth* (pp. 565–591). Springer Singapore. https://doi.org/10.1007/978-981-32-9915-3_17

Webster, T. L., Murphy, J. B., & Gosse, J. C. (2006). Mapping subtle structures with light detection and ranging (LIDAR): Flow units and phreatomagmatic rootless cones in the North Mountain Basalt, Nova Scotia. *Canadian Journal of Earth Sciences*, *43*(2), 157–176. https://doi.org/10.1139/e05-099

Weiss, K., Khoshgoftaar, T. M., & Wang, D. (2016). A survey of transfer learning. *Journal of Big Data*, *3*(1), 9. https://doi.org/10.1186/s40537-016-0043-6

Westley, K., Plets, R., Quinn, R., McGonigle, C., Sacchetti, F., Dale, M., McNeary, R., & Clements, A. (2019). Optimising protocols for high-definition imaging of historic shipwrecks using multibeam echosounder. *Archaeological and Anthropological Sciences*, *11*(7), 3629–3645. https://doi.org/10.1007/s12520-019-00831-6

Whittaker, E. T. (1922). On a New Method of Graduation. *Proceedings of the Edinburgh Mathematical Society*, *41*, 63–75. https://doi.org/10.1017/S0013091500077853

Wickham-Jones, C. (2018). *Landscape Beneath the Waves: The Archaeological Exploration of Underwater Landscapes*. Oxbow Books. https://doi.org/10.2307/j.ctvh1dhkp

Wilson, D. R. (1982). *Air Photo Interpretation for Archaeologists*. B.T. Batsford.

Wilson, J. P., & Gallant, J. C. (2000). *Terrain analysis: Principles and applications*. Wiley.

Wu, Y., Kirillov, A., Massa, F., Lo, W.-Y., & Girshick, R. (2019). *Detectron2*. https://github.com/facebookresearch/detectron2

Xu, T., & Xu, L. (2017). *Digital underwater acoustic communications*. Elsevier, Academic Press is an imprint of Elsevier.

Xue, J., & Su, B. (2017). Significant Remote Sensing Vegetation Indices: A Review of Developments and Applications. *Journal of Sensors*, *2017*, 1–17. https://doi.org/10.1155/2017/1353691

Yan, W. Y., Shaker, A., & El-Ashmawy, N. (2015). Urban land cover classification using airborne LiDAR data: A review. *Remote Sensing of Environment*, *158*, 295–310. https://doi.org/10.1016/j.rse.2014.11.001

Yang, E., LaRocque, P., Guenther, G., Reid, D., Pan, W., & Francis, K. (2007). *Shallow water depth extraction – progress and challenges*. 13.

Yoëli, P. (1967). The Mechanisation of Analytical Hill Shading. *The Cartographic Journal*, *4*(2), 82–88. https://doi.org/10.1179/caj.1967.4.2.82

Yokoya, N., Miyamura, N., & Iwasaki, A. (2010). *Preprocessing of hyperspectral imagery with consideration of smile and keystone properties* (A. M. Larar, H.-S. Chung, & M. Suzuki, Eds.; p. 78570B). https://doi.org/10.1117/12.870437

Yokoyama, R., Shirasawa, M., & Pike, R. J. (2002). Visualizing topography by openness: A new application of image processing to digital elevation models. *Photogrammetric Engineering and Remote Sensing*, *68*(3), 257–266. http://info.asprs.org/publications/pers/2002journal/march/2002_mar_257-265.pdf

Zakšek, K., Oštir, K., & Kokalj, Ž. (2011). Sky-View Factor as a Relief Visualization Technique. *Remote Sensing*, *3*(12), 398–415. https://doi.org/10.3390/rs3020398

Zhang, K., Kang, X., & Li, S. (2019). Isolation Forest for Anomaly Detection in Hyperspectral Images. *IGARSS 2019 - 2019 IEEE International Geoscience and Remote Sensing Symposium*, 437–440. https://doi.org/10.1109/IGARSS.2019.8899812

Zhang, R., Isola, P., Efros, A. A., Shechtman, E., & Wang, O. (2018). The Unreasonable Effectiveness of Deep Features as a Perceptual Metric. *ArXiv:1801.03924 [Cs]*. http://arxiv.org/abs/1801.03924

Zhang, W., Qi, J., Wan, P., Wang, H., Xie, D., Wang, X., & Yan, G. (2016). An Easy-to-Use Airborne LiDAR Data Filtering Method Based on Cloth Simulation. *Remote Sensing*, *8*(6), 501. https://doi.org/10.3390/rs8060501

Zhao, H. (2019). *Spectral Sensitivity Database*. https://nae-lab.org/~rei/research/cs/zhao/database.html

Zhao, H., Kawakami, R., Tan, R. T., & Ikeuchi, K. (2009). Estimating basis functions for spectral sensitivity of digital cameras. *Meeting on Image Recognition and Understanding*, *2009*.

Zhong, Y., Wang, X., Xu, Y., Wang, S., Jia, T., Hu, X., Zhao, J., Wei, L., & Zhang, L. (2018). Mini-UAV-Borne Hyperspectral Remote Sensing: From Observation and Processing to Applications. *IEEE Geoscience and Remote Sensing Magazine*, *6*(4), 46–62. https://doi.org/10.1109/MGRS.2018.2867592

Zhu, X. X., Tuia, D., Mou, L., Xia, G.-S., Zhang, L., Xu, F., & Fraundorfer, F. (2017). Deep Learning in Remote Sensing: A Comprehensive Review and List of Resources. *IEEE Geoscience and Remote Sensing Magazine*, *5*(4), 8–36. https://doi.org/10.1109/MGRS.2017.2762307

Guyot, Alexandre. Contribution of airborne LiDAR and hyperspectral data to archaeological mapping in terrestrial and submerged environments. 2021

LIST OF FIGURES

Figure I.1.1. Position of Digital Geoarchaeology, as an interface between geosciences, computer sciences and archaeology (adapted from Siart et al. (2018)) 17
Figure 1.1. Classification of natural threats and relation to anthropogenic threats affecting cultural heritage (Ravankhah et al., 2019) 28
Figure 1.2. The archaeological entities (total of 21,814) recorded in the "carte archéologique" for the region of Brittany for different archaeological periods (source: Sra/DRAC, June 2020, available on Geobretagne) 30
Figure 1.3. Components of a remote sensing system (adapted from Lillesand et al. (2015)) 33
Figure 1.4. Passive remote sensing vs active remote sensing 34
Figure 1.5. The electromagnetic spectrum with the spectral subdivisions of the visible and infrared wavebands 34
Figure 1.6. From spaceborne to airborne remote sensing vectors (adapted from Liao et al. (2018)) 35
Figure 1.7. Aerial photography of the archaeological site of Stonehenge (United Kingdom) by Lieutenant P.H. Sharpe in 1906 (source: Historic England) 36
Figure 1.8. Cropmarks showing multiple structures of a Gallic necropolis in Grésac of France (credit: J. Dassié) 38
Figure 1.9. Aerial view of the remains of an ancient fish-weir visible at low tide in Servel-Lannion (credit: M. Mahéo & L. Langouët) 39
Figure 1.10. Conceptual diagram presenting the relation between remote sensing data, surface anomaly and the interpreted archaeological site 42
Figure 1.11. Conceptual diagram of long-term changes in sociocultural systems, cultural inheritances, societal scale, energy use and anthropogenic geomorphic features across landscapes (adapted from Tarolli et al. (2019) 43
Figure 2.1. Airborne LiDAR systems (modified from IGN sources) 46
Figure 2.2. Representation of an Airborne LiDAR pulse (source: Fernandez-Diaz et al., (2014)). 47
Figure 2.3. Technical classification of Airborne Laser Scanning Systems (adapted from Fernandez-Diaz et al. (2014). The technical characteristics of the ALS system (Optech Titan) used within the scope of this thesis are shown with a black outline. 48
Figure 2.4. Reflectance at typical laser wavelength (532nm, green and 1064nm, near-infrared) for various surface materials (adapted from Yan et al.(2015)) 50
Figure 2.5. LiDAR scanning patterns obtained with various laser beam deviation mechanisms, (a) oscillating mirror ("seesaw pattern"), (b) polygon mirror, (c) rotating mirror, (d) rotating wedge prism. (source: Pentek, (2020)) 51
Figure 2.6. Difference between discrete returns and full waveform digitization (adapted from Vosselman & Maas (2014)) 52
Figure 2.7. Airborne LiDAR raw point cloud colorized by elevation (Z attribute) 53

Figure 2.8. Differences between DEMs : DTMs, DSMs and DFMs (adapted from Štular et al.(2021)). The outline illustrates the conceptual definition of DFM and the degree of subjectivity and archaeological interpretability which are important drawbacks for its use for large-scale prospection 56
Figure 2.9. Profile view of a ground filtering result (right) of a raw point-cloud (left)..... 57
Figure 2.10 Diagram of the progressive TIN densification proposed by Axelsson (2000), (source: Z. Chen et al., (2017))..... 59
Figure 2.11. Analysis of a 3D point cloud using local neighborhood analysis in the Kerlescan stone alignments of Carnac France (left: classification of points, right: 3D point-cloud visualization colored according to 3 local descriptor combinations)..... 61
Figure 2.12: 3D structured voxel grid (right) generated from a 3D unstructured point cloud (left) (sources : Schmohl & Sörgel, (2019))..... 62
Figure 2.13. Analytical hillshaded relief visualization (right) compared with orthoimage (left) and hypsometrically colored terrain (center). Analytical hillshading parameters: sun elevation = 35°, sun azimuth = 315°..... 64
Figure 2.14. Multidirectional (PCA) analytical hillshaded relief visualization (right) compared with orthoimage (left) and hypsometrically colored terrain (center). Multidirectional (PCA) analytical hillshaded parameters: sun elevation = 35°, number of directions = 16 65
Figure 2.15. Slope relief visualization (right) compared with orthoimage (left) and hypsometrically colored terrain (center)..... 65
Figure 2.16. Principles of Sky-view factor (SVF). SVF calculation principle is shown in 2D (a) and 3D (b) for a single observation point (source: Zakšek et al. (2011)) 66
Figure 2.17. Sky-view-factor relief visualization (right) compared with orthoimage (left) and hypsometrically colored terrain (center). Sky-view-factor parameters: number of directions = 16; maximum radius = 10 pixels 66
Figure 2.18. Positive and negative openness compared to sky-view-factor on a flat terrain (a) and a slope terrain (b) (source: M. Doneus (2013))..... 67
Figure 2.19. Positive openness relief visualization (right) compared with orthoimage (left) and hypsometrically colored terrain (center). Openness parameters: number of directions = 16; maximum radius = 10 pixels 67
Figure 2.20. Simple local relief visualization (right) compared with orthoimage (left) and hypsometrically colored terrain (center). Simple local relief parameters: radius = 10 pixels..... 68
Figure 2.21. Multiscale topographic position image (rigth) compared with orthoimage (left) and hypsometrically colored terrain (center). Multiscale topographic position parameters: micro = [1 to 10 pixels], meso=]10, 100 pixels], macro=]100, 1000 pixels] 69
Figure 2.22. Pixel-based results of the presence of burial mounds (probability from 0 to 1) using a supervised machine-learning model (random forest) trained on multiscale topographic descriptors computed from LiDAR-derived terrain model 70
Figure 2.23. (a) Traditional Computer Vision workflow vs. (b) Deep Learning workflow (source: J. Wang et al. (2018) 72

Figure 2.24. Examples of tasks using deep CNN: image classification, assigns a single label to a whole image; image segmentation, densely classifies each pixel; object detection: locates and classifies specific objects in an image by providing a bounding box; and instance segmentation, provides a segmentation mask for detected objects within a bounding box (adapted from Hoeser & Kuenzer, 2020) 73
Figure 2.25. A typical deep convolutional neural network composed of convolutional (CONV), pooling and fully connected (FC) layers 73
Figure 2.26. Hyperspectral imaging principles (credit: VITO - Flemish Institute for Technological Research) 76
Figure 2.27. Whiskbroom (left) and pushbroom (left) hyperspectral sensors (Jia et al., 2020) 78
Figure 2.28. Smile and keystone effects in hyperspectral camera (source: Yokoya et al. (2010)) .. 80
Figure 2.29. Temporal variation (from October to April) of NDVI for a standard healthy site (non-archaeological) and an archaeological site / crop-mark. The green markers identify the period of most discriminative NDVI values (source: Agapiou et al. (2013)) 84
Figure 2.30. Example of a reflectance spectrum (seagrass) in the visible domain, analyzed by 1st and 2nd derivative spectroscopy 88
Figure 2.31. Example of a reflectance spectrum (seagrass) in the visible domain, analyzed by continuum removal 88
Figure 2.32. Depth of penetration of light in the visible spectral domain, calculated from the diffuse attenuation coefficient (Kd) measured in the Great Barrier Reef (Oceanic) and central parts of the Baltic Sea (source: Kutser et al. (2020)) 91
Figure 2.33. Principles of the shallow water radiative transfer model inversion. 93
Figure 3.1. Study sites and remote sensing surveys used for the thesis 97
Figure 3.2. Region of Brittany 99
Figure 3.3. Sea-level variations from the Upper Paleolithic to current days (bottom), and related western Europe costal representations for sea-level at -130m, -60m, -10m and 0m (top) (adapted from Stéphan (2019)) 100
Figure 3.4. Carnac and the Gulf of Morbihan 102
Figure 3.5. The Molène archipelago 104
Figure 3.6. Paleogeographic evolution of the Molène archipelago between 10,000 BP to 4000 BP, by P. Stéphan (source : Billard et al., 2020) 105
Figure 3.7. LiDAR survey (2016) over Carnac and the Gulf of Morbihan 106
Figure 3.8. Airborne LiDAR Optech Titan sensor (credit: Teledyne Optech) 107
Figure 3.9. Diagram describing the workflow to compute a Multiscale Topographic Position image (MSTP) from a Digital Terrain Model (DTM) 109
Figure 3.10. Number of LiDAR returns (total and ground filtered) differentiated by laser wavelength (NIR and Green) for three different environments (open-area, deciduous forest, coniferous forest) covering 900m². Loss 'A' was mainly due to strong absorption of green laser pulse by the canopy elements, followed by a second reduction, loss 'B' due to the masking of the persistent canopy elements. 112

Figure 3.11. (Top) Building roofs without void area. (Bottom) Building roofs with void areas (no returns except for roof ridges). The bottom situation is posing problem for the ground filtering algorithm due to the gentle slope formed between the building points and their nearest ground points. This example justifies the development of the two-step ground filtering operation. 113
Figure 3.12. Hyperspectral survey (2018) over Carnac and the Gulf of Morbihan 114
Figure 3.13. VNIR-1600 HySpex sensor and IMAR iTrace-RT-F200 navigation system (left), P68-Partenavia aircraft (right) used for the hyperspectral survey (credit: Hytech-imaging) 115
Figure 3.14. Hyperspectral survey (2020) over Molène archipelago 116
Figure 3.15. Example of trajectory for the hyperspectral survey on Molène archipelago (credit: Hytech-imaging) 117
Figure 3.16. Calibration tarps positioned on the area of interest during the survey of site 2 and used for improving the atmospheric correction through empirical line fit 118
Figure 3.17. Archaeological entities (EA) on the area of Carnac and the Gulf of Morbihan. The dominance of Neolithic archaeological records is observable in the UNESCO project area..... 120
Figure 3.18. LiDAR-specific archaeological reference (195 entities) used on the area of Carnac and the Gulf of Morbihan, for the data processing in Chapter 4 and Chapter 5..... 121
Figure 3.19. Map of the fish weirs inventory (Stéphan et al., 2019) in the Molène archipelago and used as reference database (background: SCAN Littoral® from Shom/IGN) 123
Figure 3.20. An example of a "survey assistance sheet" for a targeted anomaly identified by LiDAR-based analysis and used during field campaign 125
Figure 3.21. An example of a targeted anomaly identified by LiDAR-based analysis and visualized with QField tool on a GNSS-enabled tablet used during field campaign. The digital version of the "prospection assistance sheet" is linked to the GIS entity related to the target anomaly. 126
Figure 3.22. Photography and notes collected during field campaign for a targeted anomaly identified by LiDAR-based analysis 126
Figure 3.23. Underwater verification campaign in Molène archipelago. (a, b) Briefing of divers before the dive. Spatial/spectral visualizations of the hyperspectral-derived anomaly to be verified were shared with a GIS & GNSS enabled tablet. (c) Underwater image of one of the anomalies being verified (credit: L. Schweyer / OFB). 128
Figure 4.1. Image analysis using deep learning Convolutional Neural Networks for an archaeological site (Tumulus du Moustoir, Carnac, France). (a) Image classification: a class or label associated with the image, (b) Object detection: a labeled bounding box that locates the object of interest within the image, and (c) Object segmentation: a labeled footprint that locates and delineates the object of interest within the image. 137
Figure 4.2. The study area with the location of the 195 annotated archaeological sites used in the study. Areas mentioned in the text are labeled. 139
Figure 4.3. Image dataset's workflow from DTM to enhanced Multiscale Topographic Position (eMSTP) image. 140

Figure 4.4. (a) Multiscale Topographic Position (MSTP) image, (b) Morphological visualization technique (VT) and (c) resulting enhanced multiscale topographic position (eMSTP) image of a Neolithic monument (Tumulus du Moustoir, Carnac, France). 140
Figure 4.5. Overall workflow of (semi-)automatic object detection, segmentation, and characterization of archaeological structures. eMSTP = enhanced multiscale topographic position, ROI = region of interest, BBOX = bounding box. 142
Figure 4.6. Statistical performances of the 110 models. (a) histogram of mAP values, (b) boxplots of mAP per training size and (c) boxplots of mAP per dataset. Whiskers represent 1.5 times the interquartile range. 145
Figure 4.7. Detected (BBOX) and segmented (mask) objects predicted by $A_{train10}$ and $A_{train110}$ models. Results are shown for Area 1 (Le Manio), Area 2 (Penhoët) and Area 3 (Le Net), France. 147
Figure 4.8. Prediction matrix for (a) $A_{train10}$ and (b) $A_{train110}$ models in Area 1 (Le Manio, France). 147
Figure 4.9. Burial mounds at Le Manio (France). (a) Perspective view of the predicted masks (highlighted over an enhanced multiscale topographic position image) and corresponding archaeological structures. (b) Manio 5 viewed from the southwest. 148
Figure 4.10. (a) Perspective view of Er Castellic (France) with enhanced multiscale topographic position image overlay, (b) 2D view of the predicted object over the hillshade DTM and (c and d) topographic profiles generated across the predicted object. 149
Figure 4.11. (a) Plan and cross-sectional views of the Clos Er Bé passage grave (France) (Le Rouzic et al., 1922). (b, c) Current state of the monument covered by bushes and ferns..... 150
Figure 4.12. Dolmens of Park Er Guren (France), view from south. Dolmen A lies in the background, while Dolmen B lies in the foreground. 151
Figure 4.13. $A_{train110}$ model predictions for the area of Park Er Guren (France). eMSTP = enhanced multiscale topographic position, BBOX = bounding box, TP = true positive, FP = false positive, FN = false negative. 151
Figure 4.14. Characterization of the predicted objects for Park Er Guren (France) based on the resulting (semi-)automatic approach. (a) Object segmentation results for object 1 (orange) and 2 (blue), (b) hyperscale topographic position signatures (each corresponds to a pixel included in the object footprint). Dashed curves indicate the mean signature of each object. 151
Figure 4.15: Example of prediction results outside the reference dataset, Goah Lêron area, Carnac (France). Objects A and B were considered as interesting structures for further field investigation based on human-interpretation of the eMSTP image. Objects C and D were considered as false positives. Point E highlighted the fact that no potential structure was predicted on the hill. The remaining objects (small isolated mounds) would require further investigation. 154
Figure 4.16: Example of prediction results outside the reference dataset, Brahen area, Carnac (France). Objects A and B corresponded to archaeological structures confirmed by field verification, object C being a dominating terrain including object B. Object D was considered as

Guyot, Alexandre. Contribution of airborne LiDAR and hyperspectral data to archaeological mapping in terrestrial and submerged environments. 2021

false-positive. Remaining objects were local morphological anomalies that would require further investigation. 155
Figure 5.1. Airborne Laser Scanning (ALS) coverage of the study area with archaeological reference data used to train and test the Deep convolution neural network models..... 164
Figure 5.2. Visualization techniques applied to the Le Pusso area, Carnac (France). The area has a variety of landforms, including multiple archaeological structures. 168
Figure 5.3. Architecture of Mask R-CNN for instance segmentation on visualization technique images 169
Figure 5.4. Performances of detection/segmentation using deep convolution neural network (CNN) for different visualization techniques (VTs). Visual examples of VTs with (right) the reference data and (left) mean deep CNN model performances (mAP@IoU.5) of each VT. Error bars indicate 1 standard deviation. Example 1 is a leveled Neolithic tumulus in an agricultural field. Example 2 is a megalithic complex of 3 dolmens under dense vegetation. Example 3 is a Neolithic tumulus of elongated shape in a marshland area..... 172
Figure 6.1. (**a**) Location of the study area (Er Lannic islet, Morbihan, France), (**b**) the archaeological reference data (submerged steles are numbered)..... 186
Figure 6.2. Megalithic monument of Er Lannic..... 187
Figure 6.3. Litto3D bathymetric reference data (**a**) point cloud and (**b**) 1 m resolution raster.... 188
Figure 6.4. Diagram of the method developed..... 191
Figure 6.5. Relative spectral sensitivity function of a Canon 10D digital single-lens reflex camera used to simulate a true-color red-green-blue (RGB) image from the hyperspectral imagery..... 192
Figure 6.6. (**a**) Archaeological reference map of the study site (submerged steles are numbered). True-color (RGB) images simulated from hyperspectral data and spectral sensitivity functions (**b**) without and (**c**) with gamma correction (γ=0.4). (**d**) Minimum noise fraction pseudo-color image with bands Red=9, Green=3 and Blue=4. (**e**) Anomaly score calculated using the Isolation Forest (IF) algorithm. (**f**) Anomaly score calculated using the local Reed–Xiaoli detector (LRXD) algorithm. 196
Figure 6.7. Minimum noise fraction (MNF) components 1–15 (signal-to-noise ratio ≥ 5) calculated from surface reflectance..... 196
Figure 6.8. Receiver operating characteristic (ROC) curves for Isolation Forest (IF) and local Reed–Xiaoli detector (LRXD) anomaly detection calculated for the submerged structures. 197
Figure 6.9. (**a**) Bottom depth estimated from airborne hyperspectral imagery (AHI), (**b**) Litto3D bathymetric data (Shom/IGN) and (**c**) Bottom depth estimated from AHI with extraction of visible water-bottom features (local maxima) from 0.1 m contour lines. Archaeological reference data (stele centroids) are shown in red. 199
Figure 6.10. Path profile of bottom depth estimated from airborne hyperspectral imagery (AHI) and reference Litto3D (Shom/IGN) bathymetric data over the submerged structures..... 201
Figure 6.11. (**a**) Spectral signatures of bottom reflectance showing archaeological structures and (**b**) photograph of a permanently submerged stele of Er Lannic covered by green and brown algae..... 201

Figure 7.1. Fishweir morpho-typology as a function of construction context (A: single wall between two natural rock outcrops, B: multiple walls connect several rock outcrops, C: two walls converge walls, D: one wall next to the coastline) and shape (L: linear, C: curvilinear, S: snakelike). Adapted from Langouët & Daire (2009)..... 207
Figure 7.2. Diagram of radiative transfer in shallow water (adapted from Bertels et al. (2008) and Petit (2017)). CDOM: colored dissolved organic matter, NAP: non-algal particles 209
Figure 7.3. Location and composition of the Molène archipelago..... 210
Figure 7.4. Spectral library measured using a handheld spectrometer on the foreshore area in and near the study area 212
Figure 7.5. Processing workflow 213
Figure 7.6. (a) Visualization of the anomaly and its expected characteristics (i.e. depth, size, orientation and context) on georeferenced data layers loaded onto a GNSS-enabled mobile tablet using QGIS/Qfield applications. (b) Underwater view of a diver at work. (c) Diver in action near anomaly 7.4.3"b" (images used with permission, © Yannis Turpin/OFB)..... 217
Figure 7.7. Visualization of Molène archipelago using hyperspectral imagery and a data-driven approach. (a) Above -water image, which is a true-color RGB visualization of water -surface reflectance (red: 620 nm, green: 570 nm, blue: 495 nm), (b) "in-water" spectral visualizations, (c) "target" spectral visualizations. The inventoried fishweirs were located and numbered according to the list of Stéphan et al. (2019). 218
Figure 7.8. Data-driven visualization results for three fishweirs in the reference dataset of Stéphan et al. (2019). Letters a,b,c correspond to Beg Ar Gored, Klozenn Malaga (East) and Boz Ar Muzzelog, respectively. Index numbers (1,2,3,4) correspond to "target" spectral visualization, "in-water" spectral visualization, Litto3D® topo-bathymetric reference data and above -water images, respectively. Spectral visualizations are color-composite images of the first three components (red: 1st , green: 2nd , blue: 3rd) of minimum -noise -fraction transformations. Above -water images are true-color RGB visualizations of water -surface reflectance (red: 620 nm, green: 570 nm, blue: 495 nm) (Source of above map background: Scan Littoral IGN/Géobretagne)..... 220
Figure 7.9. Visualization of the submerged landscape north of Lénédès Quéménès in the Molène archipelago: (a) RGB visualization of water -surface reflectance (red: 620 nm, green: 570 nm, blue: 495 nm); (b) RGB visualization of the water -bottom reflectance mosaic (red: 620 nm, green: 570 nm, blue: 495 nm) derived from the hyperspectral data; (c) Digital bathymetric model mosaic derived from the hyperspectral data; (d) close-up of the RGB visualization of water -surface reflectance; (e) close-up of the submerged -landscape mosaic image overlaying (b) and (c) as hillshaded terrain. white patches on the submerged -landscape mosaic corresponded to areas above the water level (land)..... 222
Figure 7.10. Bottom -reflectance spectral signatures (left: A, B) and topographic profiles (right: C, D, E) extracted from hyperspectral derived information for the characterization of the Gored Ar Litiri Vraz fishweir. 224
Figure 7.11. Location of the 28 anomalies (top) and data-driven as well as physics-based visualization results for the three anomalies that were verified by underwater surveys (a,b,c).

Index numbers (1,2,3,4) are for “target” spectral visualizations, “in-water” spectral visualizations, submerged -landscape mosaic images and interpreted anomalies overlain on water images , respectively (Source of “top map" background: Scan Littoral IGN/Géobretagne). 226
Figure 7.12. Underwater video-frame extractions during survey dives of three anomalies identified by airborne hyperspectral imagery. (a) Wide-scale view of the stone structure covered by redalgae and surrounded by golden kelp on Anomaly “a”. (b and c) Close-up view of edge-mounted stone blocks of anomaly “b”. (d) Perspective view of the edge-mounted stone blocks positioned longitudinally on each side of the structure of anomaly “c”. (Images used with permission, © Yannis Turpin, Jean-André Prat, Livier Schweyer/OFB) 229
Figure 7.13. Comparison of observed anomalies “b” and “c” using (top) AHI-derived spectral visualization images and (bottom) topo-bathymetric reference data. 232

Guyot, Alexandre. Contribution of airborne LiDAR and hyperspectral data to archaeological mapping in terrestrial and submerged environments. 2021

LIST OF TABLES

Table 3.1. Remote sensing dataset used in the thesis 98
Table 3.2. Main characteristics of the airborne LiDAR survey on the area of Carnac and the Gulf of Morbihan 107
Table 3.3. Parameters of the scale ranges used for the multiscale topographic position analysis (MSTP) 110
Table 3.4. Main characteristics of the airborne hyperspectral survey on the area of Gulf of Morbihan 114
Table 3.5. Main characteristics of the airborne hyperspectral survey on the area of Molène archipelago 116
Table 3.6. Fish weirs inventory in the Molène archipelago, published by Stéphan et al. (2019) and used as reference database 121
Table 4.1. Characterization metrics calculated for the objects detected. 144
Table 4.2. Hyperscale topographic position signatures and morphometric descriptors calculated for the predicted objects for Park Er Guren (France). 152
Table 5.1. visualization techniques compared in the study 165
Table 5.2. Main hyperparameters used to train the deep convolution neural network 169
Table 6.1. Characteristics of the HySpex Visible Near Infra-Red (VNIR)-1600 sensor. 187
Table 6.2. Parameters of the aerial survey. 187
Table 6.3. Normalized confusion matrix for Isolation Forest (IF) and local Reed–Xiaoli detector (LRXD) anomaly detection of submerged structures. 197
Table 6.4. Area of airborne hyperspectral imagery-derived water-bottom features compared those of steles from archaeological reference data. Coefficient of determination $R^2 = 0.72$. 200
Table 7.1. The number and mean depth (in parentheses, from hydrographic datum) of reference structures as a function of their degree of visibility on the “target” and “in-water” spectral visualizations. 219
Table 7.2. Number and mean depth (in parentheses, from chart datum) of the reference structures according to their degree of visibility on the submerged -landscape mosaic image and the type of the water bottom (mineral, vegetation, both). 223
Table 7.3. Characteristics of the Gored Ar Litiri Vraz fishweir 223

APPENDIX

This thesis is structured around 4 main contributions, each of them being integrated as a thesis chapter (chap. 4 to chap. 7). It also includes ancillary contributions directly related to the thesis subject, that have been made in the framework of projects conducted with Hytech-Imaging and the LETG laboratory.

Below is the list of all scientific productions (publications, reports, conferences) made during the course of this thesis.

Scientific publications

Peer-reviewed journal articles

Guyot, Alexandre, Marc Lennon, and Laurence Hubert-Moy. "Objective Comparison of Relief Visualization Techniques with Deep CNN for Archaeology." *Journal of Archaeological Science: Reports* 38 (August 2021): 103027. https://doi.org/10.1016/j.jasrep.2021.103027.

Guyot, Alexandre, Marc Lennon, Thierry Lorho, and Laurence Hubert-Moy. "Combined Detection and Segmentation of Archeological Structures from LiDAR Data Using a Deep Learning Approach." *Journal of Computer Applications in Archaeology* 4, no. 1 (February 3, 2021): 1–19. https://doi.org/10.5334/jcaa.64.

Guyot, Alexandre, Marc Lennon, Nicolas Thomas, Simon Gueguen, Tristan Petit, Thierry Lorho, Serge Cassen, and Laurence Hubert-Moy. "Airborne Hyperspectral Imaging for Submerged Archaeological Mapping in Shallow Water Environments." *Remote Sensing* 11, no. 19 (September 25, 2019): 2237. https://doi.org/10.3390/rs11192237.

Guyot, Alexandre, Laurence Hubert-Moy, and Thierry Lorho. "Detecting Neolithic Burial Mounds from LiDAR-Derived Elevation Data Using a Multi-Scale Approach and Machine Learning Techniques." *Remote Sensing* 10, no. 2 (February 1, 2018): 225. https://doi.org/10.3390/rs10020225.

Peer-reviewed conference papers

Guyot, Alexandre, Marc Lennon, Pierre Stéphan, Thibaut Péres, Marie Hascoët, Marie-Yvane Daire, and Laurence Hubert-Moy. "What Lies Beneath the Surface? Using Airborne Hyperspectral Imagery to Map Submerged Archaeological Landscapes: A Case Study in the Molène Archipelago, Brittany." *ArchéoSciences*, no. 45 (August 16, 2021): 287–90. https://doi.org/10.4000/archeosciences.10123.

Conference presentations

Guyot, Alexandre, Marc Lennon, Thierry Lorho, Laurence Hubert-Moy. "Archaeological prospection in nearshore and shallow-water areas using airborne remote-sensing: potential and limits". HOMER 2021 : Archéologie des peuplements littoraux et des interactions Homme/Milieu en Atlantique nord équateur; September 28-Octobrer 2, 2021; Ile d'Oléron, France.

Guyot, Alexandre, Marc Lennon, Pierre Stéphan, Thibaut Péres, Marie Hascoët, Marie-Yvane Daire, Laurence Hubert-Moy. "Visualization of underwater landscapes from airborne hyperspectral imagery in the shallow waters of the Molène archipelago, Brittany". ICAP2021 : 14th International Conference of Archaeological Prospection; September 9, 2021; Lyon (online), France.

Guyot, Alexandre "De la donnée au terrain : QGIS, un outil global pour la prospection archéologique par télédétection". Rencontres des Utilisateurs Francophones de QGIS ; December 15, 2020; Online, France.

Guyot, Alexandre, Marc Lennon, Thierry Lorho, Laurence Hubert-Moy. "Mapping of submerged archaeological remains from hyperspectral images: Application to the megalithic site of Er Lannic (Morbihan, France) "; Whispers conference; September 25, 2019; Amsterdam. The Netherlands.

Guyot, Alexandre, Marc Lennon, Thierry Lorho, Nicolas Thomas, Tristan Petit, Simon Guéguen, Guillaume Sicot, Serge Cassen, Laurence Hubert-Moy. "Cartographie de vestiges archéologiques immergés à partir d'images hyperspectrales : application au site d'Er Lannic". Conférence SFPT (Société Française de Photogrammétrie et de Télédétection), groupe Hyperspectral ; July 10, 2019 ; Toulouse, France.

Conference posters

Guyot, Alexandre, Marc Lennon, Pierre Stéphan, Thibaut Péres, Marie Hascoët, Marie-Yvane Daire, and Laurence Hubert-Moy. "Visualization of underwater landscapes from airborne hyperspectral imagery in the shallow waters of the Molène archipelago, Brittany". Poster presented at: HOMER 2021 : Archéologie des peuplements littoraux et des interactions Homme/Milieu en Atlantique nord équateur; September 28-Octobrer 2, 2021; Ile d'Oléron, France.

Scientific reports

Guyot, Alexandre, Philippe Bodenes, Marc Lennon, Thierry Lorho, Laurence Hubert-Moy. "Compte-Rendu d'opération d'archeologie Sous-Marine. Godec 1, Golfe Du Morbihan.", Report number OA4556. Rennes, France: DRASSM, 2020.

Guyot, Alexandre, Marc Lennon, Laurence Hubert-Moy. "Rapport 2018 de Prospection Archéologique Diachronique Par Télédétection, Zone Unesco : Carnac, Baie de Quiberon et

Golfe Du Morbihan.", Report number RAP03683. Rennes, France: Service régional de l'archéologie de Bretagne, 2019. http://bibliotheque.numerique.sra-bretagne.fr/items/show/3789.

Guyot, Alexandre, Marc Lennon, Laurence Hubert-Moy. "Rapport 2019 de Prospection Archéologique Diachronique Par Télédétection, Zone Unesco : Carnac et Rives Du Morbihan.", Report number RAP03986. Rennes, France: Service régional de l'archéologie de Bretagne, 2020. http://bibliotheque.numerique.sra-bretagne.fr/items/show/4108.

Guyot, Alexandre, Marc Lennon, Laurence Hubert-Moy. "Rapport 2020 de Prospection Archéologique Diachronique Par Télédétection, Zone Unesco : Carnac et Rives Du Morbihan.", Report number RAP04008. Rennes, France: Service régional de l'archéologie de Bretagne, 2021. http://bibliotheque.numerique.sra-bretagne.fr/items/show/4133.

RESUME ETENDU (FRANÇAIS)

A l'aube du 3ème millénaire, le patrimoine archéologique, qu'il soit terrestre ou maritime, est confronté à des menaces croissantes, qu'elles soient d'origine anthropique ou naturelle (Egloff, 2008; Flatman, 2009; McManamon et al., 2008). Préserver ce patrimoine fini et non renouvelable apparaît comme un enjeu stratégique, afin de mieux comprendre l'histoire de l'humanité et sa relation à l'environnement, mais également pour assurer la transmission de ce patrimoine aux générations futures (Holtorf, 2020).

Dans un rapport publié en 2019 (Burke et al., 2019), l'ICOMOS (International Council on Monuments and Sites), a confirmé la gravité des menaces affectant le patrimoine culturel, parmi lesquelles le changement climatique global qui -joue un rôle majeur. Il a également souligné la contribution cruciale du patrimoine culturel dans la définition de futurs durables, en particulier dans sa capacité à être une source d'information et de connaissances du passé, afin de soutenir le développement de stratégies d'adaptation au changement climatique.

Depuis les artefacts archéologiques diffus aux paysages culturels, le patrimoine archéologique présente une extraordinaire diversité de nature, de formes et de degrés de préservation (Renfrew & Bahn, 2016). Cette complexité matérielle et les questions sociales et culturelles qui en découlent alimentent la recherche archéologique depuis des siècles (Bahn, 2014). Si les approches de terrain et de fouille restent profondément liées à la démarche archéologique, le XXe siècle, notamment grâce aux travaux pionniers de David L. Clarke (Clarke, 1968), a vu l'émergence d'approches analytiques et numériques basées sur le développement d'autres disciplines scientifiques telles que l'informatique et la géographie. Cette multidisciplinarité, intégrée dans les pratiques archéologiques du 21ème siècle, est particulièrement marquée dans le domaine de la prospection archéologique. Cette approche, qui se caractérise par l'usage de méthodes non-destructives sur de larges territoires (Tabbagh, 2018) pour la localisation et la documentation de sites archéologiques, permet de soulever de nouvelles questions de recherche et constitue une aide à la gestion du patrimoine culturel (Campana, 2007). Ce travail d'inventaire archéologique est un défi permanent et l'enrichissement qualitatif et quantitatif de la connaissance archéologique constamment nécessaire. L'amélioration des inventaires archéologiques s'appuie aujourd'hui sur des moyens multiples tels que la recherche documentaire, les enquêtes de terrain, les opérations d'archéologie préventive ou l'archéologie aérienne et spatiale.

Depuis plus d'un siècle, à partir des premières photographies aériennes, la télédétection joue un rôle dans la détection et la documentation des traces archéologiques (Agache, 1999; Bewley, 2003; Chevallier, 1964; Daire, 1992; Dassié, 1978; Gautier, Guigon, Leroux, et al., 2019; Reeves, 1936;

Riley, 1985; Solecki, 1957; G. J. Verhoeven, 2017). Au cours des dernières décennies, l'essor des technologies numériques a permis l'émergence de nouveaux vecteurs et capteurs de télédétection répondant à des besoins de données plus précises, de couvertures plus larges et plus régulières et d'accès à de l'information au-delà du spectre visible (Parcak, 2017). Une revue récente de l'état de l'art de la télédétection pour l'archéologie a illustré le large spectre de données et de méthodes à disposition des scientifiques (L. Luo et al., 2019) : des plateformes aériennes aux plateformes spatiales, des capteurs passifs aux capteurs actifs opérant dans la gamme optique, thermique ou micro-ondes du spectre électromagnétique.

Dans ce contexte, les nouvelles données optiques aéroportées, telles que les données LiDAR (light detection and ranging) ou les données hyperspectrales, jouent un rôle essentiel en repoussant les limites imposées par les approches traditionnelles de l'archéologie aérienne (Cavalli et al., 2007; Corns & Shaw, 2009; Devereux et al., 2005; M. Doneus et al., 2014; Fernandez-Diaz et al., 2014). Elles permettent d'accéder à des informations sur les paysages et sites archéologiques avec une résolution spatiale sub-métrique et dans des environnements jusqu'alors largement opaques à la vision humaine et à la photographie (Aqdus et al., 2008; M. Doneus et al., 2015; M. Doneus & Briese, 2011; Georges-Leroy et al., 2011). Principalement circonscrites à la sphère de la recherche il y a encore quelques années, ces données sont aujourd'hui de plus en plus accessibles, notamment à travers des missions aériennes mutualisées pour différentes thématiques de gestion du territoire. Cette transition vers un nouvel usage pose de nouveaux défis méthodologiques, tant au niveau de l'acquisition, du traitement et de l'analyse des données, particulièrement pour les applications archéologiques (D. Cowley et al., 2021; R. Opitz & Herrmann, 2018; Rączkowski, 2020; VanValkenburgh & Dufton, 2020; G. Verhoeven & Sevara, 2016).

Les données LiDAR aéroportées, qui fournissent des informations topographiques à haute résolution spatiale et haute précision, ont changé la donne pour la prospection archéologique, en particulier en contexte forestier. L'analyse de ces données passe généralement par un processus de traitement de données basé sur la construction de modèles numérique de terrain (MNT) et l'interprétation de microreliefs mis en évidence par des techniques de visualisation. Cette approche a conduit à des découvertes archéologiques majeures ces dernières années (Chase et al., 2011; D. H. Evans et al., 2013; Fisher et al., 2017; Inomata et al., 2020). Dans le même temps, dans le domaine de la vison par ordinateur, les approches fondées sur l'intelligence artificielle telles que les réseaux de neurones convolutifs basés sur l'apprentissage profond ont largement modifié les paradigmes de la reconnaissance d'images (Krizhevsky et al., 2012; LeCun et al., 2015). Malgré leurs contributions respectives majeures, peu de recherches ont été menées pour évaluer la contribution combinée des techniques de visualisation de MNT dérivés du LiDAR et de l'analyse d'images par apprentissage profond, en particulier pour les applications archéologiques. Pourtant, la disponibilité croissante de données LiDAR à haute résolution sur de grandes étendues traitées avec des approches adaptées à la prospection archéologique à grande échelle

permettraient une détection et une caractérisation plus efficaces des anomalies topographiques dans des environnements complexes.

Les données hyperspectrales aéroportées, qui fournissent des informations spectrales uniques en décomposant, en centaines de bandes spectrales, la lumière naturelle du soleil interagissant avec la surface terrestre, ont également largement contribué au développement de la télédétection (Jia et al., 2020) notamment en géologie, en agroforesterie, en écologie ainsi qu'en archéologie (Cavalli et al., 2007; M. Doneus et al., 2014). Toutefois, l'imagerie hyperspectrale est relativement peu utilisée pour la cartographie côtière en eaux peu profondes (Kutser et al., 2020). Lorsque la lumière naturelle du soleil pénètre dans la colonne d'eau, elle subit une atténuation, par absorption et diffusion, qui varie en fonction de la longueur d'onde et des caractéristiques du milieu observé (Mobley & Mobley, 1994). L'énergie lumineuse renvoyée par la surface et enregistrée par un capteur hyperspectral est donc porteuse d'une source d'information importante pour la caractérisation de l'environnement marin (Bertels et al., 2008; Oppelt, 2012). Malgré ce constat, et un intérêt croissant pour l'usage de l'imagerie hyperspectrale en environnement côtier, à notre connaissance, aucune étude n'a jusqu'à présent évalué l'utilisation de l'imagerie hyperspectrale aéroportée pour la cartographie archéologique en milieu immergé. Or, si la zone de petits fonds à l'interface terre-mer est considérée comme l'une des zones les plus complexes à cartographier et à étudier en raison notamment de la forte dynamique et de l'accessibilité limitée du milieu (Ouellette & Getinet, 2016), elle est considérée comme une zone au potentiel archéologique important (G. Bailey et al., 2020). Cette zone a en effet été occupée autrefois par des populations humaines progressivement repoussées vers l'intérieur des terres lors de l'élévation du niveau de la mer depuis le dernier maximum glaciaire (Lambeck et al., 2014).

Dans le cadre de ce travail de thèse, nous proposons donc d'évaluer la **contribution des données LiDAR et hyperspectrales aéroportées pour la cartographie archéologique en milieux terrestres et immergés**. Plus précisément, nous proposons de répondre à deux questions principales : (1) les méthodes de prospection archéologique basées sur les données LiDAR peuvent-elles être adaptées à des prospections archéologiques à grande échelle et à une détection et une caractérisation détaillée d'anomalies topographiques subtiles dans des environnements complexes ? (2) l'imagerie hyperspectrale aéroportée peut-elle être considérée comme une source potentielle d'information pour la cartographie archéologique dans les zones côtières immergées, et quels sont ses avantages et limites dans un tel contexte ?

Dans une première partie, nous avons choisi d'**évaluer l'apport des données LiDAR aéroportées pour la détection (semi-)automatique et la caractérisation des structures archéologiques dans les paysages à dominante boisée de Carnac et du Golfe du Morbihan**. Pour cela, de nouvelles approches méthodologiques ont été développées avec l'utilisation de techniques de visualisation de MNT dérivés du LiDAR, et analysés avec des algorithmes issus du domaine de la vision par ordinateur, plus précisément des réseaux de neurones convolutifs par apprentissage profond (ou deep CNN, pour deep convolutional neural networks).

Les données de télédétection utilisées sont des données LiDAR collectées en mars 2016 (acquisition OSUR/GeoFIT-Expert pour DRAC Sra Bretagne) par un capteur aéroporté Optech Titan bi-spectral (532nm et 1064nm) et couvrant une surface utile de 200 km² pour une densité nominale de points de l'ordre de 14 points/m² et une précision absolue de 8 cm (RMSE) en vertical et 12 cm (RMSE) en horizontal. Ces données de télédétection ont été prétraitées afin de transformer le nuage de points bruts en un MNT par filtrage des points « sol », puis par la création d'un maillage triangulé irrégulier converti en une grille régulière de 50cm de résolution.

Les données de référence archéologique mobilisées dans cette première partie sont issues de la *Carte archéologique* du Service régional de l'archéologie de Bretagne (DRAC Sra Bretagne). Constituées de 195 polygones géoréférencés, ces données de référence représentent les emprises de sites archéologiques connus dans la zone d'étude et pour lesquelles les structures conservées influent sur la topographie.

Dans une première étude (chapitre 4), nous avons évalué l'apport des méthodes d'apprentissage profond pour la détection, la segmentation et la caractérisation de structures archéologiques à partir de la visualisation multi-échelle de modèles numériques de terrain dérivés du LiDAR. Plusieurs questions sont posées dans cette étude : (i) La détection et segmentation (semi-)automatique des structures archéologiques peuvent-elles être mises en œuvre avec un ensemble d'entraînement limité ? Dans quelle mesure le modèle est-il sensible à la taille du jeu de données d'apprentissage ? (ii) Au-delà de la détection d'objets, quelle est l'apport de la segmentation d'objets pour la caractérisation des structures archéologiques ?

'L'expérimentation a été réalisée sur des images composites générées à partir d'une analyse topographique multi-échelle (Guyot et al., 2018) combinée à une représentation de la morphologie locale du terrain. Ces images, nommées images eMSTP (enhanced Multiscale Topographic Position), ont ensuite été analysées par apprentissage profond afin de détecter et segmenter les anomalies d'intérêt puis les caractériser morphologiquement et contextuellement. D'une part, la méthode de détection et segmentation implémentée est basée sur une architecture de type Mask-RCNN (He et al., 2017) associée à un réseau d'extraction de caractéristiques (Resnet-101) initialisé par une stratégie d'apprentissage par transfert. Une stratégie d'échantillonnage spécifique (validation croisée et taille d'entrainement variable) a été utilisée pour évaluer la stabilité du

modèle et sa sensibilité à la taille du jeu d'entrainement. D'autre part, la méthode de caractérisation s'appuie sur l'utilisation de descripteurs morphométriques et contextuels (notamment issus de l'analyse multi-échelle) calculés au niveau objet à partir des résultats de la phase de détection/segmentation. L'évaluation de la méthode a été effectuée à différents niveaux. Premièrement, les performances de détection et de segmentation du modèle ont été évaluées à la fois globalement d'un point de vue statistique (métrique de précision de détection/segmentation : mAP) et d'un point de vue visuel sur trois cas d'études (zone 1 : Le Manio, Carnac ; zone 2 : Penhoët, Crac'h ; zone 3 : Le Net, St Gildas de Rhuys). Deuxièmement, les résultats de segmentation ont été évalués sur un site mégalithique (Park Er Guren, Crac'h). Enfin, la méthode a également été évaluée dans un contexte de prospection où les résultats sur des anomalies inédites détectées par la méthode ont été confrontés aux interprétations archéologiques sur le terrain.

Les résultats ont montré des performances de détection et de segmentation relativement élevées (mAP@IoU.5 jusqu'à 0,77) malgré la faible taille du jeu d'entrainement (maximum de 110 images d'entrainement). Cela confirme la capacité de la méthode Deep CNN mise en œuvre à obtenir de bonnes performances dans des contextes archéologiques pour lesquels le volume de données de référence disponible est limité . Cependant, ces résultats ont aussi mis en évidence une importante sensibilité des modèles à la sélection des données d'entrainement et de validation (mAP@IoU.5 variant de 0,29 à 0,77). Nous soutenons le fait qu'une partie de cette variabilité est liée aux métriques utilisées pour évaluer les performances de détection et de segmentation, mais que la principale source de variabilité est liée à la représentativité des jeux d'entraînement et de validation. L'exploitation des résultats de détection/segmentation pour la caractérisation des anomalies a permis de mettre en évidence l'intérêt des architectures de type Mask R-CNN pour disposer d'informations allant au-delà de la simple localisation d'anomalies, et permettant une délimitation spatiale de l'objet d'intérêt. Ces résultats ouvrent des perspectives intéressantes de caractérisation morphologique et contextuelle des structures archéologiques, tel que nous l'avons montré sur les dolmens de Park Er Guren. Enfin, les résultats confirment la capacité de la méthode à fournir des informations exploitables dans un contexte de prospection opérationnel, avec l'identification de plusieurs sites archéologiques jusqu'alors non répertoriés et vérifiés *a posteriori* sur le terrain. Ces performances sont notamment rendues possibles grâce à : (i) l'utilisation de données d'entrée adaptées et informatives (ici les images issues de l'analyse multi-échelle combinées à une visualisation morphologique) ; (ii) l'utilisation de méthodes d'apprentissage par transfert (transfer learning) ainsi qu'une stratégie de détection/segmentation à classe unique (« one-class ») atténuant les contraintes opérationnelles de faible représentativité ou d'incertitude de typologie dans les données archéologiques de référence. L'étude ci-dessus a fait l'objet de la publication suivante :

> Guyot, A., Lennon, M., Lorho, T., & Hubert-Moy, L. (2021). Combined Detection and Segmentation of Archeological Structures from LiDAR Data Using a Deep Learning Approach. *Journal of Computer Applications in Archaeology*, 4(1), 1–19. https://doi.org/10.5334/jcaa.64

Dans une seconde étude (chapitre 5), réalisée avec les mêmes données que celles qui ont été utilisées dans le chapitre précédent et une méthodologie similaire, **nous avons évalué un autre usage possible des approches fondées sur la vision par ordinateur.** Cette fois, la méthode développée, basée sur un deep CNN de type Detectron2 (Wu et al., 2019), est utilisée comme outil d'évaluation objective de plusieurs techniques de visualisation de modèles numériques de terrain dérivés de données LIDAR. Les principales questions abordées dans ce chapitre sont les suivantes : (i) Une approche d'apprentissage profond peut-elle être utilisée comme outil pour évaluer objectivement l'efficacité des techniques de visualisation dans un contexte de prospection archéologique ? (ii) Quel est l'apport d'une telle approche intégrant vision par ordinateur et perception humaine pour la cartographie archéologique?

Pour répondre à ces questions, nous avons comparé treize techniques de visualisation différentes en évaluant leur capacité de mise en évidence de structures archéologiques, en uilisant d'une part une approche d'interprétation visuelle et d'autre part une approche de détection/segmentation automatique. Les résultats obtenus sur la zone d'étude (Carnac et golfe du Morbihan) ont montré que les approches d'analyse topographique multi-échelle étaient les plus performantes (jusqu'à 65% de précision moyenne : mAP@IoU.5). Ces résultats confirment l'intérêt d'utiliser une approche multi-échelle pour fournir des informations contextuelles sur la position topographique et la mise en évidence de signaux faibles pour des structures de taille variable. Elle confirme également l'avantage de combiner les techniques de visualisation complémentaires par des méthodes de fusion (blending). En comparant les résultats qualitatifs obtenus avec l'approche visuelle, et les résultats quantitatifs obtenus avec l'approche automatique, nous avons également pu montrer que la perception humaine, qui est subjective, et la perception par un algorithme de vision par ordinateur, qui est objective, peuvent être corrélées.

Ces résultats mettent en évidence que les approches de vision par ordinateur deep CNN permettent d'une part d'aider à l'évaluation objective des techniques de visualisation de MNT, et d'autre part de guider la conception de techniques de visualisation avancées. Dans cette optique, nous avons proposéune nouvelle technique de visualisation, nommée e²MSTP (pour enhanced² Multiscale Topographic Position), issue de la fusion d'une analyse topographique multi-échelle, d'une représentation morphologique locale et d'une technique de suppression de continuum invariable à la pente. L'étude ci-dessus a fait l'objet de la publication suivante :

> Guyot, A., Lennon, M., & Hubert-Moy, L. (2021). Objective comparison of relief visualization techniques with deep CNN for archaeology. *Journal of Archaeological Science: Reports*, 38, 103027. https://doi.org/10.1016/j.jasrep.2021.103027

Les résultats de cette première partie démontrent l'intérêt de combiner des techniques de visualisation de MNT dérivés du LiDAR avec des approches de vision par ordinateur, notamment de détection et segmentation automatique par des réseaux neuronaux convolutifs profonds. Premièrement, nous avons pu confirmer l'intérêt des techniques de visualisation basées sur l'analyse topographique multi-échelle et leur capacité à mettre en exergue des anomalies subtiles en combinant des informations contextuelles à différentes échelles. Nous avons également montré que ces approches multi-échelles pouvaient être améliorées en y associant d'autres techniques de visualisation plus explicites dans la représentation de la morphologie locale du terrain. Deuxièmement, nous avons démontré que la segmentation automatique d'anomalies topographiques est possible grâce aux méthodes d'analyse d'image basées sur les réseaux neuronaux convolutifs profonds (deep CNN), et ce, même en utilisant des jeux de données d'entraînement relativement éparses. Les résultats obtenus par segmentation ouvrent ainsi d'intéressantes perspectives concernant la caractérisation morphologique ou contextuelle des structures archéologiques. Enfin, nous avons également montré que les approches de vision par ordinateur pouvaient être intégrées aux approches plus communes d'interprétation visuelle, non seulement en apportant une aide à la prospection archéologique, mais également en guidant la conception de nouvelles techniques de visualisation grâce à l'évaluation objective des performances de ces dernières.

Ces résultats et leurs interprétations restent toutefois limités au contexte géo-archéologique de la zone d'étude de Carnac et du Golfe du Morbihan, caractérisé par un relief peu marqué et la présence de structures archéologiques très majoritairement liées à la période Néolithique. De plus, les résultats sont également dépendants de l'utilisation exclusive du modèle de terrain dérivé des données LiDAR, ce qui, dans notre cas, a exclu implicitement certains éléments archéologiques tels que les menhirs ou stèles qui, selon leur morphologie, sont majoritairement considérés comme des éléments architecturaux non-topographiques. Enfin, la difficulté à définir un cadre conceptuel ou une ontologie partagée par les archéologues et les spécialistes de la télédétection reste un sujet ouvert, au-delà du cadre de ces études (D. Davis, 2021; R. Opitz & Herrmann, 2018; Rączkowski, 2020). Toutefois, ces résultats et limites constituent des perspectives qui sont abordées en conclusion de cette thèse.

Dans une seconde partie, nous avons choisi d'**évaluer l'apport de l'imagerie hyperspectrale aéroportée pour la cartographie de structures archéologiques immergées en zone littorale de petits fonds,** d'une part sur le **site mégalithique d'Er Lannic (Morbihan)** et d'autre part **en zone intertidale et subtidale de l'archipel de Molène (Finistère)**. Pour cela nous avons développé une méthodologie basée sur l'extraction d'informations spatio-spectrales du fond marin à partir de la réflectance de surface. Cette extraction a été effectuée d'une part en exploitant des approches orientées « données » (data-driven) afin de visualiser des variations spatio-spectrales liées à la présence d'anomalies ou de structures benthiques, et d'autre part en s'appuyant sur un modèle physique de transfert radiatif en milieu côtier (Z. Lee et al., 1998) afin d'extraire, par inversion du modèle, les composantes liées à la bathymétrie et à la réflectance du fond. Les données de télédétection utilisées ont été collectées en septembre 2018 pour la zone d'Er Lannic (acquisition Hytech-Imaging pour DRAC Sra Bretagne) et en mai 2020 pour l'archipel de Molène (acquisition Hytech-Imaging pour OFB/PNMI), respectivement à des résolutions spatiales de 50cm et 1m, à partir d'un capteur aéroporté Hyspex VNIR-1600 opérant dans la gamme spectrale du visible et proche-infrarouge (entre 400nm et 1000nm). Les données de référence archéologique utilisées sont, pour la zone d'Er Lannic, issues de relevés effectués sur le site mégalithique de 1990 à 2018, et pour l'archipel de Molène, issues d'un inventaire des anciennes pêcheries de l'estran (Stéphan, Gandois, et al., 2019).

Dans une première étude (chapitre 6), menée sur le **site mégalithique d'Er Lannic** qui est un site composé de deux hémicycles de stèles dont l'un est constamment immergé, **nous avons évalué l'imagerie hyperspectrale aéroportée pour cartographier de structures archéologiques submergées en eaux peu profondes**. Les principales questions posées dans ce chapitre sont les suivantes : (i) Les structures archéologiques immergées peuvent-elles être identifiées à l'aide de l'imagerie hyperspectrale aéroportée ? (ii) Comment peuvent-elles être détectées automatiquement et (iii) caractérisées spatialement et spectralement ?

Pour répondre à ces questions, nous avons développé une méthodologie d'analyse de l'imagerie hyperspectrale (prétraitée en réflectance de surface), incluant d'une part l'analyse des données pour la visualisation d'anomalies spatio-spectrales et d'autre part l'analyse par inversion d'un modèle de transfert radiatif pour l'estimation de paramètres physiques (réflectance du fond et hauteur d'eau) de la scène.

La première approche est basée sur l'utilisation de techniques de réduction de dimension afin de supprimer les informations spectralement redondantes ou le bruit, et ainsi mettre en évidence les variations spectrales informatives présentes dans l'image. La technique qui a été utilisée ici est la « minium noise fraction » (MNF), qui est une transformation linéaire basée sur deux analyses en composantes principales (ACP) utilisées séquentiellement (Green et al., 1988). Alors que l'ACP ordonne les composantes en fonction de leur variance, la MNF ordonne les composantes en

fonction de la qualité de l'information, mesurée par le rapport signal/bruit (SNR). Les composantes extraites par cette méthode sont ensuite exploitées de deux manières indépendantes : (1) par interprétation visuelle, où les composantes sont combinées pour générer une image composite où les anomalies spatial-spectrales sont mises en évidence. (2) par détection automatique, où l'image composite est analysée afin d'y détecter des anomalies locales (détecteur de type Reed-Xiaoli) ou globales (détecteur de type forêt d'isolation).

La seconde approche est basée sur l'inversion d'un modèle de transfert radiatif en zone de petits fonds : le modèle de Lee (Lee et al., 1998). Ce modèle semi-analytique décrit mathématiquement la relation entre les paramètres physiques de la colonne d'eau et du fond (constituants, hauteur d'eau, réflectance du fond) et la réflectance de surface. Par optimisation, ce modèle est inversé afin d'estimer pour chaque pixel de l'image (chaque mesure hyperspectrale), les caractéristiques physiques du milieu telles que la hauteur d'eau et la réflectance du fond.

D'une part, les résultats nous ont permis de montrer qu'il était possible de visualiser des structures immergées en utilisant une approche orientée « données » basée sur la réduction de dimensions spectrales (type Minimum Noise Fraction) de la réflectance de surface, et que des algorithmes de détection d'anomalies locales (type Reed-Xiaoli) et globales (forêt d'isolation) pouvaient être utilisés en complément pour faciliter l'identification de structures d'intérêt à partir des images composites dérivées de la réduction de dimensions. D'autre part, nous avons également démontré qu'une première caractérisation morphologique et spectrale des structures du fond (stèles) pouvait être envisagée en mobilisant une approche basée sur l'inversion d'un modèle de transfert radiatif en eaux peu profondes. Les résultats de cartographie, comparés aux données de référence archéologiques et aux données de topo-bathymétrie existantes (Litto3D®) ont permis de confirmer le potentiel de l'imagerie hyperspectrale aéroportée pour la cartographie archéologique en zone de petits fonds. L'étude ci-dessus a fait l'objet de la publication suivante :

> Guyot, A., Lennon, M., Thomas, N., Gueguen, S., Petit, T., Lorho, T., Cassen, S., & Hubert-Moy, L. (2019). Airborne Hyperspectral Imaging for Submerged Archaeological Mapping in Shallow Water Environments. *Remote Sensing*, 11(19), 2237. https://doi.org/10.3390/rs11192237

Dans une seconde étude (chapitre 7), nous avons poursuivi **l'évaluation de l'imagerie hyperspectrale aéroportée pour la cartographie archéologique en zone immergée dans un contexte géo-archéologique différent** : celui de **l'archipel de Molène** (Finistère) et de ses **anciennes pêcheries d'estran**, dont certaines sont aujourd'hui situées à plusieurs mètres sous le niveau des plus basses mers astronomiques. L'étude a également été menée dans un cadre d'évaluation plus large, incluant la documentation de structures immergées déjà inventoriées, mais aussi la recherche et l'identification d'anomalies potentiellement archéologiques sur le fond

marin à l'échelle de l'archipel. Les principales questions abordées dans ce chapitre sont : (i) Les structures archéologiques immergées peuvent-elles être identifiées à l'aide de l'AHI ? Avec cette deuxième étude de cas, nous posons implicitement la question dans un contexte géo-archéologique différent (ii) L'imagerie hyperspectrale aéroportée peut-elle être utilisée non seulement pour cartographier et documenter les structures connues mais aussi comme support à la prospection archéologique en zone de petits fonds ? (iii) Et plus généralement, l'imagerie hyperspectrale aéroportée peut-elle être utilisée pour visualiser des paysages immergés à grande échelle ?

Afin de répondre à ces questions, deux axes méthodologiques ont été développés : le premier est basé sur une approche orientée « données », et le second sur une approche orientée « physique ». Pour l'approche orientée « données », deux stratégies d'échantillonnage ont été utilisées pour guider la réduction de la dimensionnalité (MNF) et la visualisation des anomalies spectrales/spatiales. Ces stratégies d'échantillonnage ont consisté à définir deux modèles de variabilité spectrale : le premier, généraliste, a été défini sur l'ensemble de la zone de petits fonds ; le second, spécifique, a été limité aux structures cibles et à leur environnement proche. Ces deux modèles ont permis de calculer des transformations (réduction de dimension MNF) et de proposer des visualisations spatio-spectrales adaptées respectivement au contexte de petits fonds et au contexte des pêcheries. Pour l'approche orientée « physique », l'inversion du modèle de transfert radiatif a été réalisée à partir des données de réflectance de surface et d'un modèle linéaire de mélange spectral (librairie spectrale collectée localement sur la zone) utilisé comme support lors de l'inversion (Sicot et al., 2015). Les estimations de la bathymétrie et de la réflectance du fond issues de l'inversion du modèle ont ensuite été combinées pour proposer une visualisation à grande échelle du paysage submergé. Les résultats ont montré que les informations dérivées de l'imagerie hyperspectrale apparaissent comme la source d'information la plus pertinente (89% de détection) -comparée aux données LiDAR bathymétriques et sondeur acoustique (80%) et à l'imagerie aérienne standard (22%)- pour la détection des barrages à poissons inventoriés dans l'archipel. Les deux approches (orientée « données » et orientée « physique ») ont ensuite été appliquées pour mener une campagne de prospection archéologique afin de repérer et caractériser des anomalies du fond marin non encore identifiées. Une opération de plongée de vérification, effectuée en juillet 2021 sur 3 d'entre elles, a confirmé la présence des structures immergées détectées par imagerie hyperspectrale. Les caractéristiques de ces structures comme l'agencement de blocs sur chant, la morphologie linéaire de l'anomalie et son positionnement dans le contexte paysagé appuient l'hypothèse de structures d'origine anthropique, plus particulièrement de vestiges d'anciennes pêcheries d'estran. L'étude ci-dessus a fait l'objet d'un article soumis pour publication dans une revue internationale :

> Guyot, A., Lennon, M., Stéphan, P., Péres, T., Hascot, M., Gandois, H., Daire, M-Y., Hubert-Moy, L. (2021). Airborne hyperspectral imagery for archaeological prospection of

> submerged landscapes. A case study of the stone tidal fishweirs of the Molène archipelago, France. (submitted in october 2021 in *Archaeological Prospection*).

Les résultats de cette seconde partie démontrent le potentiel de l'imagerie hyperspectrale aéroportée dans un contexte de cartographie archéologique en zone immergée, d'une part pour la documentation de sites existants, et d'autre part pour la prospection archéologique à large échelle. A notre connaissance, ce potentiel n'avait jusqu'à présent jamais été évalué. Nous avons ainsi pu démontrer l'intérêt des approches dites « statistique » (*data-driven*) et « physiques » (*physics-based*) et leur complémentarité. Ainsi l'approche « statistique » permet la visualisation (et éventuellement la détection automatique) d'anomalies spatio-spectrales liées à la présence de structures archéologiques immergées en zone de petits fonds. L'approche « physique » permet quant à elle une description du milieu avec l'estimation des paramètres de hauteur d'eau et de réflectance du fond. Outre leur apport pour la caractérisation morphologique et spectrale des structures archéologiques, ces paramètres ont été ici également visualisés sous forme cartographique pour une représentation inédite du paysage submergé, corrigée des effets de diffusion et d'absorption de la lumière dans la colonne d'eau.

Ces résultats et leurs interprétations sont toutefois à pondérer avec les limites liées à l'usage de l'imagerie hyperspectrale en milieu côtier. Ces limites incluent notamment la dépendance aux conditions locales d'un point de vue météo-océanique (turbidité, conditions de surface de la mer, conditions d'illumination), d'un point de vue géographique (topographie côtière et nature du fond). Le contexte archéologique est également à considérer (type de site, degré de préservation). Dans notre cas, les expérimentations ont été ainsi effectuées dans un contexte de recherche restreint aux structures minérales (stèles, barrages de pêcherie) le plus souvent colonisées par la flore marine. Les contraintes liées à la validation des résultats en milieu submergés sont également à prendre en compte. Il serait ainsi intéressant de comparer les estimations de réflectance du fond avec des mesures spectrales *in-situ* (spectroscopie subaquatique). Ces résultats et limites apparaissent toutefois comme des perspectives intéressantes dans le contexte d'inventaire et de conservation du patrimoine archéologique dans un milieu aussi dynamique et complexe que l'interface terre-mer.

Pour conclure, au travers des deux axes de recherche présentés dans cette thèse, qui évaluent respectivement des données LiDAR en zones émergées et des données hyperspectrales en zones immergées, nous avons pu démontrer une partie du potentiel et des limites de la télédétection optique aéroportée et de sa contribution dans un cadre d'application à la cartographie archéologique.

Plusieurs décennies de recherche en imagerie aérienne et en analyse de données appliquées à l'archéologie avaient déjà permis de montrer l'intérêt de ces données de télédétection. L'originalité de la recherche menée dans le cadre cette thèse réside dans l'évaluation de ces données dans des contextes spécifiques, sous couvert forestier et en zone de petits fonds, et par des approches méthodologiques originales. Ces travaux contribuent au développement de nouvelles connaissances en archéologie (enrichissement qualitatif et quantitatif de la carte archéologique sur le domaine terrestre et le domaine maritime), et en télédétection appliquée.

D'un point de vue conceptuel, nous avons par exemple proposé des approches inclusives combinant d'une part la perception visuelle de l'information, notamment en utilisant des techniques de visualisation, et d'autre part l'analyse quantitative ou numérique des données à travers l'utilisation d'algorithmes de détection, ou de modèles semi-analytiques. Ce choix a été motivé par le souhait de positionner la télédétection comme un outil support intégré à une démarche de recherche archéologique. Cette intégration passe notamment par une imbrication plus forte des approches de la télédétection, considérée comme de la « desk-based research » et de la recherche archéologique de terrain, considérée dans ce cadre comme de la « field-based research ».

D'un point de vue méthodologique, l'évaluation de méthodes (semi-)automatiques de segmentation et de caractérisation de structures archéologiques sur données LiDAR est une contribution originale de cette thèse ; l'évaluation de l'imagerie hyperspectrale en contexte immergé, qui est à notre connaissance, inédite dans le paysage de la recherche archéologique, en est une autre.

Toutefois, malgré un apport indéniable, l'usage de données LiDAR et hyperspectrales aéroportées implique de prendre conscience des différentes sources d'incertitudes inhérentes à ces données et à leur analyse.

Des perspectives peuvent être envisagées sur l'ensemble de la chaîne de traitement des données, depuis l'acquisition jusqu'à l'interprétation en passant par l'analyse. Premièrement, au niveau de l'acquisition des données, l'utilisation de vecteurs et de capteurs aux caractéristiques spatiales ou spectrales différentes serait à évaluer. La miniaturisation des capteurs LiDAR et hyperspectraux qui permet de les embarquer sur des drones en est un exemple, notamment pour produire des données intermédiaires entre les données terrain et les données aéroportées pour le développement d'approches multi-échelles. Des perspectives se présentent également au niveau de l'analyse des données, notamment pour les phases de visualisation et de détection automatique. Pour la visualisation des données, cela implique en particulier d'évaluer les techniques non linéaires de réduction de la dimensionnalité telles que UMAP (uniform manifold approximation) ou les auto-encodeurs par apprentissage profond. Ces techniques pourraient être appliquées aux données hyperspectrales ainsi qu'au résultat de l'analyse topographique à grande

échelle des données de terrain dérivées du LiDAR, afin d'améliorer la perception des relations non linéaires entre les signatures spectrales ou entre les signatures topographiques. En ce qui concerne la détection automatique, la sensibilité des modèles d'apprentissage profond à la qualité et à la représentativité des données d'entrainement reste une contrainte importante, en particulier pour des domaines d'application tels que l'archéologie, où les données de référence sont rares ou incertaines. L'usage d'outils tels que Grad-CAM (Gradient-weighted Class Activation Mapping), qui favorise une meilleure compréhension des comportements de ces modèles complexes, serait à évaluer. Ces perspectives concernent principalement la télédétection LiDAR, mais elles peuvent également concerner la télédétection hyperspectrale dans le contexte de la cartographie archéologique en eaux peu profondes en tenant compte des contraintes spécifiques à la télédétection en contexte immergé. Sur cet aspect, l'étude initiée sur l'archipel de Molène a soulevé des questions concernant l'inversion du modèle de transfert radiatif en petits fonds. Afin de mieux évaluer les résultats de réflectance du fond notamment, une campagne de spectroscopie sous-marine de terrain est prévue en 2022 pour créer une bibliothèque spectrale sous-marine qui permettrait (1) d'évaluer et d'améliorer l'inversion du modèle de transfert radiatif, et (2) d'accéder à des mesures *in situ* caractérisant les structures archéologiques et naturelles immergées. Sur la base des résultats obtenus dans cette thèse, une autre perspective méthodologique apparaît : l'évaluation des données topo-bathymétriques LiDAR. Cette évaluation pourrait être réalisée en comparant ces données avec les données hyperspectrales, notamment pour estimer la bathymétrie, par exemple sur le site immergé d'Er Lannic. La complémentarité des deux types données de télédétection (passive et active) pourrait également être évaluée par la mise en œuvre de techniques de fusion de données à différents niveaux : au niveau « modèle », par exemple avec l'intégration du forçage de la bathymétrie LiDAR lors de l'inversion du modèle de transfert radiatif afin d'améliorer l'estimation de la réflectance de fond, ou au niveau « données » brutes ou dérivées, par exemple pour combiner l'information de variations topo-bathymétriques issues du capteur actif et de variations spectrales issues du capteur passif.

D'un point de vue thématique, les axes de développement que nous avons initiés avec la segmentation (semi-)automatique d'objets ouvrent des perspectives pour soutenir des approches de comparaison site/site et site/anomalie. La segmentation d'objets, en facilitant la caractérisation morphologique, spectrale, contextuelle et topologique des structures archéologiques pourrait soutenir les interprétations typo-morphologiques ou chrono-typologiques. Ces approches pourraient, par exemple, s'inspirer, voire compléter celles qui sont actuellement développées pour la classification typologique des enceintes de l'âge du fer en Bretagne (Leroux et al., 1999). Des approches spécifiques par contexte géo-archéologique pourraient aussi être développées. Par exemple, dans les zones d'estran où les préoccupations de préservation du patrimoine naturel et du patrimoine culturel des habitats naturels se font écho, les résultats intermédiaires ont mis en évidence l'apport des informations topographiques et spectrales pour la cartographie et

l'interprétation sur le terrain. Bien que ces prospections "à l'aveugle" n'aient pas encore donné lieu à des investigations spécifiques sur ces environnements, les importants jeux de données collectés (notamment la spectroscopie de terrain et l'imagerie hyperspectrale sur Molène et le Golfe du Morbihan) devraient permettre d'initier des programmes ciblés dans lesquels les méthodologies proposées dans le cadre de cette thèse -et dont le développement se poursuit- pourraient être rapidement mobilisées pour l'évaluation des données/méthodes utilisées comme support pour répondre à des questions archéologiques particulières posées sur le littoral (sites portuaires, épaves).

Ces nombreuses perspectives illustrent bien l'intérêt de développer des approches de recherche basées sur des collaborations pluridisciplinaires et dans lesquelles toutes les parties (laboratoires de recherche, autorités nationales et locales, entreprises privées) mobilisent leurs expériences et leurs connaissances pour une meilleure compréhension de notre passé et pour la protection de ce patrimoine archéologique à transmettre aux générations futures. La région Bretagne, avec ses 2470 km de côtes, un patrimoine culturel exceptionnel et un pôle de recherche actif en archéologie et dans le domaine géospatial, tant au niveau académique qu'industriel, est un lieu idéal pour poursuivre la quête stimulante initiée au cours de cette thèse.

DOCTORAT / SOCIETES
BRETAGNE \ TEMPS
LOIRE / TERRITOIRES

UNIVERSITÉ RENNES 2

Titre : **Apport des données LiDAR et hyperspectrales aéroportées pour la cartographie archéologique en milieux terrestres et immergés**

Mots clés : Télédétection ; Cartographie archéologique ; Système laser aéroporté ; Imagerie spectrale ; Analyse multi-échelle ; Deep CNN.

Résumé : Menacé par des pressions naturelles et anthropiques croissantes, le patrimoine archéologique fait l'objet d'enjeux de connaissances scientifiques et de mesures de protection. Or les prospections archéologiques sont très difficiles à mener dans des environnements forestiers ou immergés. Dans ce contexte, cette thèse vise à évaluer l'apport des données LiDAR et hyperspectrales aéroportées pour la détection et la caractérisation de structures archéologiques, ces données ayant montré leur intérêt pour accéder à des informations inédites sous la canopée ou sous l'eau. Pour répondre à cet objectif, nous avons développé de nouvelles approches de visualisation et de détection automatique basées notamment sur le deep learning.

Nous avons d'abord exploité des données LiDAR topographiques afin de détecter et caractériser des structures archéologiques datant principalement de la période mégalithique, en contexte émergé sur la région de Carnac (Morbihan). Puis nous avons évalué l'imagerie hyperspectrale en contexte immergé sur le site mégalithique d'Er Lannic (Morbihan) et sur l'archipel de Molène (Finistère). Les résultats ont montré l'intérêt des approches d'analyse multi-échelles et d'apprentissage automatique appliquées aux modèles numériques dérivés des données LiDAR, en particulier sous couvert forestier. Nous avons aussi montré l'apport original de l'imagerie hyperspectrale pour la détection et la caractérisation de structures en zone de petits fonds, ouvrant ainsi de nouvelles perspectives quant à l'exploration archéologique de paysages submergés.

Title : **Contribution of airborne LiDAR and hyperspectral data to archaeological mapping in terrestrial and submerged environments**

Keywords : Remote sensing; Archaeological mapping; Airborne laser system; Spectral imagery; Multiscale analysis; Deep CNN.

Abstract: Threatened by increasing natural and anthropic pressures, the archaeological heritage is the subject of scientific knowledge and protection measures. However, archaeological surveys are very difficult - if not impossible - to carry out in forest or submerged environments. In this context, this thesis aims to evaluate the contribution of airborne LiDAR and hyperspectral data for the detection and characterization of archaeological structures, as these data have shown their interest in providing new information under the canopy or in shallow waters. For that purpose, we have developed new visualization approaches, and automatic detection methods based on deep learning.

First, we used topographic LiDAR data to detect and characterize archaeological structures dating mainly from the megalithic period, in a terrestrial context in the Carnac region (Morbihan). Then, we evaluated hyperspectral imagery in a submerged context in the megalithic site of Er Lannic (Morbihan) and in the Molène archipelago (Finistère). The results showed the interest of multi-scale analysis and machine learning approaches applied to numerical models derived from LiDAR data, in particular under forest cover. We also demonstrated the original contribution of hyperspectral imagery for the detection and characterization of structures in shallow waters, thus opening up new perspectives for the archaeological exploration of submerged landscapes.